



TAMPEREEN TEKNILLINEN YLIOPISTO
TAMPERE UNIVERSITY OF TECHNOLOGY

Narayan Puthanmadam Subramaniam
Recurrence Network Analysis of EEG Signals
A Geometric Approach



Julkaisu 1364 • Publication 1364

Tampere 2016

Tampereen teknillinen yliopisto. Julkaisu 1364
Tampere University of Technology. Publication 1364

Narayan Puthanmadam Subramaniam

Recurrence Network Analysis of EEG Signals
A Geometric Approach

Thesis for the degree of Doctor of Science in Technology to be presented with due permission for public examination and criticism in Sähkötalo Building, Auditorium S2, at Tampere University of Technology, on the 29th of January 2016, at 12 noon.

Tampereen teknillinen yliopisto - Tampere University of Technology
Tampere 2016

ISBN 978-952-15-3671-7 (printed)
ISBN 978-952-15-3694-6 (PDF)
ISSN 1459-2045

TAMPERE UNIVERSITY OF TECHNOLOGY

Abstract

Faculty of Computing and Electrical Engineering,
Department of Electronics and Communications Engineering

Doctor of Technology

Recurrence network analysis of EEG signals

A Geometric Approach

by Narayan PUTHANMADAM SUBRAMANIYAM

Understanding the neuronal dynamics of dynamical diseases like epilepsy is of fundamental importance. For instance, establishing the presence of deterministic chaos can open up possibilities that can lead to potential medical applications, including timely prevention of seizures. Additionally, understanding the dynamics of interictal activity can greatly aid the localization of epileptic foci without the need for recording seizures. Recurrences, a fundamental property of dynamical systems, are useful for characterizing nonlinear systems. Recurrence networks, which are obtained by reinterpreting the recurrence matrix as an adjacency matrix of a complex network, are useful in characterizing the structural or geometric properties of the underlying system. Recurrence network analysis has established itself as a versatile tool in the field of nonlinear time series analysis and its applicability in investigating neural dynamics remains unexplored. Certain recurrence network measures are particularly sensitive to the presence of unstable periodic orbits (UPOs), which are important for detecting determinism and are the backbone of chaotic attractors.

In this thesis, we introduce recurrence network analysis as a tool for nonlinear time series analysis of epileptic electroencephalographic (EEG) signals. We present novel results based on the application of recurrence network analysis combined with surrogate testing to intracranial and extracranial epileptic EEG signals. In addition, using paradigmatic examples of dynamical systems, we present theoretical results exploring the effect of increasing noise levels on recurrence network measures.

Using paradigmatic model systems, we first demonstrate that recurrence network measures can distinguish between deterministic (chaos) and stochastic processes, even at short data lengths (≈ 200 samples). In particular, our results from theoretical simulations show that recurrence network measures, particularly transitivity, local clustering

coefficient, assortativity, and betweenness centrality can successfully distinguish between deterministic chaotic and stochastic processes (after additional embedding) due to their sensitivity to the presence of UPOs. Our results also show that recurrence network measures like transitivity and average path length are robust against noise and perform better than the Complexity-Entropy plane method at short data lengths. Furthermore, our results show that the effect of noise on the recurrence network measures can be minimized by increasing the recurrence rate.

For the analysis of real-world data such as EEG signals, we combined the recurrence network approach with surrogate data to test for the structural complexity in healthy and epileptic EEG signals. Here our results point to an increasing complexity of EEG recordings when moving from healthy to epileptic conditions. Furthermore, we used both univariate network measure and bivariate cross-network measure to distinguish between the structural properties of interictal EEG signals recorded from epileptic and non-epileptic brain areas. Here, our results clearly demonstrated that interictal EEG signals recorded from epileptic areas are more deterministic and interdependent compared to interictal activity recorded from non-epileptic areas. Finally, we show that recurrence network analysis can be applied to uncover the dynamical transitions in neural signals using short segments of data (≈ 150 to 500 samples). To demonstrate this, we used two kinds of neural data - epileptic EEG data and local field potential (LFP) signals recorded during a visuomotor task. We observed that the temporal fluctuations observed in the recurrence network measures are consistent with the dynamical transitions underlying the epileptic and task-based LFP signals.

To conclude, recurrence network analysis analysis can capture the complexity in the organization of EEG data in different dynamical states in a more elaborated fashion compared to other approaches such as nonlinear prediction error or correlation dimension. By means of the recurrence network measures, this difference can be assessed not only qualitatively (as when using as tests for nonlinearity), but also quantitatively. Thus, coupled with its ability to operate on short-window sizes and robustness to noise, recurrence network analysis can be a powerful tool to analyze the dynamics of multi-scale neural signals.

Acknowledgements

The work presented in this doctoral thesis was carried out during 2012-2015. This dissertation would not have been possible without the help and contribution of many people, to whom I owe great debt.

Foremost, I would like to express my deepest gratitude to my advisor Prof. Jari Hyttinen, who provided endless support and guided me throughout my research. He also gave me the freedom to conduct the research and explore, which has helped me to grow as a scientist. I thank the pre-examiners of this dissertation - Dr. Hugues Berry (*Institut national de recherche en informatique et en automatique*, France) and Prof. Pasi Karjalainen (*Itä-Suomen yliopisto*, Finland), for their careful review and helpful comments, that has helped in improving the quality of the manuscript. I also thank Prof. Jan C de Munck (*Vrije Universiteit*, Amsterdam) for agreeing to act as the opponent for my thesis.

I am deeply grateful to Dr. Jonathan Donges (*Potsdam-Institut für Klimafolgenforschung*, Germany), whose deep expertise in nonlinear time series analysis and dynamical systems theory has helped me strengthen my foundation in these subjects. I also thank Dr. Kazutaka Takahashi (*University of Chicago*, USA) for his guidance, collaboration and for hosting me in his Lab and home in Chicago. I also thank the anonymous reviewers of my publications for their advice and comments. Prof. Jakko Malmivuo has been instrumental in developing my understanding in the field of bioelectricity through his excellent lectures and I thank him for providing me the first opportunity to work in TUT. I thank Prof. Jari Viik for his valuable advice and being the go-to-guy for statistics.

I would like to take this opportunity to thank all my past and present colleagues at Finn-Medi and TUT. Firstly, I thank Dr. Outi Väisänen and Dr. Katrina Wendel-Mitoraj for guiding me at the start of my research career. I thank Dr. Jarno Tanskanen for all the invaluable discussions related to research and life in general, during the coffee hours, which I truly treasure. I thank Markus Hannula and Nathaniel Narra, for being such wonderful colleagues apart from inducting me to orienteering. I truly cherish the discussions and time spent with them. Also, a big thank you to our Jukola team - Inkeri Vornanen, Olli Koskela along with Jarno and Markus. Let us do it again (and better) next year!

I would like to thank my past and present colleagues in the EEG group - Atte Joutsen, Andrei Jakab, Dr. Jukka Peltola, Prof. Ville Jäntti, Prof. Kaisa Hartikainen and Dr. Kai Lehtimäki for encouraging discussions on various aspects of research related to EEG. I would also like to express my gratitude and appreciation to Kerstin Lenk and Dr. Michelangelo Paci for their valuable comments and feedback on my research. I thank Emre Kapucu, Florentino Caetano dos Santos, Javier Garcia, Dr. Pasi Kauppinen, Dr. Soile Nymark, Dr. Tomas Cervinka, and Dr. Ville-pekka Seppä for creating an inspiring and friendly work atmosphere. I thank Soile Lönnqvist for being almost immediately responsive to any queries I have had and for taking care of all the administrative tasks.

I am extremely grateful for the financial support from the International Graduate School for Biomedical Engineering and Medical Physics (iBioMEP) during 2013-2014 that helped complete my doctoral thesis. I would also like to acknowledge and thank the

support of EU funded 3DNeuron project and the Tekes funded Human Spare Parts II project.

I also thank the community members and countless contributors to the Open Source programs and tools like L^AT_EX, Python and Linux. I have benefited enormously from these tools and have used them to produce most of my results and to complete this thesis. I also thank the Tampere Center for Scientific Computing. Without their tools and services, I could not have completed my huge computational tasks in reasonable time.

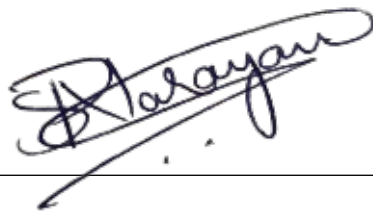
I thank my friends Karan, Sarang, Pooja and Deepa, for all their help and support, and also for organizing many trips, lunches and dinners. These were much needed breaks that helped me rejuvenate from all the publishing and thesis related stress.

I cannot express in words how grateful I am to my parents, my father Subramaniam Puthanmadam and my mother Padma Subramaniam, who have made countless sacrifices and have always supported and encouraged me to follow my (eccentric) choices. My debt of gratitude to them is beyond measure. I thank my aunt - Lakshmi Ammal for her support during my formative years. I thank my parents-in-law, Venkatraman Ramakrishnan and Sarojini Ramakrishnan, for always being supportive, encouraging, and taking pride in my little achievements.

I am deeply grateful to my wife Anusha, for being the love of my life and providing me the emotional support during this journey. Without her endless patience, sacrifices, generosity, and love, this thesis would have never materialized. I thank her for always believing in me, which reinforced my self-belief and for standing by me in good times and most importantly, in bad times. I am deeply indebted to her for helping me deal with agonizing periods during this journey in the most positive manner.

Last but not the least, to the core of my life - my son Atharv, thank you for your smiles, hugs, kisses and for making me want to be a better human being.

Signed: _____



Place and Date: _____

Esfoo, 01.01.2016

Publications List

This thesis is based on the following list of selected publications. The following publications are referred to as [P-N] in the text where N stands for the publication number. All the publications have been reprinted in this thesis with permission from the publisher.

P-I

Puthanmadam Subramaniyam, N., Friedemann Donges, J., and Hyttinen, J. **Signatures of chaotic and stochastic dynamics using ε -recurrence networks**, *Proceedings of the Royal Society of London A: Mathematical, Physical and Engineering Sciences*, 471(2183):20150349, 2015.

P-II

Puthanmadam Subramaniyam, N. and Hyttinen, J. **Dynamics of intracranial electroencephalographic recordings from epilepsy patients using univariate and bivariate recurrence networks**, *Physical Review E*, 91(2):022927, 2015.

P-III

Puthanmadam Subramaniyam, N., and Hyttinen, J. **Characterization of dynamical systems under noise using recurrence networks: Application to simulated and EEG data**, *Physics Letters A*, 378(46):3464-3474, 2014.

P-IV

Puthanmadam Subramaniyam, N., and Hyttinen, J. **Analysis of nonlinear dynamics of healthy and epileptic EEG signals using recurrence based complex network approach**, *6th International IEEE/EMBS Conference on Neural Engineering (NER)*, pages 605,608, 6-8 Nov., San Diego, USA, 2013.

P-V

Puthanmadam Subramaniyam, N., Hyttinen, J., Hatsopoulos, N., and Takahashi, K. **Recurrence network analysis of wide band oscillations of local field potentials from the primary motor cortex reveals rich dynamics**, *7th International IEEE/EMBS Conference on Neural Engineering (NER)*, pages 960-963, 22-25 Apr., Montpellier, France, 2015.

Author's contributions

The author has designed the studies, implemented the methods (except for the program to estimate recurrence networks, which was provided by Dr. Jonathan Donges), analyzed the results, prepared the figures and written the papers in case of publications [P-I]-[P-III]. In case of [P-IV], the author has designed the studies, implemented the methods, analyzed the results, prepared the figures and written the paper. The experiments described in [P-V] were already designed and conducted at Hatsopoulos Lab, University of Chicago, and the data was obtained from Dr. Kazutaka Takahashi for analysis. The author implemented the methods, analyzed the results and prepared the figures in [P-V]. The author wrote [P-V] with equal contribution from Dr. Kazutaka Takahashi. All the papers were read, commented and approved by co-authors.

CONTENTS

Abstract	ii
Acknowledgements	iv
List of original publications	vi
Author's contributions	vii
Contents	viii
List of Figures	xiii
List of Tables	xv
Acronyms	xvii
Mathematical symbols	xix
1 Introduction	1
1.1 General background	1
1.2 Goals of the thesis	4
1.3 Structure of the thesis	4
I Theoretical background and literature review	7
2 Dynamical systems	9
2.1 Continuous and discrete dynamical systems	10
2.2 Attractor	12
2.3 Poincaré recurrences	13
2.4 Poincaré sections	14

3	Nonlinear time series analysis	15
3.1	Phase space reconstruction	15
3.2	Recurrence plots	22
3.3	Fractal dimensions	29
3.4	Other nonlinear measures	30
3.5	Distinguishing chaos and noise	34
3.6	Surrogates	35
4	Complex network theory	39
4.1	Complex networks	39
4.2	Graph theory	40
4.3	Random geometric graphs	43
5	Recurrence networks	45
5.1	Time series to complex networks	45
5.2	Network measures	48
5.3	Local and global measures of dimensions	52
5.4	Bivariate ε -recurrence networks	52
5.5	Properties and applications of ε and bivariate recurrence networks	55
6	Nonlinear time series analysis of EEG	59
6.1	An overview of history and generation of EEG	59
6.2	Nonlinear EEG analysis and its role in epilepsy	60
II	Applications	65
7	Distinguishing stochastic and chaotic processes [P-I]	67
7.1	Introduction	67
7.2	Data and methods	68
7.3	Results and discussion	68
7.4	Summary	76
8	Effect of noise on recurrence networks [[P-I],[P-III]]	81
8.1	Introduction	81
8.2	Data and methods	82
8.3	Results and discussion	82
8.4	Summary	89
9	Recurrence network analysis of EEG signals [[P-III],[P-IV]]	91
9.1	Introduction	91
9.2	Data and methods	92
9.3	Results and discussion	93
9.4	Summary	94
10	Distinguishing focal and nonfocal EEG signals [P-II]	97
10.1	Introduction	97
10.2	Data and methods	99
10.3	Results and discussion	101

10.4 Summary	104
11 Moving window recurrence network analysis of EEG [[P-I],[P-V]]	105
11.1 Introduction	105
11.2 Data and methods	106
11.3 Results and discussions	108
11.4 Summary	113
III General discussions and conclusions	115
12 Overview and discussions	117
12.1 Distinguishing between chaotic and stochastic dynamics	117
12.2 Impact of noise	119
12.3 Application of recurrence network methods to EEG data	120
13 Conclusions	127
Bibliography	129
IV Original publications	
Publication I	
Publication II	
Publication III	
Publication IV	
Publication V	

LIST OF FIGURES

2.1	Lorenz attractor, $\rho = 28$, $\sigma = 10$, $\beta = 8/3$	13
2.2	Rössler attractor, $a = b = 0.1$, $c = 18$	13
3.1	Commutative diagram illustrating the embedding theorem.	16
3.2	Original and reconstructed Lorenz attractor.	17
3.3	x_1 component of the Lorenz system.	19
3.4	Estimation of the optimal lag τ (red circle) using auto mutual information for the x_1 component of the Lorenz system.	20
3.5	Estimation of the minimum embedding dimension using modified FNN method for the x_1 component of the Lorenz system.	21
3.6	Recurrence plots derived from periodic, chaotic and stochastic systems.	23
4.1	A ring lattice with $N = 30$	41
4.2	A WS small world network with $N = 30$ and $p = 0.1$	41
4.3	An Erdős and Reyni random graph with $N = 100$ and $p = 0.15$	41
4.4	A scale-free Barabási-Albert network with $N = 100$	41
4.5	An undirected graph G consisting of 6 vertices and 7 edges.	42
4.6	A subgraph of G consisting of 6 vertices and 4 edges.	42
4.7	An induced subgraph of G consisting of 3 vertices and 3 edges.	42
5.1	Example of a recurrence network derived from the Lorenz system.	48
5.2	Example of a recurrence network derived from the Rössler system.	48
7.1	Distribution of vertex-based measures for chaotic (Lorenz system) and stochastic systems.	72
7.2	Distribution of vertex-based measures for chaotic (Rössler system) and stochastic systems.	73
7.3	Distribution of vertex-based measures for hyperchaotic (Rössler system) and stochastic systems.	74
7.4	Distribution of vertex-based measures for hyperchaotic (Rössler system) and stochastic systems.	75
7.5	Color-coded representation of the local clustering coefficient for Lorenz and stochastic system.	76
7.6	Color-coded representation of the local clustering coefficient for Rössler and stochastic system.	76

7.7	Color-coded representation of the betweenness centrality for Lorenz and stochastic system.	77
7.8	Color-coded representation of the betweenness centrality for Rössler and stochastic system.	77
7.9	Color-coded representation of the closeness centrality for Lorenz and stochastic system.	78
7.10	Color-coded representation of the closeness centrality for Rössler and stochastic system.	78
7.11	Color-coded representation of the degree centrality for Lorenz and stochastic system.	78
7.12	Color-coded representation of the degree centrality for Rössler and stochastic system.	79
8.1	Complexity-Entropy plane for chaotic Lorenz system and corresponding 99 iAAFT surrogates under increasing noise levels for $N = 200$	86
8.2	Complexity-Entropy plane for chaotic Lorenz system and corresponding 99 iAAFT surrogates under increasing noise levels for $N = 1,000$	86
8.3	Color-coded representation of local clustering coefficient for the Lorenz attractor under noise levels 0% (A), 10% (B), 20% (C), 40% (D), 60% (E), and 100% (F). The data length $N = 5,000$, recurrence rate $RR = 0.05$, embedding dimension $m = 3$ and the embedding delay $\tau = 3$. Reproduced from [P-I].	88
8.4	Color-coded representation of log betweenness centrality for the Lorenz attractor under noise levels 0% (A), 10% (B), 20% (C), 40% (D), 60% (E), and 100% (F). The data length $N = 5,000$, recurrence rate $RR = 0.05$, embedding dimension $m = 3$ and the embedding delay $\tau = 3$. Reproduced from [P-I].	88
8.5	Color-coded representation of local recurrence rate (proportional to degree centrality) for the Lorenz attractor under noise levels 0% (A), 10% (B), 20% (C), 40% (D), 60% (E), and 100% (F). The data length $N = 5,000$, recurrence rate $RR = 0.05$, embedding dimension $m = 3$ and the embedding delay $\tau = 3$. Reproduced from [P-I].	89
11.1	Exemplary epileptic EEG data from channel C_4	106
11.2	Estimation of τ using the first local minima of auto mutual information.	107
11.3	Estimation of m using the false nearest neighbor method.	107
11.4	Experimental setup for the visuomotor task.	108
11.5	Location of the Utah microelectrode array in the arm area of the primary motor cortex.	108
11.6	Moving window RNA of epileptic EEG data showing $D\tau$, \mathcal{L} and \mathcal{R} before, during and after the seizure, for $m = 2, 4, 6, 8, 10$	110
11.7	Moving window RNA of epileptic EEG data showing $D\tau$, \mathcal{L} and \mathcal{R} before, during and after the seizure, for $m = 8$	111
11.8	Temporal variation of \mathcal{C} across all channels for [1-30] Hz band.	112
11.9	Temporal variation of \mathcal{C} across all channels for [30-80] Hz band.	112
11.10	Average of \mathcal{C} across all channels for [1-30] and [30-80] Hz band.	112

LIST OF TABLES

5.1 Definition of complex network measures and the corresponding interpretation in the context of recurrence networks	58
6.1 Overview of some of the nonlinear time series methods used in epileptic EEG analysis	63
7.1 Global measures for recurrences networks derived from chaotic (Lorenz) and stochastic systems	69
7.2 Global measures for recurrences networks derived from chaotic (Rössler) and stochastic systems	70
7.3 Global measures for recurrences networks derived from hyperchaotic and stochastic systems	70
7.4 Global measures for recurrences networks derived from hyperchaotic and stochastic systems	70
8.1 Results of surrogate analysis on simulated chaotic signals.	83
8.2 As in Table 8.1 , but for \mathcal{L} as discriminating statistic.	83
8.3 Comparison of recurrence network measure \mathcal{T} with Complexity-Entropy approach for various data lengths and levels of noise.	85
8.4 Effect of various data lengths and levels of noise on the recurrence network measures \mathcal{L} and \mathcal{R}	87
9.1 Five sets of EEG data	92
9.2 Result from surrogate analysis.	94
10.1 Comparison of the rejection probabilities for the focal and non-focal EEG signals.	102
10.2 Same as Table 10.1, but for bivariate measures.	102
10.3 Contrast between focal and nonfocal EEG signals using truncated Fourier transform surrogates.	103

AAFT amplitude adjusted Fourier transform.

A-NN adaptive nearest neighbor recurrence network.

CRN cross recurrence network.

CRP cross recurrence plot.

CRQA cross recurrence quantification analysis.

DVV delay vector variance.

ECoG electrocorticography.

EEG electroencephalography.

FFT fast Fourier transform.

fMRI functional magnetic resonance imaging.

FNN false nearest neighborhood.

HVG horizontal visibility graph.

iAAFT iterative amplitude adjusted Fourier transform.

JRN joint recurrence network.

JRP joint recurrence plot.

***k*-NN** *k*-nearest neighbor recurrence network.

KS-2 two-sample Kolmogorov-Smirnov.

LFP local field potential.

ODE ordinary differential equation.

RGG random geometric graph.

RN recurrence network.

RNA recurrence network analysis.

RP recurrence plot.

RQA recurrence quantification analysis.

RS random shuffling.

SSS small shuffle surrogate.

TFT truncated Fourier transform.

UPO unstable periodic orbit.

VG visibility graph.

MATHEMATICAL SYMBOLS

A	Adjacency matrix
\mathcal{A}	Attractor set
b_i	Betweenness centrality
c_i	Closeness centrality
\mathcal{C}_i	Local clustering coefficient
\mathcal{C}	Global clustering coefficient
$d(i, j)$	Geodesic distance
$\delta(i, j)$	Kronecker delta
$D_{\mathcal{T}}$	Transitivity dimension
E	Edge set
ε	Recurrence threshold
G	Graph
I	Identity matrix
k_i	Degree centrality
\mathcal{L}	Average path length
m	Embedding dimension
P	Nonlinear prediction error
R	Recurrence matrix
\mathcal{R}	Assortativity
t	Time
τ	Embedding delay or lag
$\Theta(\cdot)$	Heaviside function
\mathcal{T}	Transitivity
V	Vertex set
$\ \cdot\ $	Norm

*If our brains were simple enough for us
to understand them, we'd be so simple
that we couldn't.*

IAN STEWART (1945–)

1.1 General background

Complex systems are ubiquitous and are characterized by dynamical interactions between different subsystems, leading to emergent properties. Complex systems also display spatial and temporal patterns on a scale that is orders of magnitude bigger than the scales at which the interactions between the subsystems occur [1]. Many complex systems are inherently nonlinear and thus, cannot be adequately described by linear models and methods. There has been a steady increase in the application of methods derived from nonlinear and chaos theory to understand the processes governing the interactions in complex systems [2], that abound in the field of ecology, sociology, economics, climatology, and biology, to name a few. Understanding the dynamics of complex systems and predicting their behavior is a fascinating problem, with many practical applications, that requires an interdisciplinary approach.

The human brain, which can probably be regarded as the most complex system, comprises of more than 100 billion neurons with each of them making about 1,000 connections. It is needless to say that this intricate network of 100 trillion connections renders itself to sophisticated information processing capabilities [3] of bewildering complexity.

Even at the scale of a single neuron, the associated dynamic properties are complex, displaying bursts, bifurcations and limit cycles. A single neuron receives multiple input signals and if the sum of the signals received exceeds a threshold, a nerve pulse known as action potential is initiated. This threshold and saturation phenomena already gives rise to nonlinearity at the level of a single neuron [4]. An important achievement in the field of neurophysiology, contributed by the theory of nonlinear dynamics, is the mathematical model of action potential in the squid giant axon [5], which was proposed by Hodgkin and Huxley [6] in the year 1952. The Hodgkin and Huxley model is a system of four, nonlinear, ordinary differential equations (ODEs). Other popular models that describe the nonlinearity of neuronal dynamics include Fitzhugh-Nagumo and the NaK model. These models, despite their simplicity, are capable of describing variety of rich dynamics including spikes and bursts, limit cycles, homoclinic orbits, chaos and many more [3].

Nonlinear time series analysis of neural recordings is an important and popular theoretical approach to study the nonlinear dynamics of neurons. Such recordings are often easily available across multiple spatial scales including single neuron recordings, local field potential (LFP) recordings, intracranial electroencephalography (EEG) recordings (also known as electrocorticography (ECoG)), and surface EEG recordings. Among these recording modalities, surface EEG is noninvasive, readily accessible and cost-effective recording technique that captures the summed activity of millions of neurons. Thus, it is not surprising that nonlinear time series analysis has been extensively applied to EEG data [7]. From the initial euphoria of finding the elusive chaotic dynamics to a recently more subtle approach of simply characterizing the nonlinearity in EEG signals, the nonlinear dynamical analysis of EEG time series has motivated the development and application of numerous nonlinear measures [8] for both healthy and pathological EEG signals.

Epilepsy, which affects roughly 1 % of the world's population, is probably the most important application for nonlinear dynamical analysis of EEG time series [7, 9]. Epilepsy is characterized as a dynamical disease due to the unpredictable and recurrent nature of epileptic seizures. Generally speaking, any disease that leads to abnormal dynamics in a physiological system operating within a range of control parameters, is defined as a dynamical disease [10]. In case of epilepsy, the presupposition is that the neuronal system exhibits multistable dynamics. It has been observed that epileptic seizures (ictal state) are highly nonlinear compared to the normal, steady-state of ongoing EEG activity (known as interictal state) in epileptic patients. Additionally, a third state known as preictal state is presupposed to hold the key between the transition from an interictal state to ictal state. Thus, in the case of dynamical diseases like epilepsy, the tools from nonlinear dynamical theory are particularly attractive in studying the fingerprints of

different dynamical states and can help us to formally understand how the occurrence of manifestations of epilepsy takes place [11]. Measures like nonlinear prediction error, correlation dimension, Lyapunov exponent, and information theory based measures have been used for nonlinear analysis of epileptic EEG signals (see Chapters 3 and 6 for further reading).

Dynamical systems display two fundamental properties - **determinism** and **recurrence** [2]. A deterministic dynamical system can be defined as a system whose future behavior can be accurately predicted, given that sufficient knowledge for the current state of the system exists. Recurrence is another property which can be used to characterize the nonlinear dynamics of a system. In 1890, Henri Poincaré introduced the concept of recurrence, while addressing the three body problem [12]. Nearly a century later, in 1987, J.-P. Eckman introduced **recurrence plots (RPs)** [13], a two-dimensional graphical plot to visualize recurrent behavior of dynamical systems. RPs have been successfully applied to characterize the underlying dynamical properties of wide variety of systems [2]. A further important contribution made in the field of recurrence plots was the introduction of recurrence quantification analysis (RQA) tool to objectively quantify the structure of recurrence plots [14]. Recently, by integrating the approach from complex network theory and nonlinear dynamical systems theory, network-based nonlinear time series analysis has been proposed. Such networks constructed from time series are based on the recurrences in phase space and are known as recurrence networks (RNs). Topological characterization of such networks using tools from **graph theory** allows us to analyze the dynamically relevant structural properties of the time series data [15–17]. In particular, RNs encode the geometric information about the underlying system which can be characterized (for example using graph theoretical measures) to extract information on the geometric properties of the attractor [18]. Thus, RNs provide useful and complementary insights into phase space structures that are otherwise not provided by other methods of nonlinear time series analysis [16]. Methods based on RNs are particularly advantageous over some other nonlinear measures due to their applicability to short and non-stationary data [15].

Given the advantages and potential that recurrence network analysis (RNA) has demonstrated in characterizing the structural properties of time series, its application to the analysis of neural dynamics has not yet been explored. In particular, it has not been studied if RN measures which are derived from graph theory, can be combined with surrogate analysis to study the structural properties of EEG time series, especially in the context of epilepsy. Establishing the presence of deterministic chaos in pathologies like epilepsy can lead to useful medical applications [19]. Many RN measures are sensitive to the presence of unstable periodic orbits (UPOs), which are the backbone of chaotic attractors and thus can be used to establish determinism. With reference to the

preceding statement, the ability of recurrence networks to distinguish between (chaotic) deterministic and stochastic dynamics has not been adequately demonstrated and the effect of noise on these measures has not been hitherto investigated.

1.2 Goals of the thesis

The overarching goal of this doctoral thesis is to introduce and propose the application of RN approach in combination with surrogate analysis, for nonlinear time series analysis of EEG. The specific goals of this doctoral thesis are,

1. To demonstrate the applicability of RN methods to distinguish between chaotic and stochastic dynamics [P-I].
2. To study the effect of observational noise on RN measures [[P-I],[P-III]].
3. To introduce RN measures in combination with surrogate analysis to study the structural properties of healthy and epileptic EEG signals [[P-III],[P-IV]].
4. To demonstrate the applicability of both univariate and bivariate RN measures in distinguishing between the structural properties focal and nonfocal epileptic EEG signals and study which network measures are particularly useful for such an application [P-II].
5. To apply moving window RNA to study the dynamical transitions in epileptic EEG data and LFP data describing a visuomotor task [[P-I],[P-V]].

1.3 Structure of the thesis

This doctoral thesis is divided into four parts. Part I provides the necessary theoretical background and the literature review related to methods in nonlinear time series analysis and its application in EEG. Specifically, Chapter 2 gives a brief introduction to the concept of dynamical systems, attractors and introduces the recurrence theorem. Chapter 3 focuses on tools and methods that are necessary to perform nonlinear time series analysis, including phase space reconstruction methods. We then introduce the concept of RPs and review various RQA measures associated with it. Other popular nonlinear measures that are used for EEG time series analysis are reviewed as well. Finally, we review the concept of surrogate analysis and methods used to distinguish between chaos and noise. Chapter 4 gives a brief overview of complex network theory and presents some basic definitions in graph theory. Chapter 5 discusses and reviews RN

and its applications in various fields. It also describes various global and local network measures that are derived from graph theory and used in RNA. Chapter 6 focuses on nonlinear time series analysis of EEG and reviews the relevant literature that describes the application of methods derived from nonlinear theory to EEG, with special attention towards epilepsy.

Part II describes the data, methods and results of the work carried out in Publications [P-I] - [P-V]. In Chapter 7 we demonstrate how RN measures, both local and global, can be used to distinguish chaotic and stochastic dynamics. Chapter 8 investigates the effect of noise on recurrence network measures. Chapters 9 - 11 describes the application of recurrence network approach to various neural data including healthy and epileptic surface and intracranial EEG recordings, and to LFP data acquired during a visuomotor task.

Part III presents the overview and general discussion of the thesis including the limitations (Chapter 12) and conclusions (Chapter 13). Part IV comprises of five original publications, that the author has contributed towards the completion of this doctoral thesis.

Part I

Theoretical background and literature review

CHAPTER 2

DYNAMICAL SYSTEMS

We may regard the present state of the universe as the effect of its past and the cause of its future. An intellect which at a certain moment would know all forces that set nature in motion, and all positions of all items of which nature is composed, if this intellect were also vast enough to submit these data to analysis, it would embrace in a single formula the movements of the greatest bodies of the universe and those of the tiniest atom; for such an intellect nothing would be uncertain and the future just like the past would be present before its eyes

PIERRE-SIMON LAPLACE
(1749–1827)

In this chapter, some of the basic concepts underlying the dynamical systems theory is given. The definition and formulation of a dynamical system is given in Section 2.1. A brief description of attractors and their different types is given in Section 2.2. The concept of recurrence is introduced in Section 2.3, which is followed by Poincaré sections in Section 2.4.

2.1 Continuous and discrete dynamical systems

Dynamical systems are ubiquitous in nature. They can be defined as any mathematical model or rule that determines the future evolution of variables, which describe the state of the system, from their initial values [20]. If the evolution rule is considered to be purely deterministic, then such dynamical systems are known as **deterministic dynamical systems**. If one considers a model that includes intrinsic or external source of randomness, then such a model represents a **random dynamical system** [21]. A deterministic dynamical system (simply referred to as dynamical system in the remainder of the thesis, unless stated otherwise) can be mathematically represented using a set of ODEs

$$\dot{x}_1(t) = F_1(x_1(t), x_2(t), \dots, x_m(t)), \quad (2.1)$$

$$\dot{x}_2(t) = F_2(x_1(t), x_2(t), \dots, x_m(t)), \quad (2.2)$$

$$\vdots \quad (2.3)$$

$$\dot{x}_m(t) = F_n(x_1(t), x_2(t), \dots, x_m(t)), \quad (2.4)$$

where $t \in \mathbb{R}$ is a continuous time variable. These set of equations can be given in a compact form to represent a **continuous dynamical system**

$$\dot{\mathbf{x}} = \mathbf{F}(\mathbf{x}). \quad (2.5)$$

If the mapping $\mathbf{F} : \mathbb{R}^m \rightarrow \mathbb{R}^m$ is nonlinear, then Equation 2.5 models a nonlinear dynamical system and it is well known that nonlinear ODEs typically do not have a closed form solution. In order to deal with such ODEs, a geometric approach is adopted instead of an analytic one. Since the solution of an ODE can be represented as curves in some abstract phase X [22], a dynamical system can be thought of as a way to represent the motion in time, of all the points in X [23]. These set of points, $\mathbf{x}(t) \in \mathbb{R}^m$, that completely describe the system at time t is known as the **state**, with m being the **dimension** of the system. The space X , is known as the **phase space** (also called state space) of the system, which is a set of all possible states of the system at any moment of time. Given an initial point in X , one can determine the future states and the solution curve traced out joining these states is known as a **trajectory**. Accordingly, in a dynamical system, the trajectories cannot intersect. The direction in which one state evolves into another is given by the mapping $\phi_t : X \rightarrow X$, which is also known as the **flow**, where $\phi_t(\mathbf{x}_0)$ is the solution to Equation 2.5, which depends on the initial condition \mathbf{x}_0 . Thus, the set $\{\phi_t(\mathbf{x}_0) : -\infty < t < \infty\}$, is the trajectory through \mathbf{x}_0 in the phase space. If the time variable t takes on discrete values, then the system is a **discrete dynamical system**. Such systems result from an iterative process, described

by a difference equation (instead of a differential equation, as in the continuous case)

$$\mathbf{x}_{t+1} = f(\mathbf{x}_t) \quad (2.6)$$

where $t \in \mathbb{Z}$ and $\mathbf{x} \in \mathbb{R}^m$. Instead of a continuous flow that describes how one state evolves into another, in case of discrete dynamical system, one speaks of a **map**, that maps a state at a time index t to another state at time index $t + 1$. Such dynamical systems are sometimes simply referred to as maps.

Dynamical systems can be further categorized into **conservative** and **dissipative** dynamical systems. In conservative dynamical systems (also known as Hamiltonian systems), the phase space volume is preserved and it does not vary with time. In case of dissipative systems, the phase space volume decreases with increasing time. In other words, the phase space volume is contracting, i.e., $\nabla \cdot \mathbf{F} < 0$. Assuming the system to be bounded, as $t \rightarrow \infty$, the motion becomes confined to a set \mathcal{A} with zero phase space volume and dimension less than the phase space dimension [24]. This set \mathcal{A} is known as the **attractor** of the system and is formally defined in Section 2.2. It is important to note that a conservative system does not have an attractor. The dynamical system modeled by Equation 2.5 is also known as an **autonomous** dynamical system as the vector field \mathbf{F} does not explicitly depend on the time variable t . If the vector field changes with time, then the dynamical system is known as **non-autonomous** dynamical system and the rule that the trajectories cannot cross each other, does not hold anymore in such systems.

Definition 2.1. Formally, a dynamical system is given by the triple (X, T, ϕ_t) , where $X \subseteq \mathbb{R}^m$ is a compact or smooth manifold and ϕ_t is a continuously differentiable function, parameterized by $t \in T$ and is given by

$$\phi_t : T \times X \rightarrow X, \quad (2.7)$$

where $T \in \mathbb{R}$ (or $\in \mathbb{Z}$) and $\phi(t, \mathbf{x}) = \phi_t(\mathbf{x})$ satisfies the following two properties

1. $\phi_0(\mathbf{x}) = \mathbf{x}$ for all $\mathbf{x} \in X$.
2. $\phi_t \circ \phi_s(\mathbf{x}) = \phi_{t+s}(\mathbf{x})$ for all $\mathbf{x} \in X$ and each $s, t \in \mathbb{R}$.

The property (1) is known as the identity property and it states that when a state evolves at $t = 0$, the state remains unchanged [23, 25]. Property (2) is known as the group property and it implies that under the operation of composition, the set $\{\phi_t\}$ is a commutative group [26], i.e., solving the differential equation at time $t + s$ is same as solving it first for time t and then for time s .

2.2 Attractor

Attractor of a dynamical system can be defined as a subset of the phase space to which the trajectories emerging from typical initial conditions accumulate to, as time increases.

Definition 2.2. A set $\mathcal{A} \subset \mathbb{R}^m$, is known as an attractor of a dynamical system if the following conditions are met [27],

1. \mathcal{A} is forward invariant.
2. The **basin of attraction** $B(\mathcal{A})$ has a strictly positive measure.
3. \mathcal{A} cannot be decomposed further into nontrivial sets.

The basin of attraction is defined as the neighborhood of the attractor where the initial conditions starting in the neighborhood remain in the neighborhood and approach the attractor as $t \rightarrow \infty$. Formally, basin of attraction can be defined as

Definition 2.3. For a dynamical system described by $\dot{x} = F(x)$, let x be an asymptotically stable stationary point. Then for all $\gamma > 0$ there exists $\delta > 0$ such that [22]

$$|y - x| < \delta \implies |\phi_t(y) - x| < \gamma \quad \forall t \geq 0 \quad (2.8)$$

and

$$\exists \delta > 0 \text{ such that } |y - x| < \delta \implies |\phi_t(y) - x| \rightarrow 0 \text{ as } t \rightarrow \infty \quad (2.9)$$

then

$$B(\mathcal{A}) = \left\{ y \in \mathbb{R}^m \mid \lim_{t \rightarrow \infty} |\phi_t(y) - x| = 0 \right\} \quad (2.10)$$

is known as the basin of attraction of the point x .

There are different types of attractors. The simplest kind of attractor is a **fixed point** attractor, which is represented by a single point in phase space. It describes the equilibrium state of a system. A slightly more complicated type of attractor is the **limit cycle** attractor, which forms a closed loop in phase space. Such attractors represent stable oscillatory behavior. **Chaotic** attractors, also known as **strange** attractors, have self-similar, fractal properties. There are non-chaotic strange attractors as well, that do not emerge from a chaotic dynamical system. A chaotic dynamical system, although deterministic, is sensitive to initial conditions. Due to this sensitivity to initial conditions, two nearby trajectories emerging from two arbitrarily close initial conditions tend to diverge away from each other as time increases. However, since the system is bounded, the separation between the trajectories cannot tend to infinity and hence the trajectories start to converge. This repeated divergence and convergence (i.e., stretching and

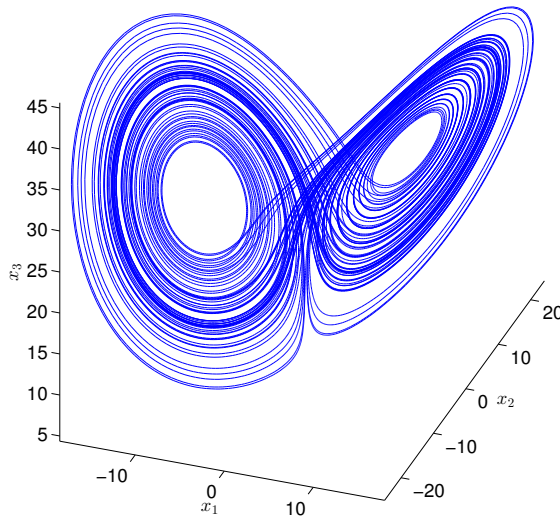


FIGURE 2.1: Lorenz attractor,
 $\rho = 28$, $\sigma = 10$, $\beta = 8/3$.

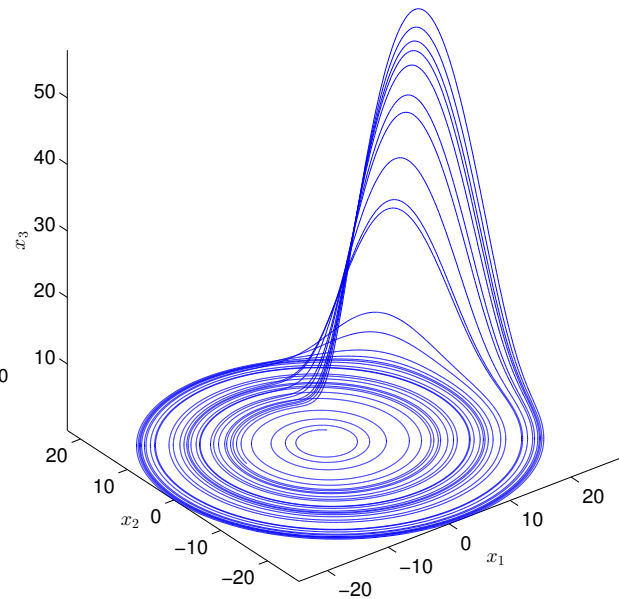


FIGURE 2.2: Rössler attractor,
 $a = b = 0.1$, $c = 18$.

folding) of trajectories on the attractor, produces very complicated structures in phase space and gives the attractor its strange and fractal nature. Some of the common examples of such chaotic attractors are given by the Lorenz system and the chaotic Rössler system, given by the following equations

$$\dot{x} = \sigma(y - x), \dot{y} = x(\rho - z), \dot{z} = xy - \beta z, \quad (2.11)$$

and

$$\dot{x} = -y - z, \dot{y} = x + ay, \dot{z} = b + z(x - c), \quad (2.12)$$

respectively. The attractors of these systems and the corresponding parameter values are shown in Figures 2.1 and 2.2.

2.3 Poincaré recurrences

The metatheorem of dynamical systems theory states that, for an appropriately bounded phase space X , the trajectories of the motion will exhibit some form of recurrence, i.e., they will return close to their initial position [28]. In 1890, Poincaré formulated the first precise result and proved that whenever a dynamical system preserves volume, almost all the trajectories return arbitrarily close to their initial position, infinite number of times [12].

Formally, let (X, \mathcal{N}, μ, f) be a measure space where \mathcal{N} is a σ -algebra, i.e., $\mathcal{N} \subset 2^X$, μ is a probability measure. Let $f: X \rightarrow X$ be a measure preserving transformation. Thus, $\mu(f^{-1}(\mathcal{A})) = \mu(\mathcal{A})$ for any measurable set $\mathcal{A} \subseteq X$. Now, Poincaré recurrence theorem can be stated as follows [29]

Theorem 2.4. *For any measurable set $\mathcal{A} \subseteq X$, almost every point $x \in \mathcal{A}$ returns infinite times in \mathcal{A}*

$$\mu(\{x \in \mathcal{A} : \text{there exists infinite positive integers } n \in \mathbb{N} \text{ such that } f^n(x) \in \mathcal{A}\}) = \mu(\mathcal{A}).$$

Although, the Poincaré's recurrence theorem talks about the existence of recurrence in a dynamical system, but does not explicitly address how long does it take for a dynamical system to recur [2]. The **first return time** for the attractor set \mathcal{A} can be defined as

$$\tau_{\mathcal{A}}(\mathbf{x}) = \min \{n \in \mathbb{N} : f^n(\mathbf{x}) \in \mathcal{A}\}, \quad (2.13)$$

which simply is the minimum number of transformations needed on \mathbf{x} , before it returns back to the set \mathcal{A} . The mean recurrence time is then given as

$$\langle \tau_{\mathcal{A}} \rangle = \int_{\mathcal{A}} \tau_{\mathcal{A}}(\mathbf{x}) d\mu_{\mathcal{A}}. \quad (2.14)$$

2.4 Poincaré sections

Consider an attractor and an arbitrary plane that cuts through an attractor. A Poincaré section can then be defined as an one-dimensional map consisting of a sequence of data points formed due to the intersection of the attractor trajectories with the plane. Such maps are useful in detecting some sort of structure in an attractor. For instance, if a plane is cut through a three dimensional chaotic attractor, one can see stretching and folding of the map as the plane is rotated through the attractor. Similarly, if the plane cuts through a stable periodic orbit, then starting from a random initial condition, one can observe a sequence of points converging on to an equilibrium point. Thus, Poincaré sections can be thought of as an interesting way of dimensionality reduction, i.e., a continuous system of dimension m is reduced to a discrete system of dimension $m - 1$.

CHAPTER 3

NONLINEAR TIME SERIES ANALYSIS

*The whole is greater than the sum of
its parts*

ARISTOTLE

In this chapter, the tools needed to perform nonlinear time series analysis are reviewed. The techniques for reconstructing the phase space from time series are discussed in Section 3.1. RPs, which are commonly used in nonlinear time series analysis and from which RNs are derived, are described in Section 3.2. Fractal dimensions, which are closely related to nonlinear dynamics arising from chaos, are discussed in Section 3.3. Self-similarity, which is a property of fractals, is observed in the geometry of chaotic (and even non-chaotic) strange attractors. In Section 3.4, we give a brief description of other commonly used measures in nonlinear time series analysis. We then discuss the issue of distinguishing chaos from noise in Section 3.5. An overview of different surrogate methods is provided in Section 3.6.

3.1 Phase space reconstruction

Signals of interest are often recorded by sensors in the time domain. Thus, there is no direct access to the hidden states of the underlying dynamical system. Many methods from nonlinear dynamical theory [8] operate on the phase space and require the attractors underlying the dynamical system. The phase space attractor can be reconstructed from a scalar time series following what is known as the **embedding theorem** [30], given below.

$$\begin{array}{ccc}
\mathbf{x}_n \in \mathcal{A} \subset \mathcal{M} & \xrightarrow{\mathbf{F}} & \mathbf{x}_{n+1} \in \mathcal{A} \subset \mathcal{M} \\
\downarrow g & & \downarrow g \\
x_n \in \mathbb{R} & & x_{n+1} \in \mathbb{R} \\
\downarrow e & & \downarrow e \\
\tilde{\mathbf{x}}_n \in \tilde{\mathcal{A}} \subset \mathbb{R}^{2m+1} & \xrightarrow{\mathbf{G}} & \tilde{\mathbf{x}}_{n+1} \in \tilde{\mathcal{A}} \subset \mathbb{R}^{2m+1}
\end{array}$$

FIGURE 3.1: Commutative diagram illustrating the embedding theorem.

3.1.1 Taken's embedding theorem

Theorem 3.1. Consider a compact, m -dimensional manifold \mathcal{M} , with $\mathbf{F} : \mathcal{M} \rightarrow \mathcal{M}$, a smooth diffeomorphism (at least in the sense of C^2). Consider a smooth (again in the sense of C^2) observation function, $g : \mathcal{M} \rightarrow \mathbb{R}$. It is a generic property that,

$$\Phi_{(\mathbf{F},g)} : \mathcal{M} \rightarrow \mathbb{R}^{2m+1}, \quad (3.1)$$

defined by,

$$\Phi_{(\mathbf{F},g)}(\mathbf{x}) = (g(\mathbf{x}), g(\phi_1(\mathbf{x})), g(\phi_2(\mathbf{x})), \dots, g(\phi_{2m}(\mathbf{x}))) \quad (3.2)$$

is an embedding, where ϕ_t is a flow of \mathbf{F} . Here $\Phi_{(\mathbf{F},g)}$ is a $2m + 1$ -fold observational map and is one-to-one between \mathcal{M} and its image, with both Φ and Φ^{-1} differentiable [31]. The components of $\Phi_{(\mathbf{F},g)}$ correspond to the time lagged observations of the dynamics on \mathcal{M} , as defined by the smooth observation function g .

The embedding theorem can be visualized using a commutative diagram as shown in Figure 3.1. Here \mathbf{x}_n represents the original state vector at time instant n and x_n represents the scalar measurement made at time n through an observation function g . The evolution of the state vector to time instant $n + 1$ is given by the dynamics \mathbf{F} . Embedding theorem states that, an embedding procedure e can be written as a map on x_n by introducing a backward shift operator (also see Equation 3.3) [8]. The vector $\tilde{\mathbf{x}}_n$ denotes the reconstructed state vector at time instant n , following the embedding procedure. The dynamics \mathbf{G} in the embedding space is uniquely determined by \mathbf{F} and g . Figure 3.2 shows an example, where the Lorenz attractor is reconstructed by applying the embedding theorem on the scalar x_1 component of the original Lorenz system.

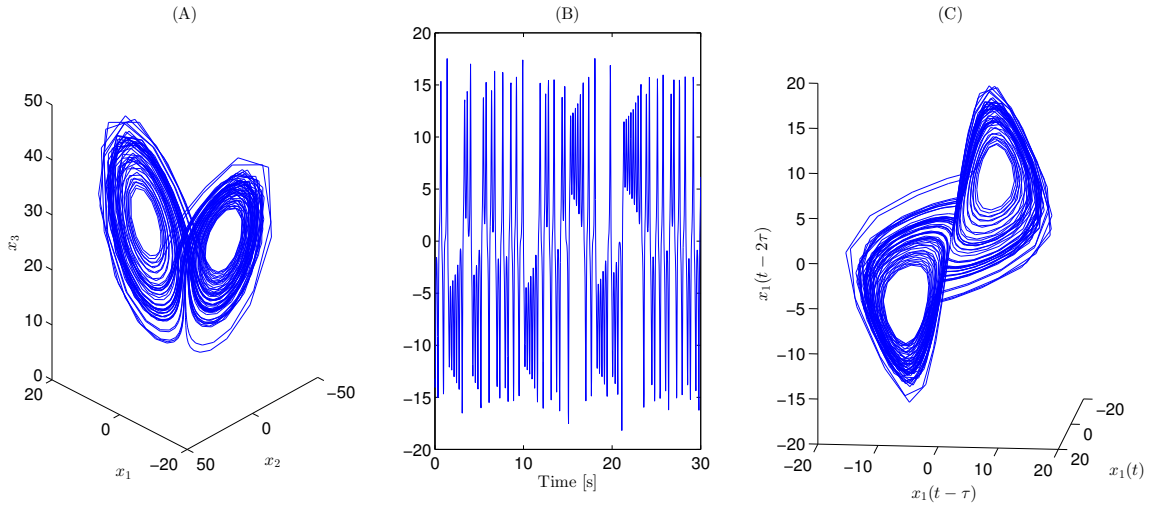


FIGURE 3.2: (A) The original Lorenz attractor. (B) The x_1 -component of the Lorenz attractor. (C) The Lorenz attractor in the reconstructed space after applying embedding theorem using the x -component. The reconstructed space (C) is diffeomorphic with the 3-dimensional manifold which contains the original Lorenz attractor (A).

3.1.2 Estimation of the embedding lag

The embedding theorem does not explicitly specify what should be the embedding lag (τ) between the successive observations to reconstruct the dynamics. In theory, the theorem will work for any arbitrary value of $\tau \in \mathbb{R}_+$ and the embedding theorem described above considers $\tau = 1$. The reconstructed embedding vector $\tilde{\mathbf{x}}_n$, for an arbitrary τ can be given as [8]

$$\tilde{\mathbf{x}}_n \in \mathcal{M} \iff (x_n, x_{n-\tau}, x_{n-2\tau}, \dots, x_{n-(m-1)\tau}). \quad (3.3)$$

However, in practical situations the selection of τ may necessitate some caution. For instance, if τ is too small, then there is almost no new information between the successive observations and the coordinates in the phase space will be too close to each other. It is beneficial to select a value of τ such that it leads to maximal separation of the data, as this ensures that the vector field is also maximally smooth, with no sharp changes in the direction [32]. In contrast, a very large τ can make the successive observations completely disconnected, relating each other in a random fashion. The situation arising due to the selection of very small and very large value for τ is known as redundance and irrelevance respectively [33]. Many methods have been proposed to choose the optimal value for τ . However, two methods based on autocorrelation [34] and mutual information [35] have gained considerable popularity and are discussed in some detail below.

3.1.2.1 Autocorrelation

Given a scalar time series $\{x_t\}$ with N samples, where $t = 0, 1, 2, \dots, (N-1)$, the linear autocorrelation function is given as

$$\rho(\tau) = \frac{\sum_{t=0}^{N-\tau-1} [x_{t+\tau} - \bar{x}][x_t - \bar{x}]}{\sum_{t=0}^{N-1} [x_t - \bar{x}]^2}, \quad (3.4)$$

where \bar{x} is the sample mean. Qualitatively speaking, an autocorrelation function tells how similar is the shape of a signal at time $t + \tau$ to that at time t , i.e., it denotes how the signal shape changes from time to time. The above equation can be simplified by normalizing the time series to zero mean and unit variance

$$\rho(\tau) = \frac{1}{N - \tau - 1} \sum_{t=1}^{N-\tau} x_{t+\tau} x_t, \quad (3.5)$$

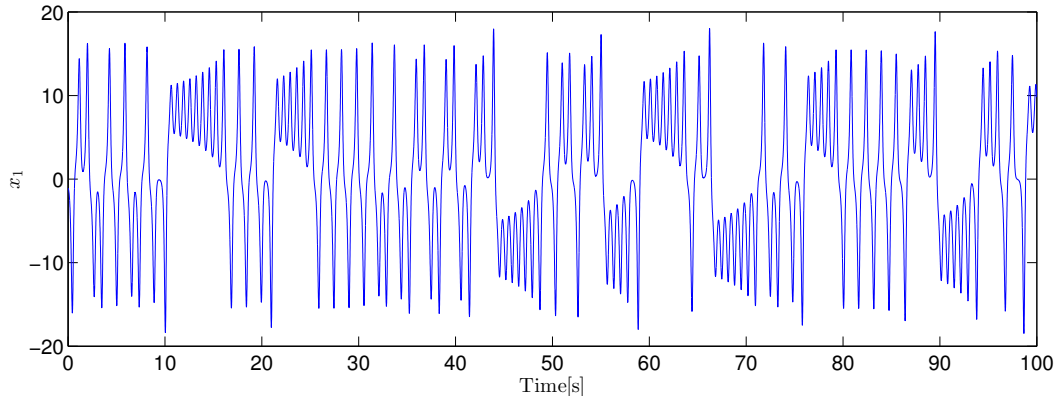
for $\tau \geq 0$. Note that $\rho(\tau) = \rho(-\tau)$ for $\tau < 0$, i.e., the autocorrelation function is an even function of τ . In order to select an optimal embedding lag, one can choose τ such that $\rho(\tau) \leq 0$. It has been observed that many simple systems give poor results for this criteria and a reasonable choice for the embedding lag can be given as the decorrelation time [8, 32], which is defined as

$$\tau_{dec} = \min \left\{ \tau : \rho(\tau) < \frac{1}{e} \right\}. \quad (3.6)$$

Although autocorrelation function is closely related to the shape of the attractor [8] and gives good hint about the independence of the coordinates, it does not address the issue of nonlinear dependence [36].

3.1.2.2 Mutual information

Information theory plays an important role in the field of dynamical systems. Despite the deterministic character of the temporal trajectory, chaotic systems exhibit long-term unpredictability [37]. In a chaotic system, the distance between two near-by points typically increases in an exponential fashion, i.e., $|\mathbf{x}_1(t') - \mathbf{x}_2(t)| \approx |\mathbf{x}_1(t) - \mathbf{x}_2(t)| e^{(\lambda|t'-t|)}$, where λ is the largest Lyapunov exponent (See Section 3.4). Due to this separation, these two near-by points that were experimentally indistinguishable, can now be resolved. Thus, instability and the resulting chaos can be thought of as an information source [36]. The Kolmogorov-Sinai entropy, which is a generalization of Shannon entropy from information theory, first introduced by Kolmogorov [38] and later refined by Sinai [39], can be used to precisely formulate the rate of the generated information and to quantify

FIGURE 3.3: x_1 component of the Lorenz system.

the complexity of a dynamical system [40]. In information theory, a message can be considered as a sequence of symbols, which corresponds to a state in a dynamical system. The dynamics of the system can be given by the shift operator, which switches the message sequence one step. Using such entropy measures, one can measure how well can the next sequence be predicted. Extending this idea, given a time series, one can learn how much information can be gained from the measurement at one time, from the measurement acquired at another time [36]. In general, given two discrete random variables X and Y , with marginal probability mass functions $p(x) = Pr(X = x), x \in X$ and $p(y) = Pr(Y = y), y \in Y$ and a joint probability mass function $p(x, y)$, the mutual information $I(X; Y)$ can be defined as [41, 42]

$$I(X; Y) = \sum_{x \in X} \sum_{y \in Y} p(x, y) \log \left(\frac{p(x, y)}{p(x)p(y)} \right) \quad (3.7)$$

If X and Y are independent, then $p(x, y) = p(x)p(y)$ and thus $I(X; Y) = 0$. In the context of a scalar time series, $\{x_n\}$ with N samples, where $n = 0, 1, 2, \dots, (N - 1)$, one can define the **auto mutual information** function as follows [35]

$$I(\tau) = \sum_{n=0}^{N-1} p(x_n, x_{n+\tau}) \log \left(\frac{p(x_n, x_{n+\tau})}{p(x_n)p(x_{n+\tau})} \right). \quad (3.8)$$

It has been suggested that the optimal value for the embedding delay is the value of τ at which $I(\tau)$ reaches the first local minimum [8, 35, 43]. This method has an obvious advantage over the autocorrelation method as it takes into account the nonlinear interrelations as well. As an example, Figure 3.3 shows the x_1 -component of the Lorenz system (Equation 2.11) and Figure 3.4 the optimal embedding lag ($\tau_{opt} = 43$) estimated using the mutual-information criterion.

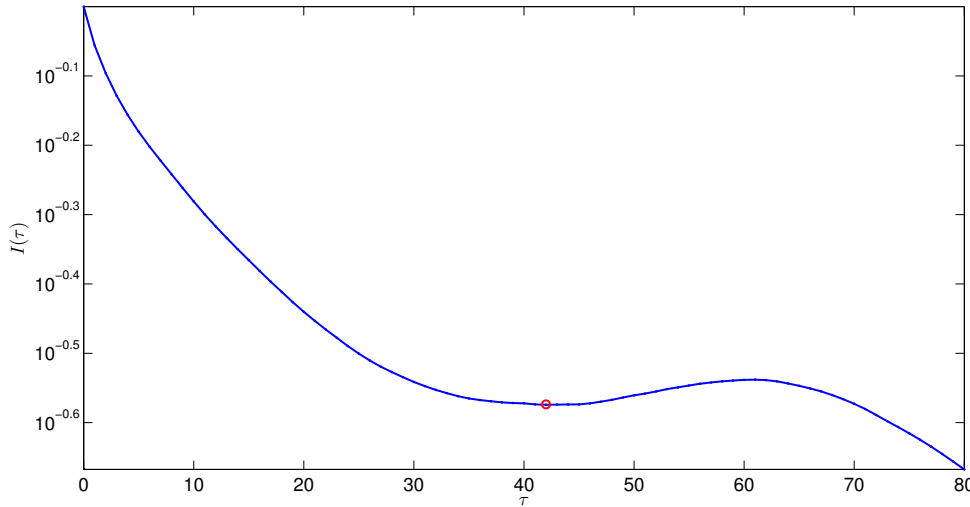


FIGURE 3.4: Estimation of the optimal lag τ (red circle) using auto mutual information for the x_1 component of the Lorenz system.

3.1.3 Estimation of the embedding dimension

In order to perform phase space reconstruction from a time series, apart from τ , another important parameter to be estimated is the embedding dimension (m). Again, there are various methods in the literature on the selection of m and many of these methods are based on false-nearest neighbor principle [32, 44, 45]. The most common method used in determining m is the **false nearest neighborhood (FNN)** method [46]. The rationale behind the FNN method is to examine if the points along a trajectory in dimension m are also neighbors in dimension $m + 1$. Since in dimensions lower than the actual dimension, many points on the trajectory will be close to each other (false neighbors) due to projection. Starting with an initial dimension of $m = 1$, one keeps incrementing m by one and for each state vector \mathbf{x}_n , the nearest neighbor is computed. For every increase in m , the percentage of false neighbors is also computed. The value of m at which the percentage of false neighbors becomes zero (or arbitrarily small due to the effect of noise) is considered as an appropriate choice for m . Given a scalar time series $\{x(n)\}$ with N samples, where $n = 0, 1, 2, \dots, (N - 1)$ and τ , one reconstructs the phase space vector at an initial dimension m . Thus we have a state vector at time sample n

$$\mathbf{x}_n^m = (x(n), x(n - \tau), \dots, x(n - (m - 1)\tau)), \quad (3.9)$$

which has a nearest neighbor

$$\mathbf{x}_{k(n)}^m = (x(k(n)), x(k(n) - \tau), \dots, x(k(n) - (m - 1)\tau)). \quad (3.10)$$

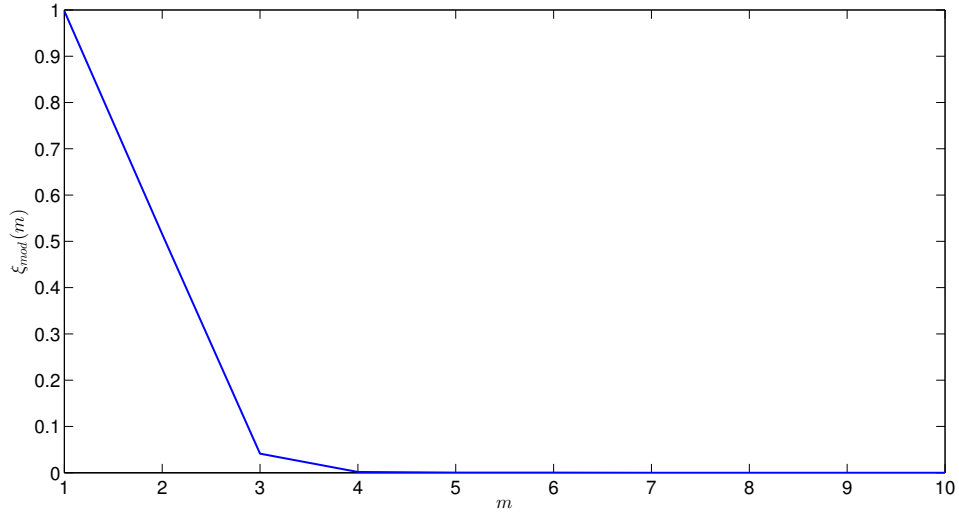


FIGURE 3.5: Estimation of the minimum embedding dimension using modified FNN method for the x_1 component of the Lorenz system.

If the above reconstruction occurred in an insufficient dimension m , then this closeness could be a result of trajectories crossing [32]. So one increases the dimension to $m + 1$ and reconstructs the phase space vector and computes the nearest neighbor for each state vector. Now let us denote a state vector point in dimension $m + 1$ as \mathbf{x}_n^{m+1} and its nearest neighbor $\mathbf{x}_{k(n)}^{m+1}$. The increase in distance from m to $m + 1$ can be given as

$$D_n = \|\mathbf{x}_n^{m+1} - \mathbf{x}_{k(n)}^{m+1}\| - \|\mathbf{x}_n^m - \mathbf{x}_{k(n)}^m\|, \quad (3.11)$$

which can be normalized and computed for all the points as

$$\xi = \sum_{n=1}^{N-m-1} \Theta \left(\frac{D_n}{\|\mathbf{x}_n^m - \mathbf{x}_{k(n)}^m\|} - r \right). \quad (3.12)$$

One can set a suitable threshold (r) to determine if \mathbf{x}_n^m and $\mathbf{x}_{k(n)}^m$ are neighbors, i.e., if ξ is greater than r then these two points can be called false neighbors. Typical r is chosen to be between 10 and 30 [32]. Thus ξ is the amount of false neighbors that one would find in dimension m . The optimal embedding dimension is then defined as the dimension for which ξ becomes zero (or very small in case of noisy time series). Hegger and Kantz proposed a modification to the FNN method by excluding points whose initial distance was already greater σ/r , where σ is the standard deviation of the data [47]. The modified FNN method is given by

$$\xi_{mod} = \frac{\sum_{n=1}^{N-m-1} \Theta \left(\frac{\|\mathbf{x}_n^{m+1} - \mathbf{x}_{k(n)}^{m+1}\|}{\|\mathbf{x}_n^m - \mathbf{x}_{k(n)}^m\|} - r \right) \Theta \left(\frac{\sigma}{r} - \|\mathbf{x}_n^m - \mathbf{x}_{k(n)}^m\| \right)}{\sum_{n=1}^{N-m-1} \Theta \left(\frac{\sigma}{r} - \|\mathbf{x}_n^m - \mathbf{x}_{k(n)}^m\| \right)}. \quad (3.13)$$

Figure 3.5 shows the minimum embedding dimension using the x_1 -component of the Lorenz system (Equation 2.11) with the modified FNN method. It can be seen at $m = 3$, already the percentage of false nearest neighbors is very close to zero and for $m > 3$, this value falls to zero.

3.2 Recurrence plots

3.2.1 Definition of a recurrence plot

Eckmann *et al.* [13] introduced RP as a method to visualize the recurrences of trajectories in the phase space of a dynamical system. An RP can be represented using a recurrence matrix \mathbf{R} [2], whose elements are given as

$$R_{i,j} = \Theta(\varepsilon - \|\mathbf{x}_i - \mathbf{x}_j\|), \quad (3.14)$$

where Θ is the Heaviside step function, $\|\cdot\|$ is a distance norm, ε is a pre-determined distance threshold, \mathbf{x}_i and \mathbf{x}_j are state vectors at time instant t_i and t_j respectively. Note that the matrix \mathbf{R} can be defined in many ways (see [17] and Section 5.1 for details) and the above definition in particular refers to ε -recurrence matrix (hereinafter simply referred as matrix \mathbf{R} , unless specified otherwise). Thus, we can write the elements of the matrix \mathbf{R} as

$$R_{i,j} = \begin{cases} 1 & \text{when } \varepsilon < \|\mathbf{x}_i - \mathbf{x}_j\|, \\ 0 & \text{when } \varepsilon > \|\mathbf{x}_i - \mathbf{x}_j\|. \end{cases} \quad (3.15)$$

This simply means that, if the trajectory in the phase space returns at time instance t_j into the ε -neighborhood of where it was at time t_i ($j > i$), then the corresponding entry $R_{i,j}$ is 1, otherwise it is 0. Thus, the matrix \mathbf{R} is a symmetric, binary matrix. Information about the temporal evolution of the trajectories can be obtained by looking at the patterns in the RPs [2]. For example, the RP of periodic dynamics contain contains non-interrupted lines, known as diagonal lines [2]. The RP of a stochastic, uncorrelated signal contains many isolated points [8, 17]. A dynamical system displaying chaos has an RP comprising of diagonals relatively shorter than the periodic system [17]. Exemplary RPs derived from sinusoidal time series, Lorenz system and uncorrelated stochastic data are shown in Figure 3.6

As evident from Equation 3.14, an RP is dependent on two parameters, ε and $\|\cdot\|$. A large ε results in a large neighborhood where every point is connected to every other point [2]. In such situations, the closeness in phase space is a consequence of temporal closeness and this results in false recurrence points. This effect is known as **tangential motion** and it causes thick and longer structures in the RP [2]. On the other hand, if ε is chosen

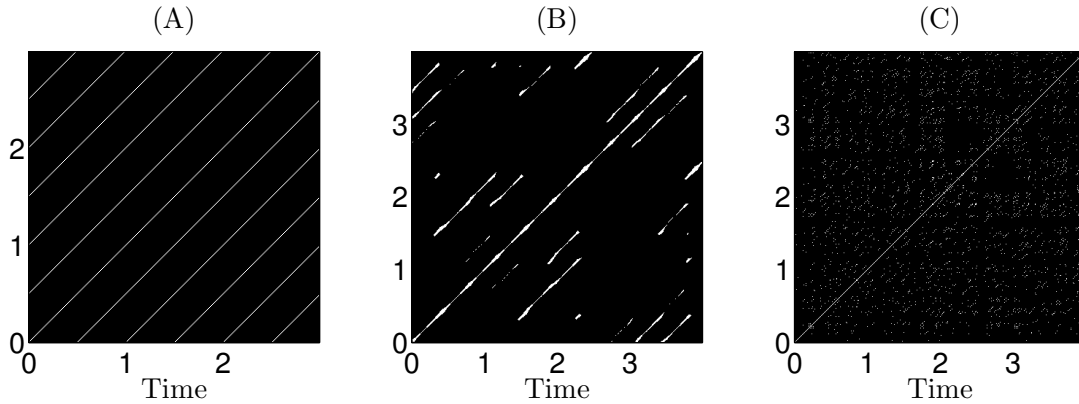


FIGURE 3.6: RPs derived from a sinusoidal time series (A), Lorenz system (B) and uncorrelated stochastic signal (C). The sinusoidal time series has a period of $T = 0.5$ seconds, which is equal to the vertical distance between diagonals in the corresponding RP. The parameters of the Lorenz system are $\rho = 28$, $\sigma = 10$, $\beta = 8/3$.

to be too small, true recurrence points might get excluded and thus the resulting RP will no longer reflect the true recurrence structure of the underlying dynamical system [2]. In dealing with experimental signals, the influence of noise also has to be taken into account before choosing ε . Thiel *et al.* [48] suggested a value of ε , that is at least five times the standard deviation of the observed noise. It has also been suggested that the value of ε should not exceed 10% of the mean or the maximum phase space diameter [14]. Regarding the $\|\cdot\|$, one can choose either euclidean or manhattan or maximum norm. Choosing maximum norm has one obvious advantage that the distance computed is independent of the embedding dimension whereas with euclidean norm, the inter-point distance increases with embedding dimension [49]. Thus, different RPs generated with different embedding dimensions can be compared directly when using maximum norm [49]. On the other hand, Zou *et al* [50] showed that euclidean norm works well for parametrized model, while maximum norm works well for phase space models. Thus, choice of the norm also plays an important role in deriving an RP.

3.2.2 Recurrence quantification analysis

Although, the visual interpretation of RPs can help in gaining insights into the dynamical system, it is still a subjective method. A more convenient and objective approach is to quantify the structures present in the RPs using RQA, introduced by Zbilut and Webber [14, 51, 52]. In this section we will define some of the important RQA measures that can be used to characterize the complexity of a dynamical system.

- **Recurrence rate** (RR) is a measure of the density of recurrences in an RP. It is closely related to the definition of correlation sum [53] and is given as

$$RR = \frac{1}{N^2} \sum_{i,j=1}^N R_{i,j}. \quad (3.16)$$

The RR is simply the sum of black dots (ones) in an RP. When number of state vectors (N) is large, RR is the probability that a state vector returns to its ε -neighborhood [2].

- **Percent determinism** (DET) can be defined as the ratio of recurrence points that form the diagonal lines of at least length l_{min} to all the recurrence points in an RP and it is given as

$$DET = \frac{\sum_{l=l_{min}}^N l P_D(l)}{\sum_{l=1}^N l P_D(l)}, \quad (3.17)$$

where $P_D(l)$ is the histogram of the lengths of the diagonal structures in an RP [2] and is given as,

$$P_D(l) = \sum_{i,j=1}^N (1 - R_{i-1,j-1})(1 - R_{i+l,j+l}) \prod_{k=0}^{l-1} R_{i+k,j+k}. \quad (3.18)$$

Since, the RP of a deterministic system exhibiting periodic dynamics contain long diagonals whereas those depicting chaotic dynamics has short lines, the parameter DET can be used as a measure of predictability of the system. However, this is not to be confused with the determinism of a process [54]. Also, the parameter DET depends on the parameter l_{min} , which can be set so as to exclude short diagonal lines that may exist due to tangential motion and not system dynamics [54]. The typical choice for l_{min} is 2 and this parameter becomes identical to RR if $l_{min} = 1$ [55].

- **Entropy** ($ENTR$) of an RP can be defined as the Shannon entropy of the frequency distribution of diagonal line lengths [54] and is given as

$$ENTR = - \sum_{l=l_{min}}^N p(l) \log(p(l)), \quad (3.19)$$

where $p(l) = \frac{P_D(l)}{\sum_{l=l_{min}}^N P_D(l)}$ is the frequency distribution of the diagonal line lengths. The parameter, $ENTR$, can be used to characterize the complexity of a deterministic structure in an RP. High values of $ENTR$ reflect increased complexity in

the system whereas low values of $ENTR$ indicate uncorrelated noise or stochastic process.

- **Maximum diagonal line length** (L_{max}) can be defined as [54]

$$L_{max} = \max(\{l_i; i = 1, 2, \dots, N_l\}), \quad (3.20)$$

where N_l is the total number of diagonal lines. A related measure known as **Divergence** (DIV) is given as the inverse of L_{max} . These two measures are related to the exponential divergence of the trajectories [2]. The faster the trajectories diverge, shorter will be the diagonal lengths leading to a lower value of L_{max} (or conversely a higher value for DIV).

- **Average diagonal line length** (L_{mean}) can be defined as the average time for which two segments of the trajectories are in proximity of each other. This measure is related to the mean prediction time and it is given as [54]

$$L_{mean} = \frac{\sum_{l=l_{min}}^N l P_D(l)}{\sum_{l=l_{min}}^N P_D(l)}. \quad (3.21)$$

- **Ratio** ($RATIO$) is defined as the ratio between the parameters DET and RR [51]. It is given as

$$RATIO = N^2 \frac{\sum_{l=l_{min}}^N l P_D(l)}{(\sum_{l=1}^N P_D(l))^2}. \quad (3.22)$$

This parameter is useful in detecting dynamic transitions [55].

- **Laminarity** LAM is a parameter similar to DET , except that it gives the ratio of recurrence points that form the vertical lines to all the recurrence points. It was proposed by Marwan *et al.* [56] and is given as

$$LAM = \frac{\sum_{l=v_{min}}^N l P_V(l)}{\sum_{l=1}^N l P_V(l)}, \quad (3.23)$$

where, $P_V(l)$, the histogram of the lengths of the vertical lines in an RP and is given as,

$$P_V(l) = \sum_{i,j=1}^N (1 - R_{i,j-1})(1 - R_{i,j+l}) \prod_{k=0}^{l-1} R_{i,j+k}. \quad (3.24)$$

In addition to these RQA measures, dynamical invariants like correlation dimension, correlation entropy and generalized mutual information can also be estimated from RPs. This is a useful feature since the RQA measures, although useful in quantitatively describing the RP, still depend on embedding parameters used to reconstruct the phase space [2].

3.2.3 Bivariate recurrence plots

Apart from analyzing univariate time series, the concept of RPs (and their quantification) can be extended to analyze bivariate signals. The RPs obtained from bivariate data can be divided into two categories, 1) cross recurrence plots (CRPs) and 2) joint recurrence plots (JRPs). Below, we discuss these two approaches in some detail.

3.2.3.1 Cross recurrence plot

The CRP [57, 58] can be used to analyze interdependencies between two different dynamical systems and it can be considered as a generalization of the linear cross-correlation function [2]. Given N -samples of two time series $\{x_t\}$ and $\{y_t\}$, where $t = 0, 1, 2, \dots, (N - 1)$, a cross recurrence matrix (\mathbf{R}^{cross}) can be defined with the elements

$$R_{i,j}^{cross} = \Theta(\varepsilon - \|\mathbf{x}_i - \mathbf{y}_j\|). \quad (3.25)$$

Following the definition of an RP (Section 3.2 and Equation 3.14), here Θ is the Heaviside step function, $\|\cdot\|$ is a distance norm, ε is a pre-determined cross-distance threshold. \mathbf{x}_i and \mathbf{y}_j are (reconstructed) state vectors at time instance t_i and t_j respectively. The matrix \mathbf{R}^{cross} is not a square matrix like \mathbf{R} , as the two time series can be of different lengths. Thus we can write the elements of \mathbf{R}^{cross} in an analogous fashion to Equation 3.15,

$$R_{i,j}^{cross} = \begin{cases} 1 & \text{when } \varepsilon < \|\mathbf{x}_i - \mathbf{y}_j\|, \\ 0 & \text{when } \varepsilon > \|\mathbf{x}_i - \mathbf{y}_j\|. \end{cases} \quad (3.26)$$

This simply means that the entry in the matrix \mathbf{R}^{cross} is 1 if the mutual distance between the phase vectors \mathbf{x}_i and \mathbf{x}_j is less than ε , else it is 0. The diagonal entries of the matrix \mathbf{R}^{cross} is not necessarily 1 always, as this entry depends on the mutual distance between state vectors from two time series. Similar to the visual interpretation of the structures in an RP, the structures of a CRP can also be interpreted in a similar fashion. For instance, if the lines in a CRP are diagonally oriented, it implies that the segments of the trajectories of both the systems run parallel for some time [2]. The length of such diagonal lines can be used to find nonlinear interdependencies between two time series [58]. If both the time series have the same dynamics, the main diagonal entry of \mathbf{R}^{cross} will be one. Furthermore, in case of time dilation or compression of one of these similar trajectories, this diagonal line will be distorted [59]. Since the CRP method compares the phase space trajectories of two systems in the same phase space, it is essential to embed both the time series with the same m . In case the minimum m for the two time series are not the same, then the higher embedding dimension is chosen to embed both the time series.

Analogous to the quantification of RPs, complexity measures can be derived by quantifying the CRPs. The RQA parameters DET , LAM and L_{mean} can be modified and redefined for the CRPs [58]. Since, the similarity between two systems is given by the main diagonal of a CRP, these modified RQA measures are determined for each diagonal line parallel to the main diagonal line and are given as a function of the distance from the main diagonal. Let $t \in (-T, \dots, T)$ be the index of the diagonal lines with $t = 0$ referring to the main diagonal, $t > 0$ referring to the diagonals above the main diagonal and $t < 0$ referring to the diagonals below the main diagonal [58]. The modified RQA measures, known as cross recurrence quantification analysis cross recurrence quantification analysis (CRQA) measures, $RR(t)$, $DET(t)$ and $L_{mean}(t)$ are defined as follows

$$RR(t) = \frac{1}{N-t} \sum_{l=1}^{N-t} lP_{Dt}(l), \quad (3.27)$$

$$DET(t) = \frac{\sum_{l=l_{min}}^{N-t} lP_{Dt}(l)}{\sum_{l=1}^{N-t} lP_{Dt}(l)}, \quad (3.28)$$

and

$$L_{mean}(t) = \frac{\sum_{l=l_{min}}^{N-t} lP_{Dt}(l)}{\sum_{l=l_{min}}^{N-t} lP_{Dt}(l)}, \quad (3.29)$$

where P_{Dt} is the histogram of the diagonal line lengths for each diagonal parallel to the main diagonal. High values of RR indicate that the probability of the occurrence of the same state in both the systems is high, whereas high values of DET and L_{mean} indicates a long time span of the occurrence of similar dynamics in both the systems [58].

3.2.3.2 Joint recurrence plot

While CRP is based on the occurrence of similar states in two different dynamical systems, JRP can be used to infer if the states of two systems recur simultaneously leading to similar recurrence structures [60]. Unlike the CRP, to derive a JRP, the two time series can be embedded in different m . The joint recurrence matrix (\mathbf{R}^{joint}) can be given as an element-wise dot product of the individual recurrence matrices obtained from time series $x(t)$ and $y(t)$ using individual distance thresholds ε^x and ε^y respectively and the elements of the matrix \mathbf{R}^{joint} can be given as

$$JR_{i,j}^{joint} = \Theta(\varepsilon^x - \|\mathbf{x}_i - \mathbf{x}_j\|)\Theta(\varepsilon^y - \|\mathbf{y}_i - \mathbf{y}_j\|), \quad (3.30)$$

which can be rewritten as,

$$JR_{i,j}^{joint} = \begin{cases} 1 & \text{when } (\varepsilon^{\mathbf{x}} < \|\mathbf{x}_i - \mathbf{x}_j\| \wedge \varepsilon^{\mathbf{y}} < \|\mathbf{y}_i - \mathbf{y}_j\|), \\ 0 & \text{else} \end{cases} \quad (3.31)$$

It is important to note here that, since the embedding dimensions of the two systems considered can be different, the phase space is extended to $\mathbb{R}^{m_1+m_2}$, where m_1 and m_2 are the dimensions of the considered systems [60]. This definition can also be extended for n systems $\mathbf{x}^{(1)}, \mathbf{x}^{(2)}, \dots, \mathbf{x}^{(n)}$ and a multivariate joint recurrence matrix can be defined as [2]

$$JR_{i,j}^{joint} = \mathbf{x}^{(1,2,\dots,n)}(\varepsilon^{\mathbf{x}^{(1)}}, \varepsilon^{\mathbf{x}^{(2)}}, \dots, \varepsilon^{\mathbf{x}^{(n)}}) = \prod_{k=1}^n R_{i,j}^{\mathbf{x}^{(k)}}(\varepsilon^{\mathbf{x}^{(k)}}) \quad (3.32)$$

where $i, j = 1, 2, \dots, N$. The JRP is invariant under the permutation of the coordinates in one or both of the considered systems [2].

The JRP can be further used to compute the joint recurrence probabilities and conditional recurrence probabilities [61]. The mean conditional recurrence (*MCR*) probabilities can be used to infer direction of couplings. Recall the definition of the *RR* (Equation 3.16), which can be thought of as the mean probability of recurrence,

$$\langle p(\mathbf{x}_j) \rangle = RR = \frac{1}{N^2} \sum_{i,j=1}^N R_{i,j}, \quad (3.33)$$

for a time series $x(t)$, representing a dynamical system X . Given another time series $y(t)$ representing a dynamical system Y , the influence of X on Y can be given as

$$MCR(X|Y) = \frac{1}{N} \sum_{j=1}^N \frac{\sum_{i=1}^N JR_{i,j}}{\sum_{i=1}^N R_{i,j}^Y}, \quad (3.34)$$

In an analogous fashion one can define,

$$MCR(Y|X) = \frac{1}{N} \sum_{j=1}^N \frac{\sum_{i=1}^N JR_{i,j}}{\sum_{i=1}^N R_{i,j}^X}. \quad (3.35)$$

If X is driving Y , then the asymmetry in the coupling is given by the inequality $MCR(Y|X) < MCR(X|Y)$, because the dimension of Y increases compared to X which in turn results in the decrease of the recurrence probability $p(\mathbf{y}_j)$ [61]. This procedure has also been extended to infer indirect coupling in a truly multivariate scenario and is known as partial *MCR* method. For more details regarding the partial *MCR* method, the reader is directed to [61].

3.3 Fractal dimensions

Geometry deals with objects in space and specifically, fractal geometry deals with non-idealized, crinkly objects that are characterized by their fractional dimensions [45]. Attractors can be considered as conceptual objects, that arise in the state space of dissipative chaotic (and in some cases even non-chaotic) systems [45] and they have complicated geometry, described by Lorenz [62] as **infinite complex of surfaces** (In describing the Lorenz attractor). Such attractors with seemingly complicated geometry are known as strange attractors, which are characterized by fractional dimension. Also, fractional dimension is usually exhibited by geometrical objects that display unusual kind of self-similarity to some degree. This means that when a tiny part of the fractal object is magnified, it resembles the whole object. This resemblance is sometime exact, but more often it is approximate or statistical [63].

The dimension of an attractor is an important and intensely studied invariant quantity for dynamical systems [36]. Consider an m -dimensional phase space, comprising of N non-empty hypercubes of length l , that is needed to fully cover the attractor embedded in the phase space. The number of hypercubes needed to cover the attractor typically scales as a function of the length parameter, $N(l) \approx l^{-D_0}$, where D_0 can be thought of as the dimension of attractor the hypercubes are covering. Thus the dimension D_0 of the attractor can be approximated as follows,

$$D_0 = \lim_{l \rightarrow 0} \frac{\log N(l)}{\log \frac{1}{l}}. \quad (3.36)$$

The term D_0 is referred to as the **box-counting dimension**. Theoretically, the largest value of D_0 as $l \rightarrow 0$, is m , the phase space dimension. If the embedding dimension is inadequate to unfold the attractor completely, only a projection of the attractor structure is observed and thus for low dimensional embeddings, the attractor will fill the phase space completely and D_0 becomes almost equal to m . Hence, one commonly computes D_0 for increasing embedding dimensions until a saturation in the value of D_0 is observed, indicating that the attractor has been properly unfolded [36]. Apart from D_0 , one can define more notions of fractal dimensions. Suppose again that $N(l)$ is the number of hypercubes needed to cover an attractor set. If the number of points of the attractor set contained in the i^{th} hypercube is N_i , then the probability p_i for a randomly chosen point of the attractor set to be in the i^{th} hypercube is $p_i = N_i/N(l)$. Now one can define the dimension spectrum as

$$D_q = \lim_{l \rightarrow 0} \frac{1}{1-q} \frac{\log \sum_{i=1}^{N(l)} p_i^q}{\log \frac{1}{l}}. \quad (3.37)$$

For $q = 0$, the Equation 3.37 reduces to Equation 3.36, which defines the box-counting dimension. Borrowing concepts from the theory of information, the notion of dimension can be extended by estimating how many bits of information are needed to specify a point on the attractor set. For $q = 1$, the the Equation 3.37 results in the definition of the **information dimension** given as,

$$D_1 = \lim_{l \rightarrow 0} \frac{-\sum_{i=1}^{N(l)} p_i \log p_i}{\log \frac{1}{l}}, \quad (3.38)$$

where the numerator in the Equation 3.38 is related to the Shanon entropy. For $q = 2$, Equation 3.37 becomes

$$D_2 = \lim_{l \rightarrow 0} \frac{\log \sum_{i=1}^{N(l)} p_i^2}{\log \frac{1}{l}}, \quad (3.39)$$

which is known as the **correlation dimension** as the numerator comprises a two-point correlation function describing the probability of finding a pair of points within a hypercube [36]. Grassberger and Procaccia [53] suggested a computationalyl simple algorithm to estimate the two-point correlation and suggested using

$$C(l) = \frac{2}{N(N-1)} \sum_{i \neq j}^N \theta(l - \|\mathbf{x}_i - \mathbf{x}_j\|), \quad (3.40)$$

where $\theta(\cdot)$ is the Heaviside function and l is the distance threshold for proximity. Now, one can compute D_2 as

$$D_2 = \lim_{l \rightarrow 0} \frac{\log C(l)}{\log l} \quad (3.41)$$

3.4 Other nonlinear measures

3.4.1 Lyapunov exponents

Chaos in a dynamical system can be characterized by the exponential separation of nearby trajectories and the Lyapunov exponent can be used to measure this separation. Since chaotic orbits are bounded, this separation and hence the mutual distance between two diverging points cannot tend to infinity. Consider two neighboring points \mathbf{x}_0 and $\mathbf{x}_0 + \delta\mathbf{x}_0$, with initial separation $\delta\mathbf{x}_0$. The divergence of these two points occurs at a rate given by

$$\delta\mathbf{x}(t) \approx e^{\lambda t} |\delta\mathbf{x}_0| \quad (3.42)$$

The parameter λ is known as the Lyapunov exponent. An m -dimensional system has m Lyapunov exponents and in general the behavior of such an m -dimensional subspace is given by the sum of m Lyapunov exponents. Evidently, positive Lyapunov exponents

result in exponential separation of trajectories and are a hallmark of chaotic behavior. If all the Lyapunov exponents are negative, it means that all the orbits are stable as the separation will exponentially decrease to zero, i.e., contraction occurs. For dissipative systems, the sum of all the Lyapunov exponents must be negative and this sum gives the rate at which a finite volume in phase space will contract to zero. Continuous flows have one zero exponent and this implies that for the occurrence of chaos at least three dimensions are required [32]. Also, using positive Lyapunov exponents, Kolmogorov-Sinai entropy can be estimated in an obvious way as [64],

$$K = \sum_{\lambda_i > 0} \lambda_i \quad (3.43)$$

3.4.2 Entropy measures

The framework of information theory can be used to characterize a dynamical system [20]. Entropy is an important and old concept, already known in the field of statistical mechanics and thermodynamics. The concept of entropy was introduced to information theory through the work of Shannon [65] in 1948. In order to use the tools from information theory, the trajectories of a dynamical system (continuous or discrete) have to be encoded into discrete symbolic sequences [20]. In case of continuous dynamical system, once can use time discretization by using a fixed sampling time T or by use of the poincaré section. The **Shannon entropy** of a system can be defined in terms of the probability, $P(\mathbf{x})$, that the system is in state \mathbf{x} [32]. It is given as [65]

$$H(\mathcal{A}) = \int_{\mathbf{x} \in \mathcal{A}} P(\mathbf{x}) \log_2(P(\mathbf{x})) d\mathbf{x}, \quad (3.44)$$

3.4.2.1 Kolmogorov-Sinai entropy

Given a trajectory, $\mathbf{X} = \{\mathbf{x}_0, \mathbf{x}_1, \dots, \mathbf{x}_n, \dots\}$, the surprise associated with $\{\mathbf{x}_n\}$ can be measured by [32] $-\frac{1}{NT+1} - \int_{n=0}^{NT} P(\mathbf{x}_n) \log_2(P(\mathbf{x}_n)) d\mathbf{x}$, where $n = 0, 1, 2, \dots, NT$ is a finite time window and T is the sampling time. Consider a partitioning of an attractor set \mathcal{A} into D boxes of size ε^m (here m is the phase space dimension), $A_1, A_2, \dots, A_D \subset \mathcal{A}$, where $A_i \neq \emptyset$ and $A_i \cap A_j = \emptyset$ for all i, j [32]. Let $\mathbf{P}_{A_{i_0}, A_{i_1}, \dots, A_{i_N}}$ be the probability that a trajectory is in the partition A_{i_0} at $t = 0$, A_{i_1} at $t = T$, A_{i_2} at $t = 2T$, \dots , A_{i_N} at $t = NT$. Let us define K_N in bits as

$$K_N = - \sum_{i_0, i_1, \dots, i_N} \mathbf{P}_{A_{i_0}, A_{i_1}, \dots, A_{i_N}} \log_2 \mathbf{P}_{A_{i_0}, A_{i_1}, \dots, A_{i_N}} \quad (3.45)$$

Now, consider the difference $K_{n+1} - K_n$, which is the information needed to identify the hypercubes visited by a trajectory between times nT and $(n+1)T$. Now, one can define the Kolmogorov entropy as

$$K \equiv \lim_{T \rightarrow 0} \lim_{\varepsilon \rightarrow 0^+} \lim_{N \rightarrow \infty} \frac{1}{NT} \sum_{n=0}^{N-1} (K_{n+1} - K_n) \quad (3.46)$$

3.4.2.2 Approximate and sample entropy

In the last two decades, the concept of entropy and its related methods have been used to define periodicity or regularity of various biological data [66]. Two most commonly used methods in this context are approximate and sample entropy. Approximate entropy, introduced by Pincus *et al.* [67], is a regularity statistic to quantify unpredictability of fluctuations over time-series data [68]. Consider a time series $\{x_i\}$ with N samples, where $i = 1, 2, \dots, N$, zero mean and unit variance. The corresponding m dimensional embedding vector for $\tau = 1$ is given as $\mathbf{x}_i^m = (x_i, x_{i-1}, \dots, x_{i-m+1})$. Define $B(i, r)$ as

$$B(i, r) = \frac{1}{N - m + 1} \sum_{j=1, j \neq i}^{N-m} \Theta(r - \|\mathbf{x}_i^m - \mathbf{x}_j^m\|) \quad (3.47)$$

where $\Theta(\cdot)$ is the Heaviside function and r is the distance threshold. Now define $B(r) = \frac{1}{N-m+1} \sum_{i=1}^{N-m+1} \log(B(i, r))$. Basically, $B(i, r)$ represents for a given threshold r , how many m -dimensional vectors are close to \mathbf{x}_i^m and $B(r)$ represents the sum taken over all time instances of $\mathbf{X}^m = (\mathbf{x}_1^m, \mathbf{x}_2^m, \dots, \mathbf{x}_{N-m+1}^m)$. In a similar vein, $A(r)$ and $A(i, r)$ are defined for the dimension $m+1$. Now, one can define the approximate entropy as

$$ApEn(m, r, N) = A(r) - B(r) \quad (3.48)$$

Approximate entropy gives the likelihood that similar patterns of observations will not be followed by additional similar observations and thus a time series containing many repetitive patterns will have small values of approximate entropy while an unpredictable and complex process will have a higher value [68]. However, approximate entropy measure introduces bias, particularly due to the length of the data and may suggest more similarity in a time series than is actually present [69]. To overcome this bias, sample entropy was introduced, which is a modification of the approximate entropy and is a measure of complexity [69]. It is defined as

$$SampEn(m, r, N) = -\log \frac{A(r)}{B(r)} \quad (3.49)$$

Thus, sample entropy is the negative logarithm of the conditional probability that if two sequences of m points are within a distance r , then two sequences of $m + 1$ points are also within a distance r . Compared to approximate entropy, sample entropy is less dependent on the data size [69] and thus converges to consistent values for smaller values of both N and r .

3.4.3 Nonlinear prediction error

Nonlinear prediction error can be used to quantify the degree to which similar present states are mapped to similar future states and this similarity can be estimated using the spatial proximity of the reconstructed state vectors [70]. For a given embedding lag τ , consider an m -dimensional embedding vector of a time series $\{x_n\}$ with N samples, where $n = 1, 2, \dots, N$, at time instant i given as $\mathbf{x}_i = (x_i, x_{i-\tau}, \dots, x_{i-(m-1)\tau}) = (x_{i,1}, x_{i,2}, \dots, x_{i,m})$. Consider an Euclidean distance (In principle, this can be any distance metric) matrix defined as

$$D_{i,j} = d(\mathbf{x}_i, \mathbf{x}_j) = \sqrt{\frac{1}{m} \sum_{dim=1}^m (x_{i,dim} - x_{j,dim})^2} \quad (3.50)$$

Following Andrzejak *et al.* [4], for a given horizon H , the nonlinear prediction error can be computed as follows for $i_{ref} = (1, 2, \dots, N - H)$,

1. Choose a reference point $\mathbf{x}_{i_{ref}}$
2. Find k -nearest neighbors in sense of Euclidean (or any distance metric) distance. Let us denote this set as $\{\mathbf{x}_{i_{ref},1}, \mathbf{x}_{i_{ref},2}, \dots, \mathbf{x}_{i_{ref},k}\}$
3. Define local prediction error for a given horizon as

$$\epsilon_{i_{ref},H} = \|\mathbf{x}_{i_{ref}+H} - \frac{1}{k} \sum_{n=1}^k \mathbf{x}_{i_{ref},n+H}\| \quad (3.51)$$

where $\|\cdot\|$ is an Euclidean distance norm.

4. Define the local prediction error for the mean of the time series as

$$\epsilon_{i_{ref},\bar{\mathbf{x}}} = \|\mathbf{x}_{i_{ref}+H} - \bar{\mathbf{x}}\| \quad (3.52)$$

where $\bar{\mathbf{x}}$ carries the mean along each of its m -dimensions.

5. The nonlinear prediction error is given as

$$P = \sqrt{\frac{\sum_{i_{ref}=1}^{N-H} \epsilon_{i_{ref},H}^2}{\sum_{i_{ref}=1}^{N-H} \epsilon_{i_{ref},\bar{x}}^2}} \quad (3.53)$$

Normally while computing nonlinear prediction error, a Thieler correction with window length W is applied to exclude neighbors that are in the temporal vicinity to avoid causality conflicts [8], i.e., $\|i_{ref}, r - i_{ref}\| > W, \forall r = 1, 2, \dots, k$.

3.5 Distinguishing chaos and noise

Distinguishing chaotic from stochastic processes is an important problem arising in many fields ranging from biology and physics to ecology and finance. Numerous approaches have been proposed to solve this critical issue of distinguishing between stochastic and chaotic dynamics, which is laced with several challenges since both chaotic and stochastic processes share some common properties, e.g., a broadband power spectra, delta-like autocorrelation function and long-term irregular behavior. It may even be practically impossible to distinguish high-dimensional chaos from a stochastic process. Since in a chaotic system, the time evolution of two nearby trajectories will diverge exponentially fast compared to a stochastic system where the separation is randomly distributed [71], methods based on short-term predictability have been applied to distinguish chaos from noise [72, 73]. Thus for a chaotic time series, the accuracy of forecast should decrease with increasing prediction-time interval and for a stochastic time series this accuracy should be independent of the prediction-time interval [73]. Kaplan and Glass [74, 75] proposed a test for determinism based on the measurement of average directional vectors in a coarse-grained phase space. This test is based on the observation that the tangents to the trajectories of a deterministic system, passing through a small region in phase space, will be well aligned, i.e., oriented in the same direction, a behavior not observed in stochastic dynamics [74, 75]. Another line of approach borrows from the concept that a chaotic attractor should have finite, non-integer values for fractal dimensions, while stochastic processes must theoretically exhibit infinite dimensions. This traditional view was challenged by Osborne and Provenzale [76], when they demonstrated that finite correlation dimension could be obtained from a simple class of colored random noise characterized by power-law spectrum. Recently, quantifiers from information theory have been used to address the issue of distinguishing between chaotic and stochastic dynamics, leading to some interesting results [37]. Rosso *et al.* [77] introduced complexity-entropy causality plane, a two-dimensional representation space that

relates two information theoretic quantities namely entropy and complexity, to distinguish between stochastic and chaotic dynamics. By explicitly including the time scale notion, Zunino *et al.* [78] proposed multiscale complexity-entropy plane to identify the time scales where stochastic and chaotic components govern the system's dynamics. The classification of stochastic or chaotic character of a given time series at different resolution scale using entropic analysis was first proposed by Cencini *et al.* [79]. Olivares *et al.* [80, 81] also proposed a combination of two information theoretic quantities, the Shannon entropy and the Fisher information, to obtain the Shannon-Fisher causality ($\mathcal{S} \times \mathcal{F}$) plane and showed that the stochastic and chaotic dynamics map to different locations in this two-dimensional plane.

By bridging the gap between nonlinear time series analysis and complex network theory, methods to transform a time series into a complex network comprising of nodes which represent the state vectors in phase space and edges that are defined based on some criteria such as mutual closeness or transition probabilities, have emerged [16, 17]. Different classes of such time-series based complex networks exist like the proximity networks [15, 16, 82–84], transition networks [85] or visibility graphs [86, 87]. A comprehensive review on these network-types is given elsewhere [16]. The underlying principle in this approach is to characterize the topology of the resultant network using tools from graph theory to gain insights into the dynamics underlying the time series. Lacasa and Toral [71] used horizontal visibility graphs (HVGs) [88], a geometrically simpler version of the visibility graph algorithm, to distinguish between chaotic and stochastic (correlated and uncorrelated) dynamics based on the node degree distribution (specifically the slope of the logarithm of the degree distribution) of the resultant networks. Recently, Ravetti *et al.* showed that the HVG approach is sensitive to the scaling zone and combined the HVG approach with information theory quantifiers (the $\mathcal{S} \times \mathcal{F}$ plane) that leads to a better characterization of deterministic and stochastic dynamics.

3.6 Surrogates

It has been previously demonstrated that nonlinear methods for time series analysis can mistake linear correlations for determinism [76] or filtered noise for chaos [89]. The idea behind surrogate data testing [90–92] is to find a simple explanation that cannot be ignored based on the data [93]. It tests against the null hypothesis (H_0), that the data under consideration belongs to a particular class of linear random process. In this section we will briefly review some of the most widely used algorithms to generate surrogates from the data

- **Random shuffling (Algorithm 0):** The simplest method of producing surrogate data involves random shuffling (RS), where random permutations of the original data is performed and was originally proposed in [94]. The surrogates generated have the same amplitude distribution but different power spectrum (equivalently the autocorrelation). Such surrogates can be only used to test the H_0 that the original data is independent and identically distributed observation.
- **Random phases or Fourier transform method (Algorithm 1):** This method preserves autocorrelation function of the original data while generating surrogates. The method was originally proposed in [95]. The H_0 is of a Gaussian linear stochastic process and the randomized sample is generated by creating surrogates containing the same second order properties as the original data, but which are otherwise random [93]. Algorithmically, one computes the fast Fourier transform (FFT) of the data and multiplies it with random phases. Transforming the data back in time domain with inverse Fourier transform results in surrogate time series $s_n(t)$ having same linear properties as the original data, but destroys any nonlinear structure.

$$s_n(t) = \frac{1}{\sqrt{N}} \sum_{k=0}^{N-1} e^{i\alpha_k} |S_k| \exp\left(\frac{-i2\pi kn}{N}\right) \quad (3.54)$$

where α_k are independent uniform random numbers ($0 \leq \alpha_k \leq 2\pi$) and S_k is the Fourier transform of the original data.

- **Amplitude adjusted Fourier transform method (Algorithm 2):** The amplitude adjusted Fourier transform (AAFT) algorithm generates surrogates that can be used to test the H_0 of a Gaussian linear stochastic process possibly transformed by a nonlinear static function [90]. The two H_0 's discussed above do not arise in realistic situations and simple explanation for the deviation from H_0 could be due to measurement function that is static and nonlinear, but assumed to be invertible [93]. The procedure involves inverting the measurement function by rescaling the original data to follow a Gaussian distribution. The Algorithm 1 is applied to the rescale data to create phase randomized surrogate and the surrogate is rescaled again to match the distribution of the original data. Although the surrogates created by this procedure have the same amplitude distribution, there are deviations in the power spectrum compared to the original data. Particularly, in case of short and strongly correlated sequence, the AAFT method introduces a bias towards slightly flatter spectrum which can lead to an incorrect test [96].
- **iterative AAFT method (Iterative algorithm 2):** The flatness bias introduced by the AAFT method can be corrected by making a iterative version of the AAFT algorithm, known as iterative amplitude adjusted Fourier transform

(iAAFT) algorithm [96]. In this method, the surrogate is filtered in an alternating fashion towards correct Fourier amplitudes and rank-ordered to obtain correct distributions. This way both amplitude distribution and as well as autocorrelation(or power spectrum) are preserved. The algorithm starts with first storing a sorted version of the data and its corresponding Fourier amplitudes. A surrogate is generated by an AAFT or RS or a random phases procedure as a starting point for the iterative procedure. Now, a FFT is performed on this randomized data and an the inverse FFT is applied , with the amplitudes replaced by the original Fourier amplitudes. Rescaling is performed using the ranks of the resulting series and the sorted copy of the original data [8].

- **Truncated Fourier transform method** The surrogates generated by the procedures described above are stationary by construction and this can cause the rejection of the H_0 if the data is nonstationary. The truncated Fourier transform (TFT) method was proposed by Nakamura *et al.* [97] to construct surrogates that preserve nonstationarity in the surrogates. In this method, the Fourier phases corresponding to the first few frequencies are preserved and the rest are randomized using AAFT or iAAFT or RS scheme. Thus, first one defines a cut-off frequency (f_c) for which the phases of the original data is preserved in the surrogates. The value of f_c can range from 0(0 Hz) to $0.5(0.5 \times F_s$, where F_s is the sampling frequency). Thus f_c represents the normalized frequency corresponding to the integer index $(0, 1, \dots, N/2)$ of the N -point Fourier transformed data. Using the TFT method, local nonstationarity can be preserved and for large values of f_c , even global nonstationarity can be preserved. Thus the H_0 addressed by the TFT method is that the irregular fluctuations in the data arise from a stationary linear system. A crucial parameter in the TFT method is the f_c which determines how much phase should be preserved. If the choice is too small, then the TFT method becomes similar to the AAFT or iAAFT approach. On the other hand, if this value is large then the surrogates contain too much of the nonlinearity present in the data.
- **Other methods:** In addition to the above mentioned methods, host of other methods have been proposed to generate surrogate data. The AAFT and the iAAFT method has been expanded to multivariate time series by Prichard and Thieler [98] and Schreiber and Schmitz [93] respectively. Ortega and Louis [99] proposed a partial surrogation scheme which is a modification of the Algorithm 1, where the degree of randomization of the phases is varied from 0% to 100% by replacing $e^{i\alpha_k}$ with $e^{iM\alpha_k}$, where $M \in [0, 1]$. Small *et al.* [100] proposed a surrogate test for pseudoperiodic time series, based on local-linear modeling methods

[73, 101] and involves reconstructing a scalar surrogate time series from a vector time series that represents a stochastic trajectory on the attractor estimated from the original data. Breakspear *et al.* [102] proposed a wavelet-based approach involving random permutations of the detail wavelet coefficients. However, the inherent periodicity of wavelet coefficients at a selected scale is not preserved when simple randomization is done. To overcome this problem an approach was proposed by Keylock [103] where iAAFT scheme is utilized to randomize the wavelet coefficients so as to preserve the periodicities of the coefficients. In order to minimize the error between the original time series and the wavelet-based surrogates, an optimal matching procedure was used in [103]. Instead of using optimal matching criteria, Keylock [104] also introduced a method that uses a threshold to retain particular wavelet coefficients in place while randomizing the rest to generate constrained surrogates. Such surrogates were shown to avoid the problems of nonstationarity in pseudo-periodic signals [104]. Nakamura and Small proposed the small shuffle surrogate (SSS) method [105] that can be used to identify dynamics of irregular time series.

A theory is a supposition which we hope to be true, a hypothesis is a supposition which we expect to be useful; fictions belong to the realm of art; if made to intrude elsewhere, they become either make-believes or mistakes

GEORGE JOHNSTONE STONEY
(1826-1911)

4.1 Complex networks

We are surrounded by networks that represent complex systems comprising of many interacting components. Such networks are known as **complex networks** and they have irregular and complex structure, which dynamically evolves with time [106]. Complex networks serve as an important tool to not only understand the **structural connectivity** between mutually interacting components of a complex system [106–108], but also to study the statistical dependencies and causal interactions between different components, where the connectivity is not necessarily physical. For examples, complex networks have been used extensively in understanding the statistical dependencies and causal interactions between different areas of the brain [109, 110, 110, 111] using functional magnetic resonance imaging (fMRI) or multivariate EEG data, which is referred to as **functional** and **effective connectivity** respectively. Similar applications have emerged with multivariate climate data [112–114] as well. Over the last two decades or so, several important

results have emerged from the study and application of complex networks, few examples of which include neural networks [115–117], food webs [118, 119], metabolic networks [120–122] social networks [123–126] the Internet and World-Wide Web [127, 128], power grids [129, 130] and transportation networks [131, 132]. Although the study and research on complex networks has emerged only under two decades ago, **graph theory** which is used in the mathematical treatment of networks, in order to study and characterize the network topology, is an old field of study, with its origins in 1736. It was the Swiss mathematician Leonhard Euler, who first gave the solution to the Königsberg bridge problem [133] and the field of graph theory was born [106].

Regular and **random** networks can be considered as two ends of the spectrum of complex network architecture. A regular network is a network in which every vertex has exactly the same number of links or edges. Such networks are highly ordered. Examples of such networks include, chains, grids, lattices and fully connected graphs [134]. The simplest type of random network was proposed by Erdős and Reyni [135], where every edge is formed independently of every other edge, with a probability p . Two important properties of these two types of networks are high clustering (i.e., high number of triangles) for regular networks and low average path length (i.e., average shortest path between two vertices) respectively. However, most real-life networks lie between these two extremes of regular and random networks and are characterized high clustering and low average path length. Such networks are known as **small-world** networks. Watts and Strogatz [136] proposed a model to generate such networks and in a bid to explain the transition from regular to random networks, this small-world effect was discovered. Starting from a regular lattice and replacing original edges by random ones, according to some probability $0 \leq p \leq 1$, one can generate a small-world network with slight rewiring of the edges [134]. For high values of p , the network transforms into a completely random network. Another important characteristic of a complex network is its degree distribution p_k , which refers to the fraction of vertices p_k that have a k edges. A random network exhibits bell-shaped Poisson distribution, but for many real networks, the degree distribution is skewed and decays as power law [134], $p_k \approx k^{-\gamma}$, with the exponent γ between 2 and 3. Such networks are known as **scale-free** networks [137, 138] as no single characteristic scale can be described for these networks, analogous to fractals [134].

4.2 Graph theory

Definition 4.1. A graph G is composed of a set of **vertices** (or nodes) $V = \{1, 2, \dots, N\}$ and **edges** (or links) $E \subseteq V \times V$, satisfying $E \subseteq [V]^2$ and is represented as $G = (V, E)$.

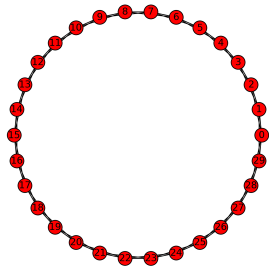


FIGURE 4.1: A ring lattice with $N = 30$.

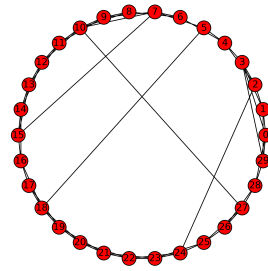


FIGURE 4.2: A WS small world network with $N = 30$ and $p = 0.1$.

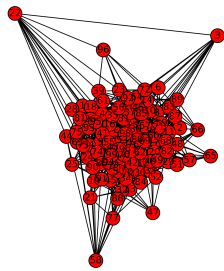


FIGURE 4.3: An Erdős and Reyni random graph with $N = 100$ and $p = 0.15$.

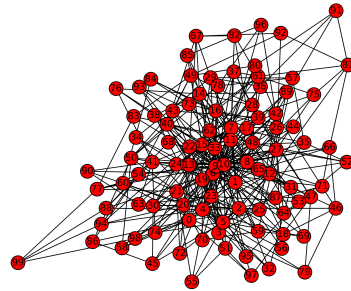
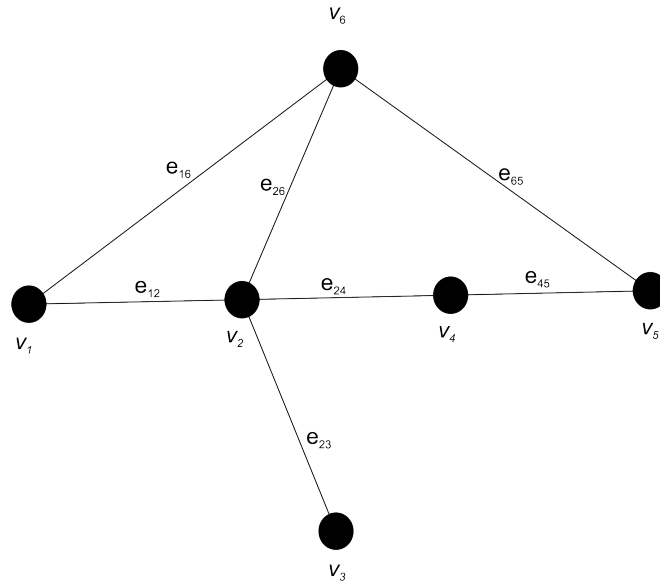
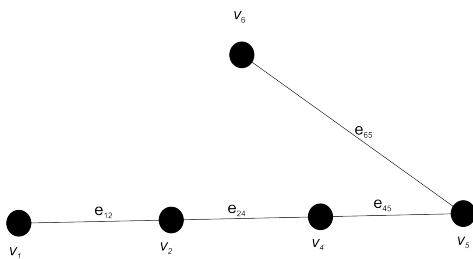
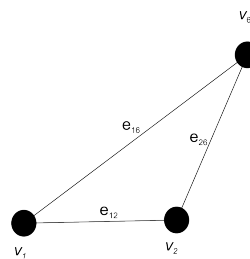


FIGURE 4.4: A scale-free Barabási-Albert network with $N = 100$.

The number of vertices and edges in a graph are denoted as $N(= |V|)$ and $K(= |E|)$ respectively. An edge e in a graph connects a pair of vertices (i, j) , where $i, j \in V$ and this connection is denoted as $e_{i,j}$. A graph is **undirected** or **directed** if the set E is unordered or ordered respectively. Thus, for an undirected graph, $e_{i,j} = e_{j,i}$, where as in case of a directed graph the order of vertices is important and hence $e_{i,j} \neq e_{j,i}$. Below, some common terminologies associated with graphs are described [106].

1. The edge e which connects two vertices i and j is said to be **incident** with vertices i and j . These two vertices are said to be **adjacent** and are also known as end vertices of the edge e .
2. A graph G with no self-loops and multiple edges is known as a **simple** graph. A simple graph with N vertices and K edges can have at most $N(N - 1)/2$ edges and a graph with $K = N(N - 1)/2$ is known as a **complete** N -graph. A **sparse** graph has $K \ll N^2$ and a **dense** graph has $K = \mathcal{O}(N^2)$.
3. A graph with no vertices is known as an **empty** graph and with one vertex is known as a **trivial** graph.

FIGURE 4.5: An undirected graph G consisting of 6 vertices and 7 edges.FIGURE 4.6: A subgraph of G consisting of 6 vertices and 4 edges.FIGURE 4.7: An induced subgraph of G consisting of 3 vertices and 3 edges.

4. The **order** of a graph is given by the number of vertices of the graph and is represented as $|G|$. The number of edges is represented as $||G||$. **Finite** graphs have finite order and **infinite** graphs have an infinite order.

Definition 4.2. A subgraph \hat{G} of a graph G is composed of the set $\hat{E} \subseteq E$ and set $\hat{V} \subseteq V$. The subgraph \hat{G} of G **induced** by the set \hat{V} contains all the edges of G that join two vertices in \hat{V} , i.e., for $i, j \in \hat{V}$, $(i, j) \in \hat{E}$ if and only if $(i, j) \in E$. Below are some examples of graphs and their corresponding subgraphs.

Definition 4.3. A **walk** in the graph G consists of alternating vertices and edges. A walk starts at the initial vertex v_{i_0} and ends at the terminal vertex v_{i_k} . If $v_{i_0} = v_{i_k}$, a walk is considered **closed**, else it is considered **open**. A walk is a **trail** if an edge is visited not more than once. A trail can be considered as a **path** if any vertex is visited at most once (except in the case of closed walk, where initial and terminal vertex is the same and such a closed path is known as a **circuit**). Given a graph, one can

compute the shortest path between two vertices i and j using Dijkstra's algorithm (for directed and undirected graph), Bellman-Ford algorithm (directed graphs with negative edge weights) and Floyd-Warshall algorithm (weighted directed graphs).

Definition 4.4. A **cycle** is a closed path on a graph G .

Definition 4.5. A graph G is **connected** if each pair of vertices belong to a path. Hence in a connected graph, starting from a vertex, one can reach any other vertex using a path. A maximal connected subgraph of G is called a **component** of G . Thus a subgraph \acute{G} of G is a component if \acute{G} is connected and \acute{G} is the subgraph induced by those edges in G that have one end vertex in \acute{G} .

Definition 4.6. [139] For a vertex $i \in V$ in a graph G , the **neighbor set** of i , $\mathcal{N}(i)$, is defined as the set of vertices that are adjacent to i . Formally,

$$\mathcal{N}(i) \stackrel{\text{def}}{=} \{k \in V \mid i \neq k, \exists e \in E: e_{i,k}\} \quad (4.1)$$

Definition 4.7. The **adjacency matrix** of a graph G is an $N \times N$ matrix and is given as

$$A_{i,j} = \begin{cases} 1 & \text{when } (i, j) \in E, \\ 0 & \text{otherwise.} \end{cases} \quad (4.2)$$

The adjacency matrix \mathbf{A} completely defines a graph up to an isomorphism. For an undirected graph, the adjacency matrix is symmetric. Further, for a simple graph the elements of an adjacency matrix $A_{i,j} \leq 1$ and $A_{i,i} = 0$.

Definition 4.8. Two graphs $G_1 = (V_1, E_1)$ and $G_2 = (V_2, E_2)$ are **isomorphic** if there exists a bijection $f: G_1 \rightarrow G_2$ with $(i, j) \in E_1 \iff (f(i), f(j)) \in E_2$ for all $i, j \in V$, where E_1 and E_2 are the edge sets of the graphs G_1 and G_2 respectively.

4.3 Random geometric graphs

In the four types of networks discussed above - regular networks, random networks, small-world networks and scale free networks, the spatial arrangement of vertices and the space in which the network exists is not considered important. The spatial arrangement of the network vertices can impose constraints on the network structure [106], with connectivity being related to spatial embedding [140]. In such cases where the spatial arrangements play an important role, the mean field theory can no longer be valid [141]. Such networks where vertices are located in a metric space are known as spatial networks. Generally speaking, a spatial network $G = (V, E)$ is a mapping $V \rightarrow S: i \rightarrow x_i$ assigning each vertex $i \in V$ to an element $x_i \in S$ of a set S and metric $l: S \times S \rightarrow \mathbb{R}: (x_i, x_j) \rightarrow l_{ij}$ [142].

A random geometric graph (RGG) [143] is the mathematically simplest spatial network, which can be constructed by placing N points (vertices) on $[0, 1]^d$ with $d \in \mathbb{N}^+$, uniformly at random, according to some probability density function $p(x)$ with $x \in \mathbb{R}^d$ [143]. RGGs have been used in the study of continuum percolation [144–146] along with modeling of wireless ad hoc networks [147, 148]. In such graphs, an edge is formed between vertices close to each other, as defined by some proximity criterion (for example, smaller than a certain neighborhood radius). Thus, the probability of being connected for any two vertices i and j in an RGG has the form $P(A_{ij}) = f(\|x_i - x_j\|)$, where f is a monotonically decreasing function. As a consequence, in RGGs, vertices that are spatially close to each other have a higher probability of being connected than the distance ones. For example, one can define the function as $f(\|x_i - x_j\|) = \Theta(\varepsilon - \|x_i - x_j\|)$ leading to an RGG whose adjacency matrix can represent a RN where the probability density function $p(x)$ is the invariant density of the dynamically invariant object, i.e., the attractor set \mathcal{A} [55]. Also, since the metric space for instance, can be an abstract space like the phase space of a dynamical system [142] and the vertices can be represented by the state vectors, ε -RN also constitute an RGG, where edges are formed between vertices within a certain distance threshold, ε .

Geometry is not true, it is advantageous.

HENRI POINCARÉ (1854 - 1912)

In this chapter, we describe the transformation of time series into complex networks using various approaches and then focus on one such approach that is central to this thesis, the RNs (Section 5.1). By borrowing from the rich toolbox of graph theory, various vertex-based, edge-based and global network measures can be defined for networks derived from time series. We briefly review some of these network measures important for the thesis and their interpretation in the context of RNs (Section 5.2). The notion of attractor dimension in terms of network transitivity and local clustering coefficient is also briefly discussed (Section 5.3) For a detailed overview on these measures, the reader is further directed to [16, 149]. Apart from the graph-theoretical measures, other novel (cross)-network measures introduced by Donges *et al.* [149] to characterize mutual interconnectivity between complex networks are also discussed (Section 5.4). Finally, some of the key properties and applications of RNs are discussed (Section 5.5).

5.1 Time series to complex networks

Nonlinear time series analysis (Chapter 3) and complex network theory (Chapter 4) are two fundamental and important tools to analyze complex systems. Particularly, due to the success of network theory in a variety of fields, transforming a time series into a complex network for nonlinear time series analysis has garnered much attention

recently and a number of different approaches have been proposed [15, 16, 82–84, 87, 150–152]. These approaches can be broadly divided into three classes - proximity networks, visibility graphs and transition networks [16]. The underlying idea is to transform a time series into a complex network and quantify their topology using tools from graph theory to gain insights into the dynamics of the underlying system. Such complex networks can be directed or undirected and the vertices are represented by state vectors or cycles and the edges between the vertices are defined based on some criteria such as mutual closeness or transition probabilities. For instance, proximity networks are derived based on the mutual closeness between different state vectors in the phase space [16, 17], where as transition networks are constructed by defining transition probabilities after coarse-graining the phase-space [85]. Visibility graphs (VGs) are based on the convexity relation between different observations in a time series [87, 153].

The proximity networks can be further divided into cycle networks, correlation networks, k -nearest neighbor recurrence network (k -NN) RNs, adaptive nearest neighbor recurrence network (A-NN) RNs and ε -RNs [16, 17]. A cycle network can be constructed by dividing a time series (pseudo-periodic) into cycles, with each cycle representing a vertex in the network. In such a network, an edge is formed between the nodes if the phase space distance between the corresponding cycles is lesser than a predetermined threshold [82]. In correlation networks, the Pearson correlation coefficient between two state vectors is used as a closeness measure to define the existence of an edge between two nodes (i.e., state vectors) [83]. k -NN RNs, A-NN RNs, and ε -RNs are particularly known as RNs as they are based on the recurrences in phase space and are obtained by reinterpreting the recurrence matrix as the adjacency matrix of a complex network [15]. A k -NN RN is formed by simply linking every vertex i to its k nearest neighbors using some distance metric (euclidean or manhattan or maximum norm) and such a network is related to the original definition of an RP by Eckmann *et al.* [13]. Such a network is asymmetric and directed because $i \in \mathcal{N}(j)$ does not imply $j \in \mathcal{N}(i)$ [17]. One simplistic approach suggested by Shimada *et al.* [84] is to convert k -nearest neighbor recurrence network into an undirected and symmetric network by artificially setting the elements of the recurrence matrix $R(j, i) = 1$ whenever $R(i, j) = 1$. Xu *et al.* first proposed the concept of transforming a time series into an undirected complex network [151], known as A-NN RNs. In this approach, if vertex $j \in \mathcal{N}(i)$, then vertex i is removed from $\mathcal{N}(j)$ to avoid the possibility of double-counting [17]. This results in a symmetric adjacency matrix with an average degree of $2K_0$, where K_0 is the fixed number of neighbors initially assigned. In case of an ε -RN, one defines a fixed phase space distance ε centered around a vertex i (i.e., a state vector in phase space) [15, 16]. All the vertices that fall within this volume are connected to the vertex i by forming an edge. Such a network is both undirected and symmetric. The k -NN RNs, A-NN RNs and ε -RNs are directly

related with the concept of Poincaré recurrence in phase space and can be used to determine the dynamical invariants of the underlying system [153] and provide an alternative framework for studying recurrences from a geometric point of view [18].

5.1.1 ε -recurrence network

Given an univariate time series $\{x_i\}$ with N samples, where $i = 0, 1, 2, \dots, (N - 1)$, one can obtain an RP (See Section 3.2) after performing the attractor reconstruction using time-delay embedding method [8, 30, 35, 46]. The (reconstructed) state vectors $\mathbf{x}_i = (x_i, x_{i+\tau}, \dots, x_{i+(m-1)\tau})$, can be transformed into a complex network by re-interpreting the matrix \mathbf{R} (Equation 3.14) as the adjacency matrix (\mathbf{A}) of an adjoint complex network embedded in a phase space,

$$\mathbf{A} = \mathbf{R} - \mathbf{I}, \quad (5.1)$$

where \mathbf{I} is the identity matrix, that eliminates the self-loops. Such a complex network is referred to as an ε -RN (In the remainder of the thesis, we will refer to ε -RNs simply as RNs, unless stated otherwise) as the corresponding RP is defined based on the definition of ε -neighborhood, i.e., for states \mathbf{x}_i and \mathbf{x}_j within an ε -neighborhood, the corresponding entry in the matrix $R_{i,j} = 1$. The matrix \mathbf{A} given by the Equation 5.1 retains the symmetry properties of the matrix \mathbf{R} . Thus, the RN represents a simple graph (see Section 4.2), where there are no multiple edges and $A_{i,i} = 0$. Selecting the threshold ε is crucial in constructing RNs. As mentioned earlier in Section 3.2 in case of RPs and discussed in detail elsewhere in case of RNs [15, 154], selecting a low value of ε can result in very few recurrence recurrence points than there are, resulting in an incorrect representation of the true recurrence structure of the underlying system. In such cases, the information obtained from RNs can be very limited [17]. If ε is set to a high value, it can result in too many recurrence points (false recurrences), i.e., the neighbors of a vertex in an RN can be due to temporal proximity and not true proximity in phase space. Although, there is no universal threshold selection criteria, based on some general considerations it has been suggested that selecting a threshold such that the corresponding $RR \leq 0.05$ is a reasonable choice to represent attractor topology faithfully in phase space [15, 16]. Additionally, it is advantageous to fix RR and then to choose ε adaptively as this approach makes sure that obtained RNs from different systems have approximately the same number of edges and hence the network measures can be compared objectively [17]. An exemplary RN for the Lorenz system is shown in Figure ??.

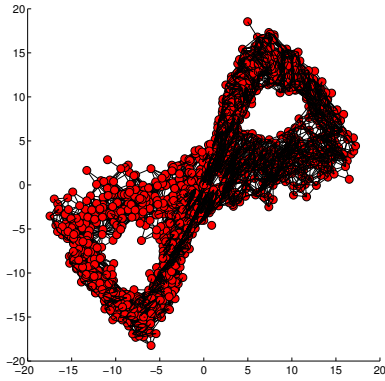


FIGURE 5.1: RN derived from the Lorenz system. The nodes (filled red circles) represent the state vectors and the existence of a link (solid black line) between two nodes depends on the distance threshold ε , which in this example is fixed by setting $RR = 0.02$.

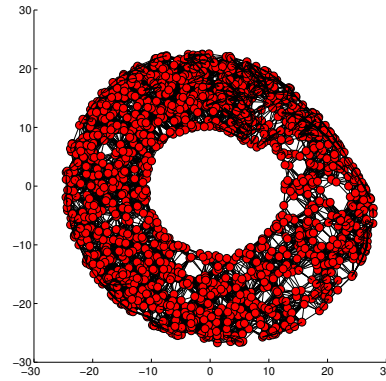


FIGURE 5.2: RN derived from the Rössler system. The nodes (filled red circles) represent the state vectors and the existence of a link (solid black line) between two nodes depends on the distance threshold ε , which in this example is fixed by setting $RR = 0.02$.

5.2 Network measures

5.2.1 Vertex-based local measures

5.2.1.1 Degree centrality

Degree centrality is a simple measure used to characterize the connectivity properties of a single vertex [18]. For a vertex i in a complex network, it can be defined as the number of vertices directly connected to i . It is given as

$$k_i = \sum_{j=1}^N A(i, j). \quad (5.2)$$

k_i can be normalized to describe the local phase space density, which gives the probability that a randomly chosen state vector in the phase space is within the ε -neighborhood of the state vector \mathbf{x}_i represented by the vertex i in the complex network. It is given as

$$\rho_i = \frac{k_i}{N - 1}, \quad (5.3)$$

which also corresponds to the definition of the local RR [16].

5.2.1.2 Closeness centrality

Closeness centrality can be defined as the inverse of the length of the shortest path (i.e., the geodesic distance) between a vertex i and all other vertices in a network. Given

the geodesic distance $d(i, j)$ between two vertices i and j in a network, the closeness centrality of the vertex i can be then defined as [155]

$$c_i = \frac{N - 1}{\sum_{j=1}^N d(i, j)} \quad (5.4)$$

Apart from Equation 5.4, other definitions for the c_i exist. The network measure c_i can also be defined as the inverse of $\sum_{j=1}^N d(i, j)$, without the factor $N - 1$ [156] and sometimes it is also defined as the mean geodesic distance between a vertex i and all other vertices in a network. We will use the definition given in Equation 5.4 throughout the thesis. For RN, c_i gives the local centeredness of a state in the phase space and characterizes its geometric centrality [18]. High values of c_i for a vertex i imply that with smaller number of ε -jumps, most of the other vertices are reachable from the vertex i [16].

5.2.1.3 Betweenness centrality

Betweenness centrality [157, 158] also describes the importance of a vertex in a network, like the other centrality measures. The betweenness centrality of a vertex i is defined as the fraction of shortest paths in a network traversing the vertex i [16, 18]. Let σ_{jk} be the total number of shortest paths between the vertices j to k and $\sigma_{jk}(i)$ be the cardinality of the subset of the total number of shortest paths σ_{jk} that pass through the vertex i [16, 18]. The betweenness centrality for a vertex i can then be defined as [159]

$$b_i = \sum_{j \neq i \neq k} \frac{\sigma_{jk}(i)}{\sigma_{jk}}. \quad (5.5)$$

In the context of an ε -recurrence network, b_i can be interpreted as a measure of local degree of attractor fragmentation [16]. Thus, the vertices belonging to a sparsely populated region in a phase space, that separates two densely populated regions, will acquire high values of b_i by bundling [18] the shortest paths between the vertices of densely populated regions to pass through them, creating geometric bottlenecks [16].

5.2.1.4 Local clustering coefficient

The local clustering coefficient of a vertex can be used to characterize the density of connections among its neighbors [18]. It gives the probability that two randomly drawn neighbors j and q of vertex i , are themselves neighbors. A triangle Δ can be considered as a subgraph of three vertices of undirected graph G representing a complex network and the number of triangles on vertex i can be defined as $\delta(i) =$

$|\{\{j, q\} \in E : \{i, j\} \in E : \{i, q\} \in E\}|$ [160]. A **triple** at a vertex i can be defined as a path of length two, for which i is the central vertex and for an undirected network, the number of triples for a vertex i is given as $T_i = \binom{k_i}{2}$ [160], where k_i is the node degree or degree centrality (Equation 5.2). Now, the local clustering coefficient can be given as the ratio

$$C_i = \frac{\delta(i)}{T_i} \quad (5.6)$$

The above expression can be given in terms of the adjacency matrix as

$$C_i = \frac{\sum_{j,q} A(i,j)A(j,q)A(q,i)}{2T_i} \quad (5.7)$$

For vertices with a degree less than 2, $C_i = 0$. In the context of RNs, C_i measures the fraction of pairs of vertices in the ε -neighborhood (i.e., the ε -ball) of vertex i (i.e., the state vector \mathbf{x}_i) that are themselves mutually ε -close [18]. Low dimensional dynamical systems are typically characterized by UPOs of low period, locally enhancing the fraction of triangles in the associated complex network and such systems display high values of C_i near regions of UPO [16, 18]. Thus, C_i is related to the geometric alignment of the state vectors in the phase space [18]. Since RNs are essentially RGGs [153], the higher the dimension in which the network is embedded, the lower will be the value of the clustering coefficient [17, 143].

5.2.2 Global network measures

5.2.2.1 Global clustering coefficient

The global clustering coefficient [136] can be defined as the average of C_i for all the vertices in a network.

$$C = \frac{1}{N} \sum_{i=1}^N C_i \quad (5.8)$$

Thus, C measures the average fraction of triangles in a network. It is important to note that in case of a heterogeneous degree distribution, this measure emphasizes weights of the low degree vertices [18].

5.2.2.2 Transitivity

Barrat and Weigt [161] introduced the concept of network transitivity, based on the redefinition of C . Let $T(G)$ and $\delta(G)$ be the total number of triples and triangles in a

graph G . The transitivity of a graph G can then be given as [162]

$$\mathcal{T} = \frac{3\delta(G)}{T(G)} \quad (5.9)$$

In terms of the matrix \mathbf{A} , \mathcal{T} can be given as [18]

$$\mathcal{T} = \frac{\sum_{i,j,q=1}^N A(i,j)A(j,q)A(q,i)}{\sum_{i,j,q=1}^N A(i,j)A(q,i)}. \quad (5.10)$$

While the \mathcal{C} is the mean, computed over all vertices, of the ratio given in Equation 5.6, \mathcal{T} is the ratio of the mean number of edges between the neighbors of a vertex and the mean number of possible links between the neighbors of a vertex [161]. Also, \mathcal{T} gives equal weight to all triangles in a network, where as the clustering coefficient is biased to vertices with low-degree and weights their contributions more heavily [163].

5.2.2.3 Assortativity

If vertices of similar degrees tend to link up with each other, then the network is said to exhibit assortative mixing. The measure assortativity can be defined as the Pearson product-moment correlation of the vertex degrees on either ends of all the edges [16, 107, 164]. It is given as

$$\mathcal{R} = \frac{\frac{1}{N} \sum_{j>i} k_i k_j A(i,j) - [\frac{1}{N} \sum_{j>i} \frac{1}{2}(k_i + k_j) A(i,j)]^2}{\frac{1}{N} \sum_{j>i} \frac{1}{2}(k_i^2 + k_j^2) A(i,j) - [\frac{1}{N} \sum_{j>i} \frac{1}{2}(k_i + k_j) A(i,j)]^2}. \quad (5.11)$$

If an RN shows assortative mixing, it implies that the density of states within an ε -ball change more slowly and continuously. Thus, \mathcal{R} can be considered as a measure of the smoothness of phase space density [16].

5.2.2.4 Average path length

The average path length for a graph can be defined as the arithmetic mean of geodesic lengths between all pairs of vertices. It is given as

$$\mathcal{L} = \frac{1}{N(N-1)} \sum_{i \neq j} d(i,j) \quad (5.12)$$

The disconnected pairs of vertices are not included in computing \mathcal{L} [15, 106]. It has been demonstrated that a continuous dynamical system with periodic trajectory has a higher

\mathcal{L} compared to a system exhibiting chaotic dynamics for comparable ε [165]. Also, \mathcal{L} varies inversely as the recurrence threshold ε (or equivalently RR), since \mathcal{L} approximates distances in phase space in the units of ε [16, 18].

5.3 Local and global measures of dimensions

Related to the network measures, the local clustering coefficient \mathcal{C}_i and transitivity \mathcal{T} , new definitions of local and global measures of dimension have been proposed respectively [163]. Hence these network measures can be used to define an alternative notion for the effective dimensionality of the system. Donner *et al.* [163] showed that the expectation value of \mathcal{C}_i and \mathcal{T} scales as $= (3/4)^d$, for RGGs in integer dimensions d , at least when using the maximum norm. The theoretical value of \mathcal{T} for periodic dynamics is 0.75 (since the effective dimensionality for such a system is 1) [18].

The local dimension measure, **clustering dimension** at a single-scale ε can be given as [163]

$$D_{\mathcal{C}_i, \varepsilon} = \frac{\log \mathcal{C}_{i, \varepsilon}}{\log(3/4)} \quad (5.13)$$

and the global dimension measure, **the transitivity dimension** at a single-scale ε can be given as [163]

$$\mathcal{D}_{\mathcal{T}_\varepsilon} = \frac{\log \mathcal{T}_\varepsilon}{\log(3/4)} \quad (5.14)$$

However, it should be noted that as ε is varied, both $D_{\mathcal{C}_i}$ and $\mathcal{D}_{\mathcal{T}}$ oscillates between two asymptotic values [163]. In order to account for this, one can define upper and lower bounds for these local and global dimension measures as ε is varied (For a detailed discussion see Donner *et al.* [18, 163]).

5.4 Bivariate ε -recurrence networks

Analogous to the bi-variate extensions extension of RPs into CRPs and JRPs [57, 58], cross recurrence networks (CRNs) and joint recurrence networks (JRN) have been proposed [166, 167] for bi-variate (and possibly multivariate) time series. In this section we will focus mainly on the construction of CRNs their associated measures due to their application in the thesis and briefly discuss JRN, which are discussed in detail elsewhere [18, 167].

5.4.1 Cross recurrence networks

If there are two observational time series $\{x_t\}$ and $\{y_t\}$ comprising of N samples, where $t = 0, 1, 2, \dots, (N - 1)$, one can define a matrix \mathbf{R}^{cross} [58] (See also Section 3.2.3, Equation 3.25). Combining the definitions of matrix \mathbf{R} derived from an univariate time series (Equation 3.14) and \mathbf{R}^{cross} derived from a bivariate time series, one can define a 2×2 inter-systems recurrence matrix [166] \mathbf{R}^{IS} , given as

$$\mathbf{R}^{IS}(\varepsilon) = \begin{pmatrix} \mathbf{R}_x(\varepsilon_x) & \mathbf{R}_{xy}^{cross}(\varepsilon_{xy}) \\ \mathbf{R}_{yx}^{cross}(\varepsilon_{yx}) & \mathbf{R}_y(\varepsilon_y) \end{pmatrix} \quad (5.15)$$

where ε_x and ε_y are single-system recurrence thresholds concerning the time series $x(t)$ and $y(t)$ respectively, and ε_{xy} and ε_{yx} are cross recurrence distance thresholds. The inter-system recurrence matrix can be transformed into an adjacency matrix using the following transformation [166]

$$\mathbf{A}^{IS}(\varepsilon) = \mathbf{R}^{IS}(\varepsilon) - \mathbb{I}, \quad (5.16)$$

where \mathbb{I} is an identity matrix of size $2N$ (given that the length of the phase space vectors reconstructed from $x(t)$ and $y(t)$ is N each). The adjacency matrix of a CRN can be described as [166]

$$\mathbf{A}^{IS}(\varepsilon) = \begin{pmatrix} \mathbf{A}_x^{self}(\varepsilon_x) & \mathbf{A}_{xy}^{cross}(\varepsilon_{xy}) \\ \mathbf{A}_{yx}^{cross}(\varepsilon_{yx}) & \mathbf{A}_y^{self}(\varepsilon_y) \end{pmatrix} \quad (5.17)$$

The adjacency matrices A_x^{self} and A_y^{self} represent the symmetric and undirected complex network derived from time series $x(t)$ and $y(t)$ individually, which is simply known as the ε -recurrence network [15, 16], as also described in Section 5.1.1. The adjacency matrices $A_{xy}^{cross}(\varepsilon_{xy})$ and $A_{yx}^{cross}(\varepsilon_{yx})$ represent the CRN derived from the time series $x(t)$ and $y(t)$. One can extend this definition to include $K > 2$ multivariate time series, resulting in a $K \times K$ inter-system recurrence matrix [18, 166].

It has to be noted here that, the CRN represents a bipartite graph [108] as it provides the information about the presence of edges between vertices belonging to different RNs representing individual time series [166]. Also, the matrices \mathbf{R}_{xy}^{cross} and \mathbf{R}_{yx}^{cross} are

asymmetric matrices, unlike the matrix \mathbf{R} as $\|\mathbf{x}_i - \mathbf{y}_j\| \neq \|\mathbf{x}_j - \mathbf{y}_i\|$. They can be non-square matrices as well if the length of the time series $x(t)$ is not equal to that of $y(t)$. To characterize a CRN and thus analyze the interaction between two or more complex networks, Donges *et al.* [149] proposed general framework and introduced several cross network measures. Below, we briefly describe the framework and some of the important cross network measures important to this thesis. The general framework for analyzing the interaction between complex networks and the associated measures are thoroughly discussed elsewhere [142, 149, 168].

To analyze the interaction between two sub-networks representing a bivariate time series $x(t)$ and $y(t)$, consider a graph $G = (V, E)$ where the set of vertices V is decomposed into two disjoint sets V_x and V_y representing the vertices of an RN derived from the time series $x(t)$ and $y(t)$ respectively [149]. Also, $V_x \cap V_y = \emptyset$, $V_x \cup V_y = V$ and $N_x = |V_x|$ and $N_y = |V_y|$ with $N = N_x + N_y$. The set of edges E_{xx} and E_{yy} represent the edges between the vertices of an RN derived from $x(t)$ and $y(t)$ respectively. The sets E_{xy} represents the (cross)-edges, that gives the mutual interaction between sub-networks represented by G_x and G_y . Also, $E_{xx} \cup E_{yy} \cup E_{xy} = E$. Now, one can define local as well as global measures to characterize the interaction between the sub-networks represented by G_x and G_y . Below we give an example of one such measure, the cross-clustering coefficient, introduced by Donges *et al.* [149] to quantify the interconnectivity structure.

5.4.1.1 cross-clustering coefficient

Let \mathbf{A}_x and \mathbf{A}_y be the adjacency matrices representing the sub-graphs G_x and G_y respectively. The local cross-clustering coefficient for vertex i in \mathbf{A}_x can be given as [149]

$$C_i^{xy} = \frac{\sum A_{xy}(i, j)A_{xy}(i, k)A_y(j, k)}{k_{i,xy}(k_{i,xy} - 1)}, \quad (5.18)$$

where $k_{i,xy}$ is the cross-degree centrality (analogous to degree centrality), which gives the number of neighbors of vertex i in V_x , but in the sub-network represented by G_y [149]. C_i^{xy} simply gives the probability that two randomly drawn neighbors, $\{j, k\} \in V_y$ of vertex $i \in V_x$ are also neighbors [149]. For the vertices that have $k_{i,xy} < 2$, C_i^{xy} is set to zero [166]. By averaging C_i^{xy} over all the vertices, we can define the global or average cross-clustering coefficient C^{xy} . In an analogous fashion one can define C_i^{yx} using A_{yx} and A_x . It has to be noted that the cross-clustering coefficient is an asymmetric measure, i.e., $C_i^{xy} \neq C_i^{yx}$. If $C_i^{xy} > C_i^{yx}$, the direction of the coupling is from y to x , $y \rightarrow x$. On the other hand, if $C_i^{xy} < C_i^{yx}$, the direction of the coupling is from x to y , $x \rightarrow y$. Also,

in case of no coupling or complete synchronization, $\mathcal{C}_i^{xy} \approx \mathcal{C}_i^{yx}$. In a similar fashion, another closely related quantity, cross-transitivity can also be defined [166].

5.4.2 Joint recurrence networks

Given two time series $\{x_t\}$ and $\{y_t\}$ comprising of N samples, where $t = 0, 1, 2, \dots, (N-1)$, one can define a joint recurrence matrix \mathbf{R}^{joint} by obtaining the element-wise dot product of the individual recurrence matrices [60]. Analogous to the general definition of a recurrence network, an adjacency matrix representing a JRN can be given as

$$\mathbf{A}^{joint} = \mathbf{R}^{joint} - \mathbb{I} = \mathbf{A}^x(\varepsilon_x) \cdot \mathbf{A}^y(\varepsilon_y), \quad (5.19)$$

where \mathbb{I} is an $N \times N$ identity matrix. A JRN can also be given as the dot product of the individual adjacency matrices \mathbf{A}^x and \mathbf{A}^y representing the RNs derived from $x(t)$ and $y(t)$, using the thresholds ε_x and ε_y respectively. The above definitions can be extended in a straightforward manner for multivariate ($K < 2$) time series [18]. It should be noted that, unlike in the case of CRN, to obtain a JRN the K time series involved should have identical length and sampling, but need not represent the same physical quantity or reside in the same phase space [167]. Another difference is that, unlike the RNs or CRNs, in the case of JRN, the vertices are explicitly associated with points in time and are thus not invariant under relabeling of vertices. Graph theoretical measures can be used to quantify JRN to reveal synchronization between different time series. One such measure, the transitivity of the JRN, known as the joint transitivity \mathcal{T}_J can be used to define the notion joint dimensionality of the composed dynamical system [167]. Since, JRN can be regarded as simple RNs for the combined dynamical system (represented by K time series) in its higher-dimensional phase space, in the absence of any synchronization one can expect the network transitivity of individual systems to be much greater than \mathcal{T}_J . In contrast, during generalized synchronization, one would expect \mathcal{T}_J to be approximately equal to network transitivity of individual systems due to mutual locking of the effective degrees of freedom [167].

5.5 Properties and applications of ε and bivariate recurrence networks

Since the seminal work of Marwan *et al.* [15], RNs have been studied and analyzed thoroughly using different paradigmatic models [16, 153, 154, 165]. Using low-dimensional

model systems, Donner *et al.* [16] provided a thorough reinterpretation of network measures in the context of phase space properties and studied the ε -dependence of global and vertex-based network measures and spatial distribution of vertex and edge-based measures. The network measure \mathcal{C}_i was shown to be useful in detecting dynamically invariant objects like the UPOs and thus related to the effective dimensionality in the vicinity of a vertex, while the centrality measures were shown to be useful in characterizing higher-order properties of phase space density [16]. The network measure b_i gives information about the local fragmentation of the attractor [16, 154]. Zou *et al.* [165] studied the performance of \mathcal{C} and \mathcal{L} in identifying the shrimp structures in parameter space of the Rössler system and demonstrated that the periodic windows are characterized by higher values of \mathcal{C} and \mathcal{L} compared to their chaotic counter-parts. Using data from both model systems as well as experiments, emergence of power-laws in degree distributions (derived from k_i) was demonstrated for RNs and it was shown that the scaling is simply not necessarily related to fractal dimensions, but is determined by singularities of the invariant densities [169]. However, as shown by Donner *et al.* [163], global network measures like the \mathcal{T} can be considered as an alternative measure of dimension and are directly related to the dimensionality of the attractor. Also, high values of \mathcal{R} indicate smooth and continuous nature of the invariant density [16, 170]. Donges *et al.* [153] provided thorough definitions of continuous geometric measures for describing continuous RNs, which constitute RGGs. Thus, these continuous measures are in general feasible for describing RGGs [153]. In general, RNs allow us to study and quantify the geometric properties of the attractors in phase space and is thus complementary to other tools of nonlinear time series analysis based on RPs [18]. Especially in the case of chaotic attractors, where geometry and dynamics are linked, RNA can be used to characterize dynamical complexity. Also, since RNs, discards all the temporal information, the RN measures can be considered invariant under vertex relabeling [16, 18, 142]. In this spirit, RNs cannot be used to distinguish between deterministic and stochastic dynamics as they have the same density in one-dimensional phase space and might generally require an additional embedding to make the distinction in the dynamics [16]. Another important property of RNs is that they do not display small-world characteristics [15, 18]. Although, systems with deterministic dynamics display high values for \mathcal{C} and \mathcal{T} , \mathcal{L} for an RN can take only specific values for a given choice of ε and are hence independent of the number of nodes in a network [18]. In case of small-world networks that display high clustering and short path lengths, \mathcal{L} depends of the network size ($\mathcal{L} \approx \log N$ as $N \rightarrow \infty$) [136]. However, k -NNs have been reported to display small-world characteristics, particularly in case of chaotic attractors [84].

Apart from the selected mention of the study of RNs using data from paradigmatic model systems, numerous applications using real-world data has emerged, particularly

in the field of climatology [15, 17, 142, 170–172]. Apart from climatology, applications in the field of fluid dynamics [173], electrochemistry [174], finance [16] and biomedical engineering [175–177] have been recently reported. Also, applications of inter-system RNs have been reported in the fields of climatology and fluid dynamics used to study the interdependencies between two main branches of Asian summer monsoon [166] and to characterize horizontal oil-water flows [178] respectively.

TABLE 5.1: Definition of complex network measures and the corresponding interpretation in the context of RNs

Network measures	Definition	Interpretation	Key references
Degree centrality (k_i)	$\sum_{j=1}^N A(i, j)$.	Local recurrence in phase space, emergence of scale-free distributions	Donner <i>et al.</i> [16] ; Zout <i>et al.</i> [169]
Closeness centrality (c_i)	$\frac{N-1}{\sum_{j=1}^N d(i, j)}$.	Identification of the attractor's center of gravity	Donner <i>et al.</i> [16]
Betweenness centrality (b_i)	$\sum_{j \neq i \neq k} \frac{\sigma_{jk}(i)}{\sigma_{jk}}$.	Local fragmentation of attractor	Donner <i>et al.</i> [16, 154]
Clustering coefficient (C_i)	$\frac{\sum_{j,q} A(i, j)A(j, q)A(q, i)}{2T_i}$, $T_i = \frac{k_i(k_i-1)}{2}$.	Presence of lower order UPOs	Donner <i>et al.</i> [16] ; Zou <i>et al.</i> [165]
Transitivity (\mathcal{T})	$\frac{\sum_{i,j,q=1}^N A(i, j)A(j, q)A(q, i)}{\sum_{i,j,q=1}^N A(i, j)A(q, i)}$.	Attractor dimension, UPOs, regularity of dynamics	Donner <i>et al.</i> [163]; Donges <i>et al.</i> [170]
Assortativity (\mathcal{R})	$\frac{\frac{1}{N} \sum_{i>j} k_i k_j A(i, j) - [\frac{1}{N} \sum_{i>j} \frac{1}{2}(k_i + k_j) A(i, j)]^2}{\frac{1}{N} \sum_{i>j} \frac{1}{2}(k_i^2 + k_j^2) A(i, j) - [\frac{1}{N} \sum_{i>j} \frac{1}{2}(k_i + k_j) A(i, j)]^2}$.	Smoothness of phase space density	Donner <i>et al.</i> [16]
Average path length (\mathcal{L})	$\frac{1}{N(N-1)} \sum_{i \neq j} d(i, j)$.	Average phase space separation, abrupt dynamical changes	Donner <i>et al.</i> [16]; Zou <i>et al.</i> [165]; Donges <i>et al.</i> [170]
Cross-clustering coefficient (\mathcal{C}_{xy})	$\frac{\sum A_{xy}(i, j) A_{xy}(i, k) A_y(j, k)}{k_{i, xy} (k_{i, xy} - 1)}$.	Mutual interaction between complex networks	Donges <i>et al.</i> [149]

CHAPTER 6

NONLINEAR TIME SERIES ANALYSIS OF EEG

There is a joke that your hammer will always find nails to hit. I find that perfectly acceptable.

BENOIT MANDELBROT
(1924 - 2010)

In this chapter, a brief introduction to the technique of EEG is given (Section 6.1), which is followed by the role of methods derived from nonlinear theory in EEG time series analysis in general and epileptic EEG analysis in particular (Section 6.2).

6.1 An overview of history and generation of EEG

The EEG is a recording of the oscillations of electrical activity in the brain. In 1875, by placing an electrode on the exposed cerebral cortex of non-human animals, Richard Caton [179] demonstrated that the brain responded electrically to a light stimulus [180]. In 1924, Hans Berger [181] showed, for the first time, that EEG can be recorded from the human scalp, without the need of opening the skull. Also, it was Hans Berger who coined the term *electroencephalogram*. Since the work of Hans Berger, EEG has been considered as a window to the brain function in health and disease. This concept gathered further momentum, when in 1934, Adrian and Matthews [182] demonstrated that the electrical oscillations around 10-12 Hz, namely the **alpha wave** was likely generated in the occipital lobes in humans [183]. Today, the clinical applications of EEG include epilepsy, sleep disorder, coma, head trauma, encephalopathies to name a

few [184]. Apart from clinical applications, EEG is also used in cognitive science and psychology. When the electrical activity is recorded by the electrodes that are placed in the brain, close to the neuronal sources, it is known as LFP, when recorded by subdural electrodes placed on the cortex, it is referred to as ECoG.

The EEG reflects the superposition of electrical activities of the neuronal population, particularly within the cerebral cortex and is typically recorded by placing the electrodes on the scalp. The cerebral cortex of the human brain contains about 10^{10} neurons that are strongly interconnected. Nonlinearity is introduced at the level of single neurons as their dynamical behavior is governed by the time-delay, threshold and saturation phenomena [185–187]. Nonlinear time series analysis has emerged as an interesting and complementary approach towards the analysis of EEG signals.

6.2 Nonlinear EEG analysis and its role in epilepsy

Epilepsy is a common neurological disorder that affects roughly 3 % of the world population. It is defined as a dynamical disorder of the brain [188], where the normal functioning brain is interrupted in a recurrent and unpredictable fashion [189]. These interruptions are called epileptic seizures and the definition of epilepsy requires the occurrence of at least one epileptic seizure [189]. It is this unpredictability, that makes epilepsy a debilitating disease and also is a major reason for psychosocial issues in patients with epilepsy. Although there are many forms of epilepsy, but they can be classified into two broad groups - generalized and focal epilepsy. In generalized epilepsy, seizures begin bilaterally and simultaneously on both sides of the brain, where as in focal epilepsy, it originates in one particular part of the brain, for example, the temporal lobe or the frontal lobe (the epileptogenic focus). EEG is an affordable and most useful tool used to aid the diagnosis epilepsy, providing temporal resolution in the millisecond range. In fact, today epilepsy is one of the few common clinical problems that still routinely demand an EEG evaluation [190]. The different states associated with epilepsy are - the interictal state (occurring between the seizures), the preictal state (occurring before the seizure), the ictal state (occurring during the seizure) and the postictal state (occurring after the seizure). Previous studies have shown that, in contrast to normal background EEG activity, ictal EEG activity shows increased nonlinearity. Thus, ictal / video EEG recordings are considered critical in localizing the epileptogenic focus [191]. Even during the interictal period, the epileptic brain is different from normal as demonstrated by several human as well as non-human animal studies. Thus, it has been hypothesized that the interictal EEG recordings also exhibit increased nonlinearity, probably due to the deterministic dynamics that is associated with the epileptic process [9]. Thus, the

analysis of the interictal EEG signals can also play a crucial role in the localization of epileptogenic areas. Besides the obvious clinical benefit, localization using interictal EEG recordings is extremely beneficial to the patient, as it minimizes the need to record seizures for the sake of localization [70]. Localization of the epileptic focus from interictal EEG recordings has been addressed using approaches from both linear and nonlinear time series analysis [185, 192–196]. In this section some of the nonlinear measures used in EEG and particularly their application to epilepsy is discussed.

Rapp *et al.* [197, 198] and Babloyantz *et al.* [199] were the first to apply nonlinear approaches to EEG time series analysis. The spontaneous neural activity in the motor cortex of a monkey was analyzed by means of 'chaos analysis' in [197], while the correlation dimension D_2 of the sleep EEG time series was estimated in [199]. Also, in [198], where the EEG data from both monkeys and humans were analyzed, a presence of low-dimensional chaotic attractor underlying these systems. Additionally, there were also both experimental and model based studies reporting the presence of an underlying chaotic attractor in the phase space for invertebrate bursting neurons [200–203]. Particularly, after Grassber and Proccaccia [53] developed an efficient algorithm to compute correlation dimension, many studies were published in an effort to find chaos in EEG data [197–199, 204–210]. Evidently, much of the nonlinear analysis of EEG between 1985 and early 1990s were concentrated on finding an evidence for low-dimensional chaotic attractors. With the introduction of **surrogate data** testing [76, 211, 212] much of the claims of an underlying, low-dimensional, chaotic dynamics for EEG signals were rejected, however the evidence for an underlying nonlinear structure, especially for epileptic EEG data was confirmed [91, 213–216]. Apart from correlation dimension, Lyapunov exponents [217–221], and various entropy measures [67, 222–224] have been estimated from EEG time series [7]. For example, permutation and approximate entropy has been used in detection of epileptic seizures [225–228] as well as in the analysis of absence seizures [229, 230]. However, the application of these classic measures (correlation dimension, Lyapunov exponents and some of the entropy-related measures), to filtered, noisy and nonstationary time series of finite length and precision (like EEG data), can falsely point towards a low-dimensional (possibly chaotic) structure [7, 89]. This has lead to the development of new nonlinear measures, where the focus is clearly on characterizing the structure of reconstructed trajectories without making strong assumptions about the nature of the underlying dynamics [7]. Particularly, nonlinear methods were introduced to distinguish between deterministic and stochastic dynamics [4, 74, 185, 231]. For instance, in [4], nonlinear prediction error was used in combination with surrogates, to compare dynamical properties of healthy (scalp) and epileptic (intracranial) EEG and strongest indications for nonlinearity in ictal EEG was reported. Gautama *et al.* [231] used the method delay vector variance (DVV) on the same dataset reported in [4], and

found an evidence for nonlinear structure in scalp EEG as well, but to a lesser degree compared to epileptic EEG (intracranial). Furthermore, Andrzejak *et al* [232] showed that a combination of nonlinear time series analysis with surrogate data provides improved performance for localization of epileptic foci compared to linear (or nonlinear) time series analysis. Additionally, various RQA [14, 51, 52] measures have also been used in the characterization of interictal, preictal and ictal signals in rats [233] as well as to distinguish preictal activity from background activity in epileptic patients [234] and in automatic detection of epileptic seizures [235, 236].

Using recordings from the cat cerebral cortex and theoretical models (integrate-and-fire neurons), and quantities such as scale dependent Lyapunov exponent and entropy measures, Boustani and Destexhe [237] showed that high-dimensional behavior (stochastic dynamics) is displayed at microscopic scales and more coherent behavior (high-dimensional chaos) is displayed at large scales. These scale-dependent results are in contrast with the findings of more stochastic behavior in large-scale EEG recordings in attentive and awake subjects and evidence of low dimensionality in epileptic EEG, for example, as shown in [4].

Apart from univariate measures, where single-channel EEG recordings are utilized, bivariate and multivariate measures have been introduced to quantify dynamical interdependencies between two or more EEG time series. Le van Quyen *et al.* [238] used nonlinear mutual predictability in combination with multivariate surrogates to quantify the degree of interdependence between intracranial EEG recordings in four patients with focal epilepsy. They found low degree of interdependence during the interictal period, but the ictal period displayed intermittent patterns of nonlinear interactions, especially during the beginning and end of the seizure. Mormann *et al.* applied the concept of phase synchronization for coupled chaotic systems [239] and found a decrease in synchronization preceding the seizures while the synchronization during the seizures increased [240]. More recently, Andrzejak *et al.* [70] used nonlinear interdependence measure on intracranial EEG recordings obtained during interictal period and found an increased degree of nonlinear interaction between electrodes located in the epileptogenic zones compared to the ones in non-epileptogenic zones. Apart from these, methods to identify the strength and correct coupling direction have also been developed [241–249], some of which have been applied to epileptic EEG data. Table 6.1 gives a summary of commonly used nonlinear methods in EEG analysis.

TABLE 6.1: Overview of some of the nonlinear time series methods used in epileptic EEG analysis

Nonlinear measures	Description
Univariate measures	
Correlation dimension	Measure of dimensionality
Lyapunov exponents	Measure of rate of separation
Entropy measures (Permutation entropy, Approximate entropy, K-S entropy)	Measure of complexity, irregularity
Nonlinear prediction error	Prediction of the future states
RQA measures	Quantification of recurrence patterns from RPs
Bivariate measures	
Nonlinear cross prediction	Prediction of states of one system based on the knowledge of the other system
Phase synchronization	Interdependencies of instantaneous phases of two time series
Nonlinear interdependence measure	Tests whether the closeness in the state space of one signal implies closeness in the state space of the other.

Part II

Applications

CHAPTER 7

DISTINGUISHING STOCHASTIC AND CHAOTIC PROCESSES [P-I]

7.1 Introduction

Distinguishing between chaotic and stochastic processes is a challenging problem in nonlinear time series analysis and several methods have been proposed to address this problem (Refer Section 3.5). In this chapter, we propose the application of local and global RN measures to distinguish between chaotic and stochastic dynamics [P-I]. The relationship between the geometric properties of a dynamical system and transitivity properties (\mathcal{C}_i and \mathcal{T}) of the associated RN has been recently demonstrated by Donner et al. [163], where it was shown that these transitivity measures can be considered as alternative measures of local and global dimensions of the dynamical system under study. Furthermore, it has also been demonstrated that the UPOs in model systems can be reliably detected using such transitivity measures [16]. Since UPOs are the backbone of chaotic attractors, we hypothesize that these transitivity properties can be used to distinguish between chaotic and stochastic dynamics.

Recently Donges et al. [153] computed continuous RN measures - transitivity, clustering coefficient, average path length and betweenness for the one-dimensional Bernoulli map and uniform noise, and showed that these measures cannot distinguish between stochastic (uniform noise) and chaotic deterministic process. This is due to the identical invariant density distribution of both the processes in the phase space and it has been proposed that an additional embedding can overcome this shortcoming [16]. However, a rigorous evaluation of the ability of RN measures to distinguish between chaotic

deterministic and stochastic dynamics and of how embedding alters the phase space distribution of these processes has hitherto not been addressed. In this study, our aim is to explore the applicability of transitivity measures such as $D_{\mathcal{T}}$ (global dimension measure) and \mathcal{C}_i as well as other local and global network measures such as \mathcal{L} , \mathcal{R} , c_i , b_i , and k_i in distinguishing between (hyper)chaotic and stochastic dynamics using paradigmatic model systems.

7.2 Data and methods

The following three paradigmatic systems, namely the Lorenz system [62],

$$\dot{x} = 10(y - x), \dot{y} = x(28 - z), \dot{z} = xy - \frac{8}{3}z, \quad (7.1)$$

the chaotic Rössler system [250],

$$\dot{x} = -y - z, \dot{y} = x + 0.1y, \dot{z} = 0.1 + z(x - 18), \quad (7.2)$$

and the hyper-chaotic Rössler system [251]

$$\dot{x} = -y - z, \dot{y} = x + 0.25y + w, \dot{z} = 3 + xz, \dot{w} = -0.5z + 0.05w. \quad (7.3)$$

were used to generate (hyper) chaotic dynamics in [P-I]. In each case, the x -component of the paradigmatic system was used to reconstruct the dynamics using the method of delays [8]. Additionally, in order to generate stochastic dynamics, we derived the iAAFT surrogates [96] (also see Section 3.6) from the original x -component and reconstructed the stochastic dynamics, again using the method of delays [P-I]. The associated RNs were derived from the reconstructed state vectors. Both local and global RN measures were computed and compared for the (hyper) chaotic and stochastic dynamics. For the estimation of RNs and the computation of the associated measures, the software pyunicorn [252] was used.

7.3 Results and discussion

7.3.1 Global measures

Tables 7.1 and 7.2 show the comparison between the global measures obtained for the chaotic dynamics (reconstructed from the x -component, see equations 7.1 and 7.2) for the Lorenz and chaotic Rössler system, respectively. The mean and the standard

deviation of the ensemble of 99 iAAFT surrogates derived from the original x -component is also shown. It is clear from the table that at embedding dimension $m = 1$, the global measures cannot distinguish between chaotic and stochastic dynamics. As m is increased, we observe that the $D_{\mathcal{T}}$ varies between 1.65 and 1.73 (< 2) for $m > 2$ in case of Lorenz system (chaotic dynamics), where as in case of the corresponding iAAFT surrogates (stochastic dynamics), the transitivity dimension increases with respect to m . Similar observation can be made for the Rössler system (Table 7.2), where $D_{\mathcal{T}}$ varies approximately between 1.74 and 1.78, where as the $D_{\mathcal{T}}$ for the corresponding iAAFT surrogates continues to increase more rapidly with increasing m . As mentioned earlier, UPOs are the skeleton of chaotic dynamics and there are infinitely many densely packed UPOs in such a system [174], while stochastic dynamics are not characterized by the presence of UPOs. Since $D_{\mathcal{T}}$ is essentially a measure of the global dimension of the system [163], presence of UPOs (especially low-periodic ones) should result in values of $D_{\mathcal{T}} < m$ for increasing values of m while in case of stochastic dynamics, the $D_{\mathcal{T}}$ should continue to increase with m . Our results reflects this behavior demonstrating how $D_{\mathcal{T}}$ can be used to distinguish between chaotic and stochastic dynamics.

The network measure \mathcal{L} for the RNs derived from iAAFT surrogates (stochastic dynamics) is lower than that of chaotic (deterministic) dynamics (Lorenz and Rössler system) for $m > 1$. This is an expected behavior for \mathcal{L} as more short-cuts are introduced in phase space in case of stochastic dynamics due to homogeneous filling of the phase space. Regarding the behavior of \mathcal{R} , it is clear that the RNs derived from chaotic dynamics are more assortative compared to their stochastic counterparts, especially at values of $m > 3$. As m increases, the RNs associated with chaotic dynamics display relatively more assortative behavior compared to RNs derived from stochastic dynamics.

TABLE 7.1: Global measures for RNs derived from chaotic (Lorenz system, $N=10,000$) and stochastic systems (derived from iAAFT surrogates) for varying embedding dimension and $RR = 0.02$

Global measures	$m = 1$	$m = 2$	$m = 3$	$m = 4$	$m = 5$
$D_{\mathcal{T}}$ (original)	0.99	1.51	1.65	1.67	1.73
$D_{\mathcal{T}}$ (surrogates)	$0.99 \pm 1.22 \times 10^{-15}$	1.92 ± 0.04	2.55 ± 0.01	2.96 ± 0.03	3.28 ± 0.04
\mathcal{L} (original)	32.75	9.98	8.84	9.06	9.44
\mathcal{L} (surrogates)	$32.75 \pm 1.42 \times 10^{-14}$	7.74 ± 0.01	5.15 ± 0.01	4.22 ± 0.01	3.73 ± 0.01
\mathcal{R} (original)	0.98	0.90	0.74	0.76	0.81
\mathcal{R} (surrogates)	$0.98 \pm 2.00 \times 10^{-15}$	0.92 ± 0.002	0.79 ± 0.005	0.72 ± 0.008	0.67 ± 0.01

Tables 7.3 and 7.4 shows the comparison between the global measures obtained for the hyperchaotic dynamics (reconstructed from the x -component of the 4D Rössler system, Equation 7.3) for $N = 10,000$ and $20,000$, respectively. The mean and the standard deviation of the ensemble of 99 iAAFT surrogates derived from the original x -component is also shown. In case of hyperchaotic Rössler system, we observe that as the number of

TABLE 7.2: Global measures for RNs derived from chaotic (Rössler system, $N=10,000$) and stochastic systems (derived from iAAFT surrogates) for varying embedding dimension and $RR = 0.02$

Global measures	$m = 1$	$m = 2$	$m = 3$	$m = 4$	$m = 5$
$D_{\mathcal{T}}$ (original)	0.99	1.66	1.74	1.76	1.78
$D_{\mathcal{T}}$ (surrogates)	$0.99 \pm 2.34 \times 10^{-15}$	1.84 ± 0.01	2.23 ± 0.04	2.45 ± 0.07	2.61 ± 0.09
\mathcal{L} (original)	33.84	8.84	8.27	8.05	7.88
\mathcal{L} (surrogates)	$33.84 \pm 2.85 \times 10^{-14}$	7.67 ± 0.29	6.29 ± 0.20	5.72 ± 0.17	5.39 ± 0.15
\mathcal{R} (original)	0.95	0.76	0.68	0.72	0.72
\mathcal{R} (surrogates)	$0.95 \pm 1.11 \times 10^{-16}$	0.77 ± 0.01	0.51 ± 0.04	0.39 ± 0.05	0.35 ± 0.05

data points N is increased, the difference between hyperchaotic and stochastic dynamics improves in case of all the global measures. This is specifically true in case of $D_{\mathcal{T}}$ and \mathcal{R} . In case of \mathcal{L} , as N increases, the spread of the hyperchaotic system also increases in the phase space resulting in more short-cuts between distant attractor points and thus smaller values for \mathcal{L} [174] as reflected in our results. However, RNs associated with stochastic dynamics contain relatively more short-cuts and are characterized by much lower values of \mathcal{L} compared to the hyperchaotic dynamics. The impact of the number of data points N ($N = 10,000, 15,000$ and $20,000$) on the global measures for the hyperchaotic system for varying m (2 to 5) is further depicted in **Figure 5** of [P-I].

TABLE 7.3: Global measures for RNs derived from hyperchaotic (4D Rössler system, $N=10,000$) and stochastic systems (derived from iAAFT surrogates) for varying embedding dimension and $RR = 0.02$

Global measures	$m = 1$	$m = 2$	$m = 3$	$m = 4$	$m = 5$
$D_{\mathcal{T}}$ (original)	0.97	1.63	2.03	1.99	1.97
$D_{\mathcal{T}}$ (surrogates)	$0.97 \pm 2.34 \times 10^{-15}$	1.58 ± 0.06	1.96 ± 0.10	2.12 ± 0.12	2.22 ± 0.15
\mathcal{L} (original)	37.77	9.94	7.95	8.00	8.71
\mathcal{L} (surrogates)	$37.77 \pm 3.57 \times 10^{-14}$	8.54 ± 0.2	6.12 ± 0.25	5.38 ± 0.34	5.18 ± 0.44
\mathcal{R} (original)	0.97	0.90	0.79	0.79	0.78
\mathcal{R} (surrogates)	$0.97 \pm 3.34 \times 10^{-16}$	0.87 ± 0.01	0.77 ± 0.02	0.70 ± 0.04	0.68 ± 0.05

TABLE 7.4: Global measures for RNs derived from hyperchaotic (4D Rössler system, $N=20,000$) and stochastic systems (derived from iAAFT surrogates) for varying embedding dimension and $RR = 0.02$

Global measures	$m = 1$	$m = 2$	$m = 3$	$m = 4$	$m = 5$
$D_{\mathcal{T}}$ (original)	0.98	1.62	2.01	2.01	1.99
$D_{\mathcal{T}}$ (surrogates)	$0.98 \pm 1.56 \times 10^{-15}$	1.67 ± 0.04	2.20 ± 0.08	2.49 ± 0.13	2.67 ± 0.15
\mathcal{L} (original)	37.56	9.03	6.17	5.69	5.56
\mathcal{L} (surrogates)	$37.56 \pm 7.14 \times 10^{-15}$	8.08 ± 0.10	5.51 ± 0.11	4.67 ± 0.13	4.35 ± 0.14
\mathcal{R} (original)	0.98	0.91	0.84	0.86	0.84
\mathcal{R} (surrogates)	$0.98 \pm 1.00 \times 10^{-15}$	0.90 ± 0.007	0.78 ± 0.02	0.69 ± 0.04	0.65 ± 0.04

The results we obtained for the global RN measures are consistent with varying recurrence rates RR (from 0.01 to 0.05) as shown in **Figures 1-4** and **Figures S1-S3** (supplementary data) of [P-I].

7.3.2 Vertex-based measures

Figures 7.1 and 7.2 show the histogram for the vertex-based measures \mathcal{C}_i , c_i , b_i (for convenience we plot $\log_{10}(b_i + 1)$), and k_i for the Lorenz system (and its corresponding iAAFT surrogate) and chaotic Rössler system (and its corresponding iAAFT surrogate) respectively. It is evident from these figures that the distribution of the vertex-based measures for the RNs associated with chaotic and stochastic dynamics are quite different. In case of chaotic dynamics, we can see that higher number of vertices acquire high values for \mathcal{C}_i and b_i compared to stochastic dynamics, due to presence of UPOs in chaotic attractors. In case of k_i , we can observe multiple peaks for chaotic dynamics compared to stochastic dynamics, again due to many UPOs embedded in the chaotic attractors [150]. Furthermore, in case of chaotic dynamics, higher number of vertices acquire low values for c_i compared to stochastic dynamics. For example, in case of the Lorenz system (Figure 7.1), most of the vertices ($\approx 6,500$) acquire c_i between 0.1 and 0.11. These vertices particularly belong to the center of gravity of the chaotic attractors [16]. In case of stochastic dynamics, due to the existence of many short-cuts, relatively broad range of values for c_i (between 0.23 and 0.3) are acquired by the vertices (Figure 7.1). Since, c_i is essentially defined as the inverse of average shortest path length of a vertex to all other vertices in a network [155], the vertices of the RN constructed from iAAFT surrogates tend to have larger values for c_i due to increased short-cuts, compared to the networks representing chaotic dynamics. Similar observation is made in case of Rössler system (Figure 7.2).

Figures 7.3 and 7.4 show the histogram plot for the vertex-based measures in case of hyperchaotic dynamics and the corresponding iAAFT surrogates for the number of data points $N = 10,000$ and $20,000$ respectively. Here we can observe that, again with the increase in N , the vertex-based measures are able to better distinguish between hyperchaotic and stochastic dynamics. Particularly, looking at the distributions for b_i and \mathcal{C}_i for the hyperchaotic Rössler system and the corresponding surrogate at $N = 10,000$ and $20,000$, it is clear that the nodes acquiring high values for b_i and \mathcal{C}_i in RNs constructed from hyperchaotic Rössler system increases compared to the networks constructed from the corresponding iAAFT surrogates as the data length is increased. Also, looking at the distributions of c_i and k_i for $N = 10,000$ and $20,000$, we again observe that vertices of the RN representing hyperchaotic dynamics tend to acquire lower values for closeness centrality c_i compared to their stochastic counterparts for the same reason as outlined above for the chaotic case. On similar lines, the distribution of degree centrality k_i show multiple peaks, which is missing in case of its stochastic counterpart.

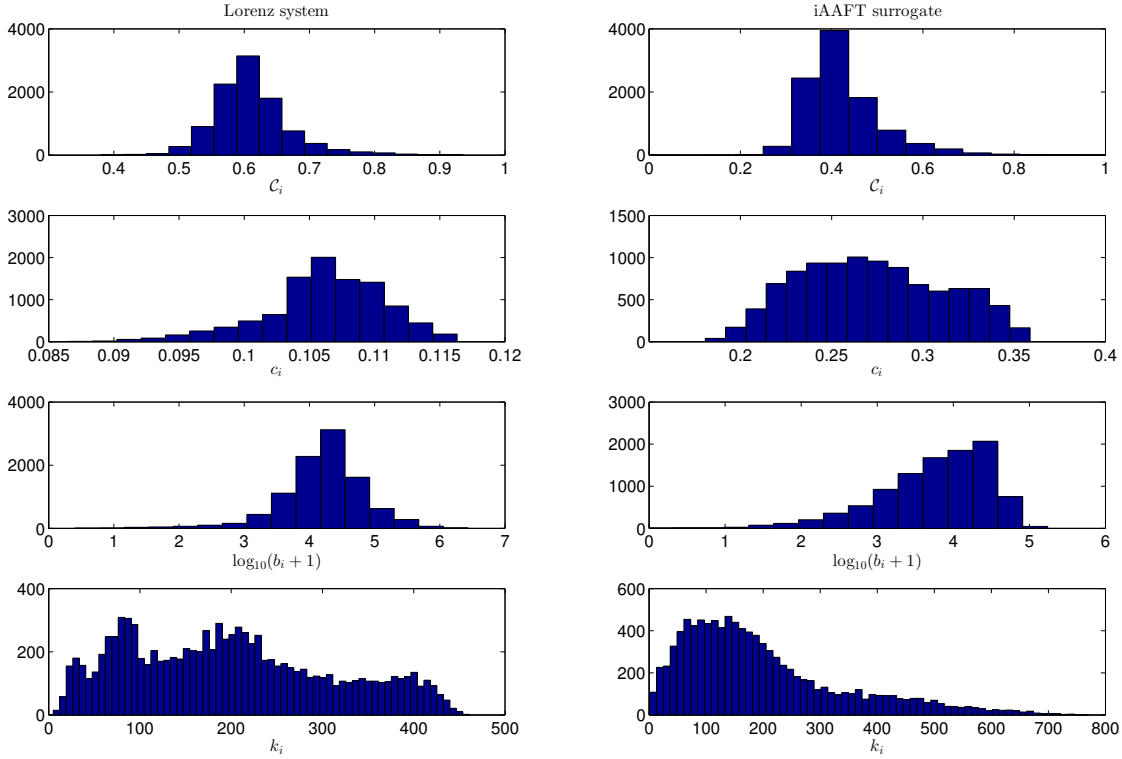


FIGURE 7.1: Distributions of the vertex-based measures, the local clustering coefficient (\mathcal{C}_i), closeness centrality (c_i), betweenness centrality ($\log_{10}(b_i + 1)$) and degree centrality k_i for the Lorenz system (left) and the corresponding iAAFT surrogate (right). For this exemplary plot, the recurrence rate $RR = 0.02$, the embedding dimension $m = 5$ and number of data points $N = 10,000$.

We used the two-sample Kolmogorov-Smirnov (KS-2) test to quantitatively compare the distribution of the vertex-based measures between the (hyper)chaotic and stochastic dynamics. The results from the KS-2 test for the Lorenz system and the corresponding iAAFT surrogate is shown in **Figure 6** of **[P-I]**, for the chaotic Rössler system in **Figure S4** of **[P-I]**, and for the hyperchaotic Rössler system in **Figure S5** of **[P-I]** and **Figure S6** of **[P-I]** for $N = 10,000$ and $20,000$ respectively. In all the cases, for embedding dimension $m > 1$, the null hypothesis that the two samples (vertex-based measures of RNs associated with chaotic and stochastic dynamics) are consistent with the same underlying distribution is rejected (at 5% significance) with p value very close to zero. In case of the hyperchaotic Rössler system, the value of the KS-2 statistic (the maximum of the absolute difference between the cumulative distribution functions of the two samples) increased as the data length was increased.

Figures 7.5 - 7.12 show the color-coded representation of the vertex-based measures in the phase space for the chaotic and stochastic dynamics. From Figures 7.5 and 7.6 it can be seen that in case of chaotic dynamics, the vertices that acquire high values for \mathcal{C}_i correspond very well to the regions of UPOs [16], whereas in case of stochastic dynamics such distinct patterns are absent. For the chaotic dynamics, it can be seen that certain

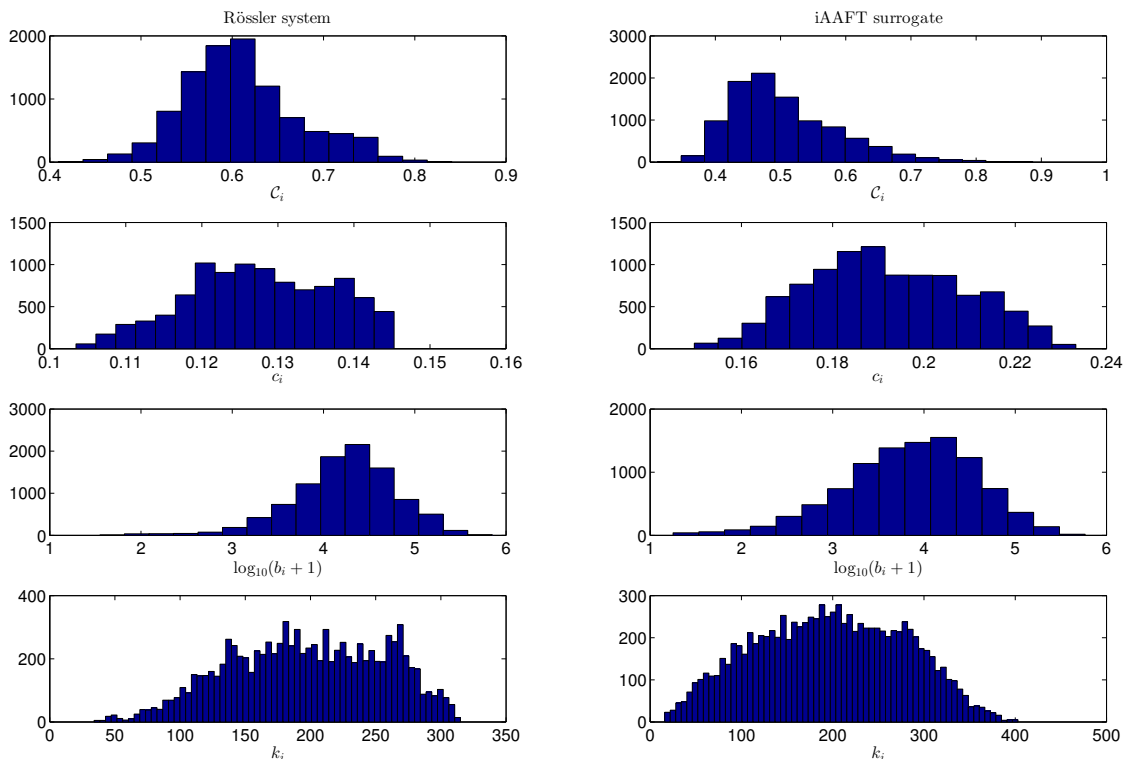


FIGURE 7.2: Distributions of the vertex-based measures, the local clustering coefficient (C_i), closeness centrality (c_i), betweenness centrality ($\log_{10}(b_i + 1)$) and degree centrality k_i for the Rössler system (left) and the corresponding iAAFT surrogate (right). For this exemplary plot, the recurrence rate $RR = 0.02$, the embedding dimension $m = 5$ and number of data points $N = 10,000$.

regions in phase space acquire high values for b_i (Figures 7.7 and 7.8) as these mainly correspond to the region between UPOs and other regions in the vicinity of the UPOs show low values for b_i . In case of stochastic dynamics, relatively lesser number of vertices acquire high values for b_i .

On comparing the spatial distribution of c_i in the phase space for chaotic and stochastic dynamics, we find that due to increased number of short-cuts in the RNs associated with stochastic dynamics, high values for c_i is displayed compared to chaotic dynamics (Figures 7.9 and 7.10). In case of k_i (or the local RR), we observe that the outer portions of the attractor, especially in case of the Lorenz system, acquire very low values for the local RR as these areas have low phase space density. Similarly, vertices belonging to the regions of high phase space density acquire high values for the local RR . The difference between the spatial distribution of this local measure for the chaotic and stochastic dynamics is evident from Figures 7.11 and 7.12

We explored the relationship between b_i and C_i for the chaotic and stochastic dynamics. In case of chaotic systems we observed that the vertices displaying low values for b_i display high values for C_i as these vertices belong to the regions in the phase space

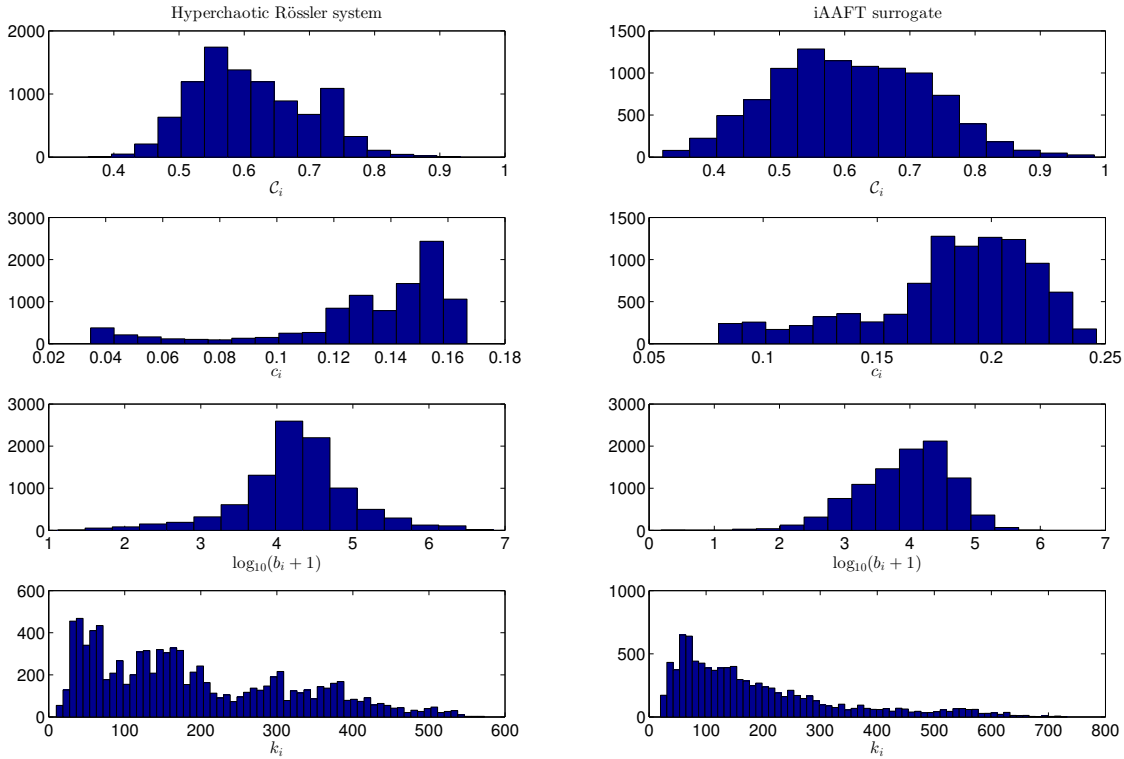


FIGURE 7.3: Distributions of the vertex-based measures, the local clustering coefficient (\mathcal{C}_i), closeness centrality (c_i), betweenness centrality ($\log_{10}(b_i + 1)$) and degree centrality k_i for the hyperchaotic Rössler system (left) and the corresponding iAAFT surrogate (right). For this exemplary plot, the recurrence rate $RR = 0.02$, the embedding dimension $m = 5$ and number of data points $N = 10,000$.

containing the UPOs (high-density clusters). The network measure \mathcal{C}_i is related to the geometric alignment of the vertices in the phase space [16] and the vertices along the stable manifold of an UPO are characterized by high values of \mathcal{C}_i . Since UPOs are the backbone of chaotic attractors, the measure \mathcal{C}_i is particularly important for the geometric characterization of chaos. Additionally, the vertices belonging to a sparse region (that exhibit low values for the local clustering coefficient \mathcal{C}_i) that separates high-density clusters, like the vertices belonging to the stable manifold of an UPO in the phase space, acquire high values for betweenness centrality b_i , as they act as transfer vertices between two high-density clusters on the either side of the sparse region [16, 253]. Since UPOs are absent in stochastic systems, there are no high-density clusters and consequently less number of vertices acting as hubs between high density clusters to acquire high values of b_i . We also observe that, in contrast to chaotic dynamics, some vertices with low values for betweenness centrality b_i also exhibit low values for the local clustering coefficient \mathcal{C}_i , again due to the absence of UPOs. This relationship is depicted in **Figure 7** of [P-I].

We also looked at the relationship between betweenness centrality b_i and degree centrality k_i for the stochastic and chaotic systems. We observed that in case of chaotic

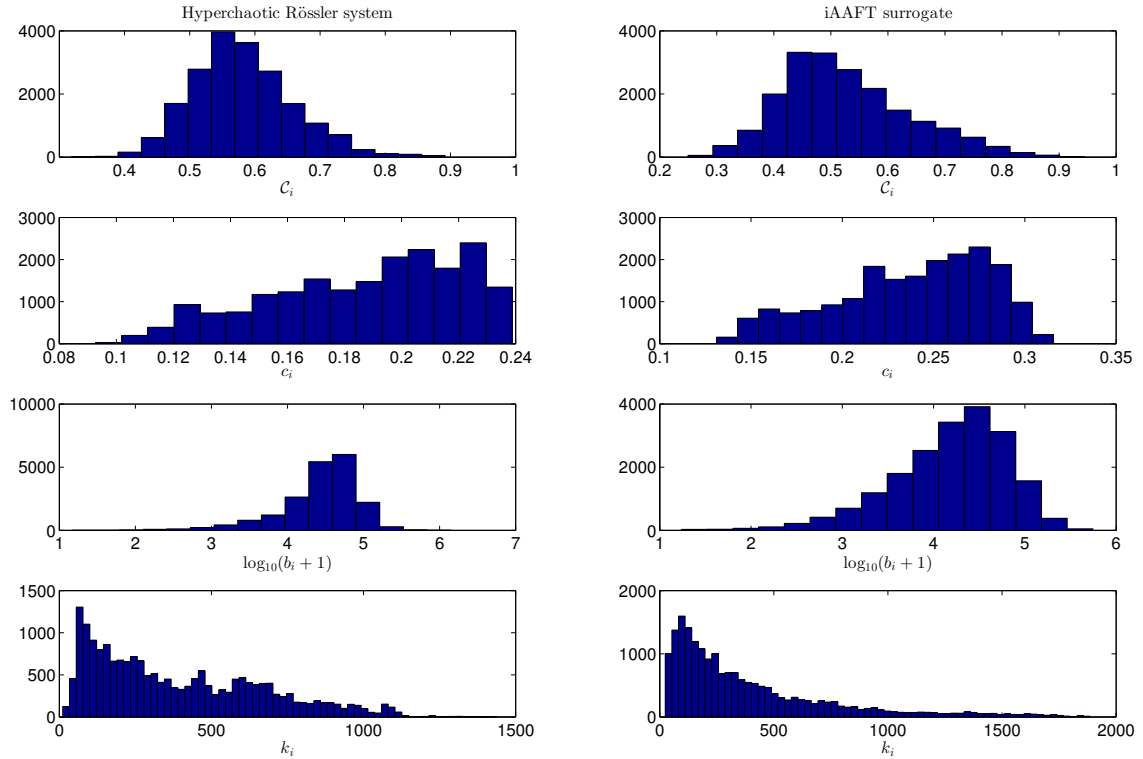


FIGURE 7.4: Distributions of the vertex-based measures, the local clustering coefficient (C_i), closeness centrality (c_i), betweenness centrality ($\log_{10}(b_i + 1)$) and degree centrality k_i for the hyperchaotic Rössler system (left) and the corresponding iAAFT surrogate (right). For this exemplary plot, the recurrence rate $RR = 0.02$, the embedding dimension $m = 5$ and number of data points $N = 20,000$.

dynamics, the vertices that acquire low value for the betweenness centrality b_i also acquire low value for degree centrality k_i . These vertices are located in the vicinity of the outer boundaries of the attractors, especially in the case of the Lorenz system, where we observe more vertices exhibiting low values for both these measures simultaneously compared to the Rössler system. We observed a similar trend in case of stochastic dynamics as well where vertices acquire low values for both these measures. Again, due to the presence of UPOs, an important difference in the relationship between these two measures is observed between chaotic and stochastic systems. Due to the accumulation of states in the vicinity of UPOs, the vertices in this region of phase space acquire low values for b_i , whereas the same vertices also acquire high values for k_i (due to trapping of states in UPO regions). This interesting region of the b_i vs k_i graph is completely missing in case of the stochastic system. Additionally, in case of chaotic dynamics, it can be seen that some of the vertices that acquire high values for b_i have a broad range of values for k_i as these vertices reside in the sparse region of phase space and mostly have vertices in the high-density clusters as their neighbors. In case of the stochastic dynamics, we can see that the range for b_i for a given value of k_i is much narrower compared to the chaotic dynamics. The reason for this narrower range is due to the

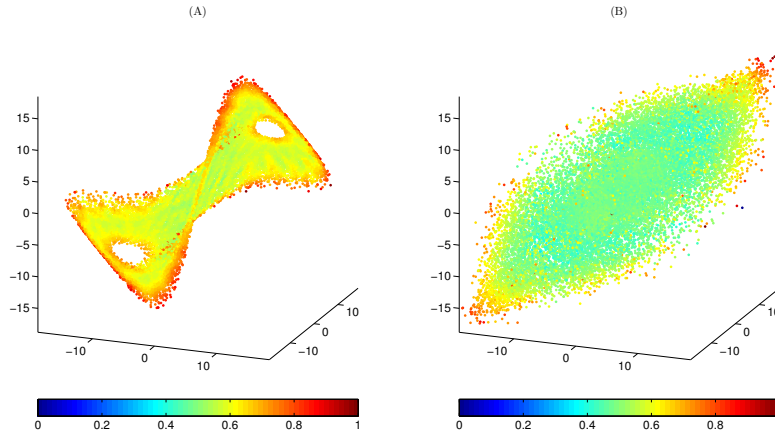


FIGURE 7.5: Color-coded representation of the local clustering coefficient C_i in phase space for the Lorenz system (A) and the corresponding iAAFT surrogate (B) for $N = 20,000$ and $RR = 0.02$.

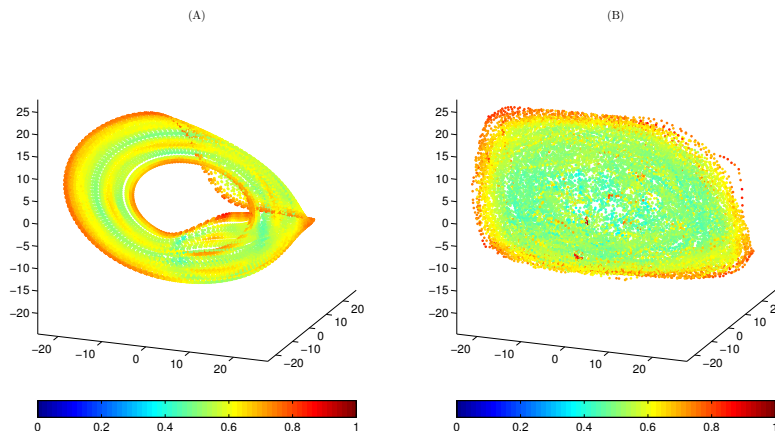


FIGURE 7.6: Color-coded representation of the local clustering coefficient C_i in phase space for the Rössler system (A) and the corresponding iAAFT surrogate (B) for $N = 20,000$ and $RR = 0.02$.

homogeneous filling of the phase space and the sparse regions between two high-density clusters do not exist. This also increases the total number of short-cuts between pairs of vertices thus reducing the b_i for a vertex i through which some of the short-cuts pass. Also, few of the vertices (which would otherwise been a part of sparse region) tend to have more neighbors due to homogeneous filling of the phase space increasing the value of k_i . These points are reflected in **Figure 9** of [P-I] where we show the variation of the log betweenness centrality $\log_{10}(b_i + 1)$ with k_i for the Lorenz and the Rössler systems and their corresponding surrogates.

7.4 Summary

In this work, we have shown that, both global and vertex-based RN measures can be used to distinguish between (hyper) chaotic and stochastic dynamics with additional

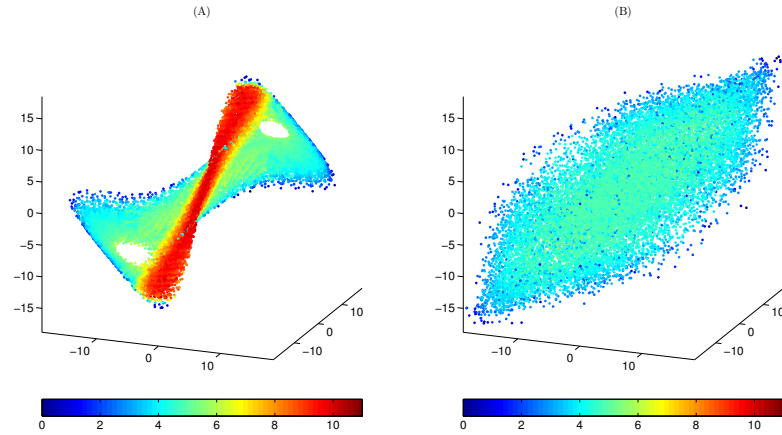


FIGURE 7.7: Color-coded representation of log betweenness centrality $\log_{10}(b_i + 1)$ in phase space for the Lorenz system (A) and the corresponding iAAFT surrogate (B) for $N = 20,000$ and $RR = 0.02$.

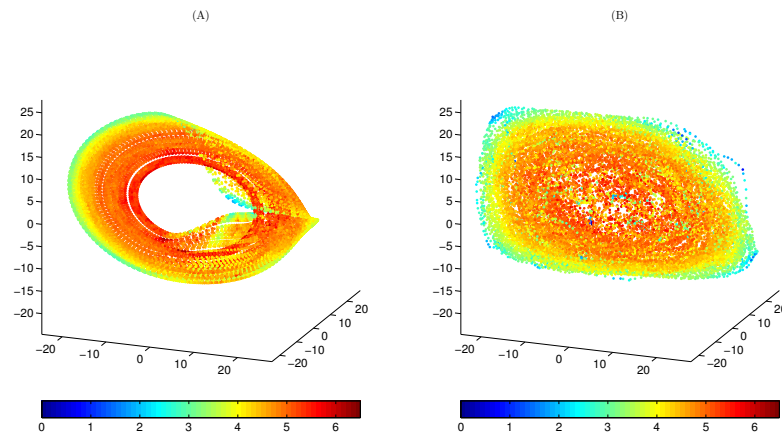


FIGURE 7.8: Color-coded representation of log betweenness centrality $\log_{10}(b_i + 1)$ in phase space for the Rössler system (A) and the corresponding iAAFT surrogate (B) for $N = 20,000$ and $RR = 0.02$.

embedding. In particular, measures like \mathcal{T} (or the related global dimension measure, $D_{\mathcal{T}}$), \mathcal{C}_i , k_i and b_i are particularly sensitive to the presence of UPOs, which are the hallmark of chaotic systems. Additionally, other measures such as c_i , \mathcal{L} and \mathcal{R} were also able to distinguish between (hyper) chaotic and stochastic dynamics.

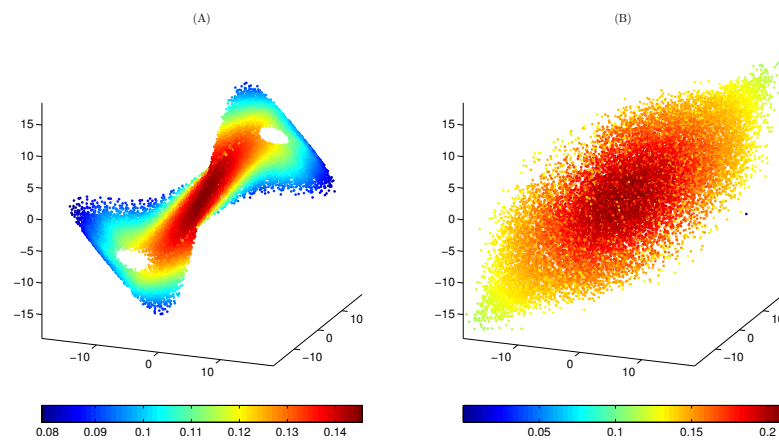


FIGURE 7.9: Color-coded representation of closeness centrality c_i in phase space for the Lorenz system (A) and the corresponding iAAFT surrogate (B) for $N = 20,000$ and $RR = 0.02$.

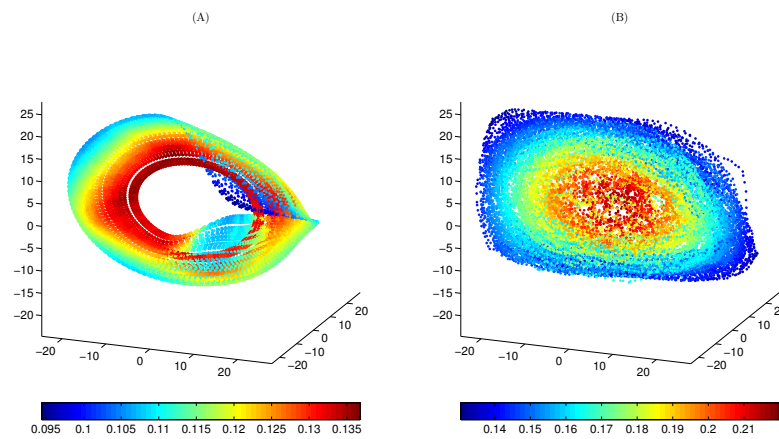


FIGURE 7.10: Color-coded representation of closeness centrality c_i in phase space for the Rössler system (A) and the corresponding iAAFT surrogate (B) for $N = 20,000$ and $RR = 0.02$.

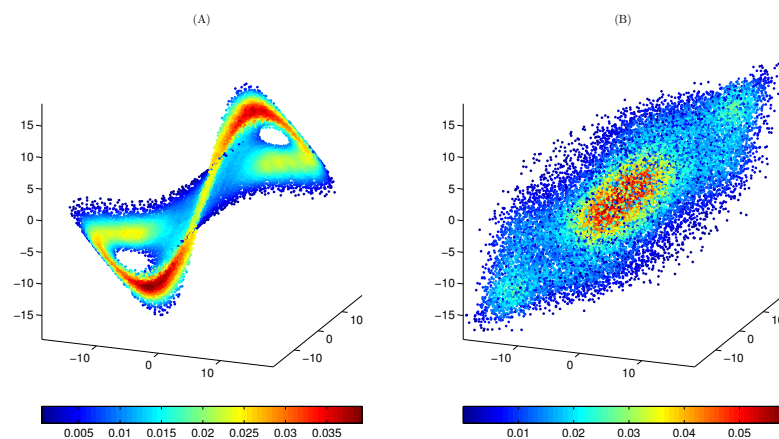


FIGURE 7.11: Color-coded representation of degree centrality k_i in phase space for the Lorenz system (A) and the corresponding iAAFT surrogate (B) for $N = 20,000$ and $RR = 0.02$.

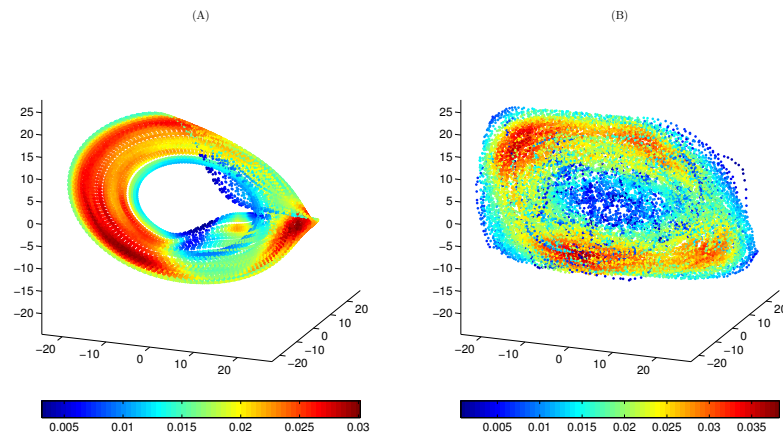


FIGURE 7.12: Color-coded representation of the local recurrence rate (proportional to degree centrality k_i) in phase space for the Rössler system (A) and the corresponding iAAFT surrogate (B) for $N = 20,000$ and $RR = 0.02$.

CHAPTER 8

EFFECT OF NOISE ON RECURRENCE NETWORKS

[[P-I],[P-III]]

8.1 Introduction

Investigating the ability of RN measures to characterize the dynamics of a system in the presence of observational noise is an important research question, as the real world data is seldom without noise. Thiel et al. [48] studied the influence of observational noise on RQA measures and found that they are susceptible to noise level of 20% or more (noise level is given as the standard deviation of the underlying noise-free data) and they proposed a threshold ε at least five times the standard deviation of the noise [48]. However, the impact of observational noise on both the local and global RN measures for various threshold parameter ε (or equivalently the recurrence rate RR) has not been sufficiently studied yet.

In this chapter our aim is to study the impact of increasing levels of noise on both local and global RN measures [[P-III],[P-I]]. Specifically, in [P-III], using the Rössler system, we investigated at what noise level is the structural complexity and detection of dynamical transitions as measured by RN measures are obscured. In [P-I], we investigate the effect of increasing noise levels as well as data lengths on the RN measures and their distributions (in case of vertex-based measures) for RNs derived from (hyper) chaotic dynamics, using various paradigmatic model systems. We also compare our results with the Complexity-Entropy plane approach to distinguish chaos from noise, proposed in [77].

8.2 Data and methods

We used the paradigmatic model systems described in Chapter 7 (the Lorenz system, the chaotic Rössler system and the hyperchaotic Rössler system). We used the x -component of the original dynamics to reconstruct the phase space using the method of delays [8]. We then added increasing levels of observational noise to the x -component of these model systems as follows [48]

$$x_{noise}(t) = x(t) + \eta(t), \quad (8.1)$$

where $\eta(t) \sim \mathcal{WN}(0, \sigma^2)$. Here, \mathcal{W} is defined as the level of noise, which is given as a percentage of the standard deviation of the noise-free data $x(t)$. We added Gaussian noise at levels 10%, 20%, 40%, 60%, and 100%. In [P-I], to study the impact of noise on the data length, we generated $N = 100,000$ data points (after discarding initial 50,000 points as transients) with a step size of 0.05 (for Lorenz and chaotic Rössler) and 0.015 (for hyperchaotic Rössler). We then randomly choose $N = 200, 500, 1,000, 5,000$ and $10,000$ points as a sample of state vectors from the chaotic attractor. In case of the hyperchaotic attractor, we used $N = 10,000, 15,000$ and $20,000$.

8.3 Results and discussion

In [P-III], we first compared the global clustering coefficient and average path length associated with noisy periodic dynamics and noise-free chaotic dynamics. Let \mathcal{C}_{c0} and \mathcal{L}_{c0} denote the global clustering coefficient and average path length of noise-free chaotic dynamics derived from the Rössler system. We first observe that under noise-free condition (0% noise), the value of \mathcal{C} and \mathcal{L} for periodic dynamics is greater than \mathcal{C}_{c0} and \mathcal{L}_{c0} (see **Figure 2** of [P-III]). Upon increasing levels of observational noise (see **Figure 4** of [P-III]), we found that at $RR < 0.03$, \mathcal{C} for periodic dynamics at noise level 10% and above is lesser than \mathcal{C}_{c0} . For $RR \geq 0.03$, at 10% noise level we can see that \mathcal{C} of periodic dynamics is greater than \mathcal{C}_{c0} . The behavior of \mathcal{L} is different. At all values of RR (0.01 to 0.05), \mathcal{L} for periodic dynamics is greater than \mathcal{L}_{c0} at noise level of 10%. For noise levels of 20% and above, both \mathcal{C} and \mathcal{L} fail to have values greater than \mathcal{C}_{c0} and \mathcal{L}_{c0} respectively (for all values of RR).

On comparing the network measure \mathcal{C} and \mathcal{L} for noisy periodic and chaotic dynamics [P-III], we find that, in case of \mathcal{C} , as RR is increased, the difference between noisy periodic and chaotic dynamics becomes clear with \mathcal{C} of noisy periodic dynamics being greater than that of chaotic dynamics. Particularly, for RR greater than 0.02, we can

still distinguish between noisy periodic and chaotic dynamics up to noise levels of 40% (see **Figure 5** of [P-III]). However at noise levels above 40%, even at $RR = 0.05$, \mathcal{C} for noisy periodic and chaotic dynamics starts becoming indistinguishable. In case of \mathcal{L} , it is evident that the difference between noisy periodic and chaotic dynamics is independent of RR . Irrespective of the value of RR , \mathcal{L} for noisy periodic dynamics is still greater than that of noisy chaotic dynamics for noise levels up to 20 %. At higher noise levels, \mathcal{L} for noisy periodic and chaotic dynamics becomes indistinguishable. In order to test for ability of global measures such as \mathcal{C} and \mathcal{L} to characterize structural complexity of chaotic signals under the influence of noise, we also generated iAAFT surrogates from chaotic signals under increasing levels of noise. The results are shown in Tables 8.1 and 8.2. Our results indicate that, specifically in case of \mathcal{C} , the influence of noise can be minimized by increasing RR .

TABLE 8.1: Results of surrogate analysis on simulated chaotic signals : Number of signals (out of 100) for which H_0 is rejected using \mathcal{C} as discriminatory statistic at various noise levels and RR . Rejections are considered not significant are marked as zero. (reproduced from [P-III].)

Noise level	0.01	0.02	0.03	0.04	0.05
0 %	100	100	100	98	98
10 %	74	94	96	96	96
20 %	0	0	38	66	76
40 %	0	0	30	38	38
60 %	0	0	16	18	24

TABLE 8.2: As in Table 8.1 , but for \mathcal{L} as discriminating statistic. (reproduced from [P-III].)

Noise level	0.01	0.02	0.03	0.04	0.05
0 %	100	100	100	100	100
10 %	100	100	100	100	100
20 %	100	100	100	100	100
40 %	28	28	28	30	30
60 %	30	24	28	34	32

In [P-I] we looked at the effect observational noise on both global and local RN measures using all the three paradigmatic model systems. For example, in case of the Lorenz system, we observed that as the level of noise is increased, the value of $D_{\mathcal{T}}$ increases above 2 at noise level of 10 % for $RR = 0.01$. As RR is further increased to 0.03, the value of $D_{\mathcal{T}}$ remains under 2 at 10% noise level. On further increasing the RR to 0.05, even at the noise level of 20% we can observe that $D_{\mathcal{T}} < 2$ (see **Figure 9** of [P-I]). In case of assortativity \mathcal{R} , the value of \mathcal{R} drops as we increase the level of noise. However, this behavior is affected by the choice of RR . For low values of RR such as 0.01, it can be seen that \mathcal{R} decreases up to a noise level of 20%. Interestingly, as the noise level is increased beyond 20%, \mathcal{R} starts to increase. However, the increase in \mathcal{R} is further constrained by the embedding dimension m and we observe that at very high noise levels (> 20 %), $\mathcal{R}_{m=5} < \mathcal{R}_{m=4} < \mathcal{R}_{m=3}$. We see this trend at other values of RR as well.

However as RR increases, at $m = 5$, \mathcal{R} continues to decrease with increase in noise levels up to 60%. Thus, at $m = 5$, \mathcal{R} shows expected behavior with the addition of noise, where \mathcal{R} decreases with the addition of noise and drops to a value less than 0.4 at 60% noise (see **Figure 9** of **[P-I]**).

We also investigated the influence of noise on vertex-based measures - \mathcal{C}_i , b_i , c_i , and k_i (see **Figure 10** of **[P-I]**). In case of \mathcal{C}_i and b_i , the number of vertices acquiring high values for both these measures decrease as noise is added. The reason for this is again related to the distortion of the clustering structure as noise is added to chaotic dynamics, which impacts both these measures. In case of closeness centrality c_i , we see that the number of vertices acquiring high values of c_i increase with the addition of noise. As noise is added, there are more short-cuts in the phase space due to homogeneous filling which reduces the length of shortest paths, which is inversely related to c_i (Equation 5.4). In case of degree centrality k_i , where one can observe multiple peaks in noise-free case (due to many UPOs), addition of noise makes the distribution more skewed (and long tailed) and the number of vertices with low degree increases as the noise is increased. Next, we studied the impact of noise on the b_i vs \mathcal{C}_i for various RR (see **Figure 11** of **[P-I]**). We observed that with the addition of noise, at $RR = 0.01$ the number of vertices exhibiting low \mathcal{C}_i and b_i increases. As the RR is increased to 0.05, we observed that the vertices having low b_i tend to acquire high values of \mathcal{C}_i , a behavior observed in noise-free chaotic dynamics. Thus increasing RR can minimize the influence of noise on the clustering property of RNs representing chaotic dynamics in phase space. Similar observations were made for Rössler and hyper-chaotic Rössler system **[P-I]**.

8.3.1 Effect of data length and comparison with Complexity-Entropy method

The number of rejections (out of 100 realizations) of null hypothesis H_0 of a linear, Gaussian correlated noise undergoing a nonlinear static transformation [96], for various noise levels and data lengths using global network measure \mathcal{T} at $RR = 0.05$ for the Lorenz system is shown in Table 8.3. For the sake of comparison, we also present results using the Complexity-Entropy causality plane method described in [77, 254], where we set $m = 3$ and $\tau = 3$.

Without making any assumption about the distribution of the test statistic, we use the non-parametric approach (based on rank ordering) to test the null hypothesis H_0 [8] (We obtained qualitatively similar results when the parametric approach using the mean and standard deviation of surrogates was used). Since a chaotic time series should produce high values of complexity compared to a stochastic signal and a stochastic signal

TABLE 8.3: Number of rejections of the H_0 from 100 realizations of the Lorenz system for various data lengths and noise levels using complexity-entropy method and the recurrence network measure \mathcal{T} . For each realization, 99 iAAFT surrogates were generated. The embedding dimension $m = 3$, embedding delay $\tau = 3$ and the recurrence rate $RR = 0.05$. Reproduced from [P-I].

Noise Level	$N = 200$		$N = 500$		$N = 1,000$		$N = 5,000$		$N = 10,000$	
	C-E	\mathcal{T}	C-E	\mathcal{T}	C-E	\mathcal{T}	C-E	\mathcal{T}	C-E	\mathcal{T}
0%	95	100	100	100	100	100	100	100	100	100
10%	88	100	100	100	100	100	100	100	100	100
20%	40	90	88	100	100	100	100	100	100	100
40%	5	60	52	77	93	100	100	100	100	100
60%	0	16	12	26	46	54	96	100	100	100
100%	0	11	3	8	7	5	20	22	28	32

displays higher entropy values compared to deterministic (chaotic) signal [77], the null hypothesis of a linear, Gaussian, stochastic process can be rejected if the complexity of the signal is greater than the maximum of the surrogates and the entropy of the signal is lesser than the minimum of the surrogates. Two exemplary plots (Figures 8.1 and 8.2) showing the application of the Complexity-Entropy method to distinguish between chaotic time series and the corresponding iAAFT surrogates under varying noise levels for data length $N = 200$ and 1,000 respectively. It is evident from these that the chaotic signal maps on to a different position on the complexity-entropy plane compared to the surrogates (stochastic signal), under noise-free condition. As the noise level is increased, we can see that at short data length, at noise levels greater than 10%, the location of the noisy chaotic signal on the Complexity-Entropy plane falls within that of the 99 surrogates and is no longer distinct. When the data length is increased to $N = 1,000$, we can see that a clear distinction between noisy chaotic signal and its corresponding iAAFT surrogates can be made up to a noise level of 40%.

In case of RN measures like \mathcal{T} , \mathcal{L} , and \mathcal{R} , the null hypothesis H_0 is rejected if the RN measure of the signal under test is greater than the maximum of the RN measures of the surrogates. Since we are using 99 surrogates, the probability with which a false rejection will occur is $1/100$ (i.e., $\alpha = 0.01$). We can see that at $N = 200$, compared to Complexity-Entropy method, \mathcal{T} gives comparatively higher rejections of H_0 , even when the noise level is 40% (see Table 8.3). Even at 60% noise level, \mathcal{T} gives a significant number of rejections (= 16), where as the Complexity-Entropy method fails to reject H_0 for all the 100 realizations. Thus, the recurrence network measure \mathcal{T} is still able to reject H_0 with high confidence for short time series corrupted with noise as high as 40 % and 60 %. As N is increased, performance of the complexity-entropy method improves and it can be seen that at larger values of N ($> 1,000$), both the complexity-entropy method and RN measure \mathcal{T} reject H_0 (almost 100 rejections) even at noise level of 60%.

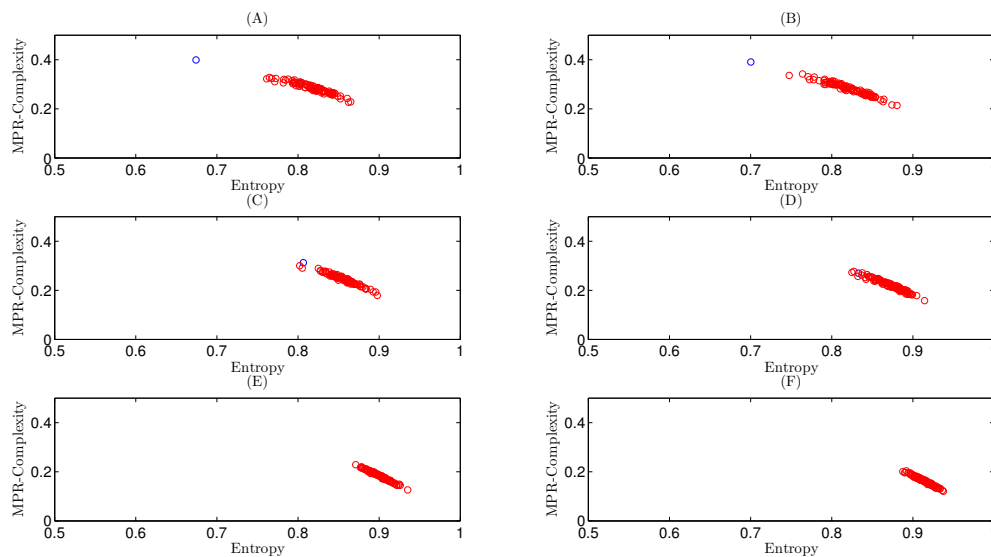


FIGURE 8.1: MPR Complexity-Entropy plane for chaotic Lorenz system (blue circle) and corresponding 99 iAAFT surrogates (red circles) under noise levels 0% (A), 10% (B), 20% (C), 40% (D), 60% (E), and 100% (F). The data length is $N = 200$. Reproduced from [P-I].

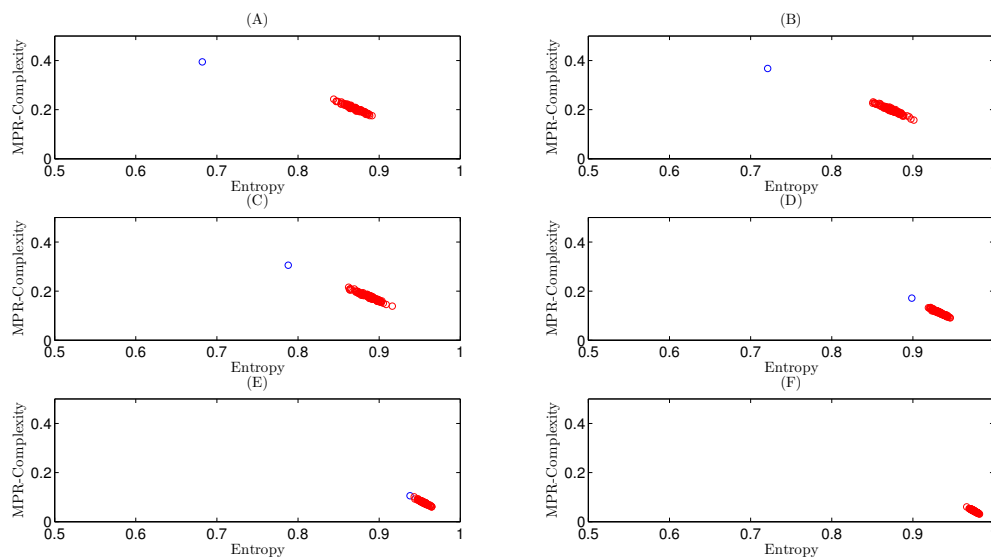


FIGURE 8.2: MPR Complexity-Entropy plane for chaotic Lorenz system (blue circle) and corresponding 99 iAAFT surrogates (red circles) under noise levels 0% (A), 10% (B), 20% (C), 40% (D), 60% (E), and 100% (F). The data length is $N = 1000$. Reproduced from [P-I].

We also computed RN measures \mathcal{L} and \mathcal{R} (see Table 8.4). In case of \mathcal{L} , we can again see that at short data lengths, the number of rejections are still considerably high for noise levels up to 60%. We can see almost 100% rejections at $N > 500$ for noise levels as high as 40%. At $N = 5,000$ and $10,000$, even at noise levels of 60%, we can see that all the 100 realizations reject H_0 . Even at 100% noise, we can see about 40 rejections of H_0 for $N = 10,000$. However, in case of \mathcal{R} , at $m = 3$, none of the realizations of the Lorenz system rejected the null hypothesis H_0 (results not shown here). As we demonstrated earlier in the thesis, in case of the network measure \mathcal{R} , a higher embedding dimension is required to distinguish chaotic from stochastic dynamics. When m was set to 5, we observed that the number of rejections of H_0 increases and reached 100% for $N > 200$ (see Table 8.4). As noise is increased beyond 20%, the network measure \mathcal{R} can no longer distinguish between chaos and noise even when $N = 10,000$.

We also observed that as the noise level is increased, the topology of the RN changes and it tends to fill the phase space (see Figures S20-S22 in supplementary data of [P-I]). However, the topology of the RN, which is reflective of the topology of the embedded attractor (Lorenz attractor in this case) is not completely destroyed even at short data length of $N = 200$ and considerably high noise levels up to 40%. As the noise level is increased (60% and 100%), we see that the topology of the RN does not resemble the shape of the Lorenz attractor and the network tends to fill the phase space.

TABLE 8.4: Number of rejections of H_0 from 100 realizations of the Lorenz system for various data lengths and noise levels using the RN measure \mathcal{L} and \mathcal{R} . For each realization, 99 iAAFT surrogates were generated. The embedding delay $\tau = 3$ and the recurrence rate $RR = 0.05$. In case of \mathcal{R} , the embedding dimension m was set to 5 instead of 3. Reproduced from [P-I].

Noise Level	$N = 200$		$N = 500$		$N = 1,000$		$N = 5,000$		$N = 10,000$	
	\mathcal{L}	\mathcal{R}	\mathcal{L}	\mathcal{R}	\mathcal{L}	\mathcal{R}	\mathcal{L}	\mathcal{R}	\mathcal{L}	\mathcal{R}
0%	97	82	100	100	100	100	100	100	100	100
10%	97	72	100	98	100	100	100	100	100	100
20%	99	30	100	52	100	74	100	100	100	100
40%	68	2	100	0	100	0	100	0	100	0
60%	33	0	63	0	94	0	100	0	100	0
100%	9	4	2	0	5	0	14	0	40	0

Figures 8.3 - 8.5 show the color-coded representation of \mathcal{C}_i , $\log(1+b_i)$, and k_i respectively for RNs derived from Lorenz system under increasing levels of noise. Under noise-free condition, most vertices have high values for \mathcal{C}_i (see Figure 8.3), but as the level of noise increases, many vertices start displaying low values for \mathcal{C}_i and the topology of the RN changes as well due to the addition of noise. This is due to the distortion of the clustering structure associated with RNs derived from chaotic system. Similarly, as noise level is increased, higher number of vertices acquire lower values of log betweenness centrality (see Figure 8.4). The local recurrence rate, which is proportional to degree centrality,

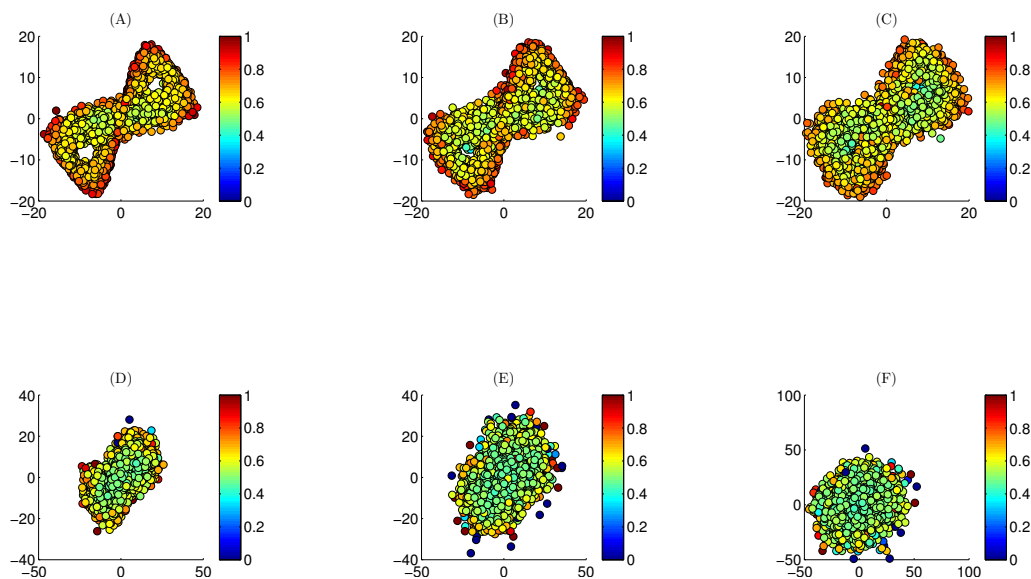


FIGURE 8.3: Color-coded representation of local clustering coefficient for the Lorenz attractor under noise levels 0% (A), 10% (B), 20% (C), 40% (D), 60% (E), and 100% (F). The data length $N = 5,000$, recurrence rate $RR = 0.05$, embedding dimension $m = 3$ and the embedding delay $\tau = 3$. Reproduced from [P-I].

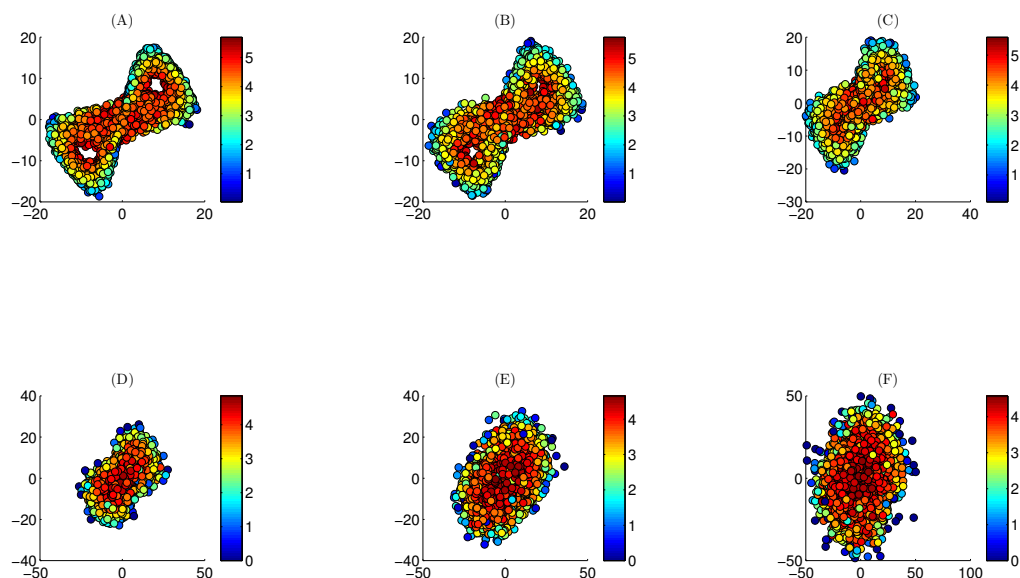


FIGURE 8.4: Color-coded representation of log betweenness centrality for the Lorenz attractor under noise levels 0% (A), 10% (B), 20% (C), 40% (D), 60% (E), and 100% (F). The data length $N = 5,000$, recurrence rate $RR = 0.05$, embedding dimension $m = 3$ and the embedding delay $\tau = 3$. Reproduced from [P-I].

for the Lorenz attractor under increasing levels of noise is shown in Figure 8.5. It is clear from the Figure 8.5 that as noise level increases, the local recurrence rate for most of the vertices decreases and at very high noise levels most of the vertices tend to have similar values for local recurrence rate.

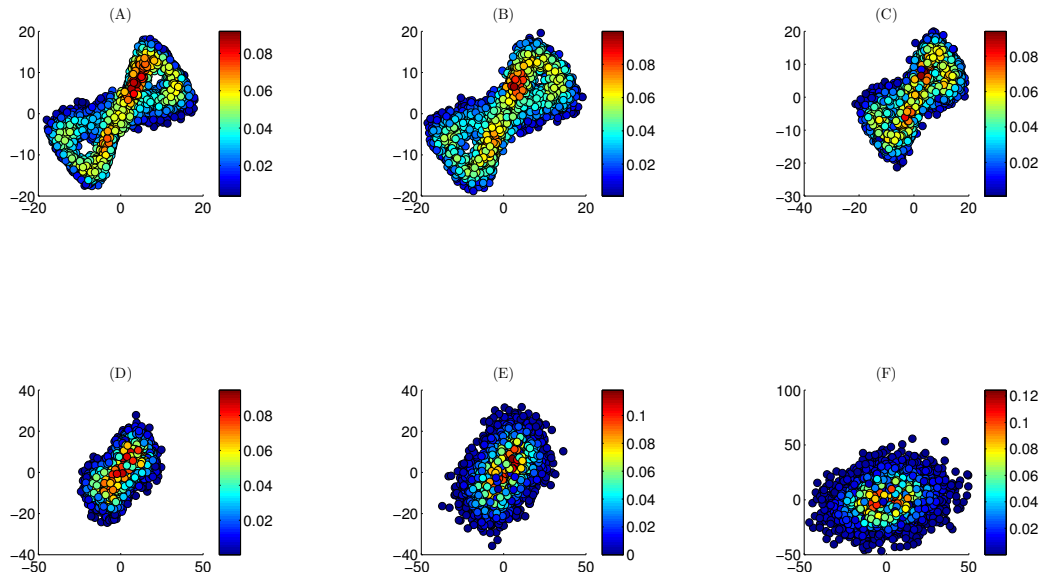


FIGURE 8.5: Color-coded representation of local recurrence rate (proportional to degree centrality) for the Lorenz attractor under noise levels 0% (A), 10% (B), 20% (C), 40% (D), 60% (E), and 100% (F). The data length $N = 5,000$, recurrence rate $RR = 0.05$, embedding dimension $m = 3$ and the embedding delay $\tau = 3$. Reproduced from [P-1].

8.4 Summary

In this study we addressed the effect of noise on RNs by adding increasing levels of observational noise to paradigmatic model systems. Effect of noise on the network measures such as C_i , b_i , and \mathcal{T} can be minimized to a certain extent by setting RR to an appropriate value. Furthermore, for noise levels greater than 40% in case of \mathcal{C} and 20% in case of \mathcal{L} , the network measures fail in distinguishing between noisy periodic and chaotic dynamics. We also demonstrated that global RN network measures like \mathcal{T} and \mathcal{L} are more robust at short data lengths compared to other approaches such as the Complexity-Entropy plane approach to distinguish chaos from noise.

CHAPTER 9

RECURRENCE NETWORK ANALYSIS OF EEG SIGNALS

[[P-III],[P-IV]]

9.1 Introduction

Our curiosity to understand the dynamical properties of brain, especially in disorders like epilepsy, has immensely benefited from nonlinear time series analysis. Andrzejak et al. [4] applied nonlinear measures like nonlinear prediction error P , and effective correlation dimension $D_{2,eff}$, to different classes of EEG data - extracranially recorded healthy EEG with eyes open and closed, intracranially recorded interictal and ictal EEG signals. They reported the strongest indication of nonlinearity for ictal EEG, while healthy EEG (eyes open) was compatible with quasilinear process. Gautama et al. [255] applied the DVV method for the data described in [4] and found indications of nonlinearity for both intracranial and surface EEG recordings. Given the potential of RN measures in characterization of dynamical systems [16, 165] and its reported advantages over other traditional nonlinear measures [15], its application in investigating the structural properties of EEG signals has hitherto not been explored. Furthermore, surrogate testing, which is an important tool in signal analysis [70] (See also Section 3.6), has not been used in combination with RN measures for the analysis of the structural property of biological time series such as EEG data. Here, our aim is to analyze the structural properties of different classes of EEG data (healthy and epileptic EEG signals) using RN measures in conjunction with the surrogate testing [P-III]. Since RN measures describe the structural properties of the attractors underlying a time series [163], we hypothesize that these measures can be used as a discriminatory statistic to test for the

structural complexity (or conversely stochasticity) of the original data in conjunction with the surrogates.

9.2 Data and methods

Table 9.1 describes the five EEG datasets used in [P-III] and [P-IV], which was originally published by Andrzejak et al. [4] and is available online for free download ⁱ. For a detailed description of these datasets, the reader is directed to [4]. Each dataset consists of 100 EEG signals recorded extracranially (eyes open - **A**, eyes closed - **B**) and intracranially (interictal EEG data recorded from Hippocampus - **C**, epileptogenic zone - **D** and ictal EEG data - **E**). The sampling frequency was 173.6 Hz and each signal was 23.6 seconds long (4096 samples).

TABLE 9.1: EEG data published by Andrzejak et al. [4] used in [P-III].(reproduced from [P-III].)

Datasets	Description	Number of signals
A	Eyes open	100
B	Eyes closed	100
C	Hippocampal-Interictal	100
D	Epileptogenic zone-Interictal	100
E	Ictal	100

We applied time-delay embedding methodology proposed by Takens to reconstruct the attractor from the time series [30] (also see Section 3.1). The optimal lag τ was estimated using the first minimum of the auto mutual information function and the minimum embedding dimension m was obtained using the modified FNN approach [47], where the threshold r was set to the standard choice of 10 [46, 47]. In [P-III], RNs were constructed from the EEG signals by fixing the RR instead of threshold ε , so that we obtain RNs with approximately the same number of edges so as to allow for objective comparison between different RNs [17]. We computed the network measures such as \mathcal{C} and \mathcal{L} for the healthy and epileptic EEG signals [P-III]. For the estimation of RNs and the computation of the associated measures, the software pyunicorn [252] was used. We performed surrogate analysis by generating univariate iAAFT surrogates [96].

In case of univariate iAAFT surrogates, the null hypothesis H_{uni}^0 , to be tested is that the underlying dynamics of the time series is a stationary, linear, stochastic, and correlated process which is measured by a static, monotonic, and possibly nonlinear observation function [4, 96]. Further, the autocorrelation, mean, and variance of the underlying process are such that the measurement results in the autocorrelation and amplitude distribution of the original time series [70]. Without making any assumption about the

ⁱhttp://epileptologie-bonn.de/cms/front_content.php?idcat=193&lang=3

underlying distribution of the data, similar to the approach given in [4], we employ a non-parametric method to test the null hypothesis H_{uni}^0 . The procedure is outlined as follows [P-III],

1. Compute the RN measure (for example, \mathcal{C} or \mathcal{L}) for the original data. Let us denote it as X^d .
2. Compute the RN measure for the corresponding iAAFT surrogates.
3. Let us denote the maximum and minimum of the RN measure for the surrogates as X_{max}^{surr} and X_{min}^{surr} respectively.
4. Reject H_{uni}^0 if ($X^d > X_{max}^{surr}$) (or if $X^d < X_{min}^{surr}$).

Let R_{max} be the number of rejections of H_{uni}^0 in a given set, due to ($X^d > X_{max}^{surr}$). For a two-tailed test, the probability p_{max} of having R_{max} or less rejections at the significance level of $\alpha = \frac{2}{1+s}$, where s is the number of surrogates, can be estimated via binomial cumulative distribution function [4, 256]

$$p_{max} = 1 - \sum_{k=0}^{R_{max}} \binom{n}{k} (\alpha)^k (1 - \alpha)^{n-k} \quad (9.1)$$

where n is the number of signals in a given set. In an analogous manner, one can compute p_{min} using R_{min} . In [P-III] we used 49 surrogates and thus, $\alpha = 0.04$. For the EEG dataset, we also performed statistical testing at the set level using non-parametric Wilcoxon signed rank test [4] to facilitate the comparison of our results with the results of Andrzejak et al. [4]. We used one surrogate per set and used $\{X_{1...100}^d\}$ and $\{X_{1...100}^{surr(1)}\}$ as paired observations for the Wilcoxon signed rank test as suggested in [4].

9.3 Results and discussion

We computed \mathcal{C} and \mathcal{L} as a function of RR for the set **A-E** of EEG signals. We observed that set **E** has the highest value for \mathcal{C} for $RR \geq 0.02$, followed by the sets **D,C,B**, and **A**. The same order is observed in decreasing values for \mathcal{L} and it is consistent for all the values of RR . Furthermore, we also observed that \mathcal{C} increases with increasing RR while \mathcal{L} decreases. This is depicted in **Figure 6** in [P-III].

Table 9.2 shows the result of surrogate analysis for EEG datasets (Table 9.1) using \mathcal{C} and \mathcal{L} as discriminatory statistic. We only show R_{max} in Table 9.2 as R_{min} was non-significant in all cases. Comparison of our results to the work of Andrzejak et al. [4] and Gautama et al. [255] is also presented in Table 9.2. It is evident from our results that the maximum rejections of H_{uni}^0 is found for the set **E** (ictal activity) followed by the sets **D** (interictal activity-epileptogenic zone), **C** (interictal activity-hippocampal zone), **B** (scalp EEG, eyes closed) and **A** (scalp EEG, eyes open). For epileptic EEG recordings capturing the epileptogenic interictal and ictal activity (**D** and **E**), we find that \mathcal{L} gives lesser rejections compared to \mathcal{C} .

TABLE 9.2: Results from surrogate analysis at individual level for EEG data at $RR = 0.05$. The number of rejections R_{max} at significance level $\alpha = 0.04$ (49 surrogates) for sets **A-E** is shown. As comparison, results from Andrzejak *et al.* [4] and Gautama *et al.* [255] are shown in columns 3, 4 and 5 respectively. (reproduced from [P-III].)

Datasets	Description	\mathcal{C}	\mathcal{L}	P [4]	$D_{2,eff}$ [4]	DVV [255]
A	Eyes open	17	20	4	0	29
B	Eyes closed	21	33	9	0	32
C	Hippocampal-Interictal	26	37	14	0	46
D	Epileptogenic Zone-Interictal	48	40	37	17	53
E	Ictal	98	76	89	56	92

The results presented in Table 9.2, clearly point towards an increasing degree of structural complexity in epileptic EEG signals by giving higher rejections of H_{uni}^0 compared to healthy EEG, which is consistent with the transition towards nonlinearity in epileptic EEG compared to healthy EEG as reported in [4, 255] [P-III]. Andrzejak et al. [4] used P and $D_{2,eff}$ to study the dynamical properties of the EEG time series and found the maximum number of rejections for ictal activity (set **E**) and thus a strong evidence for an underlying nonlinear process, while no significant rejections were found for scalp EEG in eyes open condition (set **A**). In comparison to [4], our results gave higher rejection rates for sets **A-E** using recurrence network measures. The main difference was that we could obtain higher rejections of H_{uni}^0 in sets **A** and **B** which are surface EEG recordings compared to [4]. Gautama et al. [255] applied DVV method for the EEG data described in [4] and also obtained higher rejections of H_{uni}^0 in sets **A** and **B** compared to [4]. We also applied A-NN method to the EEG data described in [4] and found that the recurrence networks associated derived from surface EEG signals are more complex than random networks and display small-world property [P-IV].

9.4 Summary

In this study, we presented the evidence for increased structural complexity in epileptic EEG, using RNs in combination with surrogate analysis. Furthermore, resting state

EEG signals in healthy subjects also show indications of structural complexity by giving significant number of rejections for the null hypothesis, but to a lesser degree compared to epileptic EEG signals. The network measure \mathcal{C} outperformed \mathcal{L} in characterizing the structural properties of epileptic EEG signals.

CHAPTER 10

DISTINGUISHING FOCAL AND NONFOCAL EEG SIGNALS

[P-II]

10.1 Introduction

Several human as well as non-human animal studies have confirmed that even during the interictal period, epileptic brain is different from normal and it has been hypothesized that the interictal EEG recordings also exhibit increased nonlinearity due to the deterministic dynamics that accompanies the epileptic process [9]. Thus, we can hypothesize that the analysis of interictal EEG signals can provide valuable information about the localization of epileptogenic areas. Besides the obvious clinical benefit, this is also extremely beneficial from the patient's point of view, as it minimizes the need to record seizures for the sake of localization, since occurrence of each seizure is a potentially debilitating event that can cause health impairment [70]. Motivated by this, Andrzejak *et al.* [70] combined iAAFT surrogates with nonlinear prediction error P , an univariate measure and nonlinear interdependence measure L , a bivariate measure, to test for randomness and nonlinear-independence respectively, in intracranial EEG signals. These EEG signals were acquired from epileptogenic (focal EEG signals) and non-epileptogenic areas (nonfocal EEG signals) of five epilepsy patients. They analyzed seizure-free recordings by excluding recordings of the seizure activity and three hours after the last seizure activity. Their results showed that the focal EEG signals had higher rejections for both the randomness test and nonlinear-independence test compared to the nonfocal EEG signals, thus indicating that the focal EEG signals are more nonrandom and have more nonlinear interdependence between them compared to the nonfocal EEG signals. They also used linear variability measures to test for stationarity in the

EEG signals. Based on the surrogate testing, their results showed that the nonfocal EEG signals are more nonstationary compared to the focal EEG signals. The nonstationarity in the time series caused an increase in the rejection probability of both the randomness test (for focal EEG signals) and nonlinear-independence test (for focal and nonfocal EEG signals). Furthermore, they also showed that the contrast between the focal and nonfocal EEG signals using the randomness test and nonlinear-independence test is further enhanced when the signals that reject the stationarity test are excluded. They also studied the dependence between the randomness and nonlinear-independence test and found that these two tests give nonredundant information and thus can contribute to characterization of EEG signals in different ways. These results are highly important from clinical as well as the physics point of view, as they reveal that the focal EEG signals are more nonrandom, more nonlinearly interdependent and more stationary compared to the nonfocal EEG signals. Thus, these measures can be used as potential biomarkers to delineate the epileptogenic brain areas from the non-epileptogenic ones. However, one important issue that remains to be addressed more adequately is the robustness of these nonlinear measures to nonstationarity in the EEG signals. Whether the contrast between the focal and nonfocal EEG signals, as measured by the randomness and nonlinear-independence test, still remains significant when we only consider those EEG signals that have rejected the stationarity test, remains to be answered. In other words, do these nonlinear measures still perform when they are applied to nonstationary signals? Moreover, In Ref. [70], iAAFT surrogates were used which are stationary by construction and therefore nonstationarity can thus violate the null hypothesis [8, 257]. This is a relevant and vexing issue as the epileptic signals often exhibit nonstationary behavior [233]. Even though the focal EEG signals are more stationary than the nonfocal EEG signals [70], there can still be considerable degree of nonstationarity present in the focal EEG signals. For instance in [70], Andrzejak *et al.* still found that out of 3750 focal EEG signals, 1750 signals rejected the stationarity test (i.e., roughly 46%). Ideally, the measures derived from the nonlinear theory should be able to distinguish between the dynamics of the focal and nonfocal EEG signals even in the presence of some degree of nonstationarity.

In this study, our aim is to apply both RN and CRN measures in combination with surrogates generated using the iAAFT scheme [96] to univariate and bivariate EEG time series described in [70]. In order to make the results more reliable, particularly in case of nonstationary EEG signals, we also use the TFT surrogates proposed by Nakamura *et al* [97]. The TFT surrogates preserve some nonstationarity present in the original data, unlike the iAAFT surrogates which can only preserve the linear properties [97, 258]. Particularly, we test for randomness based on the univariate RN measures and independence based on bivariate CRN measure using the focal and nonfocal EEG

signals. To allow for a direct comparison with the results obtained in [70] where the effect of nonstationarity on P and L was studied along with the dependence between these two measures, we also compute the same rejection probability measures [70] for the randomness and nonlinear-independence test combined with iAAFT and TFT (in case of nonstationary EEG signals) surrogates.

10.2 Data and methods

The data comprises of intracranial EEG data published by Andrzejak *et al.* [70]. The data was recorded from five patients who were candidates for epilepsy surgery and is available for free download ⁱ.

The data is divided into two parts, a) focal EEG data recorded from epileptogenic brain areas and b) nonfocal EEG data recorded from non-epileptogenic brain areas. The EEG channels where ictal signal changes were first detected by two expert neurologists are considered as focal EEG channels and all other channels are defined as non-focal EEG channels. Furthermore, the EEG activity pertaining to seizures and three hours after the last seizure were excluded, so as not to include any ictal activity [70]. In order to form the focal and non-focal EEG dataset, 3750 pairs of electrodes (X and Y) were selected randomly from two neighboring intracranial EEG channels. The selection procedure is explained in detail elsewhere [70]. Pre-processing of the data included low-pass filtering the data at 40 Hz with an eight-order Butterworth filter and downsampling to 128 Hz. The length of each EEG signal was about 20 seconds (2560 samples).

In order to construct RNs and CRNs, we fixed the parameters $\tau = 4$ and $m = 8$, as suggested in [70]. Also, we set the recurrence rate $RR = 0.02$ and the cross recurrence rate $CRR = 0.03$. We computed univariate network measures such as global clustering coefficient \mathcal{C} , average path length \mathcal{L} , assortativity \mathcal{R} , and average betweenness centrality \mathcal{BC} and the bivariate cross network measure \mathcal{C}_{cross} for the focal and nonfocal EEG [P-II]. For the estimation of RNs and the computation of the associated measures, the software **pyunicorn** [252] was used.

The steps to perform univariate surrogate testing (iAAFT or TFT) has already been discussed in Chapter 9. In [P-II] we generated 19 iAAFT and TFT surrogates. The null hypothesis H_{biv}^0 to be tested in case of iAAFT bivariate surrogates is that the original bivariate EEG time series represents a stationary, bivariate, linear, stochastic correlated Gaussian process[259]. The measurement function through which the EEG signal pairs are observed are invertible, but possibly nonlinear [259]. The surrogates

ⁱ<http://www.dtic.upf.edu/~ralph/>

generated have the same auto-correlation and cross-correlation as the original pair of EEG signals. In case of the TFT surrogates, the null hypothesis to be tested is that the irregular fluctuations in the data arise from a linear stationary system [97]. For bivariate cross network measure, the hypothesis testing is done as follows

1. Compute the cross network measure, C_{xy}^{cross} and C_{yx}^{cross} , for the original signal pairs. Let this be denoted as B_{xy}^{orig} and B_{yx}^{orig} respectively.
2. Generate 19 bivariate surrogates (iAAFT or TFT) using original pair of signals in accordance with [93].
3. Compute the cross network measures for all surrogate pairs. Let this set be denoted as $B_{xy}^{surr} = \{B_{xy}^{surr1}, B_{xy}^{surr2} \dots B_{xy}^{surr19}\}$ and $B_{yx}^{surr} = \{B_{yx}^{surr1}, B_{yx}^{surr2} \dots B_{yx}^{surr19}\}$ representing average cross-clustering coefficient C_{xy} and C_{yx} for bivariate surrogates respectively.
4. If $B_{xy}^{orig} > B_{yx}^{orig}$ and $B_{xy}^{orig} > \max(B_{xy}^{surr})$, the coupling direction $y \rightarrow x$ is considered significant and null hypothesis is rejected. Let the number of such rejections be $n(B_{xy}^{rej})$
5. Similarly, if $B_{yx}^{orig} > B_{xy}^{orig}$ and $B_{yx}^{orig} > \max(B_{yx}^{surr})$, the coupling direction $x \rightarrow y$ is considered significant and null hypothesis is rejected. Let the number of such rejections be $n(B_{yx}^{rej})$
6. The total number of signals rejecting the null hypothesis B_{biv}^0 is $n(B_1) = n(B_{xy}^{rej}) + n(B_{yx}^{rej})$

In order to generate TFT surrogates, one needs to specify the cut-off frequency f_c (see Section 3.6 in Chapter 3), which represents the normalized frequency (between 0 and 0.5) corresponding to the integer index $(0, 1, 2, \dots, N/2)$ of the N -point Fourier transformed data, where N is the number of points in the data. This way, local nonstationarity and even global nonstationarity i.e., trends (for sufficiently high f_c) are preserved in the generated TFT surrogates [258] but at the same time local structures in short-term variability are destroyed [97]. As it is evident, generation of TFT surrogates crucially depends on the choice of cut-off frequency f_c , which is the maximum preserved frequency. If this frequency is too high, the surrogates become too similar to the original data and might share too much of its nonlinear dynamics. On the other hand, if this value is too low, then the TFT surrogates might not preserve any trends and behave in a similar fashion to the iAAFT surrogates. In [P-II], we varied f_c between 0 (0 Hz) to 0.05 (25.6

Hz). Thus, we had 3750 pairs (set X and Y each containing 3750 EEG signals) of EEG signals from focal and nonfocal EEG signals.

In this study, we also compute a number of conditioned and unconditioned rejection probabilities proposed in [70]. These measures has been defined and described in [P-II]. Briefly, we compute the unconditioned rejection probability, $p(U_X^1)$, by computing the ratio between number of signals that reject the null hypothesis (using RN measures \mathcal{C} , \mathcal{R} , \mathcal{L} or \mathcal{BC} as the test statistic), $n(U_X^1)$, to the total number of signals in the set, $n(X)$, i.e., $p(U_X^1) = \frac{n(U_X^1)}{n(X)}$. Additionally, we condition these probabilities with signals that have rejected (or not rejected) the stationary test [70]. For example, in order to assess the influence of nonstationarity on univariate measures, the following conditional probabilities are estimated [70].

$$p(U_X^1 | S_X^0) = \frac{n(U_X^1 \cap S_X^0)}{n(S_X^0)} \quad (10.1)$$

$$p(U_X^1 | S_X^1) = \frac{n(U_X^1 \cap S_X^1)}{n(S_X^1)} \quad (10.2)$$

Where, S_X^0 and S_X^1 are the outcomes of the stationarity test [70] being not rejected and rejected respectively. Consequently $n(S_X^1)$ and $n(S_X^0)$ are the number of signals in a given set X (for example 3750 univariate EEG signals from focal EEG dataset) that have not rejected and rejected the stationarity test respectively. These rejection probabilities are defined analogously for bivariate measures (pair of EEG signals in focal and nonfocal EEG datasets). Following [70], we compare the rejection probabilities using the relative difference measure D suggested in Andrzejak *et al.*[70]

$$D = \frac{p_1 - p_2}{p_1 + p_2} \quad (10.3)$$

10.3 Results and discussion

Table 10.1 shows the unconditioned and conditioned rejection probabilities for the randomness test combined with iAAFT surrogates based on network measures - \mathcal{C} (first row), \mathcal{R} (second row), \mathcal{L} (third row), and \mathcal{BC} (fourth row). Since there are 3750 pairs of EEG signals from focal and nonfocal EEG dataset, we only show results from set

X . Similar results were found from set Y . Also for the sake of comparison, rejection probabilities using nonlinear prediction error P [70] is also shown (fifth row). Here D^{All} represents the contrast between unconditioned probabilities, where as $D^{S^0_X}$ and $D^{S^1_X}$ represent the contrast between rejection probabilities conditioned on S^0_X and S^1_X respectively. It is clear from our results that the contrast between all the focal and nonfocal EEG signals (III column) as given by D^{All} is the highest for the randomness test based on \mathcal{R} , followed by \mathcal{C} and nonlinear prediction error P . In contrast, it can be seen that \mathcal{L} and \mathcal{BC} give similar rejection probability for both the focal and the nonfocal EEG signals resulting in low (non-significant) values for D^{All}

TABLE 10.1: Comparison of the unconditioned rejection probability for the focal and non-focal EEG signals and the corresponding D value for the univariate measures are shown columns $II - IV$. Columns $V - VII$ and $VIII - X$ are same as columns $II - IV$ but for stationary and non-stationary signals respectively.

Measures	p^F	p^N	D^{All}	$p^F(U^1_X S^0_X)$	$p^N(U^1_X S^0_X)$	$D^{S^0_X}$	$p^F(U^1_X S^1_X)$	$p^N(U^1_X S^1_X)$	$D^{S^1_X}$
\mathcal{C}	0.37	0.14	0.43	0.42	0.17	0.40	0.31	0.12	0.43
\mathcal{R}	0.16	0.05	0.50	0.17	0.07	0.42	0.16	0.04	0.57
\mathcal{L}	0.48	0.44	0.04	0.42	0.38	0.05	0.55	0.50	0.04
\mathcal{BC}	0.35	0.32	0.04	0.31	0.31	0.01	0.40	0.34	0.08
N [70]	0.29	0.20	0.19	0.30	0.15	0.33	0.28	0.23	0.09

Also, it can be seen from Table 10.1 that the contrast between stationary focal and nonfocal EEG signals as given by D^{S^0} (VI column) is again highest for \mathcal{R} , followed by \mathcal{C} and P , with \mathcal{L} and \mathcal{BC} giving low and non-significant values. When the analysis is restricted to nonstationary signals, we can observe that the network measures \mathcal{R} and \mathcal{C} can still very well distinguish between focal and non-focal EEG signals as evidenced by D^{S^1} (IX column). The network measures \mathcal{L} , \mathcal{BC} and P give relatively much lower values for D^{S^1} .

TABLE 10.2: Same as Table 10.1, but for bivariate measures.

Measures	p^F	p^N	D^{All}	$p^F(B^1 S^0)$	$p^N(B^1 S^0)$	D^{S^0}	$p^F(B^1 S^1)$	$p^N(B^1 S^1)$	D^{S^1}
\mathcal{C}_{cross}	0.43	0.22	0.31	0.46	0.23	0.32	0.40	0.21	0.31
L [70]	0.56	0.42	0.15	0.52	0.40	0.26	0.61	0.51	0.09

Table 10.2 show the unconditioned and conditioned rejection probabilities for the nonlinear-independence test using bivariate iAAFT surrogates and based on the cross network measure \mathcal{C}_{cross} . For the sake of comparison, the rejection probabilities for the nonlinear-independence test based on L [70] is also shown. In case of bivariate analysis, we found that the cross network measure \mathcal{C}_{cross} could successfully distinguish between focal and nonfocal EEG signals, even when the analysis is restricted to nonstationary signals. In contrast, L gave low values for the contrast between focal and nonfocal EEG signals

TABLE 10.3: Contrast between focal and nonfocal EEG signals that have rejected the stationarity test. Columns II to VI shows the D^{S^1} values for $f_c = 0.01, 0.02, 0.03, 0.04$ and 0.05 respectively.

Measures	$f_c = 0.01$ (5.12 Hz)	$f_c = 0.02$ (10.24 Hz)	$f_c = 0.03$ (15.36 Hz)	$f_c = 0.04$ (20.48 Hz)	$f_c = 0.05$ (25.6 Hz)
\mathcal{C}	0.45	0.39	0.41	0.40	0.32
\mathcal{R}	0.45	0.48	0.43	0.38	0.17
\mathcal{L}	0.08	0.18	0.21	0.28	0.28
\mathcal{BC}	0.12	0.23	0.24	0.26	0.23
P [70]	0.14	0.12	0.12	0.10	-0.01

when the analysis was restricted to nonstationary signals. Furthermore, in each case, the D value for global cross-clustering coefficient \mathcal{C}_{cross} was greater than the nonlinear interdependence measure L .

Table 10.3 shows the results for the randomness test based on TFT surrogates to quantify the contrast between nonstationary focal and nonfocal signals. Our results show that as f_c is increased (up to 0.02), the rejection probability of focal and nonfocal EEG signals increase in case of the network measures \mathcal{C} and \mathcal{R} (see **Figure 4** in [P-II]). However, the contrast between focal and nonfocal signals is still maintained very well (see Table 10.3). In case of the network measures \mathcal{L} and \mathcal{BC} , we see that as f_c is increased, the contrast between focal and nonfocal EEG signals starts to improve, while the rejection probabilities start to decrease for both focal and nonfocal EEG signals (see **Figure 4** in [P-II]). Similar observations are made in case of P , but the contrast between focal and nonfocal EEG signals as given by D is lower compared to network measures (see Table 10.3). For high values of f_c (> 0.03), we observe that the rejection probabilities for both focal and nonfocal EEG signals starts to drop in case of all the measures as the surrogates start becoming increasingly similar to the original data and might contain too much of the nonlinear deterministic dynamics of the original data in them. Similar observations were made in case of the nonlinear-independence test based on TFT surrogates, \mathcal{C}_{cross} outperformed L (see **Figure 6** in [P-II]).

Additionally, in this study we also investigated the dependence between univariate and bivariate network measures by estimating the conditional probabilities $p(B^1|U_X^0 U_Y^0)$, $p(B^1|U_X^1 U_Y^0)$, and $p(B^1|U_X^1 U_Y^1)$ (see **Figure 7** in [P-II]). We observed that rejection of one of the randomness test based on \mathcal{C} increases the rejection probability of the nonlinear-independence test based on \mathcal{C}_{cross} , while rejection of both the randomness tests based on \mathcal{C} further increases the rejection probability of nonlinear-independence test based on \mathcal{C}_{cross} . Similar observations can be made when P and L as mentioned in [70] were used. However, we also observed that the value of $p(B^1|U_X^0 U_Y^0)$ was still above the significance level, indicating that rejection of randomness test alone is not a sufficient condition for the rejection of the nonlinear-independence test. To test this conjecture, following the work of Andrzejak *et al.* [70], we shuffled the pairs of stationary focal EEG

signals without replacement. Instead of pairing signal x with its neighboring contact y , it was paired with some other signal that was randomly selected without replacement from the remaining signals in set Y [70]. Thus, any potential nonlinear dependence is destroyed and we end up with pairs of signals that are independent of each other, but might possess strong individual dynamics. The result from this shuffling (see **Figure 8** in [P-II]) indicates that irrespective of the outcome of the randomness test, the rejection probabilities of the nonlinear-independence test based on \mathcal{C}_{cross} are close to the significance level and remain approximately at the same level resulting. These results indicate independence between the signals and a good specificity for \mathcal{C}_{cross} .

10.4 Summary

In this study, we proposed the application of randomness and nonlinear-independence test based on RN measures and demonstrated that these measures, combined with surrogate analysis, can distinguish between focal and nonfocal EEG signals. Our findings based on these tests reveal that focal EEG signals exhibit an increased degree of structural complexity and interdependency compared to nonfocal EEG signals. Particularly, measures such as \mathcal{C} , \mathcal{R} and \mathcal{C}_{cross} can successfully distinguish between the focal and nonfocal EEG signals, even when the analysis is restricted to nonstationary signals, irrespective of the type of surrogates used. In contrast, the network measure \mathcal{L} and \mathcal{BC} fail to distinguish between the focal and nonfocal EEG signals when iAAFT surrogates are used. However, their performance improved upon using TFT surrogates.

CHAPTER 11

MOVING WINDOW RECURRENCE NETWORK ANALYSIS OF EEG [[P-I],[P-V]]

11.1 Introduction

In this study we demonstrate the application of moving window RNA to capture the dynamical transitions in neural data. Since RN approach can handle short and non-stationary data, it can be an ideal candidate for this type of analysis, which hitherto has not been explored for EEG data. This work is divided into two separate sections related to the analysis of EEG data from two epileptic patients undergoing EEG recordings [P-I] and LFP data recorded from non-human primate performing a visuomotor task [P-V]. In this section, we will briefly introduce the motivation behind the work carried out in [P-I] and [P-V].

It is well known that epilepsy is a dynamical disorder and the epileptic brain transitions between different dynamical states - inter-ictal state, pre-ictal state, ictal state and the post-ictal state. Characterizing the dynamical transitions in an epileptic EEG signal can potentially lead to unambiguous identification of pre-ictal state, which holds the key in preventing or suppressing the seizure before it strikes. In [P-I], we look at some preliminary results obtained in this direction, where we try to characterize the dynamical shifts in the epileptic EEG data using RN measures.

In [P-V] we apply the moving window RNA to LFP data acquired from the primary motor cortex of a monkey performing a visuomotor task. It is well known that cortical rhythms like the LFPs in the β frequency range are ubiquitous in the motor cortex of mammals including monkeys and humans across the upper limb area of the primary

motor cortex. The dynamics of the LFPs has been generally characterized based on the temporal profile of the amplitude of oscillations including event related synchronization, event related desynchronization and phase locking methods. However, the dynamical properties of such LFPs have not been characterized well enough especially with respect to wide-band oscillations. Since RNA can be applied to short data segments and RN measures can be still computed reliably, in [P-V] we explore the applicability of RNA methods to wide-band LFP data (β and low γ bands) to characterize the inherent dynamics simply using evoked responses.

11.2 Data and methods

11.2.1 EEG data

The EEG data used in [P-I] was originally published by Quiroga *et al.* [260] and is available for free download at <https://vis.caltech.edu/~rodri/data.htm>. Basically, the data comprises of tonic-clonic seizures of two subjects recorded using scalp EEG with right central electrode (channel *C4* according to 10-20 system [261]). The EEG data has been filtered between 1-50 Hz and sampled at 102.4 Hz. Figure 11.1 shows 3 minutes of EEG data from one of the two patients. The beginning of the seizure is marked with a solid red line (approximately at 80 seconds). The seizure discharge lasts for about 8 seconds and the clonic phase begins at 123 seconds (marked with dashed red line) [260]. The seizure ends approximately around 155 seconds (marked with solid black line). Also at around 140 seconds (not shown in the figure), the clonic discharge begins to separate [260].

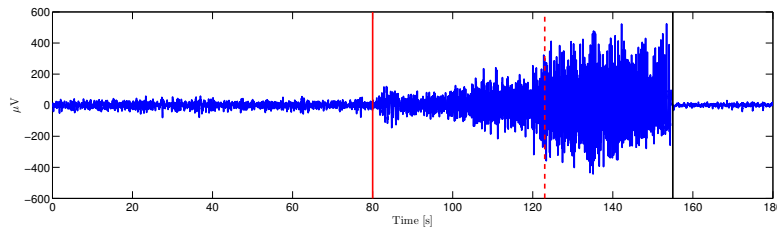


FIGURE 11.1: EEG data from channel *C4* of patient 1, with the clinical onset of seizure marked with solid red line. The dashed red line represents beginning of the clonic phase and the solid black line represents that end of seizure.

We computed global measures like $D_{\mathcal{T}}$, \mathcal{L} and \mathcal{R} for each window using moving window RNA. We divided the time series into 5 seconds window (≈ 500 samples) and 10 seconds window ($\approx 1,000$ samples) with 90 % overlap. In order to get the temporal profile of global network measures, we assigned the global measure to the mid-point of each window. Based on the first local minimum of the auto mutual information function, we

set $\tau = 18$. The embedding dimension m was varied from 2 to 8 and the recurrence rate RR was set to 0.05.

11.2.2 LFP data

The LFP data was recorded using a 96-channel (Blackrock Microsystems; 1 mm in length and 400 μm inter-electrode spacing) implanted in the primary motor cortex of a monkey (see Figure 11.5) performing a visuomotor task. Using a two-link exoskeleton manipulandum [262], the monkey performed a visuomotor task of moving a cursor on a horizontal screen (see Figure 11.4). A new target was displayed at a random location within a workspace when the monkey successfully reached the current target. The monkey was rewarded after successfully hitting five or seven consecutive targets.

The LFPs were bandpass filtered into [1, 30] Hz and [30, 80] Hz bands with a fourth-order Butterworth filter and the evoked response from 1000 consecutive successful trials were computed. We partitioned the data into a series of highly overlapping windows of length 150 ms with a step-size of 1 ms. The reader is directed to [P-V] for further details regarding data pre-processing and preparation.

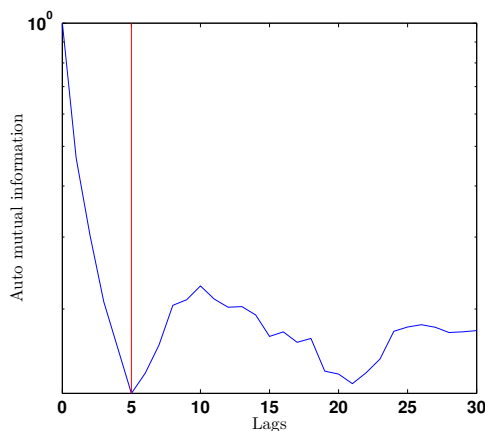


FIGURE 11.2: Estimation of τ using the first local minima of auto mutual information.

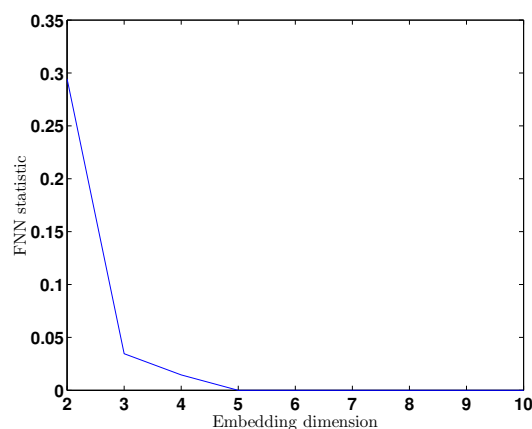


FIGURE 11.3: Estimation of m using the false nearest neighbor method.

We averaged over 1000 trials of LFP data (-100 ms before the event and 350 ms after the event) for all the 96 channels. The averaged data was divided into highly overlapping windows of length 150 ms and step size 1 ms. The optimal delay and the minimum embedding dimension was computed using first minimum of the auto mutual information and FNN method for all the channels. We found that for most of the data the embedding parameters were, $\tau = 5$ (see Figure 11.2) and $m = 3$ (see Figure 11.3). Although the FNN statistic approaches zero at $m = 5$, as a trade-off between data length and embedding dimension, we choose $m = 3$ for signals from all the channels. At $m = 3$, we can see

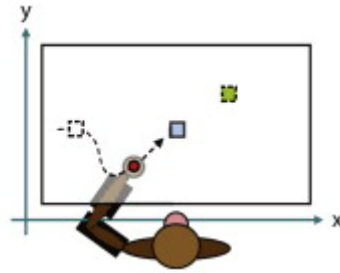


FIGURE 11.4: Experimental setup for the visuomotor task, where the monkey performs random target pursuit using two-link exoskeleton robot. The monkey moves the visual cursor (red circle) to a target (blue square). Each time monkey hits the target, a new target appears at a random location (green square). Figure reproduced with permission from [263]

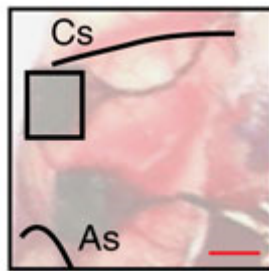


FIGURE 11.5: Location of the Utah microelectrode array in the arm area of the primary motor cortex, showing the landmarks central sulcus (Cs) and arcuate sulcus(As). Figure reproduced with permission from [264].

that the FNN statistic is already below 0.05. Using these embedding parameters we constructed same-sized recurrence networks for each window and channel. Instead of specifying the recurrence threshold ε , we fix the recurrence rate $RR = 0.05$ so that we obtain recurrence networks with approximately the same number of edges so that we can compare the networks obtained from different time windows [17].

11.3 Results and discussions

11.3.1 EEG data

Figures 11.6 (B)-(D) show the result of moving window RNA for the RN measures $D_{\mathcal{T}}$, \mathcal{L} and \mathcal{L} respectively, for EEG data of patient 1 with 10 seconds window and varying embedding dimension, m . From Figure 11.6 (B), it can be seen that $D_{\mathcal{T}}$ increases with embedding dimension m until about 80 seconds before the seizure. Beyond 80 seconds, $D_{\mathcal{T}}$ starts to drop for $m \geq 4$. For $m = 2$, we do not observe much variation in $D_{\mathcal{T}}$. This result for $D_{\mathcal{T}}$ clearly indicates that just before the beginning of the seizure at 80 seconds, the global dimension as measured by $D_{\mathcal{T}}$ begins to drop even if the m is

increased up to 10, a characteristic associated with a (low-dimensional) deterministic system. This behavior is seen again at around 120 seconds when the clonic phase of the seizure begins. Towards the end of the seizure, $D_{\mathcal{T}}$ again drops and remains at the same level for increasing values of m . The period after the seizure is characterized again by values of $D_{\mathcal{T}}$ that increase with embedding dimension m .

Regarding the behavior of \mathcal{L} , one can observe that starting around 70 seconds, there is a ramping up of \mathcal{L} for increasing m ($m \geq 4$) and \mathcal{L} peaks at around 84 seconds, which coincides with the time of the local minima for $D_{\mathcal{T}}$ for the seizure period. \mathcal{L} then starts to decrease and again begins to increase at around 140 seconds and peaking at around 150 seconds. In the post-seizure period, we can see that as the value of m increases the value of \mathcal{L} decreases (as observed in the pre-seizure period). The temporal profile of \mathcal{L} is more clearly depicted for $m = 8$ in Figure 11.7 (C).

The behavior of \mathcal{R} becomes clear only for $m \geq 6$, where \mathcal{R} begins to increase from 70 seconds reaching its local maxima at around 84 seconds, which coincides with the local minima for $D_{\mathcal{T}}$ for that period. It then begins to drop and again tends to increase at around 140 seconds and peaks at around 150 seconds. Around the seizure period, for $m \geq 6$, irrespective of the value of m , the value of \mathcal{R} remains approximately around the same value. (Also see Figure 11.7 (D)).

Figure 11.7 shows the result from moving window RNA for the EEG data from patient 1, at $m = 8$, where the temporal variations of the global measures are seen more clearly, along with the markings for beginning and ending of the seizure.

Our results from moving window RNA clearly indicates that the measures $D_{\mathcal{T}}$, \mathcal{R} and \mathcal{L} are not entirely independent and they track dynamical transitions in a related fashion. Furthermore, these three measures, as applied to the EEG data at hand, start showing signs of change well before the clinical identification of seizure (compare the clinical onset of seizure in Figure 11.7 (A) to the point when the global network measures start increasing (or decreasing in case of $D_{\mathcal{T}}$) in Figure 11.7 (B-D)). This feature represents the possibility of using these measures to predict the seizure in advance. However note that, in the dataset used, the clinical onset of the seizure occurs just 80 seconds into the data. Having a longer segment of data before the seizure onset could also reveal interesting shifts in dynamics much prior to the onset of the seizure. Recent studies have shown that it is possible to detect interesting changes in EEG tens of minutes before the actual seizure occurrence [265, 266]. However, most of these measures require long window sizes, of the order of 10 minutes, which is long in comparison to the global network measures, which are able to capture the rapidly changing dynamics using short windows of 5 seconds (512 samples) and 10 seconds (1024 samples). This is one of the key advantages of RNA compared to other existing methods. Also, In case of patient 1, the

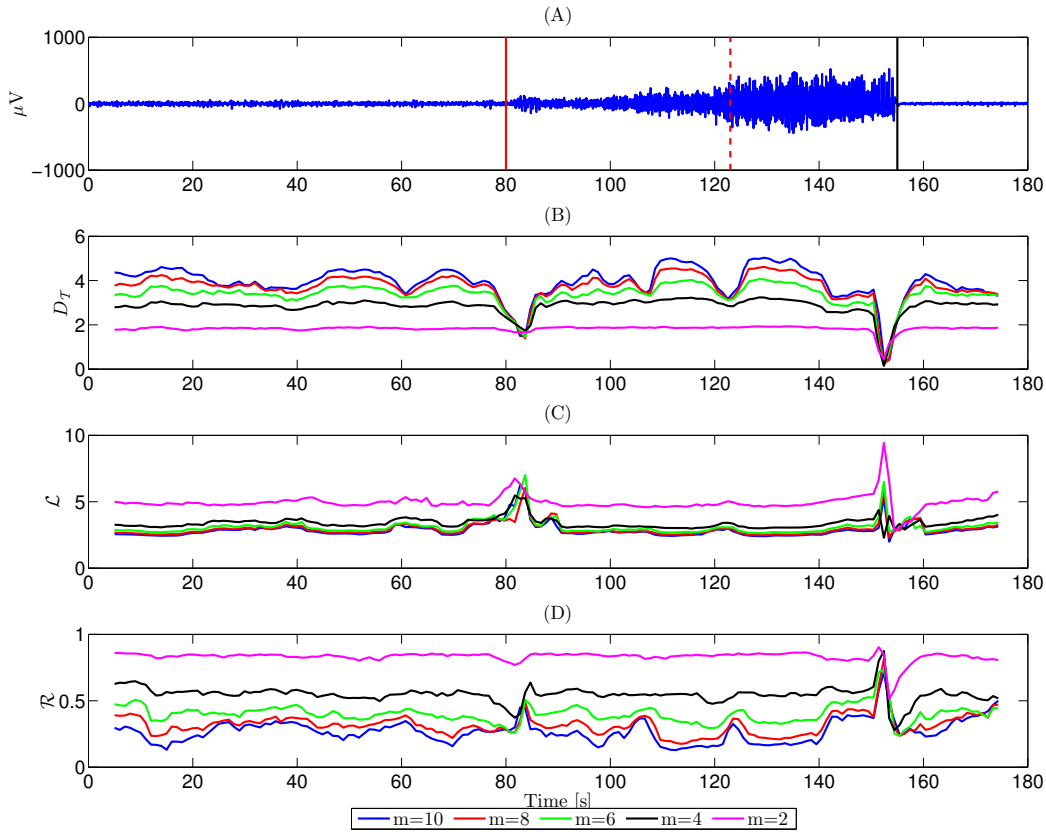


FIGURE 11.6: Moving window RNA of epileptic EEG data showing $D\tau$, \mathcal{L} and \mathcal{R} before, during and after the seizure. (A) EEG data from channel $C4$ of patient 1 with the clinical onset of seizure marked with solid red line. The dashed red line represents beginning of the clonic phase and the solid black line represents that end of seizure. (B-D) Temporal profile of the global measures (for $m = 2, 4, 6, 8, 10$) using a moving window of 10 seconds (≈ 1000 samples) with 90% overlap. Reproduced from [P-I]

clonic phase begins around 123 seconds and we observe that all the three global measures, display shift in their dynamics around this time point (See Figure 11.7 (B-D)). Also, we observed an increase in $D\tau$ and decrease in \mathcal{L} and \mathcal{R} , before these measures stabilize in the post-seizure period, which can be considered as a surrogate marker. This shift in dynamics is also consistent with the analysis in [260] using Gabor transform and could represent decrement in neural firing along with increase in inhibitory mechanisms, that could be responsible for seizure termination [260]. However, further research is needed to relate the variation of global RN towards the transition to post-ictal activity. We found qualitatively similar results were found for Patient 2 (see Figure S26 in supplementary data of [P-I]) and with window size of 5 seconds (see Figure S27 in supplementary data of [P-I]).

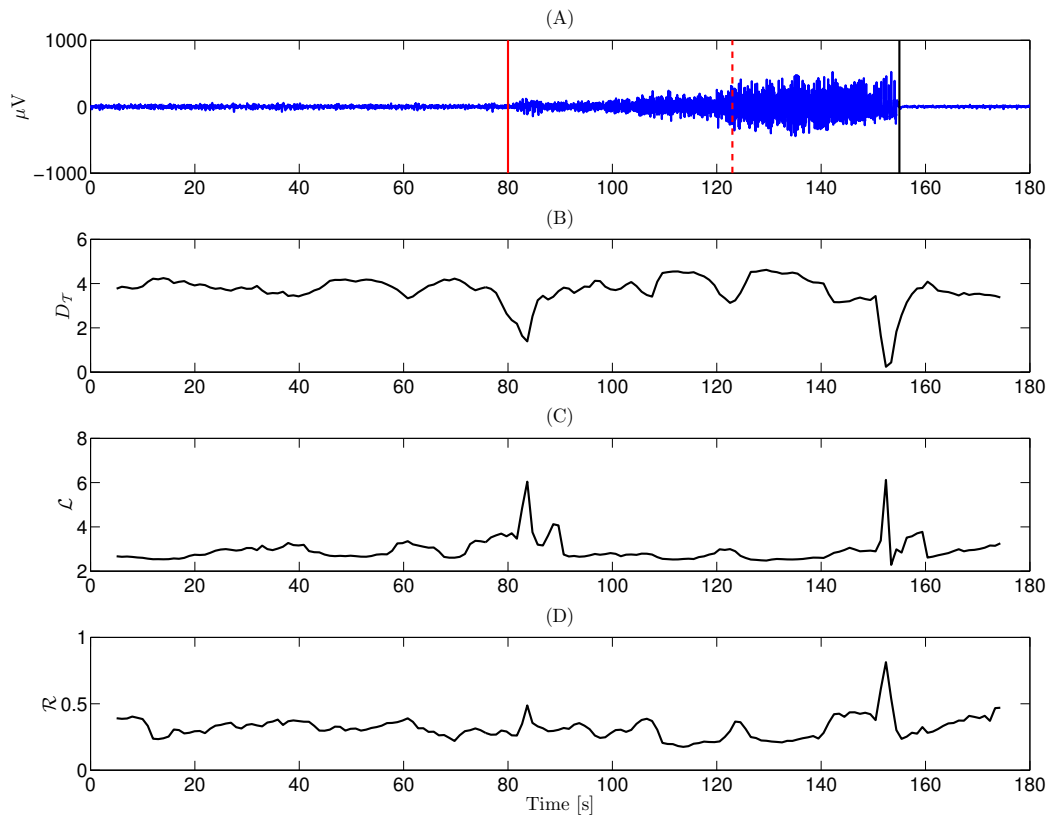


FIGURE 11.7: Moving window RNA of epileptic EEG data showing $D\tau$, \mathcal{L} and \mathcal{R} before, during and after the seizure. (A) EEG data from channel $C4$ of patient 1 with the clinical onset of seizure marked with solid red line. The dashed red line represents beginning of the clonic phase and the solid black line represents that end of seizure. (B-D) Temporal profile of the global measures (for $m = 8$) using a moving window of 10 seconds (≈ 1000 samples) with 90% overlap. Reproduced from [P-I]

11.3.2 LFP data

The measure \mathcal{C} for evoked responses of each channel across the two frequency bands were shown in Figs. 11.8 & 11.10. Within each frequency band, temporal variations across channels are somewhat similar. For [1,30] Hz band including the β peak, there is a minor peak slightly before 50 ms, and that particular timing is close to the highest phase locking of narrow band beta oscillations from this data set. However, other prominent features such as peaks at -50 ms and between 125-250 ms are unique features that either traditional magnitude or phase locking analysis based on narrow band beta oscillation did not exhibit. In contrast, low γ band apparently showed more heterogeneous temporal variations across the channels and timing at which high \mathcal{C} values are attained are almost opposite (after about 30 seconds from cue onset). Furthermore the timing at which local maxima are attained (25-120 ms) vary significantly between 0.2 to 0.4, especially compared to [1,30] Hz band where the peak \mathcal{C} timing in that time period roughly corresponds to the highest phase locking.

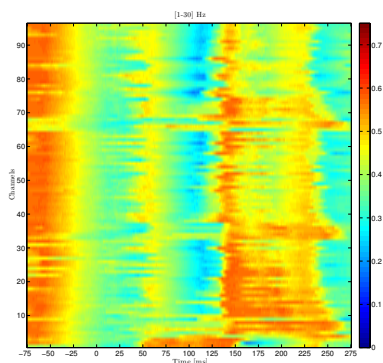


FIGURE 11.8: Temporal variation of \mathcal{C} across all channels for [1-30] Hz band.

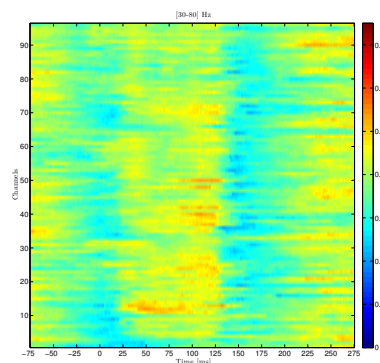


FIGURE 11.9: Temporal variation of \mathcal{C} across all channels for [30-80] Hz band.

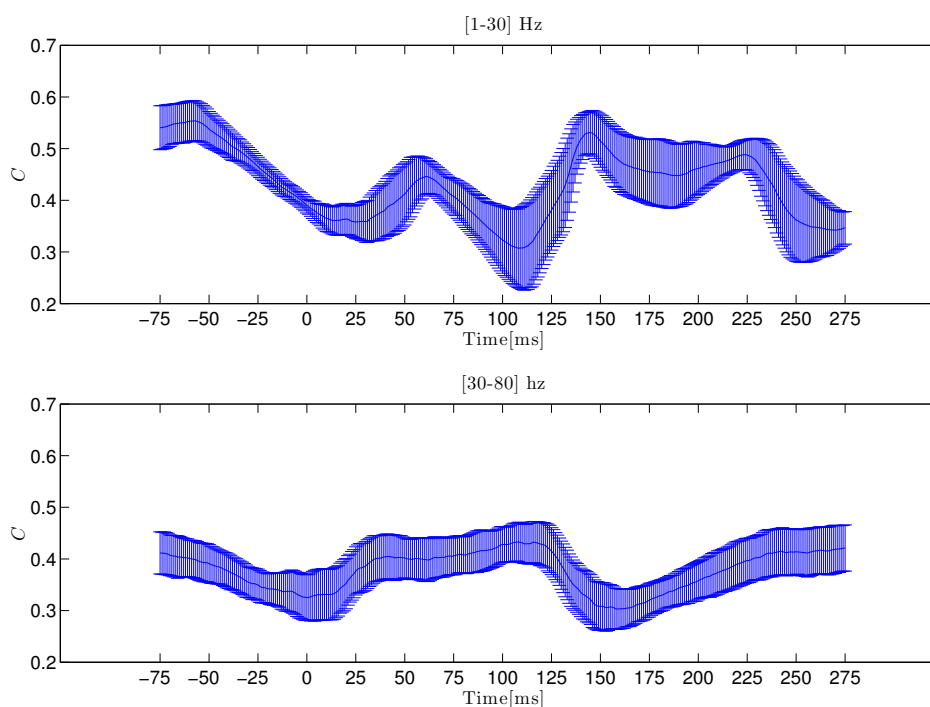


FIGURE 11.10: Average of \mathcal{C} across all channels for [1-30] and [30-80] Hz band.

The mean of the temporal variations of \mathcal{C} across all the channels for both the bands are shown in Figure 11.10. The standard deviation at any given time point for both frequency bands are somewhat compatible, but the mean trends show more or less opposite behavior. Furthermore, probably due to phase locking over the β range, the temporal trajectory of \mathcal{C} quickly changes between 25 to 125 ms. Therefore, RNA method, even at the level of evoked potential, exhibit much richer response patterns than simple narrow band phase locking or wide band amplitude trajectories.

11.4 Summary

The results presented in [P-I] represent the possibility of using RN measures as biomarkers for seizure prediction in advance. Also, we observed that RN measures capture the dynamical variations underlying the epileptic EEG signal in a related fashion. We also applied moving window RNA to characterize the dynamical characteristic of LFP oscillations from a non-human primate performing visuomotor task in [P-V]. Our results revealed that such analysis can reveal richer dynamics of wide band signals and clear control of the underlying network dynamics during the task based only on evoked responses in LFPs.

Part III

General discussions and conclusions

CHAPTER 12

OVERVIEW AND DISCUSSIONS

In this doctoral thesis, we used local and global RN measures to distinguish between chaotic and stochastic processes. We also investigated the effect of noise on RN measures. With regard to the applicability of RN measures in biological time series, we analyzed EEG signals across multiple spatial scales (intracranial EEG signals, extracranial EEG signals and LFPs). For the first time, we combined RN methods with surrogate analysis to test for the presence of deterministic structure in epileptic EEG signals. We presented novel results regarding the ability of certain global RN measures to not only distinguish between healthy and epileptic EEG signals, but also between interictal EEG signals recorded from epileptogenic and non-epileptogenic brain areas. Furthermore, we have also demonstrated the application of moving window RNA to capture dynamical transitions in EEG and LFP signals using short window sizes.

12.1 Distinguishing between chaotic and stochastic dynamics

Inferring the signatures of chaotic deterministic and stochastic processes from experimental data can lead to useful practical applications in wide array of fields such as climatology, finance, biology, to cite a few. Using RN measures and both paradigmatic models like Rössler and Lorenz systems and noisy experimental data like EEG signal, we have demonstrated that (hyper)chaotic and stochastic processes can be distinguished after additional embedding [P-I]. In contrast to some of the other approaches [8, 20], our approach based on RN properties, is both conceptually and computationally simple (particularly when transitivity-based measures are used). Also, it has been shown that

RN properties can be estimated from short time series reliably unlike other nonlinear approaches [15, 142]. In fact, Lacassa *et al.* used VGs, another network-based approach to characterize the time series, to describe stochastic and chaotic dynamics using both numerical simulations and experimental data [71].

Using model systems, it has been demonstrated that certain local RN measures like the local clustering coefficient are sensitive to the presence of UPOs [16]. The vertices close to low-periodic UPOs have relatively higher values of local clustering coefficient. Also, global measures like transitivity \mathcal{T} tend to have higher values (or consequently lower values for the transitivity dimension $D_{\mathcal{T}}$ for RNs associated with chaotic systems due to infinite number of UPOs [16]. In contrast, stochastic dynamics (for example, linear surrogates) theoretically exhibit infinite dimension and thus the associated $D_{\mathcal{T}}$ should be limited by the embedding dimension (in non-pathological cases). As mentioned above, chaotic attractors are formed differently in contrast to time-delay embedded linear-stochastic processes since only the former consists of densely packed UPOs, which cause an unique microscopic imprint to the system's invariant density. In contrast, surrogate data constructed from finite records fail to recover this structure. Therefore, we hypothesized that the RN constructed from linear surrogates should exhibit larger $D_{\mathcal{T}}$ compared to the chaotic system (or conversely higher \mathcal{T} than the surrogates). We tested these assumptions in [P-I], where we not only used $D_{\mathcal{T}}$, but several other local and global network measures and demonstrated using paradigmatic model systems that RN measures can distinguish between the signatures of deterministic (chaotic/hyperchaotic) and stochastic dynamics. Our results revealed that both local and global measures derived from RNs associated with chaotic dynamics are different (after embedding) than that of stochastic dynamics, primarily due to the presence of infinitely many UPOs in the chaotic attractor. Furthermore, these results were consistent for different values of RR . Specifically in the case of hyperchaotic attractors, the results improved with the increase in the data length N , since high-dimensional chaos is better characterized with higher number of data points.

As revealed by moving window RNA of epileptic EEG data in [P-I], RN approach can be a powerful tool to detect (chaotic) deterministic signatures in real-world data such as epileptic EEG recordings, which are characterized by irregular fluctuations and rapid transitions in dynamics that usually buried under noise. Indications of (low-dimensional) deterministic dynamics underlying the ictal period were found using short window sizes (512 samples). This result is consistent with previous findings increased nonlinearity and low-dimensionality associated with seizure activity [7].

12.2 Impact of noise

Real-world data is seldom noise-free and thus assessing the robustness of nonlinear measures against noise is important. Despite the application of RN measures in various fields, the impact of noise on local and global network measures has not been investigated. In comparison to the previous works on RNs, we have carefully considered the effects of noise in tandem with the data length. In particular, how well the time series fills out the reconstruction of the attractor as noise is added for different data lengths have not been explored yet. We studied the impact of observational noise on both global and local RN measures in [P-III] and compared the RN approach with the Complexity-Entropy [77] approach in [P-I], where effects of both increasing noise levels and data lengths were considered. In [P-III] the results obtained are system-specific, in the sense that, the values obtained for the measures \mathcal{C} and \mathcal{L} depend on the system under study and the respective parameter space values. This implies that the results we report on the tolerable noise levels strictly refer to the two reference states we consider in our simulation example in [P-III]. However, our results generally indicate that the influence of noise on certain RN measures can be minimized by increasing RR and this is not a system-specific observation. This is due to the fact that small RR correspond to small ε and thus resolve mainly small-scale structures of the attractor. Adding a noise of less than the order of epsilon will more or less fully corrupt these structures. This situation will mainly affect measures like \mathcal{C} , \mathcal{T} . Thus, as RR (and thus ε) is increased, larger scales will be captured and thus remain potentially unaffected by larger noise amplitudes. In contrast, the measure \mathcal{L} will be largely unaffected, since the general structure of shortest paths in phase space will be approximately the same as in the noise-free case for noise up to a certain limit (20 % in this specific case). Further increase in noise level creates artificial short-cuts dropping the \mathcal{L} value. In case of local or vertex-based measures like b_i , k_i , and \mathcal{C}_i which are influenced by the presence of UPOs, increasing the RR again minimizes the influence of noise, as shown in [P-I]. The only other work investigating the influence of noise on RP-based methods was by Thiel *et al.* [48], where impact of noise on RQA parameters was studied. The results obtained in [48] show that RQA measures are susceptible to observational noise, but can yield reliable results for optimal value of recurrence threshold ε . Our results are consistent with this observation, where we show that the influence of noise on RN measures can be minimized by proper choice of RR (which is related to ε). Furthermore, in [P-I] we compared global RN measures with the Complexity-Entropy approach and found out that RN measures like transitivity \mathcal{T} and the average path length \mathcal{L} outperform the Complexity-Entropy causality plane approach in distinguishing chaos and noise at very short data lengths ($\approx 200 - 500$ samples). These results are consistent with previous observations that the RN methods perform very well particularly for very short time series [142, 166].

In [P-I] and [P-III] we consider only the influence observational noise on RN measures. It is important to note that if the noise is dynamical, then the bifurcation scenario mentioned in [P-III] might be enhanced or suppressed as dynamical noise impacts the future evolution of the system.

12.3 Application of recurrence network methods to EEG data

12.3.1 Application to healthy and epileptic EEG signals

Application of RN measures such as \mathcal{C} and \mathcal{L} in combination with surrogate analysis revealed that these measures can successfully distinguish between the structural properties of healthy and epileptic EEG signals by giving different rejection rates [P-III]. It has to be noted that surrogate analysis has never been combined with RN approach to study the structural properties of time series data. In general, surrogate analysis allow us to test results from nonlinear time series analysis against a specified null hypothesis and require two ingredients - 1) surrogate data that share the same linear properties as the original data but differ in their possible nonlinear (deterministic) structure and 2) A discriminatory statistic. Typically, measures such as correlation dimension, nonlinear prediction error, entropy measures and others have been used as a discriminatory statistic. These measures differ in their sensitivity and specificity depending on specific properties of the data under study and this has an effect on their rejection rates for the specified null hypothesis.

We proposed RN properties that are derived from graph theory as an alternative discriminatory statistic. In the context of combining the RN method with surrogate analysis, it is important to explain what the rejection of null hypothesis means. The RN properties do not capture dynamical characteristics, but rather describe the geometric structure of the system (respectively its attractor) in phase space. Although geometric structure and dynamics are closely related with each other in case of chaotic dynamics [174], it is not possible to directly relate structural differences in the system's (invariant) density to either linear or nonlinear dynamics. Thus RN properties characterize are different aspects of attractor geometry [16]. In this spirit, applying the surrogate method in conjunction with RN characteristics provides a test for structural (geometric) complexity of the data rather than for nonlinearity. The theoretical foundation for this was further provided by Donges *et al.* [153]. These earlier studies correctly implied that the data sharing same invariant density (for example the data and the iAAFT surrogates constructed thereof), the probability density function in the reconstructed phase space

should be the same and hence, the RN measures cannot differ. However, this implication holds true only if embedding techniques are not employed prior to the computation of these measures. Since embedding changes the phase space properties of a deterministic system in a way different than stochastic system, particularly due to the presence of infinitely many UPOs (in case of chaotic system), the RN measures clearly differ for the original data (if the data is driven by deterministic processes) and the surrogates. In this spirit, our results clearly demonstrated that both healthy and epileptic EEG signals have structural properties that are very different than those exhibited by stochastic processes. Thus, by applying the surrogate method in conjunction with RN characteristics, we have provided a novel test for the structural (or geometric) complexity of the data.

12.3.2 Distinguishing focal and nonfocal EEG signals

We extended our application of RN methods to EEG data by using both network and cross network measures to distinguish between the structural properties of focal (interictal EEG from epileptogenic zone) and non-focal (interictal EEG from non-epileptogenic zone) time series [P-II]. We used the publicly available data from Andrzejak *et al.* [70], who applied nonlinear prediction error and nonlinear interdependence measure to distinguish between focal and nonfocal EEG signals.

As mentioned previously, localization of epileptic foci using interictal EEG is an important clinical problem and various measures (linear and nonlinear) have been proposed to address this. Previous studies have reported the presence of more nonlinearity [185, 232, 267] in the EEG signals and stronger interdependence between the EEG signals [240, 259, 268–272] derived from epileptogenic brain areas in comparison to the EEG signals derived from normal brain areas. We compared our results with the results obtained by Andrzejak *et al.* [70], in which the influence of nonstationarity was assessed for the first time, and found that global network measures \mathcal{C} and \mathcal{R} gave a better contrast between focal and nonfocal EEG signals compared to the nonlinear measure P used in [70] where it was shown that P combined with iAAFT surrogates gave higher rejections for focal EEG signals (even when analysis is restricted to nonstationary signals) compared to nonfocal EEG signals. We found that the network measure \mathcal{C} gave higher rejections in case of focal EEG signals and gave lower rejections for the null hypothesis in case of nonfocal EEG compared to P and other network measures \mathcal{L} and \mathcal{BC} . Thus, the overall contrast between focal and nonfocal EEG signals as given by \mathcal{C} was much better compared to P . This indicates that the network measure \mathcal{C} captures a more elaborated property of increased complexity in the organization of EEG data obtained from the focal areas in comparison to the nonfocal areas. In this case, the difference in the degree of structural complexity of the supposed attractors underlying the focal

and nonfocal EEG signals directly relates to the presence of a nonlinear deterministic structure in the focal EEG signals induced by the epileptic process, which is absent in nonfocal EEG signals. Although the measure \mathcal{R} gave lesser rejections compared to P in case of focal EEG signals, the overall contrast between focal and nonfocal EEG signals as given by \mathcal{R} was still superior to P . In case of bivariate analysis of focal and nonfocal EEG signals, the performance of the cross network measure \mathcal{C}_{cross} was superior to the nonlinear interdependence measure. The increased interdependency between EEG signals recorded from the focal brain areas are very well captured by the bivariate measure \mathcal{C}_{cross} , even when the analysis is restricted to nonstationary EEG signals.

It is well known that both univariate and bivariate iAAFT surrogates represent a null hypothesis that contains several assumptions. One such assumption is that of stationarity. In order to study the impact of nonstationarity on these measures, we also used TFT surrogates, which are not stationary by construction and preserve the global behavior of the original EEG data. Thus, any difference between the TFT surrogates and the original data at hand must not arise due to nonstationarity (i.e., trends) but possibly due to the difference in dynamics encoded in the irregular fluctuations of the data. Our results with TFT surrogates quantitatively show that the contrast between focal and nonfocal EEG signals, as given by RN measures (particularly \mathcal{C} and \mathcal{R}), was still high in comparison to the nonlinear prediction error P . The same observation holds true for bivariate recurrence network measure, \mathcal{C}_{cross} in comparison to the nonlinear interdependence measure L . However, it has to be noted that we have considered only two types of surrogate schemes - iAAFT and TFT surrogates. There are other surrogate techniques that can be used to preserve the nonstationarity in the surrogates. Recently, Lucio *et al.* [258] proposed an improved surrogate technique to preserve nonstationarity in the surrogates by detrending the data before computing the Fourier transform and then retrending the data after inverse Fourier transform. This technique is combined with TFT technique and can be applied using any linear surrogate generation algorithm and it preserves the linear properties of the nonstationary original data in the surrogates quite well [258]. Other methods based on wavelet surrogates have also been proposed to deal with nonstationarity [102–104]. A detailed comparative study on application of different surrogate techniques to investigate nonlinear dynamics, specifically in nonstationary epileptic EEG data would be considered in future.

The results obtained in [P-II] demonstrate their usefulness for diagnostic purposes. The RN measures like \mathcal{C} and \mathcal{R} can provide valuable information from interictal EEG signals from the point of view of localization of the epileptic foci. Especially the measure \mathcal{C} , which clearly gave high rejections for the focal EEG signals compared to the nonfocal EEG signals, could be particularly useful as it can characterize the structural properties

of the different time series better, easy to compute, has lesser computational expenditure, and does not require long segments of data compared to other nonlinear measures.

12.3.3 Moving window recurrence network analysis

Our results from moving window RNA for epileptic EEG [P-I] and LFP signals [P-V] revealed that certain global RN measures can capture the rapid shift in dynamics using very short window sizes. Typically, most methods used in nonlinear time series analysis require large datasets and one of the advantages of RNA is that the RN measures can be reliably computed even with short data segments [15, 165, 170]. This property renders the application of RNA readily to nonstationary real-world time series [142]. In the context of epileptic EEG analysis, establishing the presence of UPO is of great importance [273] as it can open up the possibility of short term prediction and control [19]. Seizure prediction and identification of a preictal state has been a central problem in the field of epileptic EEG signal analysis as the unpredictability of seizures is associated with significant morbidity. Examples of some nonlinear measures used as feature vectors for seizure prediction include correlation dimension, phase synchronization [274], dynamic similarity index [275], and very recent approaches include the use of short-term Lyapunov exponent [266] and GenericPred [265] method. Most of these measures require relatively longer window lengths ranging from 30 seconds to even 20 minutes. Using RN measures like \mathcal{C} or \mathcal{T} as feature vector in seizure prediction could be particularly advantageous due to their ability to characterize the structural property of the system and capture dynamical transitions with rather short time windows (2 seconds) and reduced computational cost. Although in our example in EEG [P-I], we did not have longer segment EEG data before the onset of seizure to check if RN measures can identify any dynamical transition related to preictal state. However, our results in EEG [P-I] suggest that global RN measures can distinguish between pre-seizure, seizure and post-seizure state. In future, we hope to explore the applicability of RN measures, including bivariate cross-network measures, for seizure prediction.

12.3.4 Interpretation of recurrence network measures

In the context of RN measures, high values for \mathcal{C} might imply regularity in the fluctuation (deterministic structure) of dynamics, whereas low values might imply an erratic or random fluctuation in the dynamics [276]. In case of deterministic chaotic systems, where the fluctuations are seemingly non-regular, the presence of UPOs contribute towards an increase in \mathcal{C} . Relating this interpretation to our findings from epileptic EEG signals, we can say that the underlying deterministic structure of the interictal signal recorded from

focal areas are strongly reflected in the measure \mathcal{C} leading to higher rejections for the null hypothesis since the iAAFT surrogates by construction are stochastic (less predictable) in nature ($\mathcal{C}_{data} > \mathcal{C}_{surr}$). Also interpreting this in the context of results obtained in [P-III], where \mathcal{C} gave highest rate of rejection for ictal EEG in comparison to other measures, we can say that \mathcal{C} is clearly able to reflect the presence of a regular or deterministic structure that is dominant in such signals. The measure \mathcal{R} reflects the homogeneity of the RN derived from the time series. The RN derived from chaotic time series show assortative mixing and those from stochastic system show disassortative mixing as already shown in [P-I]. The multiple clusters that exist in the phase space of a chaotic system, due to the presence of many UPOs, result in most of the vertices being connected to each other within the same cluster. Most of these vertices have similar degrees, barring few that exist on the boundaries of the cluster [277]. Due to the existence of edges between vertices that have similar degrees, such networks show assortative behavior. In contrast, a the phase space of a stochastic system clear do not have multiple clusters, as there are no UPOs in such systems. Our results in [P-II] show that RNs derived from EEG signals recorded from focal areas are more assortative than the EEG signals recorded from nonfocal areas. The measure \mathcal{R} also resulted in higher number of rejections of the null hypothesis for focal EEG signals compared to nonfocal EEG signals implying that RN derived from nonfocal EEG signals does not exhibit assortative mixing. Also in [P-I] we showed that \mathcal{R} increases during the seizure period compared to the pre-seizure and post-seizure period. These observations signify that RN measures, particularly \mathcal{T} , \mathcal{C} and \mathcal{R} can be used as discriminatory statistic between deterministic and stochastic processes when applied to real-world biological signals, particularly epileptic EEG signals. As mentioned before, detecting the presence of deterministic structures in epileptic EEG signals is of fundamental importance due to its possible application in seizure control techniques. Particularly, responsive neurostimulation, which is a new approach to treat epileptic seizures by stimulating the focal areas, can benefit by nonlinear dynamical analysis of interictal EEG activity [278]. In this regard, our results in [P-II] have shown that, interictal EEG activity obtained from focal areas are more deterministic compared to recordings from nonfocal areas. One way of interpreting the clear difference in the rejection rates between focal and nonfocal signals is the presence of UPOs in interictal EEG signals obtained from focal areas. This is because, the surrogates represent stochastic processes and lack UPOs and RN measures like \mathcal{C} , \mathcal{T} and \mathcal{R} are sensitive to the presence of UPOs. As noted in [70], the difference in rejection rate can also be due to the presence of nonstationarity, among other alternatives. Since, iAAFT surrogates generated by definition are stationary, presence of nonstationarity in the original data can give false rejections. To test this, we used TFT surrogates and found our results to be consistent [P-II].

The network measure \mathcal{L} for a complex network is derived by averaging the length of shortest connections between all pairs of vertices. For an RN, changes or variations in \mathcal{L} reflects a dynamical transition. This is reflected in our moving window analysis of the epileptic EEG data in [P-I], where around the seizure onset, \mathcal{L} starts to increase reflecting a change in the underlying attractor geometry. Although transitivity measures like \mathcal{T} or \mathcal{C} are unrelated to \mathcal{L} [276], our results from [P-I] shows that they can still be correlated in some cases. During the seizure, the RNA of the EEG data shows high values for both \mathcal{T} and \mathcal{L} . This could signify the underlying deterministic nature of the dynamics associated with seizure (that leads to high value for \mathcal{T}), where as high value for \mathcal{L} could result due to the fact that there is a significant change in the dynamics during seizure compared to a more baseline state after the seizure, where the value of \mathcal{L} does not vary much.

The purpose of this doctoral thesis was to propose RN measures in combination with surrogate analysis to characterize the structural properties of neural signals and study the applicability of RNA to neural signals such as extracranial EEG, intracranial EEG and LFP data. Furthermore, using paradigmatic model systems we also investigated the influence of noise on RN measures and their ability to distinguish between deterministic (chaotic) and stochastic processes. The main conclusions that can be made from the results of this doctoral thesis are

1. Both local and global RN measures can distinguish between deterministic chaotic and stochastic processes after additional embedding [\[P-I\]](#).
2. RN measures are robust against noise and perform very well in distinguishing chaos from noise, even for very short time series. The influence of noise on RN measures can be further minimized by increasing RR [\[\[P-I\],\[P-III\]\]](#).
3. Epileptic EEG signals display higher degree of structural complexity compared to healthy EEG signals. Thus, novel results regarding the application of RN measures to distinguish between the structural complexity in the organization of healthy and epileptic EEG data was obtained [\[P-III\]](#).
4. Interictal EEG signals recorded from epileptogenic brain areas are more deterministic and interdependent compared to EEG signals obtained from non-epileptogenic brain areas. This result was consistent even when the analysis was restricted to nonstationary EEG signals. Thus, univariate and bivariate RN measures can be used as reliable biomarkers for localization of epileptic foci from interictal EEG signals [\[P-II\]](#).

5. RNA of epileptic EEG data and LFP signals recorded from visuomotor task can capture the rapid dynamical transitions underlying these biological signals, using short window sizes [\[P-I\]](#).

- [1] Armin Fuchs. *Nonlinear Dynamics in Complex Systems*. Springer, 2014.
- [2] Norbert Marwan, M Carmen Romano, Marco Thiel, and Jürgen Kurths. Recurrence plots for the analysis of complex systems. *Physics Reports*, 438(5):237–329, 2007.
- [3] David D Nolte. *Introduction to Modern Dynamics: Chaos, Networks, Space and Time*. Oxford University Press, 2014.
- [4] Ralph G Andrzejak, Klaus Lehnertz, Florian Mormann, Christoph Rieke, Peter David, and Christian E Elger. Indications of nonlinear deterministic and finite-dimensional structures in time series of brain electrical activity: Dependence on recording region and brain state. *Physical Review E*, 64(6):061907, 2001.
- [5] Leon Glass. Dynamical disease: Challenges for nonlinear dynamics and medicine. *Chaos: An Interdisciplinary Journal of Nonlinear Science*, 25(9):097603, 2015.
- [6] Alan L Hodgkin and Andrew F Huxley. A quantitative description of membrane current and its application to conduction and excitation in nerve. *The Journal of physiology*, 117(4):500–544, 1952.
- [7] Cornelis J Stam. Nonlinear dynamical analysis of eeg and meg: review of an emerging field. *Clinical Neurophysiology*, 116(10):2266–2301, 2005.
- [8] Holger Kantz and Thomas Schreiber. *Nonlinear time series analysis*, volume 7. Cambridge university press, 2004.
- [9] Klaus Lehnertz, Ralph G Andrzejak, Jochen Arnhold, Thomas Kreuz, Florian Mormann, Christoph Rieke, Guido Widman, and Christian E Elger. Nonlinear eeg analysis in epilepsy: Its possible use for interictal focus localization, seizure anticipation, and. *Journal of Clinical Neurophysiology*, 18(3):209–222, 2001.

-
- [10] Michael C Mackey and John G Milton. Dynamical diseases. *Annals of the New York Academy of Sciences*, 504(1):16–32, 1987.
- [11] Fernando Lopes Da Silva, Wouter Blanes, Stiliyan N Kalitzin, Jaime Parra, Piotr Suffczynski, and Demetrios N Velis. Epilepsies as dynamical diseases of brain systems: basic models of the transition between normal and epileptic activity. *Epilepsia*, 44(s12):72–83, 2003.
- [12] Henri Poincaré. Sur le problème des trois corps et les équations de la dynamique. *Acta mathematica*, 13(1):A3–A270, 1890.
- [13] J P Eckmann, S Oliffson Kamphorst, and David Ruelle. Recurrence plots of dynamical systems. *EPL (Europhysics Letters)*, 4(9):973, 1987.
- [14] Joseph P Zbilut and Charles L Webber Jr. Embeddings and delays as derived from quantification of recurrence plots. *Physics letters A*, 171(3):199–203, 1992.
- [15] Norbert Marwan, Jonathan F Donges, Yong Zou, Reik V Donner, and Jürgen Kurths. Complex network approach for recurrence analysis of time series. *Physics Letters A*, 373(46):4246–4254, 2009.
- [16] Reik V Donner, Yong Zou, Jonathan F Donges, Norbert Marwan, and Jürgen Kurths. Recurrence networks—a novel paradigm for nonlinear time series analysis. *New Journal of Physics*, 12(3):033025, 2010.
- [17] Reik V Donner, Michael Small, Jonathan F Donges, Norbert Marwan, Yong Zou, Ruoxi Xiang, and Jürgen Kurths. Recurrence-based time series analysis by means of complex network methods. *International Journal of Bifurcation and Chaos*, 21(04):1019–1046, 2011.
- [18] Reik V Donner, Jonathan F Donges, Yong Zou, and Jan H Feldhoff. Complex network analysis of recurrences. In *Recurrence Quantification Analysis*, pages 101–163. Springer, 2015.
- [19] Nagender Mishra, Maria Hasse, B. Biswal, and Harinder P. Singh. Reliability of unstable periodic orbit based control strategies in biological systems. *Chaos*, 25(4):–, 2015.
- [20] Massimo Cencini, Fabio Cecconi, and Angelo Vulpiani. *Chaos*. World Scientific, 2009.
- [21] Ludwig Arnold. Random dynamical systems springer monographs in mathematics. 1998.

- [22] Paul Glendinning. *Stability, instability and chaos: an introduction to the theory of nonlinear differential equations*. Cambridge university press, 1994.
- [23] Morris W Hirsch, Stephen Smale, and Robert L Devaney. *Differential equations, dynamical systems, and an introduction to chaos*, volume 60. Academic press, 2004.
- [24] Antonello Provenzale and Neil J Balmforth. Chaos and structures in geophysics and astrophysics. *Proceedings of GFD (Geophysical Fluid Dynamics of Woods Hole Oceanographic Institution)*, 1999.
- [25] Henk Broer and Floris Takens. *Dynamical systems and chaos*, volume 172. Springer Science & Business Media, 2010.
- [26] James D Meiss. *Differential dynamical systems*, volume 14. Siam, 2007.
- [27] John Milnor. On the concept of attractor. In *The Theory of Chaotic Attractors*, pages 243–264. Springer, 2004.
- [28] Harry Furstenberg. *Recurrence in ergodic theory and combinatorial number theory*. Princeton University Press, 2014.
- [29] Anatole Katok and Boris Hasselblatt. *Introduction to the modern theory of dynamical systems*, volume 54. Cambridge university press, 1997.
- [30] Floris Takens. Detecting strange attractors in turbulence. In *Dynamical systems and turbulence, Warwick 1980*, pages 366–381. Springer, 1981.
- [31] James C Robinson. A topological delay embedding theorem for infinite-dimensional dynamical systems. *Nonlinearity*, 18(5):2135, 2005.
- [32] Michael Small. *Applied nonlinear time series analysis: applications in physics, physiology and finance*, volume 52. World Scientific, 2005.
- [33] H S Kim, R Eykholt, and J D Salas. Nonlinear dynamics, delay times, and embedding windows. *Physica D: Nonlinear Phenomena*, 127(1):48–60, 1999.
- [34] Maurice Bertram Priestley. Non-linear and non-stationary time series analysis. 1988.
- [35] Andrew M Fraser and Harry L Swinney. Independent coordinates for strange attractors from mutual information. *Physical review A*, 33(2):1134, 1986.
- [36] Henry Abarbanel. Analysis of observed chaotic data. 1996.

- [37] Martín Gómez Ravetti, Laura C Carpi, Bruna Amin Gonçalves, Alejandro C Frery, and Osvaldo A Rosso. Distinguishing noise from chaos: objective versus subjective criteria using horizontal visibility graph. *PLoS one*, 9(9):e108004, 2014.
- [38] Andrei Nikolaevich Kolmogorov. A new metric invariant of transient dynamical systems and automorphisms in lebesgue spaces. In *Dokl. Akad. Nauk SSSR (NS)*, volume 119, pages 861–864, 1958.
- [39] Ya Ge Sinai. On the concept of entropy of a dynamical system. In *Dokl. Akad. Nauk. SSSR*, volume 124, pages 768–771, 1959.
- [40] Peter Walters. *An introduction to ergodic theory*, volume 79. Springer, 2000.
- [41] Thomas M Cover and Joy A Thomas. *Elements of information theory*. John Wiley & Sons, 2012.
- [42] Claude Elwood Shannon. A mathematical theory of communication. *ACM SIG-MOBILE Mobile Computing and Communications Review*, 5(1):3–55, 2001.
- [43] Robert Shaw. The dripping faucet as a model chaotic system. 1984.
- [44] J Doyne Farmer, Edward Ott, and James A Yorke. The dimension of chaotic attractors. *Physica D: Nonlinear Phenomena*, 7(1):153–180, 1983.
- [45] James Theiler. Estimating fractal dimension. *JOSA A*, 7(6):1055–1073, 1990.
- [46] Matthew B Kennel, Reggie Brown, and Henry DI Abarbanel. Determining embedding dimension for phase-space reconstruction using a geometrical construction. *Physical review A*, 45(6):3403, 1992.
- [47] Rainer Hegger and Holger Kantz. Improved false nearest neighbor method to detect determinism in time series data. *Physical Review E*, 60(4):4970, 1999.
- [48] Marco Thiel, M Carmen Romano, Jürgen Kurths, Riccardo Meucci, Enrico Allaria, and F Tito Arcelli. Influence of observational noise on the recurrence quantification analysis. *Physica D: Nonlinear Phenomena*, 171(3):138–152, 2002.
- [49] Joseph S Iwanski and Elizabeth Bradley. Recurrence plots of experimental data: To embed or not to embed? *Chaos: An Interdisciplinary Journal of Nonlinear Science*, 8(4):861–871, 1998.
- [50] Y Zou, D Pazó, MC Romano, M Thiel, and J Kurths. Distinguishing quasiperiodic dynamics from chaos in short-time series. *Physical Review E*, 76(1):016210, 2007.
- [51] Charles L Webber Jr and Joseph P Zbilut. Dynamical assessment of physiological systems and states using recurrence plot strategies. *Journal of Applied Physiology*, 76(2):965–973, 1994.

- [52] Joseph P Zbilut and Charles L Webber Jr. Recurrence quantification analysis: introduction and historical context. *International Journal of Bifurcation and Chaos*, 17(10):3477–3481, 2007.
- [53] Peter Grassberger and Itamar Procaccia. Characterization of strange attractors. *Physical review letters*, 50(5):346, 1983.
- [54] Norbert Marwan. *Encounters with neighbours: current developments of concepts based on recurrence plots and their applications*. Norbert Marwan, 2003.
- [55] Norbert Marwan and Charles L Webber Jr. Mathematical and computational foundations of recurrence quantifications. In *Recurrence Quantification Analysis*, pages 3–43. Springer, 2015.
- [56] Norbert Marwan, Niels Wessel, Udo Meyerfeldt, Alexander Schirdewan, and Jürgen Kurths. Recurrence-plot-based measures of complexity and their application to heart-rate-variability data. *Physical Review E*, 66(2):026702, 2002.
- [57] Joseph P Zbilut, Alessandro Giuliani, and Charles L Webber Jr. Detecting deterministic signals in exceptionally noisy environments using cross-recurrence quantification. *Physics Letters A*, 246(1):122–128, 1998.
- [58] Norbert Marwan and Jürgen Kurths. Nonlinear analysis of bivariate data with cross recurrence plots. *Physics Letters A*, 302(5):299–307, 2002.
- [59] N Marwan, M Thiel, and NR Nowaczyk. Cross recurrence plot based synchronization of time series. *Nonlinear Processes in Geophysics*, 9:325–331, 2002.
- [60] M Carmen Romano, Marco Thiel, Jürgen Kurths, and Werner von Bloh. Multivariate recurrence plots. *Physics letters A*, 330(3):214–223, 2004.
- [61] Y Zou, M Carmen Romano, Marco Thiel, Norbert Marwan, and Jürgen Kurths. Inferring indirect coupling by means of recurrences. *International Journal of Bifurcation and Chaos*, 21(04):1099–1111, 2011.
- [62] Edward N Lorenz. Deterministic nonperiodic flow. *Journal of the atmospheric sciences*, 20(2):130–141, 1963.
- [63] Steven H Strogatz. *Nonlinear dynamics and chaos: with applications to physics, biology and chemistry*. Perseus publishing, 2001.
- [64] Yakov Borisovich Pesin. Characteristic lyapunov exponents and smooth ergodic theory. *Russian Mathematical Surveys*, 32(4):55–114, 1977.
- [65] Claude E Shannon. A mathematical theory of communication. *Bell System Tech. J*, 27:623, 1948.

- [66] Jennifer M Yentes, Nathaniel Hunt, Kendra K Schmid, Jeffrey P Kaipust, Denise McGrath, and Nicholas Stergiou. The appropriate use of approximate entropy and sample entropy with short data sets. *Annals of biomedical engineering*, 41(2):349–365, 2013.
- [67] Steven M Pincus, Igor M Gladstone, and Richard A Ehrenkranz. A regularity statistic for medical data analysis. *Journal of clinical monitoring*, 7(4):335–345, 1991.
- [68] Kalon KL Ho, George B Moody, Chung-Kang Peng, Joseph E Mietus, Martin G Larson, Daniel Levy, and Ary L Goldberger. Predicting survival in heart failure case and control subjects by use of fully automated methods for deriving nonlinear and conventional indices of heart rate dynamics. *Circulation*, 96(3):842–848, 1997.
- [69] Joshua S Richman and J Randall Moorman. Physiological time-series analysis using approximate entropy and sample entropy. *American Journal of Physiology-Heart and Circulatory Physiology*, 278(6):H2039–H2049, 2000.
- [70] Ralph G Andrzejak, Kaspar Schindler, and Christian Rummel. Nonrandomness, nonlinear dependence, and nonstationarity of electroencephalographic recordings from epilepsy patients. *Physical Review E*, 86(4):046206, 2012.
- [71] Lucas Lacasa and Raul Toral. Description of stochastic and chaotic series using visibility graphs. *Physical Review E*, 82(3):036120, 2010.
- [72] Matthew B Kennel and Steven Isabelle. Method to distinguish possible chaos from colored noise and to determine embedding parameters. *Physical Review A*, 46(6):3111, 1992.
- [73] George Sugihara and Robert M May. Nonlinear forecasting as a way of distinguishing chaos from measurement error in time series. *Nature*, 344(6268):734–741, 1990.
- [74] Daniel T Kaplan and Leon Glass. Direct test for determinism in a time series. *Physical review letters*, 68(4):427, 1992.
- [75] Daniel T Kaplan and Leon Glass. Coarse-grained embeddings of time series: random walks, gaussian random processes, and deterministic chaos. *Physica D: Nonlinear Phenomena*, 64(4):431–454, 1993.
- [76] A Ro Osborne and A Provenzale. Finite correlation dimension for stochastic systems with power-law spectra. *Physica D: Nonlinear Phenomena*, 35(3):357–381, 1989.

- [77] OA Rosso, HA Larrondo, MT Martin, A Plastino, and MA Fuentes. Distinguishing noise from chaos. *Physical review letters*, 99(15):154102, 2007.
- [78] Luciano Zunino, Miguel C Soriano, and Osvaldo A Rosso. Distinguishing chaotic and stochastic dynamics from time series by using a multiscale symbolic approach. *Physical Review E*, 86(4):046210, 2012.
- [79] M Cencini, M Falcioni, E Olbrich, H Kantz, and A Vulpiani. Chaos or noise: Difficulties of a distinction. *Physical Review E*, 62(1):427, 2000.
- [80] Felipe Olivares, Angelo Plastino, and Osvaldo A Rosso. Ambiguities in bandt–pompe’s methodology for local entropic quantifiers. *Physica A: Statistical Mechanics and its Applications*, 391(8):2518–2526, 2012.
- [81] Felipe Olivares, Angelo Plastino, and Osvaldo A Rosso. Contrasting chaos with noise via local versus global information quantifiers. *Physics Letters A*, 376(19):1577–1583, 2012.
- [82] Jie Zhang and Michael Small. Complex network from pseudoperiodic time series: Topology versus dynamics. *Physical Review Letters*, 96(23):238701, 2006.
- [83] Yue Yang and Huijie Yang. Complex network-based time series analysis. *Physica A: Statistical Mechanics and its Applications*, 387(5):1381–1386, 2008.
- [84] Yutaka Shimada, Takayuki Kimura, and Tohru Ikeguchi. Analysis of chaotic dynamics using measures of the complex network theory. In *Artificial Neural Networks-ICANN 2008*, pages 61–70. Springer, 2008.
- [85] Grégoire Nicolis, A Garcia Cantu, and Catherine Nicolis. Dynamical aspects of interaction networks. *International Journal of Bifurcation and Chaos*, 15(11):3467–3480, 2005.
- [86] Jonathan F Donges, Reik V Donner, and Jürgen Kurths. Testing time series irreversibility using complex network methods. *EPL (Europhysics Letters)*, 102(1):10004, 2013.
- [87] Lucas Lacasa, Bartolo Luque, Fernando Ballesteros, Jordi Luque, and Juan Carlos Nuño. From time series to complex networks: The visibility graph. *Proceedings of the National Academy of Sciences*, 105(13):4972–4975, 2008.
- [88] Bartolo Luque, Lucas Lacasa, Fernando Ballesteros, and Jordi Luque. Horizontal visibility graphs: Exact results for random time series. *Physical Review E*, 80(4):046103, 2009.

-
- [89] Paul E Rapp, Alfonso M Albano, TI Schmah, and LA Farwell. Filtered noise can mimic low-dimensional chaotic attractors. *Physical review E*, 47(4):2289, 1993.
- [90] James Theiler, Stephen Eubank, André Longtin, Bryan Galdrikian, and J Doyne Farmer. Testing for nonlinearity in time series: the method of surrogate data. *Physica D: Nonlinear Phenomena*, 58(1):77–94, 1992.
- [91] James Theiler. On the evidence for low-dimensional chaos in an epileptic electroencephalogram. *Physics Letters A*, 196(5):335–341, 1995.
- [92] James Theiler and Dean Prichard. Constrained-realization monte-carlo method for hypothesis testing. *Physica D: Nonlinear Phenomena*, 94(4):221–235, 1996.
- [93] Thomas Schreiber and Andreas Schmitz. Surrogate time series. *Physica D: Nonlinear Phenomena*, 142(3):346–382, 2000.
- [94] Jose A Scheinkman and Blake LeBaron. Nonlinear dynamics and stock returns. *Journal of Business*, pages 311–337, 1989.
- [95] AR Osborne, AD Kirwan, A Provenzale, and L Bergamasco. A search for chaotic behavior in large and mesoscale motions in the pacific ocean. *Physica D: Nonlinear Phenomena*, 23(1):75–83, 1986.
- [96] Thomas Schreiber and Andreas Schmitz. Improved surrogate data for nonlinearity tests. *Physical Review Letters*, 77(4):635, 1996.
- [97] Tomomichi Nakamura, Michael Small, and Yoshito Hirata. Testing for nonlinearity in irregular fluctuations with long-term trends. *Physical Review E*, 74(2):026205, 2006.
- [98] Dean Prichard and James Theiler. Generating surrogate data for time series with several simultaneously measured variables. *Physical Review Letters*, 73(7):951, 1994.
- [99] Guillermo J Ortega and Enrique Louis. Smoothness implies determinism in time series: A measure based approach. *Physical review letters*, 81(20):4345, 1998.
- [100] Michael Small, Dejin Yu, and Robert G Harrison. Surrogate test for pseudoperiodic time series data. *Physical Review Letters*, 87(18):188101, 2001.
- [101] Alistair I Mees. Dynamical systems and tessellations: Detecting determinism in data. *International Journal of Bifurcation and Chaos*, 1(04):777–794, 1991.
- [102] Michael Breakspear, Mick Brammer, and Peter A Robinson. Construction of multivariate surrogate sets from nonlinear data using the wavelet transform. *Physica D: Nonlinear Phenomena*, 182(1):1–22, 2003.

-
- [103] CJ Keylock. Constrained surrogate time series with preservation of the mean and variance structure. *Physical Review E*, 73(3):036707, 2006.
- [104] Christopher J Keylock. A wavelet-based method for surrogate data generation. *Physica D: Nonlinear Phenomena*, 225(2):219–228, 2007.
- [105] Tomomichi Nakamura and Michael Small. Small-shuffle surrogate data: Testing for dynamics in fluctuating data with trends. *Physical Review E*, 72(5):056216, 2005.
- [106] Stefano Boccaletti, Vito Latora, Yamir Moreno, Martin Chavez, and D-U Hwang. Complex networks: Structure and dynamics. *Physics reports*, 424(4):175–308, 2006.
- [107] L da F Costa, Francisco A Rodrigues, Gonzalo Travieso, and Paulino Ribeiro Villas Boas. Characterization of complex networks: A survey of measurements. *Advances in Physics*, 56(1):167–242, 2007.
- [108] Mark EJ Newman. The structure and function of complex networks. *SIAM review*, 45(2):167–256, 2003.
- [109] Ed Bullmore and Olaf Sporns. Complex brain networks: graph theoretical analysis of structural and functional systems. *Nature Reviews Neuroscience*, 10(3):186–198, 2009.
- [110] Mikail Rubinov and Olaf Sporns. Complex network measures of brain connectivity: uses and interpretations. *Neuroimage*, 52(3):1059–1069, 2010.
- [111] Michael D Greicius, Ben Krasnow, Allan L Reiss, and Vinod Menon. Functional connectivity in the resting brain: a network analysis of the default mode hypothesis. *Proceedings of the National Academy of Sciences*, 100(1):253–258, 2003.
- [112] Jonathan F Donges, Yong Zou, Norbert Marwan, and Jürgen Kurths. The backbone of the climate network. *EPL (Europhysics Letters)*, 87(4):48007, 2009.
- [113] Jonathan F Donges, Yong Zou, Norbert Marwan, and Jürgen Kurths. Complex networks in climate dynamics. *The European Physical Journal-Special Topics*, 174(1):157–179, 2009.
- [114] AA Tsonis and PJ Roebber. The architecture of the climate network. *Physica A: Statistical Mechanics and its Applications*, 333:497–504, 2004.
- [115] Theodore B Achacoso and William S Yamamoto. *AY's Neuroanatomy of C. elegans for Computation*. CRC Press, 1991.

-
- [116] Danielle Smith Bassett and ED Bullmore. Small-world brain networks. *The neuroscientist*, 12(6):512–523, 2006.
- [117] Danielle S Bassett and Edward T Bullmore. Human brain networks in health and disease. *Current opinion in neurology*, 22(4):340, 2009.
- [118] Richard J Williams and Neo D Martinez. Simple rules yield complex food webs. *Nature*, 404(6774):180–183, 2000.
- [119] Joel E Cohen, Frédéric Briand, and Charles M Newman. *Community food webs: data and theory*. 1990.
- [120] Kurt W Kohn. Molecular interaction map of the mammalian cell cycle control and dna repair systems. *Molecular biology of the cell*, 10(8):2703–2734, 1999.
- [121] Leland H Hartwell, John J Hopfield, Stanislas Leibler, and Andrew W Murray. From molecular to modular cell biology. *Nature*, 402:C47–C52, 1999.
- [122] Hawoong Jeong, Bálint Tombor, Réka Albert, Zoltan N Oltvai, and A-L Barabási. The large-scale organization of metabolic networks. *Nature*, 407(6804):651–654, 2000.
- [123] Peter J Carrington, John Scott, and Stanley Wasserman. *Models and methods in social network analysis*, volume 28. Cambridge university press, 2005.
- [124] Mark EJ Newman. The structure of scientific collaboration networks. *Proceedings of the National Academy of Sciences*, 98(2):404–409, 2001.
- [125] Sidney Redner. How popular is your paper? an empirical study of the citation distribution. *The European Physical Journal B-Condensed Matter and Complex Systems*, 4(2):131–134, 1998.
- [126] Albert-Laszlo Barabási, Hawoong Jeong, Zoltan Néda, Erzsebet Ravasz, Andras Schubert, and Tamas Vicsek. Evolution of the social network of scientific collaborations. *Physica A: Statistical mechanics and its applications*, 311(3):590–614, 2002.
- [127] Andrei Broder, Ravi Kumar, Farzin Maghoul, Prabhakar Raghavan, Sridhar Rajagopalan, Raymie Stata, Andrew Tomkins, and Janet Wiener. Graph structure in the web. *Computer networks*, 33(1):309–320, 2000.
- [128] Michalis Faloutsos, Petros Faloutsos, and Christos Faloutsos. On power-law relationships of the internet topology. In *ACM SIGCOMM Computer Communication Review*, volume 29, pages 251–262. ACM, 1999.

- [129] Réka Albert, István Albert, and Gary L Nakarado. Structural vulnerability of the north american power grid. *Physical review E*, 69(2):025103, 2004.
- [130] Sergio Arianos, E Bompard, A Carbone, and Fei Xue. Power grid vulnerability: A complex network approach. *Chaos: An Interdisciplinary Journal of Nonlinear Science*, 19(1):013119, 2009.
- [131] Roger Guimera, Stefano Mossa, Adrian Turttschi, and LA Nunes Amaral. The worldwide air transportation network: Anomalous centrality, community structure, and cities' global roles. *Proceedings of the National Academy of Sciences*, 102(22):7794–7799, 2005.
- [132] Vito Latora and Massimo Marchiori. Is the boston subway a small-world network? *Physica A: Statistical Mechanics and its Applications*, 314(1):109–113, 2002.
- [133] L Euler. Solutio problematis ad geometriam situs pertinentis, commentarii academiae scientiarum imperialis petropolitanae 8 (1736), 128–140. Reprinted in: *Leonhardi Euleri–Opera Omnia–Series Prima–Opera Mathematica–Commentationes Algebraicae*, LG du Pasquier Ed., Teubner, Leipzig, pages 1–10, 1923.
- [134] Steven H Strogatz. Exploring complex networks. *Nature*, 410(6825):268–276, 2001.
- [135] Paul Erdős and A Rényi. On the evolution of random graphs. *Publ. Math. Inst. Hungar. Acad. Sci.*, 5:17–61, 1960.
- [136] Duncan J Watts and Steven H Strogatz. Collective dynamics of ‘small-world’ networks. *nature*, 393(6684):440–442, 1998.
- [137] Albert-László Barabási and Réka Albert. Emergence of scaling in random networks. *science*, 286(5439):509–512, 1999.
- [138] Albert-László Barabási, Réka Albert, and Hawoong Jeong. Mean-field theory for scale-free random networks. *Physica A: Statistical Mechanics and its Applications*, 272(1):173–187, 1999.
- [139] Maarten Van Steen. Graph theory and complex networks. *An Introduction*, 2010.
- [140] Lionel Barnett, Ezequiel Di Paolo, and Seth Bullock. Spatially embedded random networks. *Physical Review E*, 76(5):056115, 2007.
- [141] H Eugene Stanley. Introduction to phase transitions and critical phenomena. *Introduction to Phase Transitions and Critical Phenomena*, by H Eugene Stanley, pp. 336. Foreword by H Eugene Stanley. Oxford University Press, Jul 1987. ISBN-10: 0195053168. ISBN-13: 9780195053166, 1, 1987.

-
- [142] Jonathan Friedemann Donges. *Functional network macroscopes for probing past and present Earth system dynamics*. PhD thesis, Humboldt-Universität zu Berlin, Mathematisch-Naturwissenschaftliche Fakultät I, 2013.
- [143] Jesper Dall and Michael Christensen. Random geometric graphs. *Physical Review E*, 66(1):016121, 2002.
- [144] Jayanth R Banavar, Amos Maritan, and Andrea Rinaldo. Size and form in efficient transportation networks. *Nature*, 399(6732):130–132, 1999.
- [145] W Xia and MF Thorpe. Percolation properties of random ellipses. *Physical Review A*, 38(5):2650, 1988.
- [146] U Alon, A Drory, and I Balberg. Systematic derivation of percolation thresholds in continuum systems. *Physical Review A*, 42(8):4634, 1990.
- [147] Ingmar Glauche, Wolfram Krause, Rudolf Sollacher, and Martin Greiner. Continuum percolation of wireless ad hoc communication networks. *Physica A: Statistical Mechanics and its Applications*, 325(3):577–600, 2003.
- [148] Wolfram Krause, Ingmar Glauche, Rudolf Sollacher, and Martin Greiner. Impact of network structure on the capacity of wireless multihop ad hoc communication. *Physica A: Statistical Mechanics and its Applications*, 338(3):633–658, 2004.
- [149] Jonathan F Donges, H CH Schultz, Norbert Marwan, Yong Zou, and Juergen Kurths. Investigating the topology of interacting networks. *The European Physical Journal B-Condensed Matter and Complex Systems*, 84(4):635–651, 2011.
- [150] Jie Zhang, Junfeng Sun, Xiaodong Luo, Kai Zhang, Tomomichi Nakamura, and Michael Small. Characterizing pseudoperiodic time series through the complex network approach. *Physica D: Nonlinear Phenomena*, 237(22):2856–2865, 2008.
- [151] Xiaoke Xu, Jie Zhang, and Michael Small. Superfamily phenomena and motifs of networks induced from time series. *Proceedings of the National Academy of Sciences*, 105(50):19601–19605, 2008.
- [152] Michael Small, Jie Zhang, and Xiaoke Xu. Transforming time series into complex networks. In *Complex Sciences*, pages 2078–2089. Springer, 2009.
- [153] Jonathan F Donges, Jobst Heitzig, Reik V Donner, and Jürgen Kurths. Analytical framework for recurrence network analysis of time series. *Physical Review E*, 85(4):046105, 2012.
- [154] Reik V Donner, Yong Zou, Jonathan F Donges, Norbert Marwan, and Jürgen Kurths. Ambiguities in recurrence-based complex network representations of time series. *Physical Review E*, 81(1):015101, 2010.

- [155] Murray A Beauchamp. An improved index of centrality. *Behavioral Science*, 10(2):161–163, 1965.
- [156] Gert Sabidussi. The centrality index of a graph. *Psychometrika*, 31(4):581–603, 1966.
- [157] John P. Scott. *Social Network Analysis: A Handbook*. SAGE Publications, January 2000.
- [158] Stanley Wasserman. *Social network analysis: Methods and applications*, volume 8. Cambridge university press, 1994.
- [159] Linton C. Freeman. A Set of Measures of Centrality Based on Betweenness. *Sociometry*, 40(1):35–41, March 1977.
- [160] Thomas Schank and Dorothea Wagner. *Approximating clustering-coefficient and transitivity*. Universität Karlsruhe, Fakultät für Informatik, 2004.
- [161] Alain Barrat and Martin Weigt. On the properties of small-world network models. *The European Physical Journal B-Condensed Matter and Complex Systems*, 13(3):547–560, 2000.
- [162] Mark EJ Newman, Duncan J Watts, and Steven H Strogatz. Random graph models of social networks. *Proceedings of the National Academy of Sciences*, 99(suppl 1):2566–2572, 2002.
- [163] Reik V Donner, Jobst Heitzig, Jonathan F Donges, Yong Zou, Norbert Marwan, and Jürgen Kurths. The geometry of chaotic dynamics—a complex network perspective. *The European Physical Journal B-Condensed Matter and Complex Systems*, 84(4):653–672, 2011.
- [164] Mark EJ Newman. Assortative mixing in networks. *Physical review letters*, 89(20):208701, 2002.
- [165] Yong Zou, Reik V Donner, Jonathan F Donges, Norbert Marwan, and Jürgen Kurths. Identifying complex periodic windows in continuous-time dynamical systems using recurrence-based methods. *Chaos: An Interdisciplinary Journal of Nonlinear Science*, 20(4):043130, 2010.
- [166] Jan H Feldhoff, Reik V Donner, Jonathan F Donges, Norbert Marwan, and Jürgen Kurths. Geometric detection of coupling directions by means of inter-system recurrence networks. *Physics Letters A*, 376(46):3504–3513, 2012.
- [167] JH Feldhoff, Reik V Donner, Jonathan F Donges, Norbert Marwan, and Jürgen Kurths. Geometric signature of complex synchronisation scenarios. *EPL (Europhysics Letters)*, 102(3):30007, 2013.

- [168] Marc Wiedermann, Jonathan F Donges, Jobst Heitzig, and Jürgen Kurths. Node-weighted interacting network measures improve the representation of real-world complex systems. *EPL (Europhysics Letters)*, 102(2):28007, 2013.
- [169] Y Zou, J Heitzig, RV Donner, JF Donges, JD Farmer, R Meucci, S Euzzor, N Marwan, and J Kurths. Power-laws in recurrence networks from dynamical systems. *EPL (Europhysics Letters)*, 98(4):48001, 2012.
- [170] JF Donges, RV Donner, K Rehfeld, N Marwan, MH Trauth, and J Kurths. Identification of dynamical transitions in marine palaeoclimate records by recurrence network analysis. *Nonlinear Processes in Geophysics*, 18(5):545–562, 2011.
- [171] Jan H Feldhoff, Stefan Lange, Jan Volkholz, Jonathan F Donges, Jürgen Kurths, and Friedrich-Wilhelm Gerstengarbe. Complex networks for climate model evaluation with application to statistical versus dynamical modeling of south american climate. *Climate Dynamics*, pages 1–15.
- [172] JF Donges, RV Donner, N Marwan, SFM Breitenbach, K Rehfeld, and J Kurths. Nonlinear regime shifts in holocene asian monsoon variability: potential impacts on cultural change and migratory patterns. *Climate of the Past Discussions*, 10(2):895–975, 2014.
- [173] Zhong-Ke Gao, Xin-Wang Zhang, Meng Du, and Ning-De Jin. Recurrence network analysis of experimental signals from bubbly oil-in-water flows. *Physics Letters A*, 377(6):457–462, 2013.
- [174] Yong Zou, Reik V Donner, Mahesh Wickramasinghe, István Z Kiss, Michael Small, and Jürgen Kurths. Phase coherence and attractor geometry of chaotic electrochemical oscillators. *Chaos: An Interdisciplinary Journal of Nonlinear Science*, 22(3):033130, 2012.
- [175] Fuyuan Liao and Yih-Kuen Jan. Using recurrence network approach to quantify nonlinear dynamics of skin blood flow in response to loading pressure. In *Engineering in Medicine and Biology Society (EMBC), 2012 Annual International Conference of the IEEE*, pages 4196–4199. IEEE, 2012.
- [176] GM Ramírez Ávila, A Gapelyuk, N Marwan, H Stepan, J Kurths, Th Walther, and N Wessel. Classifying healthy women and preeclamptic patients from cardiovascular data using recurrence and complex network methods. *Autonomic Neuroscience*, 178(1):103–110, 2013.

- [177] Gonzalo Marcelo Ramírez Ávila, Andrej Gapelyuk, Norbert Marwan, Thomas Walther, Holger Stepan, Jürgen Kurths, and Niels Wessel. Classification of cardiovascular time series based on different coupling structures using recurrence networks analysis. *Philosophical Transactions of the Royal Society A: Mathematical, Physical and Engineering Sciences*, 371(1997):20110623, 2013.
- [178] Zhong-Ke Gao, Xin-Wang Zhang, Ning-De Jin, Norbert Marwan, and Jürgen Kurths. Multivariate recurrence network analysis for characterizing horizontal oil-water two-phase flow. *Physical Review E*, 88(3):032910, 2013.
- [179] Richard Caton. Electrical currents of the brain. *The Journal of Nervous and Mental Disease*, 2(4):610, 1875.
- [180] Charles Shagass. *Evoked brain potentials in psychiatry*. Springer Science & Business Media, 1972.
- [181] Hans Berger. Über das elektrenkephalogramm des menschen. *European Archives of Psychiatry and Clinical Neuroscience*, 87(1):527–570, 1929.
- [182] Edgar D Adrian and BHC Matthews. The interpretation of potential waves in the cortex. *The Journal of physiology*, 81(4):440–471, 1934.
- [183] Fernando Lopes da Silva. Eeg: Origin and measurement. In *EEG-fMRI*, pages 19–38. Springer, 2010.
- [184] Paul L Nunez and Ramesh Srinivasan. *Electric fields of the brain: the neurophysics of EEG*. Oxford university press, 2006.
- [185] RG Andrzejak, G Widman, K Lehnertz, C Rieke, P David, and CE Elger. The epileptic process as nonlinear deterministic dynamics in a stochastic environment: an evaluation on mesial temporal lobe epilepsy. *Epilepsy research*, 44(2):129–140, 2001.
- [186] Thomas Elbert, William J Ray, Zbigniew J Kowalik, James E Skinner, Karl Eugen Graf, and Niels Birbaumer. Chaos and physiology: deterministic chaos in excitable cell assemblies. *Physiological Reviews*, 74(1):1–47, 1994.
- [187] S Micheloyannis, N Flitzanis, E Papanikolaou, M Bourkas, D Terzakis, S Arvanitis, and CJ Stam. Usefulness of non-linear eeg analysis. *Acta neurologica scandinavica*, 97(1):13–19, 1998.
- [188] Leon D Iasemidis. Epileptic seizure prediction and control. *Biomedical Engineering, IEEE Transactions on*, 50(5):549–558, 2003.

- [189] Robert S Fisher, Walter van Emde Boas, Warren Blume, Christian Elger, Pierre Genton, Phillip Lee, and Jerome Engel. Epileptic seizures and epilepsy: definitions proposed by the international league against epilepsy (ilae) and the international bureau for epilepsy (ibe). *Epilepsia*, 46(4):470–472, 2005.
- [190] Jerome Engel. A practical guide for routine eeg studies in epilepsy. *Journal of Clinical Neurophysiology*, 1(2):109–142, 1984.
- [191] Soheyl Noachtar and Jan Rémi. The role of eeg in epilepsy: a critical review. *Epilepsy & Behavior*, 15(1):22–33, 2009.
- [192] Marc R Numer. Frequency analysis and topographic mapping of eeg and evoked potentials in epilepsy. *Electroencephalography and clinical neurophysiology*, 69(2):118–126, 1988.
- [193] Antonio Gambardella, Jean Gotman, Fernando Cendes, and Frederick Andermann. Focal intermittent delta activity in patients with mesiotemporal atrophy: a reliable marker of the epileptogenic focus. *Epilepsia*, 36(2):122–129, 1995.
- [194] Miles E Drake, Hosi Padamadan, and Sharon A Newell. Interictal quantitative eeg in epilepsy. *Seizure*, 7(1):39–42, 1998.
- [195] K Lehnertz and CE Elger. Spatio-temporal dynamics of the primary epileptogenic area in temporal lobe epilepsy characterized by neuronal complexity loss. *Electroencephalography and clinical Neurophysiology*, 95(2):108–117, 1995.
- [196] B Weber, K Lehnertz, CE Elger, and HG Wieser. Neuronal complexity loss in interictal eeg recorded with foramen ovale electrodes predicts side of primary epileptogenic area in temporal lobe epilepsy: a replication study. *Epilepsia*, 39(9):922–927, 1998.
- [197] PE Rapp, ID Zimmerman, AM Albano, GC Deguzman, and NN Greenbaun. Dynamics of spontaneous neural activity in the simian motor cortex: The dimension of chaotic neurons. *Physics Letters A*, 110(6):335–338, 1985.
- [198] PE Rapp, ID Zimmerman, AM Albano, NN Greenbaun, TR Bashore, et al. Experimental studies of chaotic neural behavior: cellular activity and electroencephalographic signals. In *Nonlinear oscillations in biology and chemistry*, pages 175–205. Springer, 1986.
- [199] A Babloyantz. Evidence of chaotic dynamics of brain activity during the sleep cycle. In *Dimensions and entropies in chaotic systems*, pages 241–245. Springer, 1986.

- [200] CC Canavier, DA Baxter, JW Clark, and JH Byrne. Nonlinear dynamics in a model neuron provide a novel mechanism for transient synaptic inputs to produce long-term alterations of postsynaptic activity. *Journal of neurophysiology*, 69(6):2252–2257, 1993.
- [201] CC Canavier, JW Clark, and JH Byrne. Routes to chaos in a model of a bursting neuron. *Biophysical journal*, 57(6):1245, 1990.
- [202] T Ree Chay and JOHN Rinzel. Bursting, beating, and chaos in an excitable membrane model. *Biophysical Journal*, 47(3):357, 1985.
- [203] George J Mpitsos, Robert M Burton, H Clayton Creech, and Seppo O Soynila. Evidence for chaos in spike trains of neurons that generate rhythmic motor patterns. *Brain Research Bulletin*, 21(3):529–538, 1988.
- [204] A Destexhe, JA Sepulchre, and A Babloyantz. A comparative study of the experimental quantification of deterministic chaos. *Physics letters A*, 132(2):101–106, 1988.
- [205] Ivan Dvorak and Jaromir Siska. On some problems encountered in calculating the correlation dimension of eeg. Technical report, International Centre for Theoretical Physics, Trieste (Italy), 1986.
- [206] L Rensing, U an der Heiden, and MC Mackey. Temporal disorder in human oscillatory systems. *Springer Series in Synergetics*, 36, 1987.
- [207] GOTTFRIED MAYER-KRESS and Scott P Layne. Dimensionality of the human electroencephalogram. *Annals of the New York Academy of Sciences*, 504(1):62–87, 1987.
- [208] G Mayer-Kress, F Eugene Yates, Laurel Benton, M Keidel, W Tirsch, SJ Pöppl, and K Geist. Dimensional analysis of nonlinear oscillations in brain, heart, and muscle. *Mathematical Biosciences*, 90(1):155–182, 1988.
- [209] Paul E Rapp, Theodore R Bashore, Jacques M Martinerie, AM Albano, ID Zimmerman, and Alistair I Mees. Dynamics of brain electrical activity. *Brain Topography*, 2(1-2):99–118, 1989.
- [210] GW Frank, T Lookman, MAH Nerenberg, C Essex, J Lemieux, and W Blume. Chaotic time series analyses of epileptic seizures. *Physica D: Nonlinear Phenomena*, 46(3):427–438, 1990.
- [211] James Theiler. Spurious dimension from correlation algorithms applied to limited time-series data. *Physical Review A*, 34(3):2427, 1986.

- [212] Jan Pieter Pijn, Jan Van Neerven, André Noest, and Fernando H Lopes da Silva. Chaos or noise in eeg signals; dependence on state and brain site. *Electroencephalography and clinical Neurophysiology*, 79(5):371–381, 1991.
- [213] James Theiler. Detecting nonlinear structure in time series. Technical report, Los Alamos National Lab., NM (United States). Funding organisation: USDOE, Washington, DC (United States), 1991.
- [214] SARB Rombouts, RWM Keunen, and CJ Stam. Investigation of nonlinear structure in multichannel eeg. *Physics Letters A*, 202(5):352–358, 1995.
- [215] James Theiler and Paul E Rapp. Re-examination of the evidence for low-dimensional, nonlinear structure in the human electroencephalogram. *Electroencephalography and clinical Neurophysiology*, 98(3):213–222, 1996.
- [216] Walter S Pritchard, Dennis W Duke, and Kelly K Kriebel. Dimensional analysis of resting human eeg ii: Surrogate-data testing indicates nonlinearity but not low-dimensional chaos. *Psychophysiology*, 32(5):486–491, 1995.
- [217] Alan Wolf, Jack B Swift, Harry L Swinney, and John A Vastano. Determining lyapunov exponents from a time series. *Physica D: Nonlinear Phenomena*, 16(3):285–317, 1985.
- [218] Masaki Sano and Yasuji Sawada. Measurement of the lyapunov spectrum from a chaotic time series. *Physical review letters*, 55(10):1082, 1985.
- [219] Michael T Rosenstein, James J Collins, and Carlo J De Luca. A practical method for calculating largest lyapunov exponents from small data sets. *Physica D: Nonlinear Phenomena*, 65(1):117–134, 1993.
- [220] Leonidas D Iasemidis and J CHRIS Sackellares. The evolution with time of the spatial distribution of the largest lyapunov exponent on the human epileptic cortex. *Measuring chaos in the human brain*, pages 49–82, 1991.
- [221] Leonidas D Iasemidis, J Chris Sackellares, Hitten P Zaveri, and William J Williams. Phase space topography and the lyapunov exponent of electrocorticograms in partial seizures. *Brain topography*, 2(3):187–201, 1990.
- [222] Laurent Pezard, Jacques Martinerie, Johannes Müller-Gerking, Francisco J Varela, and Bernard Renault. Entropy quantification of human brain spatio-temporal dynamics. *Physica D: Nonlinear Phenomena*, 96(1):344–354, 1996.
- [223] David J Wales. Calculating the rate of loss of information from chaotic time series by forecasting. 1991.

- [224] ME Torres, MM Anino, LG Gamero, and MA Gemignani. Automatic detection of slight changes in nonlinear dynamical systems using multiresolution entropy tools. *International Journal of Bifurcation and Chaos*, 11(04):967–981, 2001.
- [225] Hasan Ocak. Automatic detection of epileptic seizures in eeg using discrete wavelet transform and approximate entropy. *Expert Systems with Applications*, 36(2):2027–2036, 2009.
- [226] N Kannathal, Min Lim Choo, U Rajendra Acharya, and PK Sadasivan. Entropies for detection of epilepsy in eeg. *Computer methods and programs in biomedicine*, 80(3):187–194, 2005.
- [227] Iman Veisi, Naser Pariz, and Ali Karimpour. Fast and robust detection of epilepsy in noisy eeg signals using permutation entropy. In *Bioinformatics and Bioengineering, 2007. BIBE 2007. Proceedings of the 7th IEEE International Conference on*, pages 200–203. IEEE, 2007.
- [228] Nadia Mammone and Francesco Carlo Morabito. Analysis of absence seizure eeg via permutation entropy spatio-temporal clustering. In *Neural Networks (IJCNN), The 2011 International Joint Conference on*, pages 1417–1422. IEEE, 2011.
- [229] Naoto Burioka, Germaine Cornélissen, Yoshihiro Maegaki, Franz Halberg, Daniel T Kaplan, Masanori Miyata, Yasushi Fukuoka, Masahiro Endo, Hisashi Suyama, Yutaka Tomita, et al. Approximate entropy of the electroencephalogram in healthy awake subjects and absence epilepsy patients. *Clinical EEG and neuroscience*, 36(3):188–193, 2005.
- [230] Xiaoli Li, Gaoxian Ouyang, and Douglas A Richards. Predictability analysis of absence seizures with permutation entropy. *Epilepsy research*, 77(1):70–74, 2007.
- [231] Temujin Gautama, Danilo P. Mandic, and Marc M. Van Hulle. Indications of nonlinear structures in brain electrical activity. *Phys. Rev. E*, 67:046204, Apr 2003.
- [232] Ralph G Andrzejak, Florian Mormann, Guido Widman, Thomas Kreuz, Christian E Elger, and Klaus Lehnertz. Improved spatial characterization of the epileptic brain by focusing on nonlinearity. *Epilepsy research*, 69(1):30–44, 2006.
- [233] Xiaoli Li, Gaoxiang Ouyang, Xin Yao, and Xinping Guan. Dynamical characteristics of pre-epileptic seizures in rats with recurrence quantification analysis. *Physics Letters A*, 333(1):164–171, 2004.
- [234] Nitza Thomasson, Thomas J Hoeppepner, Charles L Webber, and Joseph P Zbilut. Recurrence quantification in epileptic eegs. *Physics Letters A*, 279(1):94–101, 2001.

- [235] Gaoxiang Ouyang, Lijuan Xie, Huanwen Chen, Xiaoli Li, Xinping Guan, and Huihua Wu. Automated prediction of epileptic seizures in rats with recurrence quantification analysis. In *Engineering in Medicine and Biology Society, 2005. IEEE-EMBS 2005. 27th Annual International Conference of the*, pages 153–156. IEEE, 2006.
- [236] U Rajendra Acharya, S Vinitha Sree, Subhagata Chattopadhyay, Wenwei Yu, and Peng Chuan Alvin Ang. Application of recurrence quantification analysis for the automated identification of epileptic eeg signals. *International journal of neural systems*, 21(03):199–211, 2011.
- [237] Sami El Boustani and Alain Destexhe. Brain dynamics at multiple scales: can one reconcile the apparent low-dimensional chaos of macroscopic variables with the seemingly stochastic behavior of single neurons? *International Journal of Bifurcation and Chaos*, 20(06):1687–1702, 2010.
- [238] Michel Le Van Quyen, Jacques Martinerie, Michel Baulac, and Francisco Varela. Anticipating epileptic seizures in real time by a non-linear analysis of similarity between eeg recordings. *Neuroreport*, 10(10):2149–2155, 1999.
- [239] Michael G Rosenblum, Arkady S Pikovsky, and Jürgen Kurths. Phase synchronization of chaotic oscillators. *Physical Review Letters*, 76(11):1804, 1996.
- [240] Florian Mormann, Klaus Lehnertz, Peter David, and Christian E Elger. Mean phase coherence as a measure for phase synchronization and its application to the eeg of epilepsy patients. *Physica D: Nonlinear Phenomena*, 144(3):358–369, 2000.
- [241] Michael G Rosenblum and Arkady S Pikovsky. Detecting direction of coupling in interacting oscillators. *Physical Review E*, 64(4):045202, 2001.
- [242] Yonghong Chen, Govindan Rangarajan, Jianfeng Feng, and Mingzhou Ding. Analyzing multiple nonlinear time series with extended granger causality. *Physics Letters A*, 324(1):26–35, 2004.
- [243] Dmitry A Smirnov and Ralph G Andrzejak. Detection of weak directional coupling: Phase-dynamics approach versus state-space approach. *Physical Review E*, 71(3):036207, 2005.
- [244] Björn Schelter, Matthias Winterhalder, Rainer Dahlhaus, Jürgen Kurths, and Jens Timmer. Partial phase synchronization for multivariate synchronizing systems. *Physical review letters*, 96(20):208103, 2006.
- [245] Nicola Ancona, Daniele Marinazzo, and Sebastiano Stramaglia. Radial basis function approach to nonlinear granger causality of time series. *Physical Review E*, 70(5):056221, 2004.

- [246] Thomas Schreiber. Measuring information transfer. *Physical review letters*, 85(2):461, 2000.
- [247] Matthäus Staniek and Klaus Lehnertz. Symbolic transfer entropy. *Physical Review Letters*, 100(15):158101, 2008.
- [248] Martin Vejmelka and Milan Paluš. Inferring the directionality of coupling with conditional mutual information. *Physical Review E*, 77(2):026214, 2008.
- [249] M Carmen Romano, Marco Thiel, Jürgen Kurths, and Celso Grebogi. Estimation of the direction of the coupling by conditional probabilities of recurrence. *Physical Review E*, 76(3):036211, 2007.
- [250] Otto E Rössler. An equation for continuous chaos. *Physics Letters A*, 57(5):397–398, 1976.
- [251] OE Rossler. An equation for hyperchaos. *Physics Letters A*, 71(2):155–157, 1979.
- [252] Jonathan F Donges, Jobst Heitzig, Boyan Beronov, Marc Wiedermann, Jakob Runge, Qing Yi Feng, Liubov Tupikina, Veronika Stolbova, Reik V Donner, Norbert Marwan, et al. Unified functional network and nonlinear time series analysis for complex systems science: The pyunicorn package. *arXiv preprint arXiv:1507.01571*, 2015.
- [253] Ruoxi Xiang, Jie Zhang, Xiao-Ke Xu, and Michael Small. Multiscale characterization of recurrence-based phase space networks constructed from time series. *Chaos: An Interdisciplinary Journal of Nonlinear Science*, 22(1):013107, 2012.
- [254] Osvaldo A Rosso, Laura C Carpi, Patricia M Saco, Martín Gómez Ravetti, Angelo Plastino, and Hilda A Larrondo. Causality and the entropy–complexity plane: Robustness and missing ordinal patterns. *Physica A: Statistical Mechanics and its Applications*, 391(1):42–55, 2012.
- [255] Temujin Gautama, Danilo P Mandic, and Marc M Van Hulle. Indications of nonlinear structures in brain electrical activity. *Physical Review E*, 67(4):046204, 2003.
- [256] Charles W Wang. *Nonlinear phenomena research perspectives*. Nova Publishers, 2007.
- [257] J Timmer. Power of surrogate data testing with respect to nonstationarity. *Physical Review E*, 58(4):5153, 1998.
- [258] JH Lucio, R Valdés, and LR Rodríguez. Improvements to surrogate data methods for nonstationary time series. *Physical Review E*, 85(5):056202, 2012.

- [259] RG Andrzejak, D Chicharro, K Lehnertz, and F Mormann. Using bivariate signal analysis to characterize the epileptic focus: The benefit of surrogates. *Physical Review E*, 83(4):046203, 2011.
- [260] R Quiñan Quiroga, S Blanco, OA Rosso, H Garcia, and A Rabinowicz. Searching for hidden information with gabor transform in generalized tonic-clonic seizures. *Electroencephalography and clinical Neurophysiology*, 103(4):434–439, 1997.
- [261] Herbert Henri Jasper. The ten twenty electrode system of the international federation. *Electroencephalography and clinical neurophysiology*, 10:371–375, 1958.
- [262] SH Scott. Apparatus for measuring and perturbing shoulder and elbow joint positions and torques during reaching. *J Neurosci Methods*, 89:119–127, July 1999.
- [263] Aaron J Suminski, Dennis C Tkach, and Nicholas G Hatsopoulos. Exploiting multiple sensory modalities in brain-machine interfaces. *Neural Networks*, 22(9):1224–1234, 2009.
- [264] Kazutaka Takahashi, Sanggyun Kim, Todd P Coleman, Kevin A Brown, Aaron J Suminski, Matthew D Best, and Nicholas G Hatsopoulos. Large-scale spatiotemporal spike patterning consistent with wave propagation in motor cortex. *Nature communications*, 6, 2015.
- [265] Abbas Golestani and Robin Gras. Can we predict the unpredictable? *Scientific reports*, 4, 2014.
- [266] Shouyi Wang, Wanpracha Chaovalitwongse, Simon Wong, et al. Online seizure prediction using an adaptive learning approach. *Knowledge and Data Engineering, IEEE Transactions on*, 25(12):2854–2866, 2013.
- [267] Martin C Casdagli, Leonidas D Iasemidis, Robert S Savit, Robin L Gilmore, Steven N Roper, and J Chris Sackellares. Non-linearity in invasive eeg recordings from patients with temporal lobe epilepsy. *Electroencephalography and clinical Neurophysiology*, 102(2):98–105, 1997.
- [268] Vernon L Towle, Ibrahim Syed, Catherine Berger, Robert Grzesczczuk, John Milton, Robert K Erickson, Philip Cogen, Eric Berkson, and Jean-Paul Spire. Identification of the sensory/motor area and pathologic regions using ecog coherence. *Electroencephalography and clinical neurophysiology*, 106(1):30–39, 1998.
- [269] Hitten P Zaveri, Steven M Pincus, Irina I Goncharova, Robert B Duckrow, Dennis D Spencer, and Susan S Spencer. Localization-related epilepsy exhibits significant connectivity away from the seizure-onset area. *Neuroreport*, 20(9):891–895, 2009.

- [270] Christian Rummel, Markus Müller, Gerold Baier, Frédérique Amor, and Kaspar Schindler. Analyzing spatio-temporal patterns of genuine cross-correlations. *Journal of neuroscience methods*, 191(1):94–100, 2010.
- [271] Eshel Ben-Jacob, Stefano Boccaletti, Anna Pomyalov, Itamar Procaccia, and Vernon L Towle. Detecting and localizing the foci in human epileptic seizures. *Chaos: An Interdisciplinary Journal of Nonlinear Science*, 17(4):043113, 2007.
- [272] Gaele Bettus, Fabrice Wendling, Maxime Guye, Luc Valton, Jean Régis, Patrick Chauvel, and Fabrice Bartolomei. Enhanced eeg functional connectivity in mesial temporal lobe epilepsy. *Epilepsy research*, 81(1):58–68, 2008.
- [273] Michel Le Van Quyen, Jacques Martinerie, Claude Adam, and Francisco J Varela. Unstable periodic orbits in human epileptic activity. *Physical Review E*, 56(3):3401, 1997.
- [274] Florian Mormann, Ralph G Andrzejak, Thomas Kreuz, Christoph Rieke, Peter David, Christian E Elger, and Klaus Lehnertz. Automated detection of a pre seizure state based on a decrease in synchronization in intracranial electroencephalogram recordings from epilepsy patients. *Physical Review E*, 67(2):021912, 2003.
- [275] Michel Le Van Quyen, Jacques Martinerie, Vincent Navarro, Paul Boon, Michel D’Havé, Claude Adam, Bernard Renault, Francisco Varela, and Michel Baulac. Anticipation of epileptic seizures from standard eeg recordings. *The Lancet*, 357(9251):183–188, 2001.
- [276] JF Donges, RV Donner, Norbert Marwan, Sebastian FM Breitenbach, Kira Rehfeld, and Jürgen Kurths. Non-linear regime shifts in holocene asian monsoon variability: potential impacts on cultural change and migratory patterns. *Climate of the Past*, (11):709–741, 2015.
- [277] Zhongke Gao and Ningde Jin. Flow-pattern identification and nonlinear dynamics of gas-liquid two-phase flow in complex networks. *Physical Review E*, 79(6):066303, 2009.
- [278] Pen-Ning Yu, Min-Chi Hsiao, Dong Song, Charles Y Liu, Christi N Heck, David Millett, and Theodore W Berger. Unstable periodic orbits in human epileptic hippocampal slices. In *Engineering in Medicine and Biology Society (EMBC), 2014 36th Annual International Conference of the IEEE*, pages 5800–5803. IEEE, 2014.

Part IV

Original publications

Puthanmadam Subramaniam, N., Donges, J. and Hyttinen, J.

Signatures of chaotic and stochastic dynamics using ε -recurrence networks

Proceedings of the Royal Society of London A: Mathematical, Physical and Engineering Sciences, 471(2183):20150349, 2015.

Reprinted with permission from the publisher.



Article submitted to journal

Subject Areas:

xxxxx, xxxxx, xxxxx

Keywords:

xxxx, xxxx, xxxx

Author for correspondence:

Insert corresponding author name

e-mail: xxx@xxxx.xx.xx

Signatures of chaotic and stochastic dynamics uncovered with ε -recurrence networks

N P Subramaniam^{1,3}, J F Donges^{2,4} and J Hyttinen^{1,3}

¹ Department of Electronics and Communications Engineering, Tampere University of Technology, Tampere, Finland

² Potsdam Institute for Climate Impact Research, Potsdam, Germany

³ BioMediTech, Tampere, Finland

⁴ Planetary Boundary Research Lab, Stockholm University, Stockholm, Sweden.

An old and important problem in the field of nonlinear time series analysis entails the distinction between chaotic and stochastic dynamics. Recently, ε -recurrence networks have been proposed as a tool to analyse the structural properties of a time series. In this paper, we propose the applicability of local and global ε -recurrence network measures to distinguish between chaotic and stochastic dynamics using paradigmatic model systems like the Lorenz system, and, the chaotic and hyper-chaotic Rössler system. Additionally, we also demonstrate the effect of increasing levels of noise on these network measures and provide a real-world application of analysing electroencephalographic data comprising of epileptic seizures. Our results show that both local and global ε -recurrence network measures are sensitive to the presence of unstable periodic orbits and other structural features associated with chaotic dynamics that are otherwise absent in stochastic dynamics. These network measures are still robust at high noise levels and short data lengths. Furthermore, ε -recurrence network analysis of the real-world epileptic data revealed the capability of these network measures in capturing dynamical transitions using short window sizes. ε -recurrence network analysis is a powerful method in uncovering the signatures of chaotic and stochastic dynamics based on the geometric properties of time series.

© The Authors. Published by the Royal Society under the terms of the Creative Commons Attribution License <http://creativecommons.org/licenses/by/4.0/>, which permits unrestricted use, provided the original author and source are credited.

1. Introduction

Distinguishing chaotic from stochastic processes is an important problem arising in many fields ranging from biology and physics to ecology and finance. In this paper, we propose an approach based on ε -recurrence networks [1], obtained by transforming time series into complex networks, to distinguish between chaotic and stochastic dynamics. Numerous approaches have been proposed to solve this critical issue of distinguishing between stochastic and chaotic dynamics, which is laced with several challenges since both chaotic and stochastic processes share some common properties, e.g., a broadband power spectrum, delta-like autocorrelation function and long-term irregular behavior [2,3]. It may even be practically impossible to distinguish high-dimensional chaos from a stochastic process. Since in a chaotic system, the time evolution of two nearby trajectories will diverge exponentially fast compared to a stochastic system where the separation is randomly distributed [4], methods based on short-term predictability have been applied to distinguish chaos from noise [5,6]. Thus, for a chaotic time series, the accuracy of forecast should decrease with increasing prediction-time interval and for a stochastic time series this accuracy should be independent of the prediction-time interval [6]. Kaplan and Glass [7,8] proposed a test for determinism based on the measurement of average directional vectors in a coarse-grained phase space. This test is based on the observation that the tangents to the trajectories of a deterministic system, passing through a small region in phase space, will be well aligned, i.e., oriented in the same direction, a behavior not observed in stochastic dynamics [7,8]. Another line of approach borrows from the concept that a chaotic attractor should have finite, non-integer values for fractal dimensions, while stochastic processes must theoretically exhibit infinite dimensions. This traditional view was challenged by Osborne and Provenzale [9], when they demonstrated that finite correlation dimension could be obtained from a simple class of colored random noise characterized by power-law spectra. Recently, quantifiers from information theory have been used to address the issue of distinguishing between chaotic and stochastic dynamics, leading to some interesting results [10]. Rosso *et al.* [3] introduced the complexity-entropy causality plane, a two-dimensional representation space that relates the two information theoretic quantities namely entropy and complexity, to distinguish between stochastic and chaotic dynamics. By explicitly including the time scale notion, Zunino *et al.* [2] proposed the multiscale complexity-entropy plane to identify the time scales where stochastic and chaotic components govern the system's dynamics. The classification of stochastic or chaotic character of a given time series at different resolution scale using entropic analysis was first proposed by Cencini *et al.* [11]. Olivares *et al.* [12,13] also proposed a combination of two information theoretic quantities, the Shannon entropy and the Fisher information, to obtain the Shannon-Fisher causality ($S \times \mathcal{F}$) plane and showed that stochastic and chaotic dynamics map to different locations on this two-dimensional plane.

By bridging the gap between nonlinear time series analysis and complex network theory, methods to transform a time series into a complex network comprising of nodes which represent the state vectors in phase space and edges that are defined based on some criteria such as mutual closeness or transition probabilities, have emerged [14,15]. Different classes of such time-series based complex networks exist like proximity networks [1,14,16–18], transition networks [19] or visibility graphs [20,21]. A comprehensive review on these network-types is given elsewhere [14]. The underlying principle in this approach is to characterize the topology of the resultant network using tools from graph theory to gain insights into the dynamics underlying the time series. Complex network-based univariate and multivariate time series analysis has been successfully applied in different fields including climatology [1,15,22,23] fluid dynamics [24–27] and neuroscience [28–31], to cite a few.

Lacasa and Toral [4] used horizontal visibility graphs (HVG) [32], a geometrically simpler version of the visibility graph algorithm, to distinguish between chaotic and stochastic (correlated and uncorrelated) dynamics based on the node degree distribution (specifically the slope of the logarithm of the degree distribution) of the resultant networks. Recently, Ravetti *et al.* [10]

showed that the HVG approach is sensitive to the scaling zone and combined the HVG approach with information theory quantifiers (the $\mathcal{S} \times \mathcal{F}$ plane) that leads to a better characterization of deterministic and stochastic dynamics.

Recurrence is a fundamental property of dynamical systems [33] and using the recurrence matrix derived from a time series, one can define a recurrence network by reinterpreting the recurrence matrix as an adjacency matrix of a complex, undirected network [1,14]. Xu *et al.* first proposed the concept of transforming a time series into an undirected complex network [34]. Such networks, known as recurrence networks, belong to the class of proximity networks where the existence of an edge in the network is defined based on the mutual closeness between two state vectors (nodes). Since such a recurrence matrix can be defined in many ways, depending on the chosen neighborhood criteria there are different types of recurrence networks [14] namely k -nearest neighbor recurrence networks [18,35], adaptive nearest neighbor recurrence networks [34] and ε -recurrence networks [1,14]. Specifically, the neighborhood can be defined in terms of either fixed number of edges (k -nearest or adaptive nearest neighbor recurrence networks) [18,34–36] or fixed phase space distance (ε -recurrence networks) centered around a node i (i.e., a state vector in phase space) [1]. All the nodes that fall within this volume are connected to the node i by forming an edge. ε -recurrence networks are both symmetric and undirected. In this work, we will be dealing only with ε -recurrence networks.

Over the recent years, ε -recurrence networks have gained much popularity and they have been thoroughly analyzed and applied using data from simulated as well as real world systems. Using model systems, Donner *et al.* [14] studied the ε -dependence of local and global network properties. Donges *et al.* [37] provided a thorough analytical framework for ε -recurrence network analysis of periodic/quasiperiodic dynamics, chaotic maps, stochastic processes and higher-dimensional symmetric sets. Zou *et al.* [38] showed that global network measures like global clustering coefficient \mathcal{C} and average path length \mathcal{L} derived from ε -recurrence networks can be used to distinguish between periodic and chaotic dynamics in both discrete and continuous-time dynamical systems. Furthermore, using the Rössler system, they showed that these network measures can reliably identify complex periodic windows in parameter space. Since an ε -recurrence network can be considered as a random geometric graph, the distribution of the nodes in the space where the network is embedded is determined by the probability density function of the system's invariant measure [37]. Furthermore, the edges are formed only between those nodes that are spatially close to each other as determined by some distance threshold. Thus, based on the theory of random geometric graphs [39], Donner *et al.* [40] provided the relationship between geometric properties of a dynamical system and the transitivity properties like the local clustering coefficient and transitivity of the associated ε -recurrence networks. Specifically, it was shown that these transitivity measures can be considered as an alternative notion of fractal dimension of the dynamical system under study [40]. Also, it has been demonstrated that the ε -recurrence networks display power-law degree distributions and the scaling exponent of the degree distribution is related to system's invariant density [38]. It has also been demonstrated that the transitivity properties can reliably detect unstable periodic orbits (UPOs) in model systems [14].

Since transitivity properties can be understood as some notion of fractal dimension, the associated transitivity dimension should exhibit non-integer values for dissipative chaotic systems. This feature could be particularly useful in distinguishing whether the observed dynamics is chaotic or stochastic. Thus, in case of a stochastic process (which theoretically exhibits infinite dimensions), the estimated dimension should be limited by the phase space dimension. Characterizing and differentiating a chaotic process from a stochastic process based on the transitivity dimension has not been studied so far. It was shown by Donges *et al.* [37] that ε -recurrence network measures cannot distinguish between stochastic and deterministic process if both have identical invariant density distribution in phase space. This observation was based on the analytical computation of continuous ε -recurrence network measures - transitivity, clustering coefficient, average path length and betweenness for the 1D-Bernoulli map and uniform noise.

This observation, as mentioned by the authors themselves, holds true when embedding is not used and it has been proposed that an additional embedding can overcome this shortcoming [14]. One reason for this could be the difference in the structure of chaotic attractors, primarily due to the presence of densely packed unstable periodic orbits, compared to time-delay embedded stochastic processes which fail to recover this structure. However, this has not been studied or tested elaborately using well known model systems. Thus, we hypothesize that the transitivity dimension of the chaotic attractors should be lower than that of stochastic dynamics, which should have a transitivity dimension close to the embedding dimension. Previously we have shown that by combining ε -recurrence network measures with iterative amplitude adjusted Fourier transform (iAAFT) surrogates [41] which represent stationary, linearly correlated, stochastic processes (colored Gaussian), different classes of electroencephalography (EEG) data can be distinguished [29]. Particularly we observed that the rejection rate of the null hypothesis based on iAAFT surrogates for network measures the global clustering coefficient \mathcal{C} and the average path length \mathcal{L} was higher for pathological EEG compared to normal EEG [29]. However, a rigorous evaluation of the ability of ε -recurrence network measures to particularly distinguish deterministic from stochastic processes and of how embedding alters the phase space distribution of these processes is missing. Also, a careful consideration of the effects of noise on the recurrence networks to distinguish between stochastic and chaotic process and the impact of data length on such distinction has not been addressed so far. In particular, detecting and distinguishing chaotic from stochastic processes could pose great challenge when the data is short and noisy. Since an important advantage of network-based time series analysis is that network measures can be reliably estimated from rather short time series with high confidence, we hypothesize that such an approach could be particularly useful in addressing this challenge compared to other classical approaches of nonlinear time series analysis.

Using ε -recurrence networks constructed from stochastic and chaotic dynamics, we investigate the applicability of global measures - transitivity dimension, assortativity, average path length and the vertex based measures - local clustering coefficient, betweenness centrality, closeness centrality and degree centrality in distinguishing deterministic (chaos) processes from stochastic processes. As an example of low and high dimensional chaotic systems, we use Lorenz, chaotic Rössler and 4D Rössler systems respectively. Specifically, we use the x -component of these systems and the corresponding iAAFT surrogates (stochastic, linearly correlated process, sharing the power spectrum and amplitude distribution with the original chaotic time series) derived from the x -component to construct ε -recurrence networks representing chaotic and stochastic dynamics, respectively. We construct the ε -recurrence networks representing chaotic and stochastic dynamics for varying embedding dimensions and recurrence rates (related to the threshold ε). Additionally, we also investigate the effect of increasing noise levels and data length on the network measures and their distributions (in case of vertex-based measures) for ε -recurrence networks derived from chaotic dynamics. We compare our results with complexity-entropy plane approach proposed in [3]. In addition to the theoretical simulation described above, we also present results from the application of ε -recurrence network analysis to epileptic EEG data, which contains pre-seizure, seizure and post-seizure segments. Here, we investigate if ε -recurrence network measures, when applied to rather short window-sizes can track dynamical changes underlying such real-world, noisy biological signals.

2. Recurrence networks and measures

(a) Recurrence networks

Given a phase space vector, a recurrence matrix can be defined as [33]

$$R(i, j) = \Theta(\varepsilon - \|\mathbf{x}_i - \mathbf{x}_j\|), \quad (2.1)$$

where ε is a predefined global threshold, \mathbf{x}_i and \mathbf{x}_j are the m -dimensional phase space vectors at time t_i and t_j (with $t_j < t_i$) respectively. If only the univariate time series is available, then

one can reconstruct the phase space vector using time-delay embedding [42], $\mathbf{x}_i = (x(t_i), x(t_i + \tau), \dots, x(t_i + (m-1)\tau))$. Here m is the embedding dimension and τ is the optimal time lag that can be determined using standard methods like false nearest neighbor and first minimum of auto-mutual information function respectively [43].

One can define an adjacency matrix A of a recurrence network using the recurrence matrix defined above as follows [1]

$$A(i, j) = R(i, j) - \delta(i, j), \quad (2.2)$$

where $\delta(i, j)$ is the Kronecker delta, introduced to avoid artificial self-loops [33]. Each vertex i of a recurrence network represents a state vector \mathbf{x}_i and the edges between the nodes are formed based on their mutual closeness as defined by euclidean or manhattan or maximum norm. Note that due to the way recurrence networks are formed, they can be considered as random geometric graphs [37]. In this work, we use the maximum norm as the distance norm. Furthermore, instead of fixing ε , we fix the recurrence rate $RR = \frac{1}{N^2} \sum_{i,j=1}^N R(i, j)$, where N is the number of state vectors, since we are essentially interested in comparing the properties of systems (chaotic and stochastic) with different phase space diameters [14]. Thus, we vary RR from 0.01 to 0.05 in steps of 0.01. Additionally, we also vary the embedding dimension m from 1 to 5.

(b) Recurrence network measures

(i) Degree centrality

Degree centrality of a vertex i can be defined as the number of vertices directly connected to i . It is given as

$$k_i = \sum_{j=1}^N A(i, j). \quad (2.3)$$

This measure can be normalized to yield the local connectivity, which describes the local phase space density [14] i.e., the local recurrence rate

$$\rho_i = \frac{k_i}{N-1}, \quad (2.4)$$

where N is the the data length (or the embedded state vectors).

(ii) Closeness centrality

Closeness centrality can be defined as the inverse of the average geodesic distance (i.e., the length of the shortest path) between a vertex i and all other vertices in a network. According to this definition, a vertex is considered central, if it is close to all the other vertices in the network. Let $d(i, j)$ be the shortest-path between two vertices i and j . The closeness centrality of the vertex i is then defined as [44]

$$c_i = \frac{N-1}{\sum_{j=1}^N d(i, j)}. \quad (2.5)$$

Other definitions for the closeness centrality exist. For instance, in [45], c_i is simply defined as the inverse of $\sum_{j=1}^N d(i, j)$, without the factor $N-1$ and sometimes it is also defined as the mean geodesic distance between a vertex i and all other vertices in a network. In this work, we adapt the definition given in Equation 2.5. For a recurrence network, closeness centrality gives the local centeredness of a state in the phase space and with a small number of ε -jumps, most of the vertices are reachable from a vertex with high centrality [14].

(iii) Betweenness centrality

Betweenness centrality, like other centrality measures, also describes the importance of a vertex in a network and was first introduced in [46,47]. The betweenness centrality of a vertex i is defined as the total number of the fraction of shortest paths between all pairs of vertices that pass through

i . Let σ_{jk} be the total number of shortest paths from a vertex j to k in a network and $\sigma_{jk}(i)$ be the number of short paths (from a total of σ_{jk}) that pass through vertex i . The betweenness centrality for a vertex i can be defined as [48]

$$b_i = \sum_{j \neq i \neq k} \frac{\sigma_{jk}(i)}{\sigma_{jk}}. \quad (2.6)$$

When this measure is applied to a recurrence network, where the vertices represent the states of a dynamical system, a high value of betweenness is acquired by those vertices belonging to a sparse region in phase space that separates different high density clusters [14].

(iv) Local clustering coefficient

The local clustering coefficient for a vertex i gives the probability that two randomly drawn neighbors j and q are themselves neighbors. In an undirected graph, since the maximum possible number of connections between the neighbors of a vertex i is given as $k_i(k_i - 1)/2$, the local clustering coefficient can be given by the ratio

$$c_i = \frac{\sum_{j,q} A(i,j)A(j,q)A(q,i)}{k_i(k_i - 1)}. \quad (2.7)$$

(v) Transitivity dimension

Network transitivity measures the fraction of the connected triples in a network that form triangles, where a connected triple is defined as a single vertex connected to an unordered pair of vertices [49]. It was first introduced in [50]. It can be given by the following ratio

$$\mathcal{T} = \frac{\sum_{i,j,q=1}^N A(i,j)A(j,q)A(q,i)}{\sum_{i,j,q=1}^N A(i,j)A(q,i)}. \quad (2.8)$$

Essentially, \mathcal{T} also measures the probability that if two vertices are neighbors of another vertex, then the two vertices themselves are neighbors. This definition is similar to the notion of clustering coefficient, but there is a slight difference between these two measures. While the averaged network clustering coefficient is the mean, computed over all vertices, of the ratio given in Equation 2.7, the network transitivity is the ratio of the mean number of edges between the neighbors of a vertex and the mean number of possible edges between neighbors of a vertex [50]. Also, network transitivity gives equal weight to all triangles in a network, where as the clustering coefficient is biased to vertices with low-degree and weights their contributions more heavily [40,49]. In [40], a new measure of global dimension known as transitivity dimension was introduced, which can be considered as some notion of fractal dimension. The transitivity dimension at a single scale ε is given as [40]

$$\mathcal{T}_\varepsilon = \frac{\log \mathcal{T}}{\log(3/4)}. \quad (2.9)$$

For the sake of simplicity, in the remainder of this paper we will always refer to single-scale transitivity dimension as *transitivity dimension*, $D_{\mathcal{T}}$.

(vi) Assortativity

A network is said to be assortative if vertices of similar degrees tend to link up with each other. The measure assortativity can be defined as a Pearson product-moment correlation of the vertex degrees on either ends of all the edges [14,51,52]

$$\mathcal{R} = \frac{\frac{1}{N} \sum_{j>i} k_i k_j A(i, j) - [\frac{1}{N} \sum_{j>i} \frac{1}{2}(k_i + k_j) A(i, j)]^2}{\frac{1}{N} \sum_{j>i} \frac{1}{2}(k_i^2 + k_j^2) A(i, j) - [\frac{1}{N} \sum_{j>i} \frac{1}{2}(k_i + k_j) A(i, j)]^2}. \quad (2.10)$$

A recurrence network showing assortative mixing implies that the density of states change more slowly and continuously and, hence, \mathcal{R} can be considered as a measure of the fragmentation of the attractor [14].

(vii) Average path length

The average path length \mathcal{L} for a graph can be defined as the mean value of geodesic lengths over all pairs of nodes. It is given as

$$\mathcal{L} = \frac{1}{N(N-1)} \sum_{i \neq j} d(i, j). \quad (2.11)$$

The disconnected pairs of nodes are not included in computing the average [1,53]. Dynamical transitions in complex systems can be identified by changes in the values of \mathcal{L} [1,22,54,55]. For example, a continuous dynamical system with periodic trajectory has a higher \mathcal{L} compared to a system exhibiting chaotic dynamics for comparable ε [38].

3. Simulations and results

(a) Model systems

In this study we consider the Lorenz system [56],

$$\dot{x} = 10(y - x), \dot{y} = x(28 - z), \dot{z} = xy - \frac{8}{3}z, \quad (3.1)$$

and the chaotic Rössler system [57],

$$\dot{x} = -y - z, \dot{y} = x + 0.1y, \dot{z} = 0.1 + z(x - 18), \quad (3.2)$$

as examples for three-dimensional chaotic oscillators. Additionally we also consider the hyper-chaotic Rössler system [58],

$$\dot{x} = -y - z, \dot{y} = x + 0.25y + w, \dot{z} = 3 + xz, \dot{w} = -0.5z + 0.05w. \quad (3.3)$$

In each case, we consider the x -component of the system and reconstruct the dynamics for varying embedding dimension using the method of delays. The optimal embedding lag in each case was found using the auto mutual information criterion [59]. We obtained $\tau=3, 28$, and 107 for the x -component of the Lorenz, Rössler and hyper-chaotic Rössler systems respectively. For the chaotic systems, the number of data points generated were $N = 10,000$ (after discarding initial $5,000$ points as transients) with step size of 0.05 . In case of the hyper-chaotic Rössler system, we considered (again discarding initial $5,000$ points as transients) $N = 10,000, 15,000$ and $20,000$, with step size of 0.01 . We also generated 99 iAAFT surrogates in each case using the x -component. Furthermore, to study the effect of noise, we generated 100 realizations from the chaotic systems described above, for data lengths $N = 200, 500, 1,000, 5,000$ and $10,000$. We added observational noise to the x -component of each system

$$x_{noise}(t) = x(t) + \eta(t), \quad (3.4)$$

where $\eta(t) \sim \mathcal{WN}(0, \sigma^2)$. Here, \mathcal{W} is defined as the level of noise, which is given as a percentage of the standard deviation of the noise-free data $x(t)$. We added Gaussian noise at levels $10\%, 20\%, 40\%, 60\%$ and 100% .

(b) Global network measures

Figures 1 - 3 show the variation of $D_{\mathcal{T}}$, \mathcal{L} and \mathcal{R} with respect to the embedding dimension m for different RR , for the chaotic and stochastic dynamics reconstructed from the x -component of the Lorenz system and its iAAFT surrogates respectively. It can be seen from Figure 1 that $D_{\mathcal{T}}$ for the Lorenz attractor (chaotic dynamics) saturates at a fractal dimension < 2 (it varies approximately between 1.5 for $RR = 0.05$ to 1.8 for $RR = 0.01$), whereas in case of the stochastic dynamics, the $D_{\mathcal{T}}$ continues to increase with the embedding dimension m , consistent with the theory (see Section 1). The classical measures, correlation dimension and the upper box-counting dimension, which theoretically represent respectively the upper and lower bounds of the fractal dimension of a dynamical system, were estimated to be 2.06 and 2.33 respectively for a Lorenz system [60].

UPOs are the skeleton of chaotic dynamics and there are infinitely many densely packed UPOs in such a system [61], whereas stochastic dynamics are not characterized by the presence of UPOs. Since $D_{\mathcal{T}}$ is essentially a measure of the global dimension of the system [40], presence of UPOs (especially low-periodic ones) should result in values of $D_{\mathcal{T}} < m$ for increasing values of m while in case of stochastic dynamics, $D_{\mathcal{T}}$ should continue to increase with m . Our results reflect this behaviour and show how $D_{\mathcal{T}}$ can be used to distinguish between chaotic and stochastic dynamics. Note that at $m = 1$, $D_{\mathcal{T}}$ of both chaotic and stochastic dynamics is the same, i.e., ≈ 1 , and as m is increased, the difference in the $D_{\mathcal{T}}$ emerges between these two systems. This is due to the fact that at $m = 1$, both the x -component of the Lorenz system and its corresponding iAAFT surrogate share the same invariant density [15,37]. Regarding the behaviour of \mathcal{L} , we can see from Figure 2 that the ε -recurrence networks derived from iAAFT surrogates exhibit lower values of \mathcal{L} compared to that of the Lorenz system and this difference increases with m . These observations for \mathcal{L} are also expected as more short-cuts are introduced in the phase space (due to homogeneous filling of the phase space) for the stochastic data leading to lower average number of hops between two vertices in phase space. Thus, \mathcal{L} for the stochastic dynamics decreases with increasing m , while \mathcal{L} for chaotic dynamics slightly increases with increasing m . Note that, in a chaotic system there exist such short-cuts as well leading to lower values of \mathcal{L} compared to periodic systems, again due to relatively more homogeneous filling of the phase space, for a comparable attractor diameter and threshold ε [38]. However, compared to stochastic dynamics, the \mathcal{L} of chaotic dynamics is still higher as evident from our results. Similar results were obtained for $D_{\mathcal{T}}$ and \mathcal{L} in case of the chaotic Rössler system.

Figure 3 shows the behaviour of \mathcal{R} for the chaotic (Lorenz system) and stochastic dynamics (iAAFT surrogates). In case of chaotic dynamics, \mathcal{R} remains around the same level for $m > 1$ and only shows a slight tendency to increase with m at high values of RR . For instance, $\mathcal{R} \approx 0.85$, 0.81 and 0.78 for $RR = 0.01$, 0.02 and 0.03, respectively, for all values of $m > 1$, whereas \mathcal{R} ranges between 0.74 – 0.76 and 0.71 – 0.75 for $RR = 0.04$ and 0.05 respectively as m is increased from 2 to 5. Meanwhile, we observe that in case of stochastic dynamics, \mathcal{R} decreases linearly with increasing m and for $m > 3$, the value of \mathcal{R} for stochastic dynamics drops below that of chaotic dynamics. As a network measure, \mathcal{R} measures the correlation of the degrees of the vertices on either ends of an edge. In a chaotic system, due to the presence of UPOs, there exists high density clusters comprising of vertices that roughly have the same degree and at an appropriately chosen threshold, this clustering property of the chaotic systems in the phase space is maintained and the recurrence networks representing such systems should exhibit assortative mixing leading to high values of \mathcal{R} [62]. In our results, we consistently observe high values of \mathcal{R} (> 0.7) for all values of RR and m for the Lorenz system, explaining the presence of densely packed UPOs, that form clusters. In case of stochastic dynamics, the behavior of \mathcal{R} is a bit ambiguous and difficult to interpret for $m \leq 3$. For higher values of m , we observe that the ε -recurrence networks representing the stochastic dynamics exhibits lower values of \mathcal{R} ($0.68 < \mathcal{R} < 0.52$) for $m = 5$ at various RR . Also, it can be seen that with the increase in RR , the value of \mathcal{R} drops. Following Donner *et al.* [14], this behaviour can be attributed to the larger coverage of the phase space due to increasing RR leading to much stronger variation in phase space density, thus less

similar degrees for neighbouring vertices. Also, the behaviour of \mathcal{R} also seems to be system-specific as in case of the chaotic Rössler system (Figure 4) it can be seen that at low values of $RR(< 0.04)$, \mathcal{R} can distinguish between chaotic and stochastic dynamics for $m > 2$. However, from our results it is clear that \mathcal{R} can distinguish successfully between chaotic and stochastic dynamics at a sufficiently high embedding dimension, with ε -recurrence networks derived from chaotic dynamics exhibiting more assortative mixing compared to stochastic dynamics.

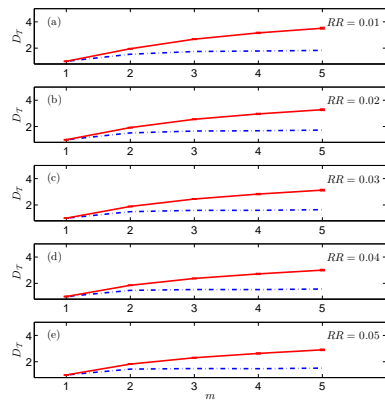


Figure 1. Transitivity dimension $D_{\mathcal{T}}$ of the ε -recurrence networks constructed from the x -component of Lorenz system (dashed blue lines) and corresponding iAAFT surrogates (solid red lines) for varying embedding dimension m and recurrence rate RR ($N=10,000$). The $D_{\mathcal{T}}$ for surrogates are averaged over 100 realizations with error bars representing the standard deviation.

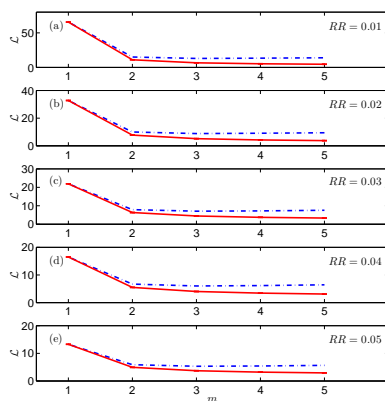


Figure 2. Average path length \mathcal{L} of the ε -recurrence networks constructed from the x -component of Lorenz system (dashed blue lines) and corresponding iAAFT surrogates (solid red lines) for varying embedding dimension m and recurrence rate RR ($N=10,000$). \mathcal{L} for surrogates are averaged over 100 realizations with error bars representing the standard deviation.

In case of the hyperchaotic Rössler system, it was observed that the difference between the (chaotic) deterministic and stochastic dynamics particularly improved as the number of data points was increased. We observed that, for low values of $RR (< 0.03)$ and $m (\leq 3)$, there is an overlapping of $D_{\mathcal{T}}$ for hyper-chaos and stochastic processes (See Figure S1 from supplementary data). Similar observations were made for the network measures \mathcal{L} and \mathcal{R} (Figures S2 and S3 from supplementary data). From Figure 5 it can be seen that \mathcal{L} distinguishes between hyperchaotic

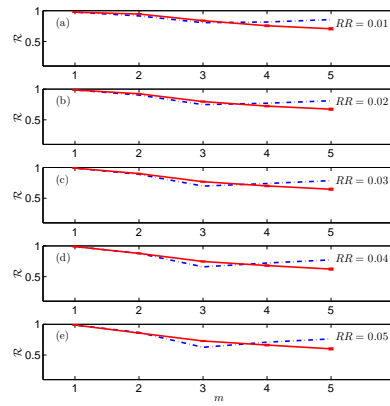


Figure 3. Assortativity \mathcal{R} of the ε -recurrence networks constructed from the x -component of Lorenz system (dashed blue lines) and corresponding iAAFT surrogates (solid red lines) for varying embedding dimension m and recurrence rate RR ($N=10,000$). \mathcal{R} for surrogates are averaged over 100 realizations with error bars representing the standard deviation.

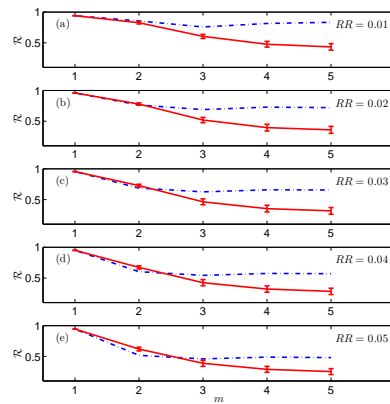


Figure 4. Assortativity \mathcal{R} of the ε -recurrence networks constructed from the x -component of the chaotic Rössler system (dashed blue lines) and corresponding iAAFT surrogates (solid red lines) for varying embedding dimension m and recurrence rate RR ($N=10,000$). \mathcal{R} for surrogates are averaged over 100 realizations with error bars representing the standard deviation.

and stochastic dynamics quite well for increasing m . As N is increased, \mathcal{L} for the hyper-chaotic system begins to decrease as the spread of the attractor increases in the phase space (hyper-chaos is better characterized geometrically with increasing data length) and this creates shortcuts between distant attractor points [61]. Also, in case of network measures $D_{\mathcal{T}}$ and \mathcal{R} (Figure 5), the distinction between hyperchaotic and stochastic dynamics improved with increasing N and m . These results are expected as a higher number of data points leads to a better characterization of the underlying hyperchaotic dynamics. Figure 5 summarizes the dependence of these global measures on data length N and m for the hyperchaotic Rössler system and their corresponding iAAFT surrogates at $RR = 0.02$. Similar observations were made for other values of RR (not shown here).

(c) Vertex-based network measures

The results for the vertex-based measures \mathcal{C}_i , c_i , k_i and b_i for the Lorenz system, chaotic Rössler system, hyperchaotic Rössler system and their corresponding iAAFT surrogates are presented

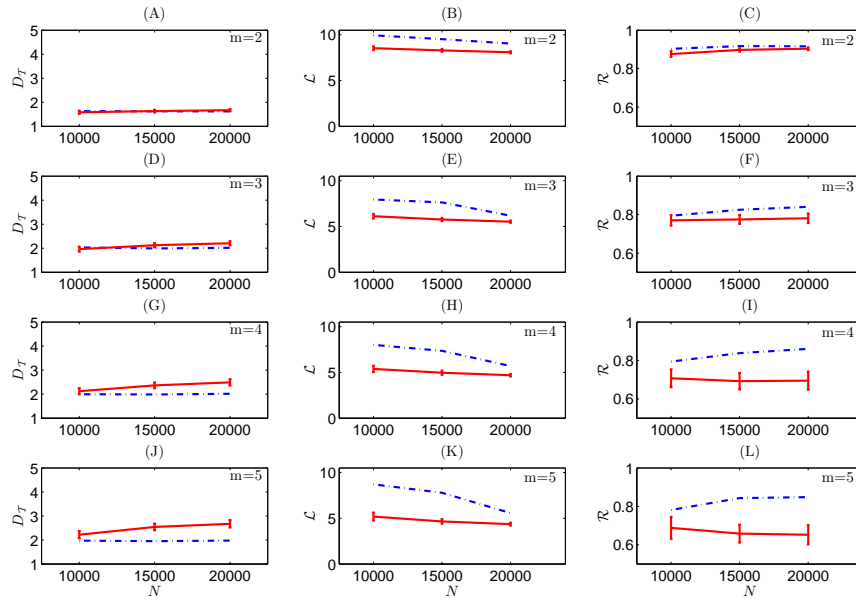


Figure 5. Transitivity dimension $D_{\mathcal{T}}$ (A), average path length \mathcal{L} (B), and assortativity \mathcal{R} (C) of the ε -recurrence networks constructed from the x -component of hyper-chaotic Rössler system (dashed blue lines) and corresponding iAAFT surrogates (solid red lines) for embedding dimension $m = 2$ and increasing data length N at recurrence rate $RR = 0.02$. The surrogates are averaged over 100 realizations with error bars representing the standard deviation. (D-F), (G-I), and (J-L) likewise in (A-C) but for $m = 3, 4$ and 5 respectively.

and discussed in this section. In order to compare the distribution of the local measures for the (hyper) chaotic attractor and the corresponding iAAFT surrogate, we used the two-sample Kolmogorov-Smirnov (KS-2) test. The result from the KS-2 test for the vertex-based measures is shown in Figure 6 for the Lorenz system. For the Lorenz system, it can be seen that the KS statistic, which gives the maximum of the absolute difference between the cumulative distribution functions of the two samples (for example, between the Lorenz attractor and the iAAFT surrogate), for the vertex-based measure C_i increases with the embedding dimension m for all values of the recurrence rate RR . For $m > 1$ and all values of RR , the null hypothesis that the two samples are consistent with the same underlying distribution was rejected (at 5% significance level) with the p value being very close to 0. Similar observations were made in case of c_i , b_i and k_i . We also repeated the KS-test for different realizations of the original data and its corresponding iAAFT surrogate and found similar results as in 6. Thus, the distributions of the vertex-based measures for the chaotic attractors were significantly different from their iAAFT surrogates for $m > 1$ and for all values of RR . An exemplary result from the KS-2 test for the chaotic Rössler attractor and the corresponding iAAFT surrogate is shown in Figure S4 (from the supplementary data). Additionally, Figures S8-S11 from supplementary data show the colour-coded representation of the vertex-based measures for the chaotic attractors (Lorenz and Rössler attractor) and their corresponding surrogates. It is evident from these figures that there exists clear difference in the spatial distribution of the vertex-based measures for chaotic and stochastic dynamics.

Figure 7 shows the relationship between b_i and C_i for the reconstructed chaotic attractors (Lorenz and Rössler) and their corresponding iAAFT surrogates. As a vertex-based measure, C_i reflects for a given vertex, the density of the links between its neighbours. In the context of an ε -recurrence network, the measure C_i is related to the geometric alignment of the vertices in the phase space [14]. For instance, the vertices along the stable manifold of an UPO are characterized by high values of C_i and since UPOs are the backbone of chaotic attractors, the measure C_i

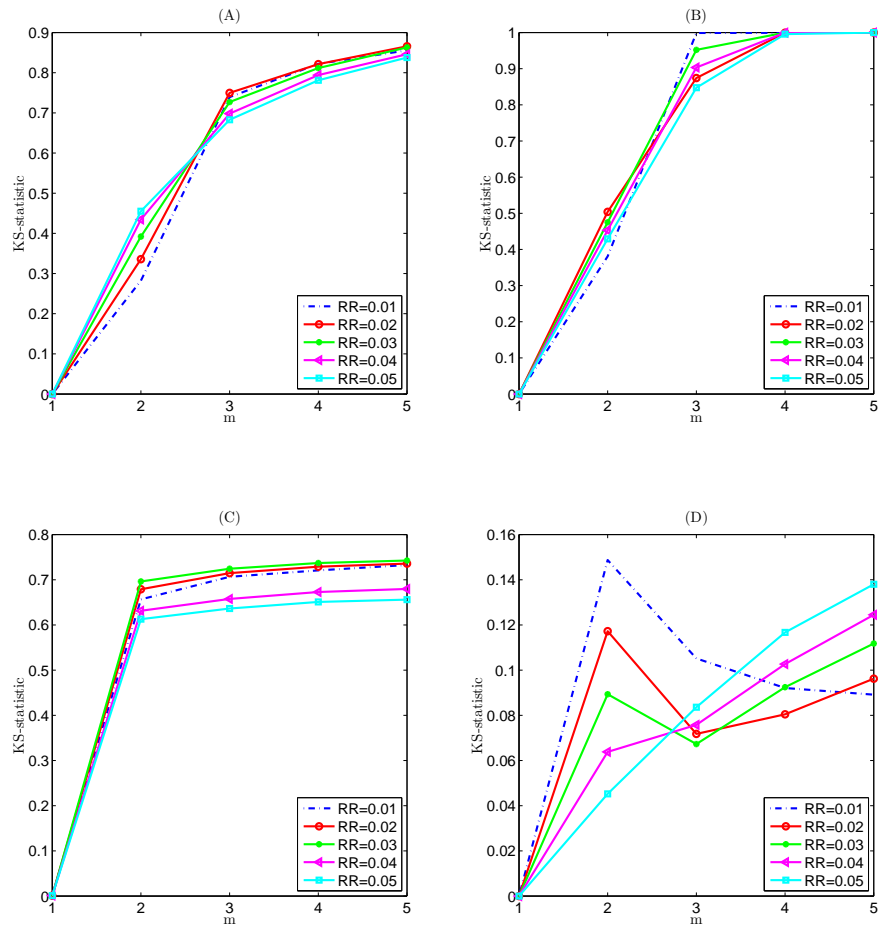


Figure 6. KS-statistic for the local clustering coefficient C_i (A), closeness centrality c_i (B), betweenness centrality b_i (C), and degree centrality k_i (D) for the Lorenz system ($N = 10,000$) and the corresponding iAAFT surrogate for varying embedding dimension m and recurrence rate RR .

is particularly important for the geometric characterization of chaos. Furthermore, the vertices belonging to a sparse region (that separate high-density clusters like the vertices belonging to the stable manifold of an UPO) in the phase space acquire high values of b_i as they act as transfer vertices or hubs between two high-density clusters on the either side of the sparse region [14,63]. Also, these vertices exhibit low values of C_i as they belong to sparse region in phase space and lack clustering properties compared to the vertices within the high-density clusters. Thus, the vertices belonging to the high-density cluster in the phase space must exhibit high values of C_i and low values of b_i . These points are clearly reflected in Figure 7 (A-C) where it can be seen that for the chaotic dynamics (Lorenz and Rössler system), more vertices with low values of b_i (for convenience we have plotted $\log_{10}(b_i + 1)$) exhibit high values of C_i compared to the stochastic dynamics (Figure 7 (B-D)). The obvious reason for this difference is that the stochastic dynamics are not characterized by the presence of UPOs and, hence, there are no high-density clusters and consequently less number of vertices acting as hubs between high density clusters to acquire high values of b_i . Also, we can see the expected trend of vertices with high values of b_i exhibiting low values of C_i from Figure 7. The difference between chaotic and stochastic dynamics is evident here as well, as the value of C_i acquired by vertices (displaying high values of b_i) belonging to ε -recurrence networks constructed from iAAFT surrogates are much lower than their chaotic

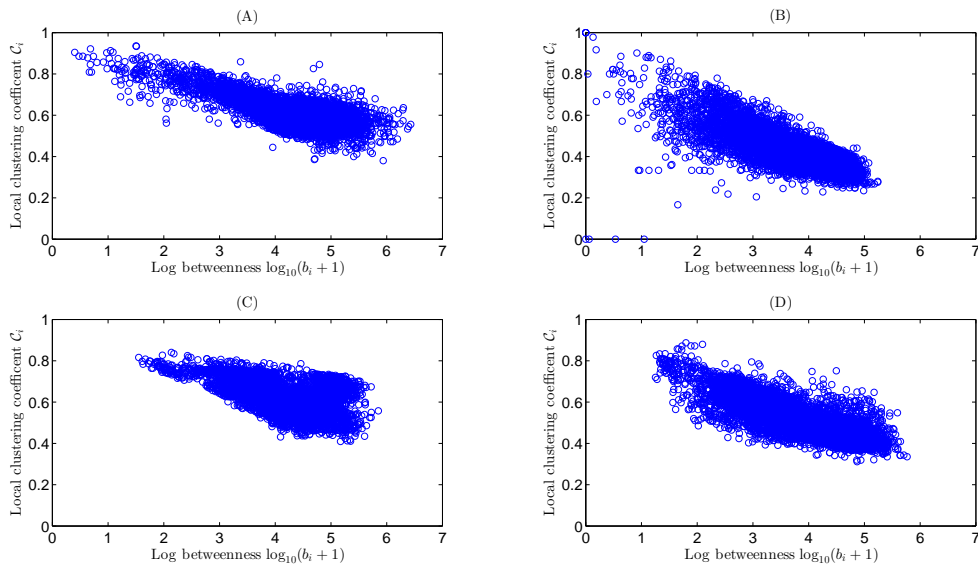


Figure 7. Variation of log betweenness centrality $\log_{10}(b_i + 1)$ with the local clustering coefficient C_i for the Lorenz attractor (A) and the corresponding iAAFT surrogate (B). (C)-(D) same as (A)-(B) but for the chaotic Rössler attractor and the corresponding iAAFT surrogate. The parameters for the exemplary plot are, embedding dimension $m = 5$ and $RR = 0.02$.

counterparts. Xiang *et al.* [63] studied the relationship between C_i and b_i with adaptive nearest neighbor recurrence networks for the chaotic Rössler system and found that vertices with low b_i display high C_i , an observation our results as shown in Figure 7 (A) and (C) supports.

The ε -recurrence networks constructed from chaotic systems contain more vertices that display high values of b_i (> 3000 vertices with approximately 10^4 shortest paths) and C_i (> 3000 vertices with $C_i \approx 0.6$) compared to the ε -recurrence networks constructed from the stochastic dynamics in case of the Lorenz attractor and the corresponding iAAFT surrogate (Figure S12 from supplementary data). Thus, the presence of UPOs in the chaotic dynamics is captured geometrically by the local vertex-based measures like C_i and b_i . However, it has to be noted here that, in case of chaotic dynamics, although vertices with low betweenness exhibit very high C_i , there exists broad range of values for betweenness centrality for vertices displaying high C_i (≈ 0.6) and as noted in [64], b_i alone cannot confirm the presence of UPOs.

Next we looked at the relationship between b_i and k_i in chaotic and stochastic systems. The vertex measure k_i is related to the local phase space density while the measure b_i depends on the relative number of shortest paths that pass through i . It can be seen from Figure 8 that in case of chaotic dynamics (Lorenz and Rössler), the vertices that exhibit low value for b_i ($< 10^3$ shortest paths) also exhibit low value for k_i . These are specifically the vertices in the vicinity of the outer boundaries of the attractors. This effect is enhanced in case of Lorenz attractor, where we observe more vertices exhibiting low values for b_i and k_i simultaneously compared to the Rössler attractor as in case of the Lorenz system the outer parts of the attractor that are not involved in the shortest paths, exhibit low phase space density [64]. In case of stochastic dynamics, we see this trend as well where vertices with low b_i also acquire low k_i . However, due to the presence of UPOs, an interesting region is observed in b_i vs k_i graph in case of chaotic dynamics which is missing in stochastic dynamics. The vertices that are in the vicinity of UPOs acquire somewhat low values for b_i due to the accumulation of states leading to increased shortest paths [64]. But, these vertices in the vicinity of the UPOs, acquire relatively high values for k_i due to the very same reason of accumulation of states. This fact is clearly reflected in Figure 8 (A-C) where vertices with

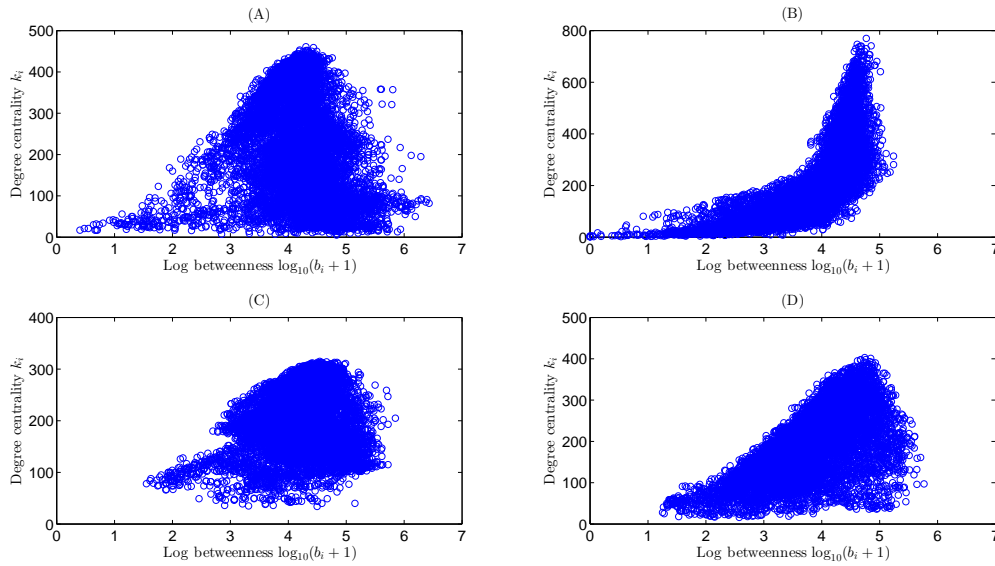


Figure 8. Variation of log betweenness centrality $\log(b_i + 1)$ with the degree k_i for the Lorenz attractor (A) and the corresponding iAAFT surrogate (B). (C)-(D) same as (A)-(B) but for Rössler attractor and the corresponding iAAFT surrogate. The parameters for the exemplary plot are, embedding dimension $m = 5$ and $RR = 0.02$.

$10^4 \leq b_i \leq 10^6$ acquire $200 < k_i < 300$. This middle region of the graph is completely missing in case of the corresponding iAAFT surrogates (Figure 8 (B-D))

Furthermore, in case of chaotic dynamics, it can be seen that some of the vertices that acquire high values of b_i ($> 10^4$) have a broad range of k_i (50 to 400) as these vertices reside in the sparse region of phase space and mostly have vertices in the high density clusters as their neighbors. In case of the stochastic dynamics, we can see that the range for b_i for a given value of k_i is much narrower compared to chaotic dynamics. The reason for this can be that in case of stochastic dynamics, the sparse regions between two high-density clusters do not exist as in the case of chaotic dynamics, but rather the space is uniformly filled with vertices. This increases the total number of short-cuts between pairs of vertices thus reducing the b_i for a vertex i through which some of the short-cuts pass. Furthermore, few of the vertices (which would otherwise be a part of sparse region) tend to have more neighbors due to homogeneous filling of the phase space increasing the value of k_i (up to 800). However, most of the vertices in case of stochastic dynamics tend to have low degree that display b_i between 10^3 and 10^5 .

The distribution of c_i in case of chaotic dynamics (Lorenz attractor) is clearly different compared to the stochastic dynamics. Specifically, in case of chaotic dynamics, most of the vertices ($\approx 6,500$) acquire c_i between 0.1 and 0.11. these vertices particularly belong to the centre of gravity of the chaotic attractors [14]. In case of stochastic dynamics, due to the existence of many short-cuts, relatively broad range of c_i (between 0.23 and 0.3) is acquired by the vertices. Since c_i used in this work follows the definition in [44], where c_i is essentially defined as the inverse of average shortest path length of a vertex to all other vertices in a network (see Equation 2.5), the vertices of ε -recurrence networks constructed from iAAFT surrogates tend to have larger values due to increased short-cuts, compared to the networks representing chaotic dynamics. The distribution of k_i has multiple peaks due to many UPOs embedded in chaotic attractors [62] (for example at 100, 200 and 400 in Figure S13 from supplementary data) whereas the distribution of k_i in case of stochastic dynamics is skewed and most of the vertices have a low degree of around 150 to 200.

In case of the hyperchaotic Rössler system, the value of the KS-statistic increased as the data length was increased (See Figures S5 - S7 from the supplementary data), specifically in

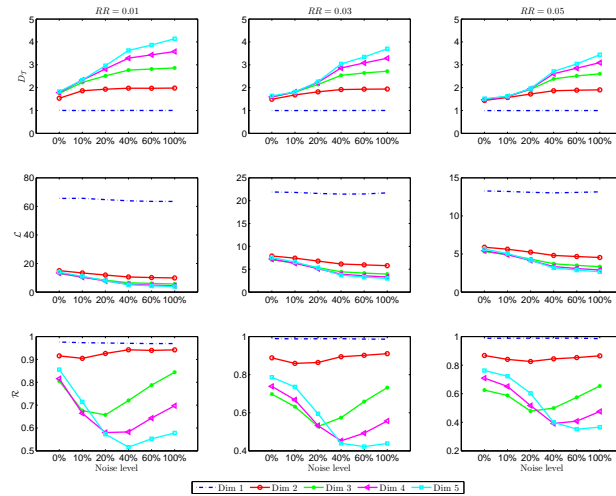


Figure 9. Impact of noise on the global measures for the Lorenz system for varying embedding dimension m and recurrence rate $RR = 0.01, 0.03$ and 0.05 .

the case of the vertex-based measures \mathcal{C}_i and b_i . Looking at the distributions of b_i and \mathcal{C}_i for the hyper-chaotic Rössler attractor and the corresponding surrogate at $N = 10,000$ and $20,000$ (Figures S14 and S16 from supplementary data), it is clear that the nodes acquiring high values of b_i and \mathcal{C}_i in ε -recurrence networks constructed from hyper-chaotic Rössler system increases compared to the networks constructed from the corresponding iAAFT surrogates as data length is increased. Also, looking at the distributions of c_i and k_i (Figures S15 and S17 from supplementary for $N = 10,000$ and $20,000$ respectively), we again observe that vertices of the ε -recurrence networks representing hyper-chaotic dynamics tend to acquire lower values of c_i compared to their stochastic counterparts for the same reason as outlined above for the chaotic case. On similar lines, the distribution of k_i again shows multiple peaks in case of hyper-chaotic dynamics, which is missing in case of its stochastic counterpart.

Thus, the vertex-based measures are able to better distinguish between the hyperchaotic and stochastic dynamics with increasing data length (similar to the global measures). With respect to the relationship between b_i and \mathcal{C}_i , we also noticed that in case of hyper-chaotic dynamics, more vertices with low values of b_i exhibit high values of \mathcal{C}_i compared to the stochastic dynamics (not shown here).

(d) Effect of noise

Figure 9 shows the impact of noise on the global measures $D_{\mathcal{T}}$, \mathcal{L} and \mathcal{R} . In case of $D_{\mathcal{T}}$ it can be seen that at 0% noise (i.e., noise-free case) the value of $D_{\mathcal{T}}$ is less than 2 for increasing dimension for various RR . More specifically, as RR is increased the value of $D_{\mathcal{T}}$ drops. For instance, at $RR = 0.05$, $D_{\mathcal{T}}$ is around 1.7 to 1.8, while at $RR = 0.01$, $D_{\mathcal{T}}$ is around 1.4 to 1.5, and these values remain approximately at the same level for $m > 2$. In the following, we will only discuss results pertaining to $m > 2$ since $m = 3$ is the minimum dimension needed to unfold the dynamics of the Lorenz system. As the level of noise is increased, the value of $D_{\mathcal{T}}$ increases above 2 at noise level of 10 % for $RR = 0.01$. As the RR is further increased to 0.03 the value of $D_{\mathcal{T}}$ remains under 2 at 10 % noise level. On further increasing the RR to 0.05, even at the noise level of 20 % we can observed that $D_{\mathcal{T}} < 2$ for $m > 3$.

At noise levels greater than 20 %, irrespective of RR , the value of $D_{\mathcal{T}}$ becomes greater than 2 and continues to increase with noise. For example, at the noise level of 40 %, $D_{\mathcal{T}} = 2.38$ at $RR = 0.05$ and $m = 3$. This is due to the homogeneous filling of the phase space due to the

addition of the noise which makes the dynamics more stochastic, thus leading to an increase in the fractal dimension. Alternatively, as noise level increases, the local microscopic fine-structure of the chaotic attractors, namely the densely packed UPOs, is destroyed. Since \mathcal{T} essentially measures the clustering property, the distortion of the clustering property due to the presence of UPOs results in lower values for \mathcal{T} (equivalently a higher value for $D_{\mathcal{T}}$) for noise levels greater than 20 %. Regarding the behaviour of \mathcal{L} under noise, it can be seen from Figure 9 that as noise increases, \mathcal{L} expectedly decreases since more short-cuts are introduced with increasing noise levels in phase space leading to shorter paths. We can observe a drop of about 40 to 50 % in the value of \mathcal{L} at noise level of 40 % for $m > 2$. Also, the drop is sharper at low values of RR . Previously, we have shown that the global clustering coefficient (different from \mathcal{T} but still related to the triangles in a network) and \mathcal{L} cannot distinguish between noisy periodic dynamics and noise-free chaotic dynamics at noise level greater than 20 % and the influence of noise on global clustering coefficient can be minimized by increasing the RR [29]. By increasing the RR and thus the ε , larger scales are captured due to which the impact of noise amplitudes on measures like \mathcal{T} and global clustering coefficient is reduced. With respect to the behavior of \mathcal{R} under noise, it can be seen from Figure 9 that for $m > 2$, the value of \mathcal{R} decreases as noise levels increase, however this behavior is modulated by the choice of RR . For low values of RR such as 0.01, it can be seen that \mathcal{R} decreases up to noise level of 20 %. Interestingly, as the noise level is increased beyond 20 %, \mathcal{R} starts to increase. However, the increase in \mathcal{R} is further constrained by the embedding dimension m and we observe that very high noise levels (> 20 %), $\mathcal{R}_{m=5} < \mathcal{R}_{m=4} < \mathcal{R}_{m=3}$. We see this trend at other values of RR as well, however as RR increases, at $m = 5$, \mathcal{R} continues to decrease with increase in noise levels up to 60 %. Thus, at $m = 5$, \mathcal{R} shows expected behavior with the addition of noise, where \mathcal{R} decreases with the addition of noise and drops to a value less than 0.4 at 60 % noise. As mentioned previously (see Section (b)), sufficiently higher m ($m = 5$ in case of Lorenz attractor) is required for reliable structural characterization of chaotic attractors with \mathcal{R} .

Next, we investigated the influence of noise on the vertex based measures C_i , b_i , c_i and k_i . In case of C_i and b_i , as noise is increased the number of vertices acquiring high values for both these measures decrease compared to the noise-free case as shown in the first two columns of Figure 10 where it is evident that the distributions shift left with increasing noise. In case of b_i , in the noise-free case there are ≈ 3000 vertices with approximately 10^4 shortest paths and this drops to approximately 2,000 at 40 % noise. In case of C_i , there are $\approx 3,000$ vertices with $C_i \approx 0.6$ and this drops to ≈ 500 vertices at 40 % noise. The reason for this is again related to the distortion of the clustering structure as noise is added to chaotic dynamics, which impacts both these measures.

In case of c_i , we see that the number of vertices acquiring high values of c_i increase with the addition of noise (third column from left, Figure 10). As noise is added, there are more short-cuts in the phase space due to homogeneous filling which reduces the length of shortest paths, which is inversely related to c_i (Equation 2.5). In case of k_i , where one can observe multiple peaks in noise-free case (due to many UPOs), addition of noise makes the distribution more skewed (and long tailed) and the number of vertices with low degree increases as the noise is increased (last column, Figure 10).

Figure 11 show the impact of noise on the b_i vs C_i for various RR . From Figure 11 (A-C) it can be seen that with the addition of noise, at $RR = 0.01$ the number of vertices exhibiting low C_i and b_i increases. As the RR is increased to 0.05 (Figure 11 (G-I)), we can see that vertices having low b_i tend to acquire high values of C_i , a behavior observed in noise-free chaotic dynamics. Thus increasing RR can minimize the influence of noise on the clustering property ε -recurrence networks representing chaotic dynamics in phase space. Similar observations were made for Rössler and hyperchaotic Rössler system.

(i) Effect of data length and comparison with complexity-entropy method

Table 1 shows the number of rejections (out of 100 realizations) for various noise levels and data lengths using global network measure \mathcal{T} at $RR = 0.05$ for the Lorenz system. Results using

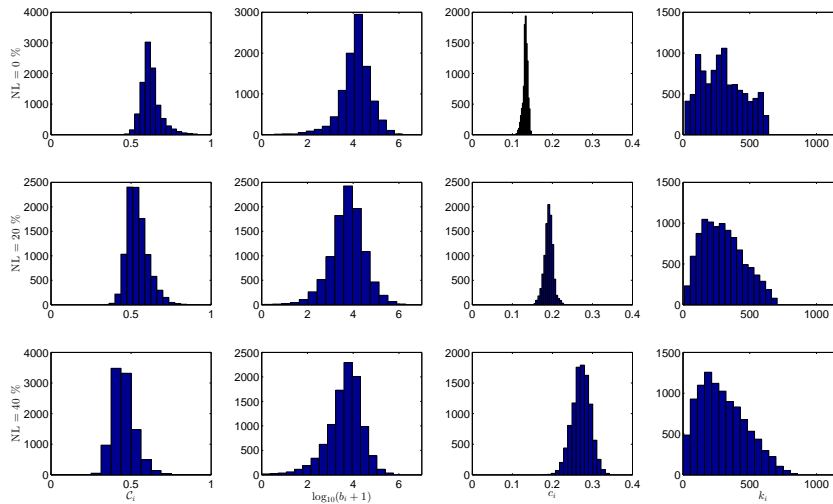


Figure 10. Impact of noise on vertex-based measures for the Lorenz system. Parameters for the exemplary plot are $RR = 0.03$ and $m = 5$.

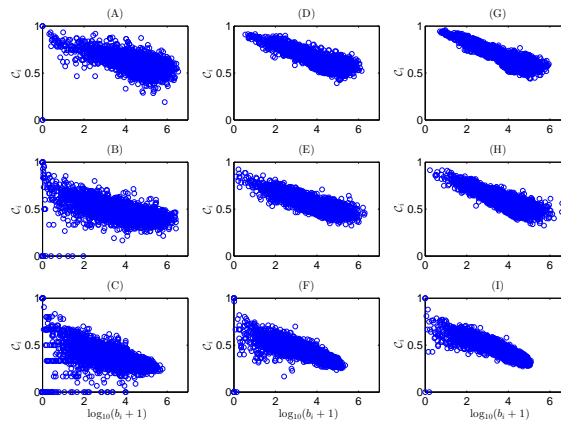


Figure 11. (A-C) Variation of log betweenness centrality $\log(b_i + 1)$ with the local clustering coefficient C_i for the Lorenz attractor for $RR = 0.01$ at noise level 0% (A), 20% (B) and 60% (C). (D-F) and (G-I) same as (A-C) but for $RR = 0.03$ and $RR = 0.05$ respectively.

the complexity-entropy (C-E) causality plane method described in [3,65] to distinguish between chaos and noise is also shown for comparison, where we set $m = 3$ and $\tau = 3$. The C-E method uses two quantifiers - the Shannon entropy [66] and the MPR statistical complexity measure proposed by Lamberti *et al.* [67]. Before estimating quantifiers based on Information Theory like entropy or the statistical complexity measure, a probability distribution associated with the time series must be provided. As described in [3], we use Bandt-Pompe methodology [68] to estimate the probability distribution P using the details of attractor reconstruction procedure (Taken's theorem) and causal information is incorporated in the construction process yielding $P \in \Omega$, where Ω is the probability space. The entropy estimates the uncertainty associated with the processes described by P , whereas the MPR complexity measure is capable of distinguishing different degrees of periodicity and chaos. The details of the C-E method and computation of the probability distribution using Bandt-Pompe methodology is explained in detail elsewhere [3,65].

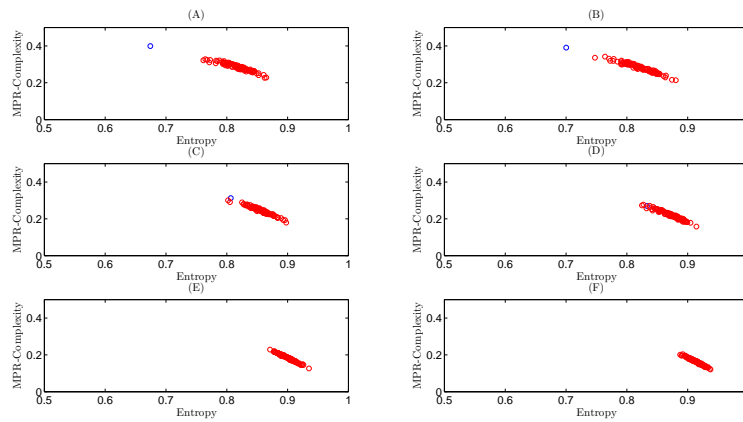


Figure 12. MPR Complexity-Entropy plane for chaotic Lorenz system (blue circle) and corresponding 99 iAAFT surrogates (red circles) under noise levels 0% (A), 10% (B), 20% (C), 40% (D), 60% (E), and 100% (F). The data length $N = 200$.

We provide freely downloadable MATLAB [code](#) based on [3,65] to compute the C-E causality plane.

Two exemplary plots (Figures 12 and 13) are shown using the C-E method to distinguish between chaotic time series and the corresponding iAAFT surrogates under varying noise levels for data length $N = 200$ and 1,000 respectively. It is evident from these figures that under noise-free condition, the position of the chaotic signal maps on to a different position on the C-E plane compared to the surrogates (stochastic signal). The complexity of the chaotic signal is higher than that of the surrogates, whereas the entropy of the chaotic signal is lower than that of the surrogates. As the chaotic signal is corrupted with noise, we can see that at short data length (Figure 12), at noise levels greater than 10%, the location of the noisy chaotic signal on the C-E plane falls within that of the 99 surrogates and is no longer distinct. When the data length is increased to $N = 1,000$, we can see that a clear distinction between noisy chaotic signal and its corresponding iAAFT surrogates can be made up to a noise level of 40%.

Without making any assumption about the distribution of the test statistic, we use the non-parametric approach (based on rank ordering) to test the null hypothesis H_0 [43] (We obtained qualitatively similar results when the parametric approach using the mean and standard deviation of surrogates was used). Since a chaotic time series should produce high values of complexity compared to a stochastic signal and a stochastic signal displays higher entropy values compared to deterministic (chaotic) signal [3], the null hypothesis of a linear, Gaussian, stochastic process can be rejected if the complexity of the signal is greater than the maximum of the surrogates and the entropy of the signal is lesser than the minimum of the surrogates. In case of ε -recurrence network measures like \mathcal{T} , \mathcal{L} , and \mathcal{R} , the null hypothesis H_0 is rejected if the ε -recurrence network measure of the signal under test is greater than the maximum of the ε -recurrence network measures of the surrogates [29,69]. Since we are using 99 surrogates, the probability with which a false rejection will occur is 1/100 (i.e., $\alpha = 0.01$).

We can see that at $N = 200$, compared to C-E method, \mathcal{T} gives comparatively higher rejections of H_0 , even when the noise level is 40% (see Table 1). Even at 60% noise level, \mathcal{T} gives significant number of rejections (= 16), whereas C-E method fails to reject H_0 for all the 100 realizations. Thus, the recurrence network measure \mathcal{T} is still able to reject H_0 with high confidence for short time series corrupted with noise as high as 40% and 60%. As N is increased, performance of C-E method improves and it can be seen that at larger values of $N (> 1,000)$, both C-E method and ε -recurrence network measure \mathcal{T} reject H_0 (almost 100 rejections) even at noise level of 60%.

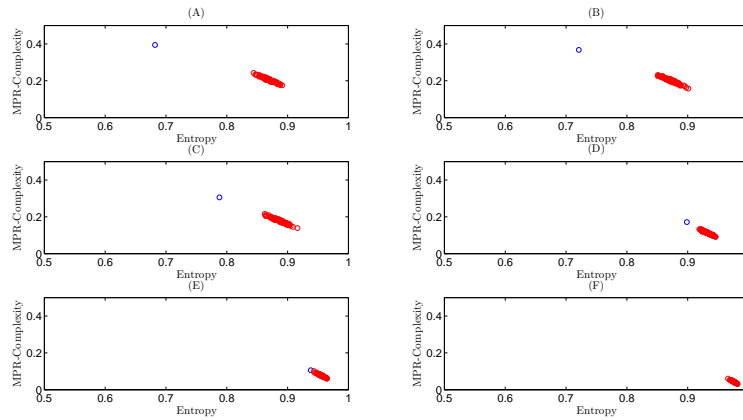


Figure 13. MPR Complexity-Entropy plane for chaotic Lorenz system (blue circle) and corresponding 99 iAAFT surrogates (red circles) under noise levels 0% (A), 10% (B), 20% (C), 40% (D), 60% (E), and 100% (F). The data length $N = 1000$.

Table 1. Number of rejections of the H_0 from 100 realizations of the Lorenz system for various data lengths and noise levels using C-E method and ε -recurrence network measure \mathcal{T} . For each realization, 99 iAAFT surrogates were generated. The embedding dimension $m = 3$, embedding delay $\tau = 3$ and the recurrence rate $RR = 0.05$.

Noise Level	$N = 200$		$N = 500$		$N = 1,000$		$N = 5,000$		$N = 10,000$	
	C-E	\mathcal{T}	C-E	\mathcal{T}	C-E	\mathcal{T}	C-E	\mathcal{T}	C-E	\mathcal{T}
0%	95	100	100	100	100	100	100	100	100	100
10%	88	100	100	100	100	100	100	100	100	100
20%	40	90	88	100	100	100	100	100	100	100
40%	5	60	52	77	93	100	100	100	100	100
60%	0	16	12	26	46	54	96	100	100	100
100%	0	11	3	8	7	5	20	22	28	32

We also computed ε -recurrence network measure \mathcal{L} and \mathcal{R} (see Table 2). In case of \mathcal{L} , we can again see that at short data lengths, the number of rejections are still considerably high for noise levels up to 60%. We can see almost 100 % rejections at $N > 500$ for noise levels as high as 40%. At $N = 5,000$ and 10,000, even at noise levels of 60%, we can see that all the 100 realizations reject H_0 . Even at 100% noise, we can see about 40 rejections of H_0 for $N = 10,000$. However, in case of \mathcal{R} , at $m = 3$, none of the realizations of the Lorenz system rejected the null hypothesis H_0 (results not shown here). As we demonstrated earlier (See Figure 3), in case of the network measure \mathcal{R} , a higher embedding dimension is required to distinguish chaotic from stochastic dynamics. When m was set to 5, we observed that the number of rejections of H_0 increases and reached 100% for $N > 200$ (see Table 2). As noise is increased beyond 20%, the network measure \mathcal{R} can no longer distinguish between chaos and noise even when $N = 10,000$.

Thus, both \mathcal{T} and \mathcal{L} outperform the C-E method to distinguish between noisy chaotic time series and noise at very short data length ($N = 200$). Particularly, \mathcal{L} seems to be very effective metric in this regard giving upto 94 rejections for $N = 1,000$ and 60 % noise compared to \mathcal{T} and C-E method, both of which manage about 50% rejections. However as N is increased ($> 5,000$), C-E method, ε -recurrence network measures \mathcal{T} and \mathcal{L} , give equally high rejections of H_0 even at noise levels as high as 60%. Qualitatively similar observations were made for the Rössler system (results not shown here).

We also observed that as noise level is increased, the topology of the ε -recurrence network changes and it tends to fill the phase space (see Figures S18-S20 in supplementary data). However,

Table 2. Number of rejections of the H_0 from 100 realizations of the Lorenz system for various data lengths and noise levels using the ε -recurrence network measure \mathcal{L} and \mathcal{R} . For each realization, 99 iAAFT surrogates were generated. The embedding delay $\tau = 3$ and the recurrence rate $RR = 0.05$. In case of \mathcal{R} , the embedding dimension m was set to 5 instead of 3.

Noise Level	$N = 200$		$N = 500$		$N = 1,000$		$N = 5,000$		$N = 10,000$	
	\mathcal{L}	\mathcal{R}	\mathcal{L}	\mathcal{R}	\mathcal{L}	\mathcal{R}	\mathcal{L}	\mathcal{R}	\mathcal{L}	\mathcal{R}
0%	97	82	100	100	100	100	100	100	100	100
10%	97	72	100	98	100	100	100	100	100	100
20%	99	30	100	52	100	74	100	100	100	100
40%	68	2	100	0	100	0	100	0	100	0
60%	33	0	63	0	94	0	100	0	100	0
100%	9	4	2	0	5	0	14	0	40	0

the topology of the ε -recurrence network, which is reflective of the topology of the embedded attractor (Lorenz attractor in this case) is not completely destroyed even at short data length of $N = 200$ and considerably high noise levels up to 40%. As noise level is increased (60% and 100%), we see that the topology of the ε -recurrence network does not resemble the shape of the Lorenz attractor and the network tends to fill the phase space.

Figures S21 and S22 from supplementary data show the colour-coded representation of the local clustering coefficient and log betweenness centrality respectively for the ε -recurrence networks under increasing levels of noise for the Lorenz system. Under noise-free condition, most of the vertices have high values for C_i , but as the level of noise increases, many vertices start displaying low values for C_i and the topology of the ε -recurrence network changes as well due to the addition of noise. As mentioned earlier (also see Figure 10), due to the addition of noise, the clustering structure associated with ε -recurrence networks derived from chaotic systems gets distorted leading to lower values of C_i for many vertices. Similarly, as noise level is increased, higher number of vertices acquire lower values of log betweenness centrality (see Figure ??).

Figure S23 shows the colour-coded representation of the local recurrence rate, which is proportional to degree centrality, for the Lorenz attractor under increasing levels of noise. It is clear from the figure that as noise level increases, the local recurrence rate for most of the vertices decreases and at very high noise levels most of the vertices tend to have similar values for local recurrence rate. This effect can also be seen from Figure 10 where the shape of the degree distribution changes from having multiple peaks (due to the presence of UPOs) under noise-free case to approaching Poisson distribution with the addition of noise.

4. Experimental EEG data with seizures

(a) EEG data

In this section we will demonstrate the ability of ε -network measures to capture dynamical transitions in noisy biological signals such as EEG data using rather short window sizes. Epilepsy affects nearly 1% of the world’s population and epileptic seizures arise due to unpredictable and irregular interruptions in the neuronal activity [70]. The EEG data used in this work was originally published by Quiroga *et al.* [71] and is available for free download at <https://vis.caltech.edu/~rodri/data.htm>. Basically, the data comprises of tonic-clonic seizures of two subjects recorded using scalp EEG with right central electrode (channel C4 according to 10-20 system [72]). The EEG data has been filtered between 1-50 Hz and sampled at 102.4 Hz. Figure 14 (A) shows 3 minutes of EEG data from one of the two patients. The beginning of the seizure is marked with a solid red line (approximately at 80 seconds). The seizure discharge lasts for about 8 seconds and the clonic phase begins at 123 seconds (marked with dashed red

line) [71]. The seizure ends approximately around 155 seconds (marked with solid black line). Also at around 140 seconds (not shown in the figure), the clonic discharge begins to separate [71].

(b) Moving window ε -recurrence network analysis

We used moving window ε -recurrence network analysis to compute global measures like $D_{\mathcal{T}}$, \mathcal{L} and \mathcal{R} for each window. We divided the time series into 5 seconds window (≈ 500 samples) and 10 seconds window ($\approx 1,000$ samples) with 90 % overlap. In order to get the temporal profile of global network measures, we assigned the global measure to the mid-point of each window. Based on the first local minimum of the auto mutual information function, we set $\tau = 18$. The embedding dimension m was varied from 2 to 8 and the recurrence rate RR was set to 0.05. Figures 14 (B)-(D) show the result of ε -recurrence network analysis for the EEG data with 10 seconds window.

- **Transitivity dimension** : It can be seen that $D_{\mathcal{T}}$ increases with embedding dimension m until about 80 seconds before the seizure. Beyond 80 seconds, $D_{\mathcal{T}}$ starts to drop for $m \geq 4$. For $m = 2$, we do not observe much variation in $D_{\mathcal{T}}$. This result for $D_{\mathcal{T}}$ clearly indicates that just before the beginning of the seizure at 80 seconds, the global dimension as measured by $D_{\mathcal{T}}$ begins to drop even if the m is increased up to 10, a characteristic associated with (low-dimensional) deterministic system. This behavior is seen again at around 120 seconds when the clonic phase of the seizure begins. Towards the end of the seizure, $D_{\mathcal{T}}$ again drops and remains at the same level for increasing values of m . The period after the seizure is characterized again by values of $D_{\mathcal{T}}$ that increase with embedding dimension m .
- **Average path length** : Regarding the behavior of \mathcal{L} , one can observe that starting around 70 seconds, there is a ramping up of \mathcal{L} for increasing m ($m \geq 4$) and \mathcal{L} peaks at around 84 seconds, which coincides with the time of the local minima for $D_{\mathcal{T}}$ for the seizure period. \mathcal{L} then starts to decrease and again begins to increase at around 140 seconds and peaking at around 150 seconds. In the post-seizure period, we can see that as the value of m increases the value of \mathcal{L} decreases (as observed in the pre-seizure period). The temporal profile of \mathcal{L} is more clearly depicted for $m = 8$ in Figure 15 (C).
- **Assortativity** : The behavior of \mathcal{R} becomes clear only for $m \geq 6$, where \mathcal{R} begins to increase from 70 seconds reaching its local maxima at around 84 seconds, which coincides with the local minima for $D_{\mathcal{T}}$ for that period. It then begins to drop and again tends to increase at around 140 seconds and peaks at at around 150 seconds. Around the seizure period, for $m \geq 6$, irrespective of the value of m , the value of \mathcal{R} remains approximately around the same value. (Also see Figure 15 (D)).

We make the following crucial observations based on the application of ε -recurrence network analysis to the EEG data.

- (i) It is clear from the above results that the measures $D_{\mathcal{T}}$, \mathcal{R} and \mathcal{L} are not entirely independent and they track dynamical transitions in a related fashion.
- (ii) These three measures, as applied to the EEG data at hand, start showing signs of change well before the clinical identification of seizure (compare the clinical onset of seizure in Figure 15 (A) to the point when the global network measures start increasing (or decreasing in case of $D_{\mathcal{T}}$) in Figure 15 (B-D)). This feature represents the possibility of using these measures to predict the seizure in advance. However note that, in the dataset used, the clinical onset of the seizure occurs just 80 seconds into the data. Having a longer segment of data before the seizure onset could also reveal interesting shift in dynamics much prior to the onset of the seizure. Recent studies have shown that it is possible to detect interesting changes in EEG tens of minutes before the actual seizure occurrence [73,74]. However, most of these measures require long window sizes, of the order of 10 minutes, which is related to our next observation.

- (iii) The global network measures are able to capture the rapidly changing dynamics using short windows of 5 seconds (512) and 10 seconds (1024) samples, which is one of the key advantages of ε -RNA compared to other methods. It is well known that the epileptic seizures exhibit high nonlinearity compared to the normal background EEG activity [75] as demonstrated in [76,77]. Previously, we have also demonstrated that ε -recurrence networks derived from EEG recorded during the seizures display high values for the global clustering coefficient and average path length compared to networks derived from normal and inter-ictal (EEG between seizures) activity, thus capturing the increase in nonlinearity and the associated structural complexity of the data [29]. However, the results in [29] were obtained with EEG data of length 20 seconds (2560 samples) which is still long compared to the window size of 5 (512 samples) and 10 seconds (1024 samples) chosen in this study
- (iv) In case of patient 1, the clonic phase begins around 123 seconds and we observe that all the three global measures, display shift in their dynamics around this time point (See Figure 15 (B-D)). Also, we observed an increase in $D_{\mathcal{T}}$ and decrease in \mathcal{L} and \mathcal{R} , before these measures stabilize in the post-seizure period, which can be considered as a surrogate marker. This shift in dynamics is also consistent with the analysis in [71] using Gabor transform and could represent decrement in neural firing along with increase in inhibitory mechanisms, that could be responsible for seizure termination [71]. However, further research is needed to relate the variation of global ε -recurrence network measures towards the transition to post-ictal activity.
- (v) The results based on these global measures suggest that the EEG signals before and after the seizure are more consistent with stochastic dynamics and during the seizure, the dynamics is more deterministic.

Qualitatively similar results were found for Patient 2 (Figure S24 in supplementary data) and with window size of 5 seconds (Figure S25 in supplementary data). These are novel and interesting results for the application of ε -recurrence network analysis to epileptic EEG data. However, these observations are based on the dataset from only two patients and would need an extensive further study involving data from a large number of patients and different types of epilepsies to draw a more substantiated conclusion. Also, we have considered data from only one channel. Recent studies have shown evidence of seizure onset within network of brain regions known as epileptic networks [78–80]. Hence, an approach taking into account functionally connected brain regions [81] is more advantageous. The possibility of using cross and joint recurrence network measures [82,83] to derive functional networks [84] using multivariate epileptic EEG data will be considered in the future.

5. Conclusions

In summary, we have shown that ε -network measures, both global and vertex-based, can be used to distinguish between (hyper-) chaotic and stochastic dynamics. We also demonstrated the effect of noise on these network measures. As a real world application, we have showed that moving window ε -recurrence network analysis can detect dynamical shifts in epileptic EEG data.

We have shown that measures like transitivity \mathcal{T} (or the related global dimension measure, the transitivity dimension $D_{\mathcal{T}}$), local clustering coefficient \mathcal{C}_i , degree centrality k_i and betweenness centrality b_i are particularly sensitive to the presence of unstable periodic orbits, which are the geometric backbone of the chaotic attractors. Additionally, other global measures such as average path length \mathcal{L} and assortativity \mathcal{R} were also able to distinguish between (hyper-) chaotic and stochastic dynamics. With assortativity \mathcal{R} , we particularly observed that the difference between chaotic and stochastic dynamics increased with embedding dimension and generally a large embedding dimension (for example $m = 5$ in case of Lorenz system) is required for successful characterization of chaos. The vertex-based measure closeness centrality c_i is also sensitive to the geometry of chaos leading to small values for chaotic dynamics compared to stochastic dynamics.

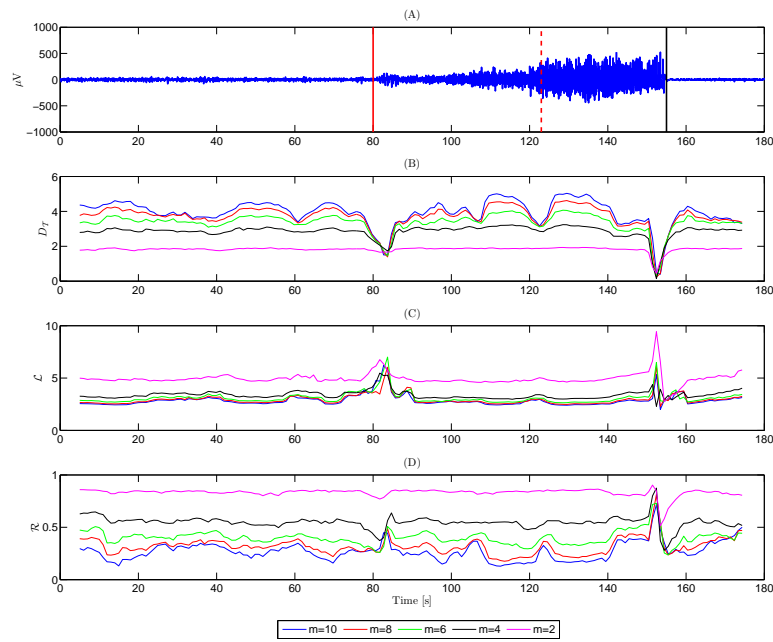


Figure 14. Moving window ε -recurrence network analysis of epileptic EEG data showing $D_{\mathcal{T}}$, \mathcal{L} and \mathcal{R} before, during and after the seizure. (A) EEG data from channel $C4$ of patient 1 with the clinical onset of seizure marked with solid red line. The dashed red line represents beginning of the clonic phase and the solid black line represents that end of seizure. (B-D) Temporal profile of the global measures (for $m = 2, 4, 6, 8, 10$) using a moving window of 10 seconds (≈ 1000 samples) with 90% overlap.

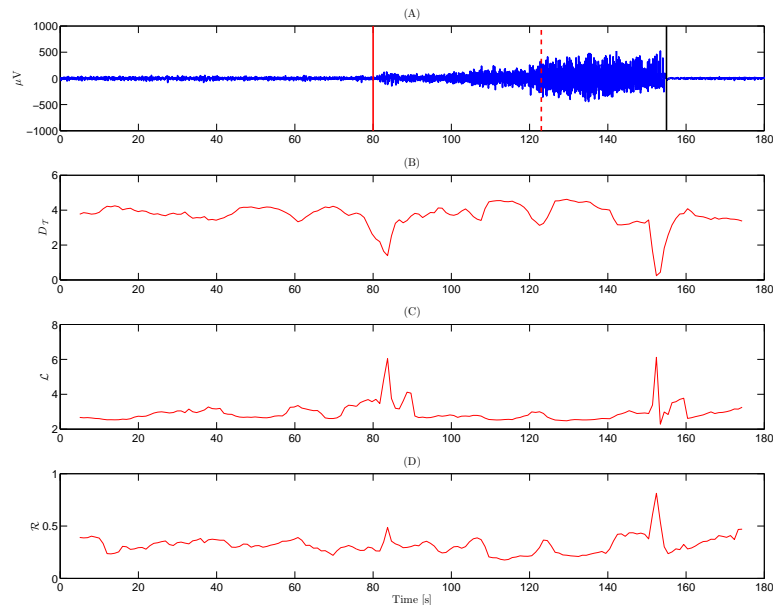


Figure 15. Moving window ε -recurrence network analysis of epileptic EEG data showing $D_{\mathcal{T}}$, \mathcal{L} and \mathcal{R} before, during and after the seizure. (A) EEG data from channel $C4$ of patient 1 with the clinical onset of seizure marked with solid red line. The dashed red line represents beginning of the clonic phase and the solid black line represents that end of seizure. (B-D) Temporal profile of the global measures (for $m = 8$) using a moving window of 10 seconds (≈ 1000 samples) with 90% overlap.

For the first time, we have demonstrated that the topological statistics derived from ε -recurrence networks can distinguish between chaotic and stochastic dynamics. In case of hyper-chaotic dynamics, we further find that the distinction between chaotic and stochastic dynamics increases with data length. We have also shown in this study that, addition of noise impacts both global and vertex-based measures. Influence of noise levels on the clustering property of the ε -recurrence networks and the presence of unstable periodic orbits was evident with the increase in transitivity dimension $D_{\mathcal{T}}$, decrease in number of vertices with high values for local clustering coefficient C_i and betweenness centrality b_i and disappearance of peaks (which is related to the unstable periodic orbits) in the distribution of degree centrality k_i . The influence of noise on these measures can be minimized to some extent by increasing the recurrence rate RR , but a large recurrence rate RR can present additional issues [40]. We also demonstrated that global ε -recurrence network measures like transitivity \mathcal{T} and the average path length \mathcal{L} are more robust at short data lengths compared to other approaches such as complexity-entropy method [3] to distinguish chaos from noise.

We also demonstrated the applicability of the ε -recurrence network measures to the real-world EEG data containing epileptic seizures. Using a small window size (≈ 500 or 1000 samples) and global network measures like transitivity dimension $D_{\mathcal{T}}$, assortativity \mathcal{R} and average path length \mathcal{L} , we were able to capture the rapidly changing dynamics representing pre-seizure, seizure and post-seizure states. The drop in the transitivity dimension $D_{\mathcal{T}}$ and increase in assortativity \mathcal{R} and average path length \mathcal{L} during the seizure is possibly an indication of a deterministic dynamics and is correlated with increased nonlinearity associated with the seizure activity. These results from the real data provide an useful conclusion that ε -recurrence network measures can successfully detect different states associated with epileptic EEG using rather short window sizes, that can potentially open up some interesting future possibilities in the field of seizure prediction.

Data accessibility. The computations involving recurrence networks were performed using the python package - **pyUnicorn** [85](available at <http://tocsy.pik-potsdam.de/pyunicorn.php>) developed at the Potsdam institute for Climate Impact Research and provided by JFD. The **simulated data** and other **codes** generated in this work is freely available for download.

Acknowledgements. NPS and JH thank the 3DNeuroN project in the European Union's Seventh Framework Programme, Future and Emerging Technologies, (grant agreement no. 296590) for the financial support. JFD thanks the Stordalen foundation (via the PB.net initiative) and BMBF (project GLUES) for financial support. The authors would like to thank the anonymous reviewers for their comments and suggestions, that has helped us improve the quality of the manuscript.

Conflict of interests. We have no competing interests.

References

References

1. Norbert Marwan, Jonathan F Donges, Yong Zou, Reik V Donner, and Jürgen Kurths. Complex network approach for recurrence analysis of time series. *Physics Letters A*, 373(46):4246–4254, 2009.
2. Luciano Zunino, Miguel C Soriano, and Osvaldo A Rosso. Distinguishing chaotic and stochastic dynamics from time series by using a multiscale symbolic approach. *Physical Review E*, 86(4):046210, 2012.
3. OA Rosso, HA Larrondo, MT Martin, A Plastino, and MA Fuentes. Distinguishing noise from chaos. *Physical review letters*, 99(15):154102, 2007.
4. Lucas Lacasa and Raul Toral. Description of stochastic and chaotic series using visibility graphs. *Physical Review E*, 82(3):036120, 2010.
5. Matthew B Kennel and Steven Isabelle.

- Method to distinguish possible chaos from colored noise and to determine embedding parameters.
Physical Review A, 46(6):3111, 1992.
6. George Sugihara and Robert M May.
Nonlinear forecasting as a way of distinguishing chaos from measurement error in time series.
Nature, 344(6268):734–741, 1990.
 7. Daniel T Kaplan and Leon Glass.
Direct test for determinism in a time series.
Physical review letters, 68(4):427, 1992.
 8. Daniel T Kaplan and Leon Glass.
Coarse-grained embeddings of time series: random walks, gaussian random processes, and deterministic chaos.
Physica D: Nonlinear Phenomena, 64(4):431–454, 1993.
 9. A Ro Osborne and A Provenzale.
Finite correlation dimension for stochastic systems with power-law spectra.
Physica D: Nonlinear Phenomena, 35(3):357–381, 1989.
 10. Martín Gómez Ravetti, Laura C Carpi, Bruna Amin Gonçalves, Alejandro C Frery, and Osvaldo A Rosso.
Distinguishing noise from chaos: objective versus subjective criteria using horizontal visibility graph.
PloS one, 9(9):e108004, 2014.
 11. M Cencini, M Falcioni, E Olbrich, H Kantz, and A Vulpiani.
Chaos or noise: Difficulties of a distinction.
Physical Review E, 62(1):427, 2000.
 12. Felipe Olivares, Angelo Plastino, and Osvaldo A Rosso.
Ambiguities in bandt–pompe’s methodology for local entropic quantifiers.
Physica A: Statistical Mechanics and its Applications, 391(8):2518–2526, 2012.
 13. Felipe Olivares, Angelo Plastino, and Osvaldo A Rosso.
Contrasting chaos with noise via local versus global information quantifiers.
Physics Letters A, 376(19):1577–1583, 2012.
 14. Reik V Donner, Yong Zou, Jonathan F Donges, Norbert Marwan, and Jürgen Kurths.
Recurrence networks—a novel paradigm for nonlinear time series analysis.
New Journal of Physics, 12(3):033025, 2010.
 15. Reik V Donner, Michael Small, Jonathan F Donges, Norbert Marwan, Yong Zou, Ruoxi Xiang, and Jürgen Kurths.
Recurrence-based time series analysis by means of complex network methods.
International Journal of Bifurcation and Chaos, 21(04):1019–1046, 2011.
 16. Jie Zhang and Michael Small.
Complex network from pseudoperiodic time series: Topology versus dynamics.
Physical Review Letters, 96(23):238701, 2006.
 17. Yue Yang and Huijie Yang.
Complex network-based time series analysis.
Physica A: Statistical Mechanics and its Applications, 387(5):1381–1386, 2008.
 18. Yutaka Shimada, Takayuki Kimura, and Tohru Ikeguchi.
Analysis of chaotic dynamics using measures of the complex network theory.
In VÁlra KÁrkovÁa, Roman Neruda, and Jan KoutnÁk, editors, *Artificial Neural Networks - ICANN 2008*, volume 5163 of *Lecture Notes in Computer Science*, pages 61–70. Springer Berlin Heidelberg, 2008.
 19. Grégoire Nicolis, A Garcia Cantu, and Catherine Nicolis.
Dynamical aspects of interaction networks.
International Journal of Bifurcation and Chaos, 15(11):3467–3480, 2005.
 20. Jonathan F Donges, Reik V Donner, and Jürgen Kurths.
Testing time series irreversibility using complex network methods.
EPL (Europhysics Letters), 102(1):10004, 2013.
 21. Lucas Lacasa, Bartolo Luque, Fernando Ballesteros, Jordi Luque, and Juan Carlos Nuño.
From time series to complex networks: The visibility graph.
Proceedings of the National Academy of Sciences, 105(13):4972–4975, 2008.
 22. JF Donges, RV Donner, N Marwan, SFM Breitenbach, K Rehfeld, and J Kurths.

- Non-linear regime shifts in holocene asian monsoon variability: potential impacts on cultural change and migratory patterns.
Climate of the Past, 11(5):709–741, 2015.
23. J. F. Donges, R. V. Donner, K. Rehfeld, N. Marwan, M. H. Trauth, and J. Kurths.
Identification of dynamical transitions in marine palaeoclimate records by recurrence network analysis.
Nonlinear Processes in Geophysics, 18(5):545–562, 2011.
 24. Zhong-Ke Gao, Xin-Wang Zhang, Ning-De Jin, Reik V Donner, Norbert Marwan, and Jürgen Kurths.
Recurrence networks from multivariate signals for uncovering dynamic transitions of horizontal oil-water stratified flows.
EPL (Europhysics Letters), 103(5):50004, 2013.
 25. Zhong-Ke Gao, Yu-Xuan Yang, Peng-Cheng Fang, Yong Zou, Cheng-Yi Xia, and Meng Du.
Multiscale complex network for analyzing experimental multivariate time series.
EPL (Europhysics Letters), 109(3):30005, 2015.
 26. Zhong-Ke Gao, Xin-Wang Zhang, Ning-De Jin, Norbert Marwan, and Jürgen Kurths.
Multivariate recurrence network analysis for characterizing horizontal oil-water two-phase flow.
Physical Review E, 88(3):032910, 2013.
 27. Zhong-Ke Gao, Yu-Xuan Yang, Peng-Cheng Fang, Ning-De Jin, Cheng-Yi Xia, and Li-Dan Hu.
Multi-frequency complex network from time series for uncovering oil-water flow structure.
Scientific reports, 5:8222, 2015.
 28. Narayan Puthanmadam Subramaniam and Jari Hyttinen.
Analysis of nonlinear dynamics of healthy and epileptic eeg signals using recurrence based complex network approach.
In *Neural Engineering (NER), 2013 6th International IEEE/EMBS Conference on*, pages 605–608. IEEE, 2013.
 29. Narayan Puthanmadam Subramaniam and Jari Hyttinen.
Characterization of dynamical systems under noise using recurrence networks: Application to simulated and eeg data.
Physics Letters A, 378(46):3464–3474, 2014.
 30. Narayan Puthanmadam Subramaniam and Jari Hyttinen.
Dynamics of intracranial electroencephalographic recordings from epilepsy patients using univariate and bivariate recurrence networks.
Phys. Rev. E, 91:022927, Feb 2015.
 31. Narayan Puthanmadam Subramaniam, Jari Hyttinen, Nicholas G Hatsopoulos, and Kazutaka Takahashi.
Recurrence network analysis of wide band oscillations of local field potentials from the primary motor cortex reveals rich dynamics.
In *Neural Engineering (NER), 2015 7th International IEEE/EMBS Conference on*, pages 960–963. IEEE, 2015.
 32. Bartolo Luque, Lucas Lacasa, Fernando Ballesteros, and Jordi Luque.
Horizontal visibility graphs: Exact results for random time series.
Physical Review E, 80(4):046103, 2009.
 33. Norbert Marwan, M Carmen Romano, Marco Thiel, and Jürgen Kurths.
Recurrence plots for the analysis of complex systems.
Physics Reports, 438(5):237–329, 2007.
 34. Xiaoke Xu, Jie Zhang, and Michael Small.
Superfamily phenomena and motifs of networks induced from time series.
Proceedings of the National Academy of Sciences, 105(50):19601–19605, 2008.
 35. Jean-Pierre Eckmann, S Oliffson Kamphorst, and David Ruelle.
Recurrence plots of dynamical systems.
Europhys. Lett, 4(9):973–977, 1987.
 36. Michael Small, Jie Zhang, and Xiaoke Xu.
Transforming time series into complex networks.
In *Complex Sciences*, pages 2078–2089. Springer, 2009.
 37. Jonathan F Donges, Jobst Heitzig, Reik V Donner, and Jürgen Kurths.
Analytical framework for recurrence network analysis of time series.

- Physical Review E*, 85(4):046105, 2012.
38. Yong Zou, Reik V Donner, Jonathan F Donges, Norbert Marwan, and Jürgen Kurths.
Identifying complex periodic windows in continuous-time dynamical systems using recurrence-based methods.
Chaos: An Interdisciplinary Journal of Nonlinear Science, 20(4):043130, 2010.
 39. Jesper Dall and Michael Christensen.
Random geometric graphs.
Physical Review E, 66(1):016121, 2002.
 40. Reik V Donner, Jobst Heitzig, Jonathan F Donges, Yong Zou, Norbert Marwan, and Jürgen Kurths.
The geometry of chaotic dynamics—a complex network perspective.
The European Physical Journal B-Condensed Matter and Complex Systems, 84(4):653–672, 2011.
 41. Thomas Schreiber and Andreas Schmitz.
Improved surrogate data for nonlinearity tests.
Physical Review Letters, 77(4):635, 1996.
 42. Floris Takens.
Detecting strange attractors in turbulence.
In David Rand and Lai-Sang Young, editors, *Dynamical Systems and Turbulence, Warwick 1980*, volume 898 of *Lecture Notes in Mathematics*, pages 366–381. Springer Berlin Heidelberg, 1981.
 43. Holger Kantz and Thomas Schreiber.
Nonlinear time series analysis, volume 7.
Cambridge university press, 2004.
 44. Murray A Beauchamp.
An improved index of centrality.
Behavioral Science, 10(2):161–163, 1965.
 45. Gert Sabidussi.
The centrality index of a graph.
Psychometrika, 31(4):581–603, 1966.
 46. John P. Scott.
Social Network Analysis: A Handbook.
SAGE Publications, January 2000.
 47. Stanley Wasserman.
Social network analysis: Methods and applications, volume 8.
Cambridge university press, 1994.
 48. Linton C. Freeman.
A Set of Measures of Centrality Based on Betweenness.
Sociometry, 40(1):35–41, March 1977.
 49. Mark EJ Newman.
The structure and function of complex networks.
SIAM review, 45(2):167–256, 2003.
 50. Alain Barrat and Martin Weigt.
On the properties of small-world network models.
The European Physical Journal B-Condensed Matter and Complex Systems, 13(3):547–560, 2000.
 51. Mark EJ Newman.
Assortative mixing in networks.
Physical review letters, 89(20):208701, 2002.
 52. L da F Costa, Francisco A Rodrigues, Gonzalo Travieso, and Paulino Ribeiro Villas Boas.
Characterization of complex networks: A survey of measurements.
Advances in Physics, 56(1):167–242, 2007.
 53. Stefano Boccaletti, Vito Latora, Yamir Moreno, Martin Chavez, and D-U Hwang.
Complex networks: Structure and dynamics.
Physics reports, 424(4):175–308, 2006.
 54. JF Donges, RV Donner, K Rehfeld, N Marwan, MH Trauth, and J Kurths.
Identification of dynamical transitions in marine palaeoclimate records by recurrence network analysis.
Nonlinear Processes in Geophysics, 18(5):545–562, 2011.
 55. Jonathan F Donges, Reik V Donner, Martin H Trauth, Norbert Marwan, Hans-Joachim Schellnhuber, and Jürgen Kurths.

- Nonlinear detection of paleoclimate-variability transitions possibly related to human evolution.
Proceedings of the National Academy of Sciences, 108(51):20422–20427, 2011.
56. Edward N Lorenz.
Deterministic nonperiodic flow.
Journal of the atmospheric sciences, 20(2):130–141, 1963.
 57. Otto E Rössler.
An equation for continuous chaos.
Physics Letters A, 57(5):397–398, 1976.
 58. OE Rössler.
An equation for hyperchaos.
Physics Letters A, 71(2):155–157, 1979.
 59. Andrew M Fraser and Harry L Swinney.
Independent coordinates for strange attractors from mutual information.
Physical review A, 33(2):1134, 1986.
 60. Melvin Leok and Boon Tiong.
Estimating the attractor dimension of the equatorial weather system 1.
1995.
 61. Yong Zou, Reik V Donner, Mahesh Wickramasinghe, István Z Kiss, Michael Small, and Jürgen Kurths.
Phase coherence and attractor geometry of chaotic electrochemical oscillators.
Chaos: An Interdisciplinary Journal of Nonlinear Science, 22(3):033130, 2012.
 62. Jie Zhang, Junfeng Sun, Xiaodong Luo, Kai Zhang, Tomomichi Nakamura, and Michael Small.
Characterizing pseudoperiodic time series through the complex network approach.
Physica D: Nonlinear Phenomena, 237(22):2856–2865, 2008.
 63. Ruoxi Xiang, Jie Zhang, Xiao-Ke Xu, and Michael Small.
Multiscale characterization of recurrence-based phase space networks constructed from time series.
Chaos: An Interdisciplinary Journal of Nonlinear Science, 22(1):013107, 2012.
 64. Reik V Donner, Yong Zou, Jonathan F Donges, Norbert Marwan, and Jürgen Kurths.
Ambiguities in recurrence-based complex network representations of time series.
Physical Review E, 81(1):015101, 2010.
 65. Osvaldo A Rosso, Laura C Carpi, Patricia M Saco, Martín Gómez Ravetti, Angelo Plastino, and Hilda A Larrondo.
Causality and the entropy–complexity plane: Robustness and missing ordinal patterns.
Physica A: Statistical Mechanics and its Applications, 391(1):42–55, 2012.
 66. Claude E Shannon and W Weaver.
77ie mathematical theory of communication.
Urbana: University of Illinois Press, 1949.
 67. PW Lamberti, MT Martin, A Plastino, and OA Rosso.
Intensive entropic non-triviality measure.
Physica A: Statistical Mechanics and its Applications, 334(1):119–131, 2004.
 68. Christoph Bandt and Bernd Pompe.
Permutation entropy: a natural complexity measure for time series.
Physical review letters, 88(17):174102, 2002.
 69. Narayan Puthanmadam Subramaniam and Jari Hyttinen.
Dynamics of intracranial electroencephalographic recordings from epilepsy patients using univariate and bivariate recurrence networks.
Physical Review E, 91(2):022927, 2015.
 70. Robert S Fisher, Walter van Emde Boas, Warren Blume, Christian Elger, Pierre Genton, Phillip Lee, and Jerome Engel.
Epileptic seizures and epilepsy: definitions proposed by the international league against epilepsy (ilae) and the international bureau for epilepsy (ibe).
Epilepsia, 46(4):470–472, 2005.
 71. R Quian Quiroga, S Blanco, OA Rosso, H Garcia, and A Rabinowicz.
Searching for hidden information with gabor transform in generalized tonic-clonic seizures.
Electroencephalography and clinical Neurophysiology, 103(4):434–439, 1997.
 72. Herbert Henri Jasper.

- The ten twenty electrode system of the international federation.
Electroencephalography and clinical neurophysiology, 10:371–375, 1958.
73. Abbas Golestani and Robin Gras.
Can we predict the unpredictable?
Scientific reports, 4:6834–6834, 2014.
 74. Shouyi Wang, Wanpracha Art Chaovalitwongse, and Stephen Wong.
Online seizure prediction using an adaptive learning approach.
Knowledge and Data Engineering, IEEE Transactions on, 25(12):2854–2866, 2013.
 75. Cornelis J Stam.
Nonlinear dynamical analysis of eeg and meg: review of an emerging field.
Clinical Neurophysiology, 116(10):2266–2301, 2005.
 76. Ralph G Andrzejak, Klaus Lehnertz, Florian Mormann, Christoph Rieke, Peter David, and Christian E Elger.
Indications of nonlinear deterministic and finite-dimensional structures in time series of brain electrical activity: Dependence on recording region and brain state.
Physical Review E, 64(6):061907, 2001.
 77. Temujin Gautama, Danilo P Mandic, and Marc M Van Hulle.
The delay vector variance method for detecting determinism and nonlinearity in time series.
Physica D: Nonlinear Phenomena, 190(3):167–176, 2004.
 78. Susan S Spencer.
Neural networks in human epilepsy: evidence of and implications for treatment.
Epilepsia, 43(3):219–227, 2002.
 79. Louis Lemieux, Jean Daunizeau, and Matthew C Walker.
Concepts of connectivity and human epileptic activity.
Frontiers in systems neuroscience, 5, 2011.
 80. A Bragin, CL Wilson, and J Engel.
Chronic epileptogenesis requires development of a network of pathologically interconnected neuron clusters: a hypothesis.
Epilepsia, 41(s6):S144–S152, 2000.
 81. Karl J Friston et al.
Functional and effective connectivity in neuroimaging: a synthesis.
Human brain mapping, 2(1-2):56–78, 1994.
 82. Jan H Feldhoff, Reik V Donner, Jonathan F Donges, Norbert Marwan, and Jürgen Kurths.
Geometric detection of coupling directions by means of inter-system recurrence networks.
Physics Letters A, 376(46):3504–3513, 2012.
 83. Jonathan F Donges, Hanna CH Schultz, Norbert Marwan, Yong Zou, and Jürgen Kurths.
Investigating the topology of interacting networks.
The European Physical Journal B, 84(4):635–651, 2011.
 84. Ed Bullmore and Olaf Sporns.
Complex brain networks: graph theoretical analysis of structural and functional systems.
Nature Reviews Neuroscience, 10(3):186–198, 2009.
 85. Jonathan F Donges, Jobst Heitzig, Jakob Runge, Hanna CH Schultz, Marc Wiedermann, Alraune Zech, Jan Feldhoff, Aljoscha Rheinwald, Hannes Kutza, Alexander Radebach, et al.
Advanced functional network analysis in the geosciences: the pyunicorn package.
In *EGU General Assembly Conference Abstracts*, volume 15, page 3558, 2013.

PROCEEDINGS A

rspa.royalsocietypublishing.org

Research



Article submitted to journal

Author for correspondence:

Insert corresponding author name

e-mail: xxx@xxxx.xx.xx

Supplementary Materials for "Signatures of chaotic and stochastic dynamics uncovered with ϵ -recurrence networks"

N P Subramaniam^{1,3}, J F Donges^{2,4} and
J Hyttinen^{1,3}

¹ Department of Electronics and Communications
Engineering, Tampere University of Technology,
Tampere, Finland

² Potsdam Institute for Climate Impact Research,
Potsdam, Germany

³ BioMediTech, Tampere, Finland

⁴ Planetary Boundary Research Lab, Stockholm
University, Stockholm, Sweden.

THE ROYAL SOCIETY
PUBLISHING

© The Authors. Published by the Royal Society under the terms of the
Creative Commons Attribution License <http://creativecommons.org/licenses/by/4.0/>, which permits unrestricted use, provided the original author and
source are credited.

1. Supplementary figures

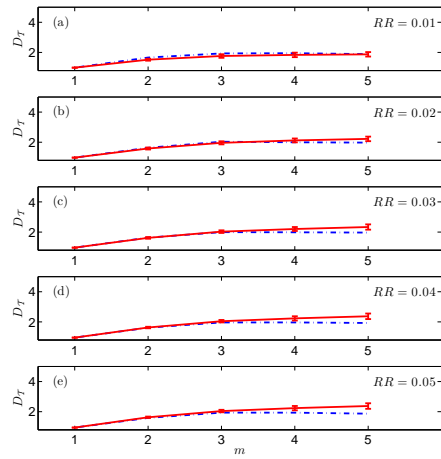


Figure S1. Transitivity dimension $D_{\mathcal{T}}$ of the ε -recurrence networks constructed from the x -component of the hyperchaotic Rössler system (dashed blue lines) and corresponding iAAFT surrogates (solid red lines) for varying embedding dimension m and recurrence rate RR ($N=10,000$). $D_{\mathcal{T}}$ for surrogates are averaged over 100 realizations with error bars representing the standard deviation.

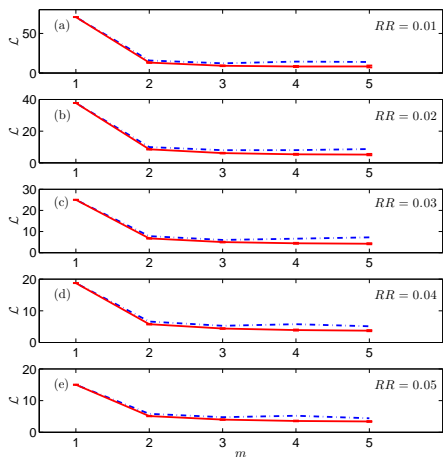


Figure S2. Average path length \mathcal{L} of the ε -recurrence networks constructed from the x -component of the hyperchaotic Rössler system (dashed blue lines) and corresponding iAAFT surrogates (solid red lines) for varying embedding dimension m and recurrence rate RR ($N=10,000$). \mathcal{L} for surrogates are averaged over 100 realizations with error bars representing the standard deviation.

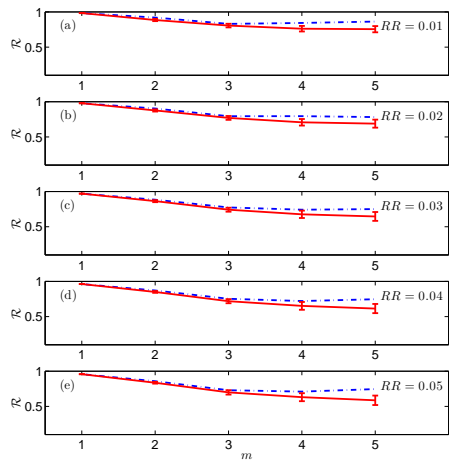


Figure S3. Assortativity \mathcal{R} of the ε -recurrence networks constructed from the x -component of the hyper-chaotic Rössler system (dashed blue lines) and corresponding iAAFT surrogates (solid red lines) for varying embedding dimension m and recurrence rate RR ($N=10,000$). \mathcal{R} for surrogates are averaged over 100 realizations with error bars representing the standard deviation.

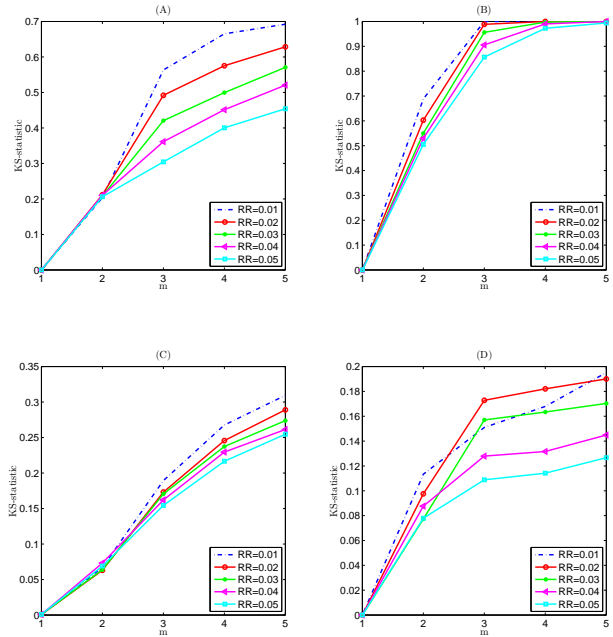


Figure S4. KS-statistic for the local clustering coefficient C_i , closeness centrality c_i , betweenness centrality b_i and degree centrality k_i for the chaotic Rossler system ($N = 10,000$) and the corresponding iAAFT surrogate for varying embedding dimension m and recurrence rate RR .

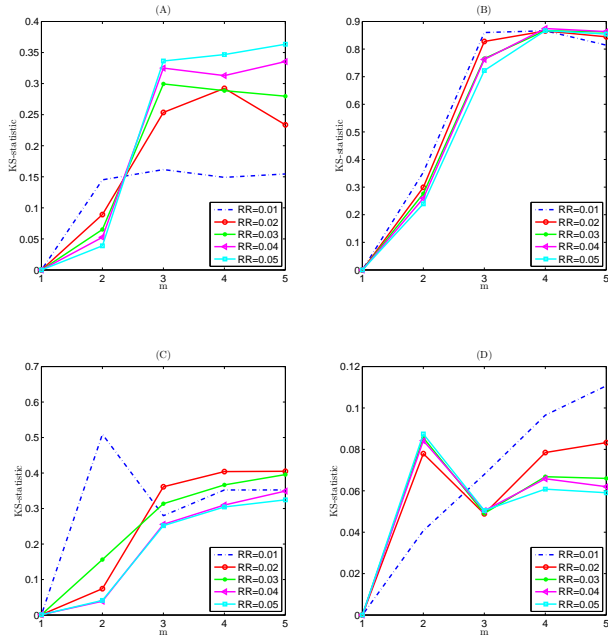


Figure S5. KS-statistic for the local clustering coefficient C_i , closeness centrality c_i , betweenness centrality b_i and degree centrality k_i for the hyper-chaotic Rössler system ($N = 10,000$) and the corresponding iAAFT surrogate for varying embedding dimension m and recurrence rate RR .

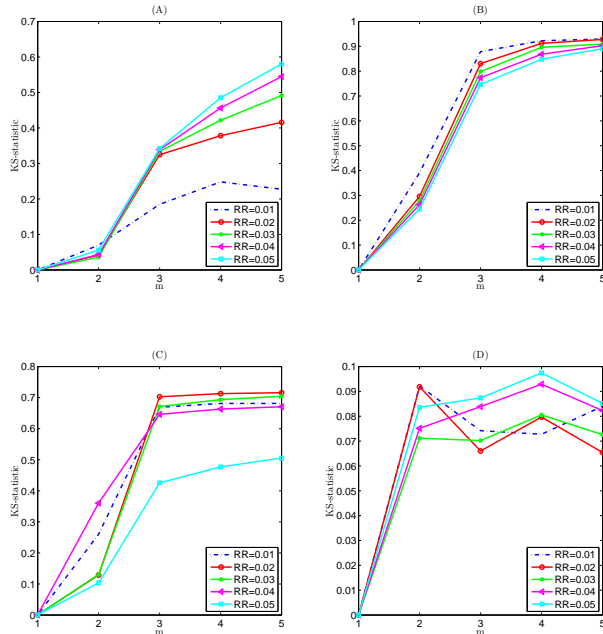


Figure S6. KS-statistic for the local clustering coefficient C_i , closeness centrality c_i , betweenness centrality b_i and degree centrality k_i for the hyper-chaotic Rössler system ($N = 15,000$) and the corresponding iAAFT surrogate for varying embedding dimension m and recurrence rate RR .

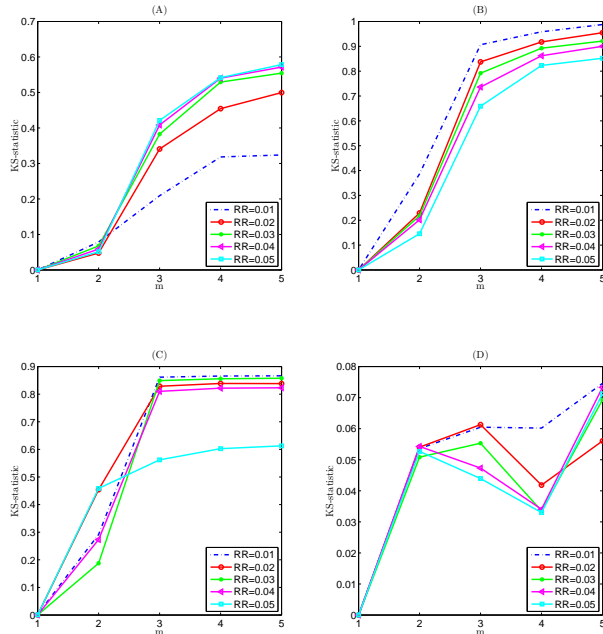


Figure S7. KS-statistic for the local clustering coefficient C_i , closeness centrality c_i , betweenness centrality b_i and degree centrality k_i for the hyper-chaotic Rössler system ($N = 20,000$) and the corresponding iAAFT surrogate for varying embedding dimension m and recurrence rate RR .

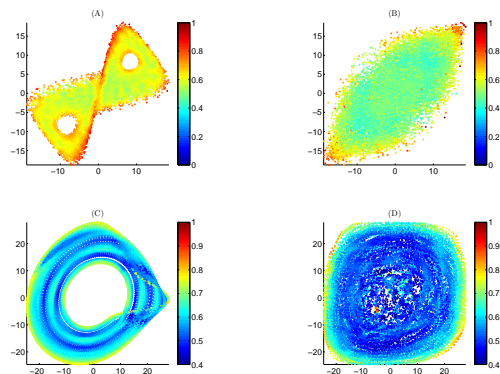


Figure S8. Color-coded representation of the local clustering coefficient C_i for the reconstructed Lorenz attractor (A) and the corresponding iAAFT surrogate (B) for $N = 20,000$ and $RR = 0.02$. (C-D) likewise in (A-B) but for reconstructed chaotic Rössler attractor and the corresponding iAAFT surrogate.

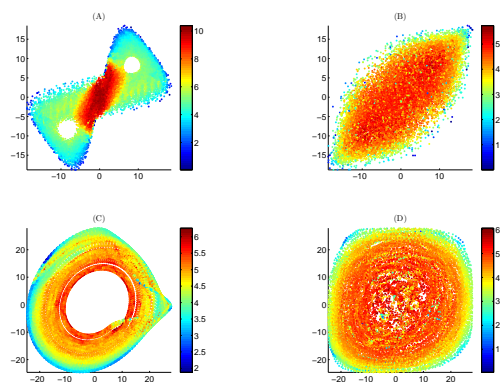


Figure S9. Color-coded representation of the logarithm of betweenness centrality $\log_{10}(b_i + 1)$ for the reconstructed Lorenz attractor (A) and the corresponding iAAFT surrogate (B) for $N = 20,000$ and $RR = 0.02$. (C-D) likewise in (A-B) but for reconstructed chaotic Rössler attractor and the corresponding iAAFT surrogate.

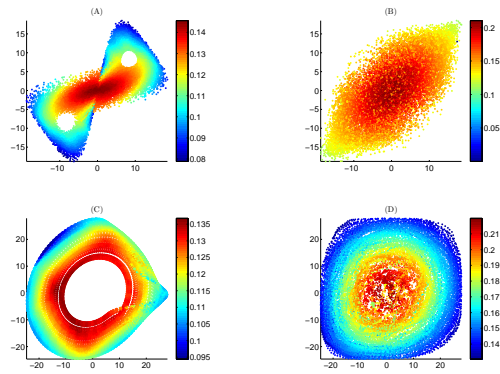


Figure S10. Color-coded representation of the closeness centrality c_i for the reconstructed Lorenz attractor (A) and the corresponding iAAFT surrogate (B) for $N = 20,000$ and $RR = 0.02$. (C-D) likewise in (A-B) but for reconstructed chaotic Rössler attractor and the corresponding iAAFT surrogate.

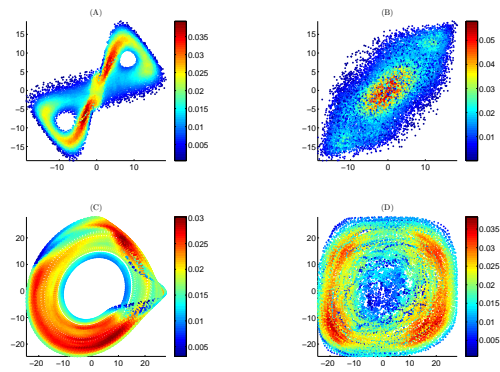


Figure S11. Color-coded representation of the local recurrence rate (proportional to degree centrality k_i) for the reconstructed Lorenz attractor (A) and the corresponding iAAFT surrogate (B) for $N = 20,000$ and $RR = 0.02$. (C-D) likewise in (A-B) but for reconstructed chaotic Rössler attractor and the corresponding iAAFT surrogate.

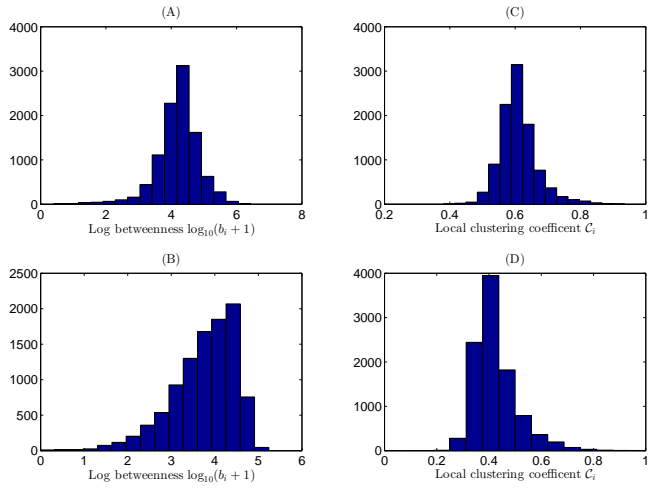


Figure S12. Distribution of log betweenness centrality $\log(b_i + 1)$ for the Lorenz attractor (A) and the corresponding iAAFT surrogate (B). (C)-(D) same as (A)-(B) but for local clustering coefficient C_i . The parameters for the exemplary plot are, embedding dimension $m = 5$ and $RR = 0.02$.

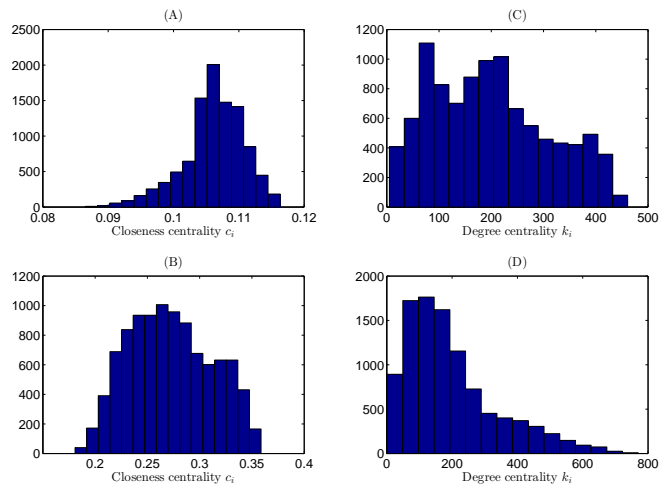


Figure S13. Distribution of closeness centrality c_i for the Lorenz attractor (A) and the corresponding iAAFT surrogate (B). (C)-(D) same as (A)-(B) but for degree centrality k_i . The parameters for the exemplary plot are, embedding dimension $m = 5$ and $RR = 0.02$.

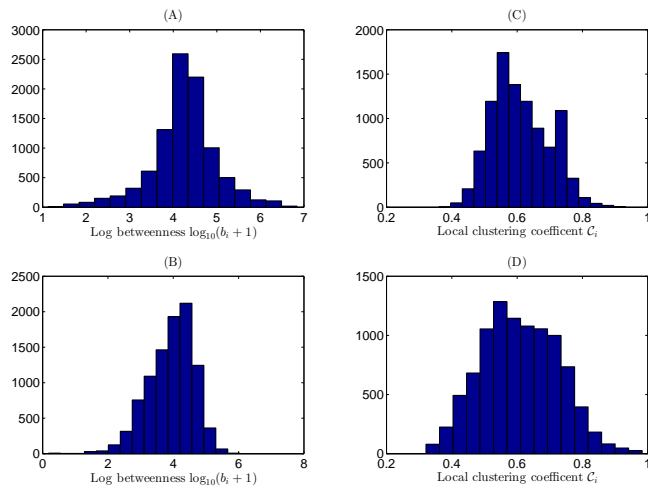


Figure S14. Distribution of log betweenness centrality $\log_{10}(b_i + 1)$ for the hyper-chaotic Rössler attractor (A) and the corresponding iAAFT surrogate (B). (C)-(D) same as (A)-(B) but for local clustering coefficient C_i . The parameters for the exemplary plot are, embedding dimension $m = 5$, $RR = 0.02$ and $N = 10,000$.

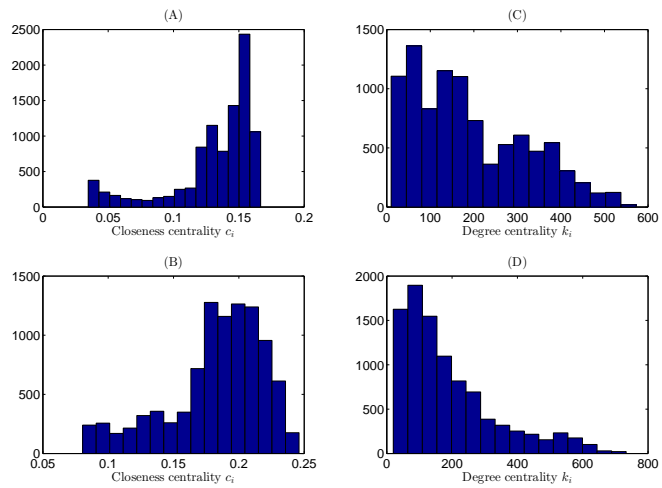


Figure S15. Distribution of closeness centrality c_i for the hyper-chaotic Rössler attractor (A) and the corresponding iAAFT surrogate (B). (C)-(D) same as (A)-(B) but for degree centrality k_i . The parameters for the exemplary plot are, embedding dimension $m = 5$, $RR = 0.02$ and $N = 10,000$.

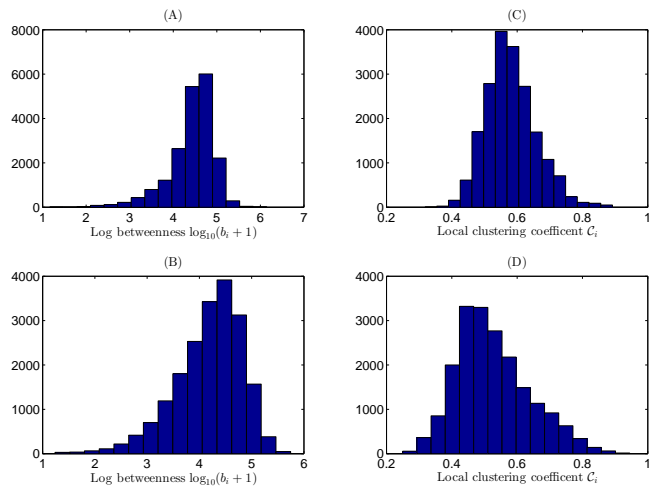


Figure S16. Distribution of log betweenness centrality $\log_{10}(b_i + 1)$ for the hyper-chaotic Rössler attractor (A) and the corresponding iAAFT surrogate (B). (C)-(D) same as (A)-(B) but for local clustering coefficient C_i . The parameters for the exemplary plot are, embedding dimension $m = 5$, $RR = 0.02$ and $N = 20,000$.

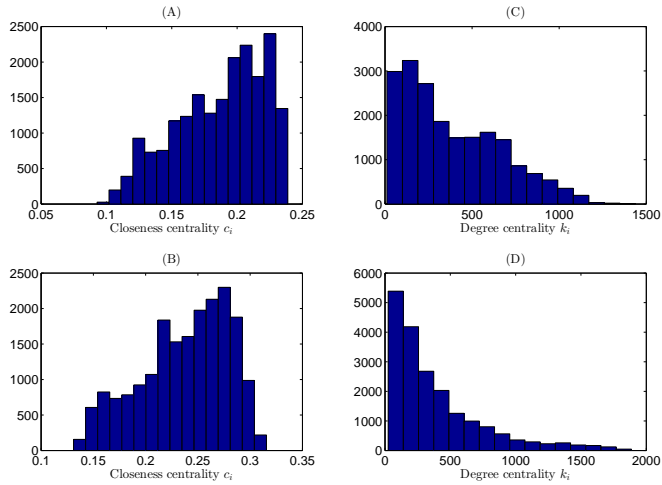


Figure S17. Distribution of closeness centrality c_i for the hyper-chaotic Rössler attractor (A) and the corresponding iAAFT surrogate (B). (C)-(D) same as (A)-(B) but for degree centrality k_i . The parameters for the exemplary plot are, embedding dimension $m = 5$, $RR = 0.02$ and $N = 20,000$.

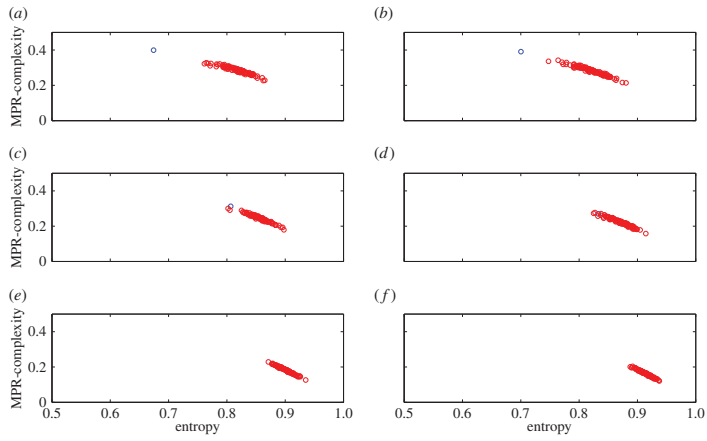


Figure 518. MPR complexity–entropy plane for chaotic Lorenz system (blue circle) and corresponding 99 iAAFT surrogates (red circles) under noise levels (a) 0%, (b) 10%, (c) 20%, (d) 40%, (e) 60% and (f) 100%. The data length is $N = 200$.

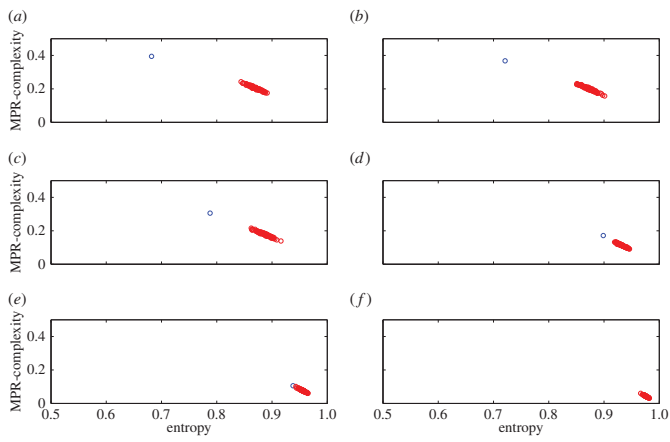


Figure 519. MPR complexity–entropy plane for chaotic Lorenz system (blue circle) and corresponding 99 iAAFT surrogates (red circles) under noise levels (a) 0%, (b) 10%, (c) 20%, (d) 40%, (e) 60% and (f) 100%. The data length is $N = 1000$.

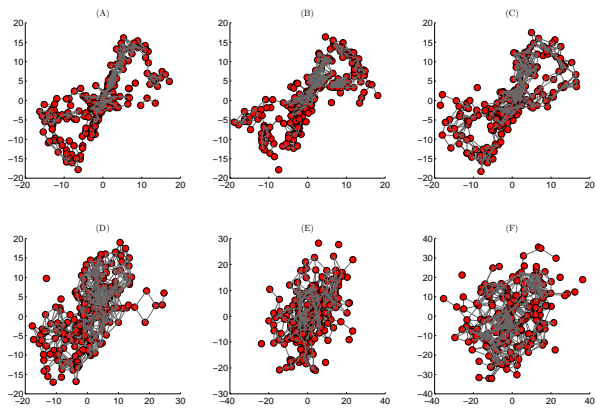


Figure S20. Recurrence networks associated with the Lorenz system under noise levels 0% (A), 10% (B), 20% (C), 40% (D), 60% (E), and 100% (F). The data length $N = 200$, recurrence rate $RR = 0.05$, embedding dimension $m = 3$ and the embedding delay $\tau = 3$. The red circles represent the vertices (state vectors) and the gray lines represent the edges between the vertices.

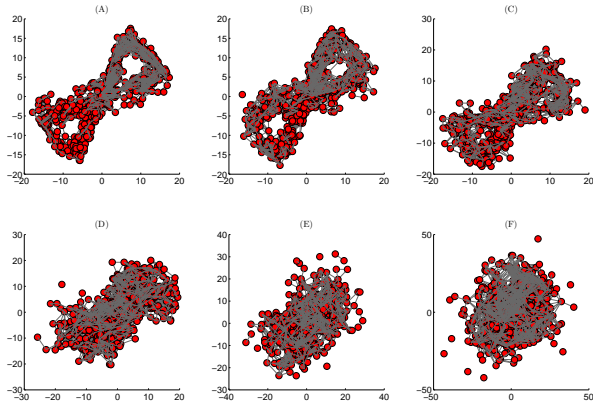


Figure S21. Recurrence networks associated with the Lorenz system under noise levels 0% (A), 10% (B), 20% (C), 40% (D), 60% (E), and 100% (F). The data length $N = 500$, recurrence rate $RR = 0.05$, embedding dimension $m = 3$ and the embedding delay $\tau = 3$. The red circles represent the vertices (state vectors) and the gray lines represent the edges between the vertices.

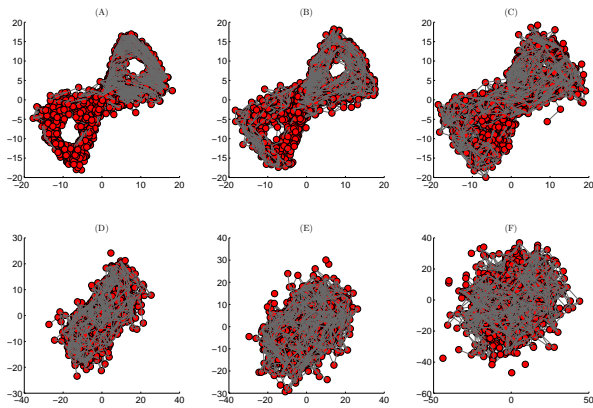


Figure S22. Recurrence networks associated with the Lorenz system under noise levels 0% (A), 10% (B), 20% (C), 40% (D), 60% (E), and 100% (F). The data length $N = 1000$, recurrence rate $RR = 0.05$, embedding dimension $m = 3$ and the embedding delay $\tau = 3$. The red circles represent the vertices (state vectors) and the gray lines represent the edges between the vertices.

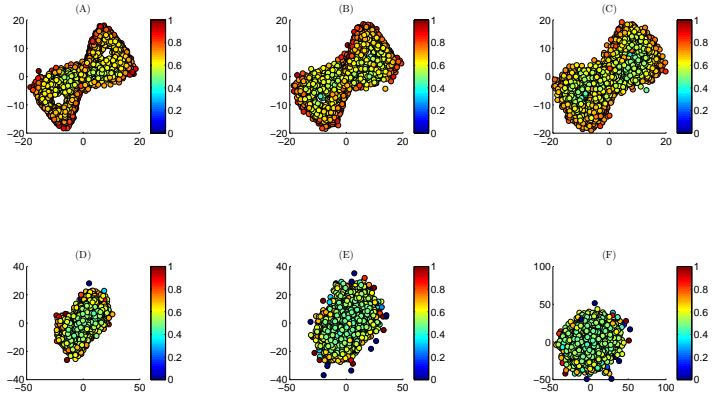


Figure S23. Color-coded representation of local clustering coefficient for the Lorenz attractor under noise levels 0% (A), 10% (B), 20% (C), 40% (D), 60% (E), and 100% (F). The data length $N = 5,000$, recurrence rate $RR = 0.05$, embedding dimension $m = 3$ and the embedding delay $\tau = 3$.

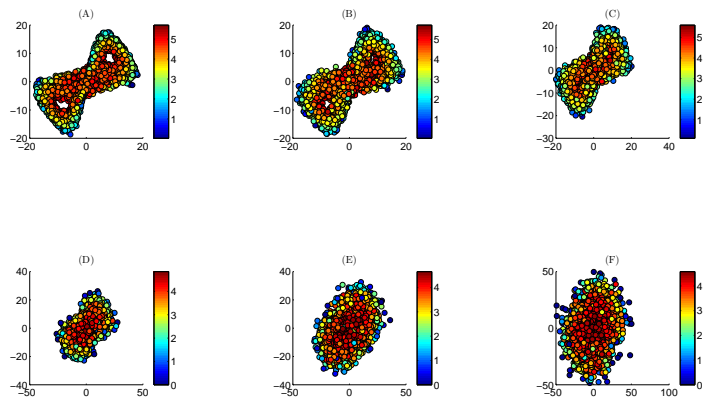


Figure S24. Color-coded representation of log betweenness centrality for the Lorenz attractor under noise levels 0% (A), 10% (B), 20% (C), 40% (D), 60% (E), and 100% (F). The data length $N = 5,000$, recurrence rate $RR = 0.05$, embedding dimension $m = 3$ and the embedding delay $\tau = 3$.

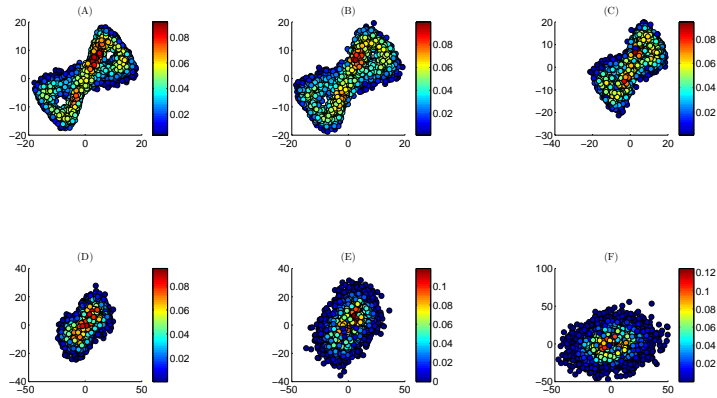


Figure S25. Color-coded representation of local recurrence rate (proportional to degree centrality) for the Lorenz attractor under noise levels 0% (A), 10% (B), 20% (C), 40% (D), 60% (E), and 100% (F). The data length $N = 5,000$, recurrence rate $R/R = 0.05$, embedding dimension $m = 3$ and the embedding delay $\tau = 3$.

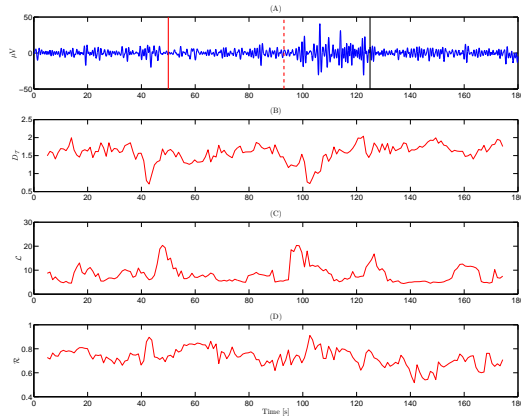


Figure S26. Moving window ε -recurrence network analysis of epileptic EEG data showing D_T , \mathcal{L} and \mathcal{R} before, during and after the seizure. (A) EEG data from channel C_4 of patient 2 with the clinical onset of seizure marked with solid red line. The dashed red line represents beginning of the clonic phase and the solid black line represents that end of seizure. (B-D) Temporal profile of the global measures (for $m = 8$) using a moving window of 10 seconds (≈ 1000 samples) with 90% overlap.

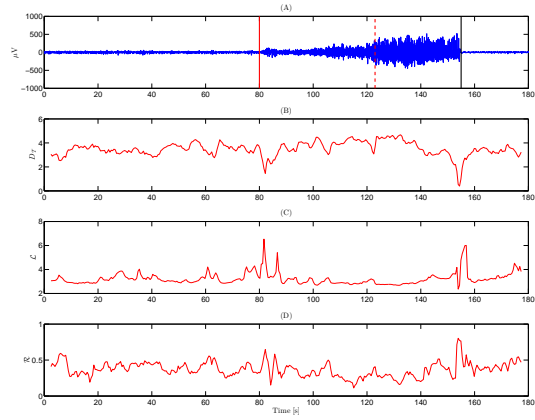


Figure S27. Moving window ε -recurrence network analysis of epileptic EEG data showing D_T , L and R before, during and after the seizure. (A) EEG data from channel $C4$ of patient 1 with the clinical onset of seizure marked with solid red line. The dashed red line represents beginning of the clonic phase and the solid black line represents that end of seizure. (B-D) Temporal profile of the global measures (for $m = 8$) using a moving window of 5 seconds (≈ 500 samples) with 90% overlap.

Puthanmadam Subramaniam, N. and Hyttinen, J.

Dynamics of intracranial electroencephalographic recordings from epilepsy patients using univariate and bivariate recurrence networks

Physical Review E, 91(2):022927, 2015.

Reprinted with permission from the publisher.

Dynamics of intracranial electroencephalographic recordings from epilepsy patients using univariate and bivariate recurrence networks

Narayan Puthanmadam Subramaniyam* and Jari Hyttinen

Department of Electronics and Communications, Tampere University of Technology, BioMediTech, Tampere, Finland
(Received 23 September 2014; revised manuscript received 17 December 2014; published 27 February 2015)

Recently Andrezek *et al.* combined the randomness and nonlinear independence test with iterative amplitude adjusted Fourier transform (iAAFT) surrogates to distinguish between the dynamics of seizure-free intracranial electroencephalographic (EEG) signals recorded from epileptogenic (focal) and nonepileptogenic (nonfocal) brain areas of epileptic patients. However, stationarity is a part of the null hypothesis for iAAFT surrogates and thus nonstationarity can violate the null hypothesis. In this work we first propose the application of the randomness and nonlinear independence test based on recurrence network measures to distinguish between the dynamics of focal and nonfocal EEG signals. Furthermore, we combine these tests with both iAAFT and truncated Fourier transform (TFT) surrogate methods, which also preserves the nonstationarity of the original data in the surrogates along with its linear structure. Our results indicate that focal EEG signals exhibit an increased degree of structural complexity and interdependency compared to nonfocal EEG signals. In general, we find higher rejections for randomness and nonlinear independence tests for focal EEG signals compared to nonfocal EEG signals. In particular, the univariate recurrence network measures, the average clustering coefficient C and assortativity \mathcal{R} , and the bivariate recurrence network measure, the average cross-clustering coefficient C_{cross} , can successfully distinguish between the focal and nonfocal EEG signals, even when the analysis is restricted to nonstationary signals, irrespective of the type of surrogates used. On the other hand, we find that the univariate recurrence network measures, the average path length L , and the average betweenness centrality BC fail to distinguish between the focal and nonfocal EEG signals when iAAFT surrogates are used. However, these two measures can distinguish between focal and nonfocal EEG signals when TFT surrogates are used for nonstationary signals. We also report an improvement in the performance of nonlinear prediction error N and nonlinear interdependence measure L used by Andrezek *et al.*, when TFT surrogates are used for nonstationary EEG signals. We also find that the outcome of the nonlinear independence test based on the average cross-clustering coefficient C_{cross} is independent of the outcome of the randomness test based on the average clustering coefficient C . Thus, the univariate and bivariate recurrence network measures provide independent information regarding the dynamics of the focal and nonfocal EEG signals. In conclusion, recurrence network analysis combined with nonstationary surrogates can be applied to derive reliable biomarkers to distinguish between epileptogenic and nonepileptogenic brain areas using EEG signals.

DOI: 10.1103/PhysRevE.91.022927

PACS number(s): 05.45.Tp, 02.10.Ox, 87.19.la

I. INTRODUCTION

Epilepsy is a dynamical disorder of the brain [1]. It is characterized by epileptic seizures which interrupt the normal functioning of the brain in a recurrent and unpredictable manner [2]. It is generally accepted that the epileptic brain transitions between different dynamical states, namely the interictal state (occurring between the seizures), the preictal state (occurring before the seizure), the ictal state (occurring during the seizure) [3], and the postictal state (occurring after the seizure). Removal of the brain areas responsible for seizure generation (known as epileptogenic areas) is a widely accepted therapeutic option for a subset of patients diagnosed with drug-resistant focal epilepsy [4]. Intracranial electroencephalographic (EEG) recordings obtained from the brain surface or from deeper structures within the brain are used for the purpose of localizing the epileptogenic areas [5]. In contrast to the normal background EEG activity, epileptic EEG shows increased nonlinearity [6] and thus ictal EEG recordings can play an important role in the localization of the epileptogenic areas.

However, it has also been shown by several human as well as nonhuman animal studies that even during the interictal period, the epileptic brain is different from normal and it has been hypothesized that the interictal EEG recordings also exhibit increased nonlinearity due to the deterministic dynamics that accompanies the epileptic process [3]. Thus, we can hypothesize that the analysis of interictal EEG signals can provide valuable information about the localization of epileptogenic areas. Besides the obvious clinical benefit, this is also extremely beneficial from the patient's point of view, as it minimizes the need to record seizures for the sake of localization, since occurrence of each seizure is a potentially debilitating event that can cause health impairment [5].

Recently, Andrezek *et al.* [5] combined iterative amplitude adjusted Fourier transform (iAAFT) surrogates with nonlinear prediction error N , a univariate measure, and nonlinear interdependence measure L , a bivariate measure, to test for randomness and nonlinear independence respectively, in intracranial EEG signals. These EEG signals were acquired from epileptogenic (focal EEG signals) and nonepileptogenic areas (nonfocal EEG signals) of five epilepsy patients. They analyzed seizure-free recordings by excluding recordings of the seizure activity and three hours after the last seizure activity. Their results showed that the focal EEG signals had higher rejections for both the randomness test and nonlinear independence test

*npsubramaniyam@gmail.com

compared to the nonfocal EEG signals, thus indicating that the focal EEG signals are more nonrandom and have more nonlinear interdependence between them compared to the nonfocal EEG signals. They also used linear variability measures to test for stationarity in the EEG signals. Based on the surrogate testing, their results showed that the nonfocal EEG signals are more nonstationary compared to the focal EEG signals. The nonstationarity in the time series caused an increase in the rejection probability of both the randomness test (for focal EEG signals) and nonlinear independence test (for focal and nonfocal EEG signals). Furthermore, they also showed that the contrast between the focal and nonfocal EEG signals using the randomness test and nonlinear independence test is further enhanced when the signals that reject the stationarity test are excluded. They also studied the dependence between the randomness and nonlinear independence test and found that these two tests give nonredundant information and thus can contribute to characterization of EEG signals in different ways. These results are highly important from clinical as well as the physics point of view, as they reveal that the focal EEG signals are more nonrandom, more nonlinearly interdependent and more stationary compared to the nonfocal EEG signals. Thus, these measures can be used as potential biomarkers to delineate the epileptogenic brain areas from the nonepileptogenic ones.

However, one important issue that remains to be addressed more adequately is the robustness of these nonlinear measures to nonstationarity in the EEG signals. Whether the contrast between the focal and nonfocal EEG signals, as measured by the randomness and nonlinear independence test, still remains significant when we only consider those EEG signals that have rejected the stationarity test remains to be answered. In other words, do these nonlinear measures still perform when they are applied to nonstationary signals? Moreover, in Ref. [5], iAAFT surrogates were used which are stationary by construction and therefore nonstationarity can thus violate the null hypothesis [7,8]. This is a relevant and vexing issue as the epileptic signals often exhibit nonstationary behavior [9]. Even though the focal EEG signals are more stationary than the nonfocal EEG signals as per the findings reported in Ref. [5], there can still be a considerable degree of nonstationarity present in the focal EEG signals. For instance in Ref. [5], Andrzejak *et al.* still found that out of 3750 focal EEG signals, 1750 signals rejected the stationarity test (i.e., roughly 46%). Ideally, the measures derived from the nonlinear theory should be able to distinguish between the dynamics of the focal and nonfocal EEG signals even in the presence of some degree of nonstationarity.

The brain is a complex dynamical system and the dynamics associated with complex systems can also be described using the method of recurrence plots [10]. This method makes use of the concept of recurrence, which is one of the fundamental properties of a complex dynamical system. Recurrence plot (RP) based techniques can be used for the analysis of short and nonstationary data [10]. An RP is a graphical representation of the binary recurrence matrix that encodes the relationship between the two states that are neighbors in phase space (as per some proximity criterion) [11]. This recurrence matrix can be reinterpreted as an adjacency matrix of an undirected complex network, which is known as the recurrence network. There are many ways of transforming a time series into a complex network. The recurrence networks fall under the

category of proximity networks. There are different types of recurrence networks, namely the k nearest neighbor networks, the adaptive nearest neighbor networks, and the ε -recurrence networks. In k nearest neighbor networks, the neighborhood of each vertex (state) is defined in terms of a fixed mass, i.e., k nearest neighbors are fixed for each vertex in the network resulting in a directed network [12]. A symmetric and undirected version of the k nearest neighbor networks has also been proposed in Ref. [13]. In adaptive nearest neighbor networks, suggested in Refs. [14,15], undirected networks are obtained after correcting for a constant number of edges for each vertex [16]. ε networks are the most extensively studied and applied networks, where the neighborhood of each vertex is defined in terms of a fixed phase space volume ε [11,17]. The underlying common factor in all the above mentioned recurrence networks is that the vertices of the network are represented by the state vectors and the edges between the vertices are represented by the recurrence of the states. Different measures derived from graph theory can then be used for the quantitative characterization of the recurrence networks to gain an insight into the phase space properties of the dynamical system underlying a time series.

ε networks have been applied to model systems as well as real world data like paleoclimate records and biomedical data [11,18–26]. Network measures, like the average clustering coefficient \bar{C} and the average path length \bar{L} , have been used to discriminate between chaotic and periodic dynamics [20]. The transitivity \mathcal{T} (local and global) has been shown to trace unstable periodic orbits [17]. In [27], local clustering coefficient and transitivity \mathcal{T} were used to define measures of dimension in phase space. As an example of the application of ε networks to real world data Donner *et al.* [16] used the network measures average path length \bar{L} , transitivity \mathcal{T} , assortativity \mathcal{R} , and the network diameter \mathcal{D} to identify hidden transitions in marine terrigenous dust flux record. They found that the intervals identified by these network measures correlated with important transitions in climate system.

Apart from ε networks which can be used for the dynamical characterization of univariate time series, recently a bivariate extension of the recurrence network approach has been proposed to quantify the interdependence between two dynamical systems that share the same phase space [28]. This approach is basically a straightforward extension of the cross-recurrence plot method proposed in Ref. [29]. After embedding two time series $x(t)$ and $y(t)$ in the same phase space, a cross-recurrence matrix can be derived using the test for closeness (based on some proximity criterion) between each point in the phase space of $x(t)$ with each point in the phase space of $y(t)$. Now one can define the intersystem recurrence network (IRN) [28], which is basically comprised of (1) two monopartite graphs, representing the recurrence networks associated with time series $x(t)$ and $y(t)$ individually, (2) a bipartite graph known as the cross-recurrence network, including links between vertices of two recurrence networks associated with $x(t)$ and $y(t)$. Cross-network measures like cross-average clustering coefficient C_{cross} , and cross-transitivity $\mathcal{T}_{\text{cross}}$ [30] have been proposed to study the topology of cross-recurrence networks to characterize and identify the coupling direction between two time series [28]. Cross-network measures have been applied to model systems like coupled chaotic oscillators and real world

data like the paleoclimate data [28] and also to characterize horizontal oil-water two-phase flows [31].

Given the ability of recurrence network measures to characterize dynamics of the underlying complex system using the time series data, its application to EEG time series has not been fully explored. Recurrence network measures like the average clustering coefficient \mathcal{C} and average path length \mathcal{L} have been used to compare the dynamical properties of EEG signals derived from healthy and epileptic patients [32,33]. Particularly, bivariate measures derived from cross-recurrence networks have not been investigated to identify interdependence between two EEG time series. Also the robustness of recurrence network measures (both univariate and bivariate) against nonstationarity has not been investigated using any real world data like the EEG time series. Also, whether or not the univariate recurrence network measure and the bivariate cross-recurrence network measure give redundant information about the dynamics of the underlying system has hitherto not been studied.

To address these issues, combined with surrogates generated using the iAAFT scheme [34], we apply ε -recurrence network measures (henceforth simply referred as recurrence network measures) derived from univariate and bivariate EEG time series described in Ref. [5]. In order to make the results more reliable, particularly in the case of nonstationary EEG signals, we also use the truncated Fourier transform (TFT) surrogates proposed by Nakamura *et al.* [35]. TFT surrogates are particularly useful in preserving some nonstationarity present in the original data in the surrogates, unlike the iAAFT surrogates which can only preserve the linear properties [35,36]. Particularly, we test for randomness based on network measures, the average clustering coefficient \mathcal{C} , assortativity \mathcal{R} , the average path length \mathcal{L} , and the average betweenness centrality BC and independence based on cross-network measure, the average cross-clustering coefficient $\mathcal{C}_{\text{cross}}$ in the focal and nonfocal EEG signals. To facilitate a direct comparison with the results obtained in Ref. [5] where the effect of nonstationarity on nonlinear prediction error N and nonlinear interdependence measure L was studied along with the dependence between these two measures, we also compute the same rejection probability measures for the randomness and nonlinear independence test combined with iAAFT and TFT (in the case of nonstationary EEG signals) surrogates.

II. MATERIALS AND METHODS

A. EEG data and preprocessing

The EEG data used in this study is described in Ref. [5] and is publicly available for download at [37]. Therefore, we will only briefly describe the composition of EEG signals and the preprocessing steps involved. For a detailed explanation about the EEG data and recording conditions the reader is directed to Ref. [5].

Intracranial EEG recordings were obtained from five patients who were candidates for epilepsy surgery. The dataset is comprised of two sets of EEG data, namely (a) focal EEG signals recorded from epileptogenic areas and (b) nonfocal EEG signals recorded from nonepileptogenic areas. The signal has been digitally bandpass filtered between 0.5 and 150 Hz. The signals were originally recorded at 1024 Hz and were

down-sampled to 512 Hz. Further, each set of this dataset is comprised of randomly selected 3750 pairs of simultaneously recorded signals, from two neighboring channels. This random selection procedure involved selecting one of the five patients randomly and then selecting a recording of 20 sec long from the focal EEG channel (each EEG recording was divided into a 20-sec-long window comprised of 10240 samples) and its neighboring channel for the focal EEG signal pair. Likewise selection was done for the nonfocal EEG signal pairs. It is important to note that the focal EEG channels are defined as those channels where ictal EEG signal changes were first detected by two expert neurologists. All other channels are defined as nonfocal EEG channels. Also, recordings of any seizure activity and three hours after the last seizure were excluded [5]. Recording samples contaminated by artifacts were also excluded. Finally, before computing any nonlinear measure, the data are low-pass filtered with a cutoff frequency of 40 Hz with an eighth order Butterworth filter and further downsampled to 128 Hz [5]. Thus, each EEG signal was 20 sec long and contained 2560 samples.

B. Recurrence networks

A univariate time series $x(t)$ can be transformed into a complex network based on the concept of recurrences. In particular, recurrence occurs if at some time instance t_j , the trajectory of a complex dynamical system returns into the neighborhood of its previous state \mathbf{x}_i at previous time instance t_i , where $t_i < t_j$ [17]. If this neighborhood is defined in terms of an ε ball centered at \mathbf{x}_i [17], one can define a binary recurrence matrix $\mathbf{R}(\varepsilon)$ with elements [11,38]

$$R_{i,j}(\varepsilon) = \Theta(\varepsilon - \|\mathbf{x}_i - \mathbf{x}_j\|), \quad (1)$$

where $\mathbf{x}_i = (x(t_i), x(t_i + \tau), \dots, x[t_i + (m-1)\tau])$ is the reconstructed m -dimensional phase space vector corresponding to the observation point $t = t_i$ in the time series, $\Theta(\cdot)$ is the Heaviside function, τ is the embedding delay, $\|\cdot\|$ is any distance norm, and ε is the recurrence threshold specifying the maximum spatial distance between the neighboring states.

If there are two observational time series $x(t)$ and $y(t)$ (for instance, a signal recorded from a pair of EEG electrodes) emerging from same complex dynamical system, one can define a cross-recurrence matrix $\mathbf{R}_{xy}^{\text{cross}}(\varepsilon)$ with elements [29]

$$R_{i,j}^{\text{cross}}(\varepsilon) = \Theta(\varepsilon - \|\mathbf{x}_i - \mathbf{y}_j\|), \quad (2)$$

where \mathbf{x}_i and \mathbf{y}_j are the reconstructed m -dimensional phase space vectors from the observed time series at point $t = t_i$ for $x(t)$ and $t = t_j$ for $y(t)$ respectively. In this case, ε is known as the cross-recurrence threshold. Combining Eqs. (1) and (2), one can define a 2×2 intersystems recurrence matrix [28] $\mathbf{R}^{\text{IS}}(\varepsilon)$ as follows:

$$\mathbf{R}^{\text{IS}}(\varepsilon) = \begin{pmatrix} \mathbf{R}_x(\varepsilon) & \mathbf{R}_{xy}^{\text{cross}}(\varepsilon) \\ \mathbf{R}_{yx}^{\text{cross}}(\varepsilon) & \mathbf{R}_y(\varepsilon) \end{pmatrix}, \quad (3)$$

where $\mathbf{R}_{yx}^{\text{cross}}(\varepsilon) = [\mathbf{R}_{xy}^{\text{cross}}(\varepsilon)]^T$, is the cross-recurrence matrix derived from the bivariate time series $x(t)$ and $y(t)$, $\mathbf{R}_x(\varepsilon)$ and $\mathbf{R}_y(\varepsilon)$ are recurrence matrices derived individually from univariate time series $x(t)$ and $y(t)$ respectively. The intersystem recurrence matrix can be transformed into an adjacency matrix

using the following transformation [28]:

$$\mathbf{A}(\varepsilon) = \mathbf{R}^{\text{IS}}(\varepsilon) - \mathbb{I} \quad (4)$$

resulting in

$$\mathbf{A}(\varepsilon) = \begin{pmatrix} \mathbf{A}_x^{\text{self}}(\varepsilon) & \mathbf{A}_{xy}^{\text{cross}}(\varepsilon) \\ \mathbf{A}_{yx}^{\text{cross}}(\varepsilon) & \mathbf{A}_y^{\text{self}}(\varepsilon) \end{pmatrix}, \quad (5)$$

where \mathbb{I} is an identity matrix of size $2N$ [given that the length of the phase space vectors reconstructed from $x(t)$ and $y(t)$ is N each]. The adjacency matrices $\mathbf{A}_x^{\text{self}}$ and $\mathbf{A}_y^{\text{self}}$ represent the unweighted and undirected complex network derived from time series $x(t)$ and $y(t)$ individually, which is simply known as the recurrence network [11,17]. On the other hand the adjacency matrices $\mathbf{A}_{xy}^{\text{cross}}(\varepsilon)$ and $\mathbf{A}_{yx}^{\text{cross}}(\varepsilon)$ represent the cross-recurrence network derived from bivariate time series $x(t)$ and $y(t)$ jointly. Together these adjacency matrices represent the IRN.

Now one can estimate complex (cross-)network measures using the $\mathbf{A}^{\text{self}}(\varepsilon)$ and $\mathbf{A}^{\text{cross}}(\varepsilon)$ to derive univariate and bivariate measures for a single channel and two channel time series respectively. Instead of specifying the recurrence threshold ε , we specified the recurrence rate RR, so that the resulting recurrence networks have approximately the same number of edges. This allows for an objective comparison of the network topologies using graph theoretical measures. In this work, we set embedding delay $\tau = 4$ and embedding dimension $m = 8$ as suggested in Ref. [5]. Further, we fixed the recurrence rate RR at 0.03 [11,17,19] and the cross-recurrence rate CRR at 0.02. In general, it is advisable to set $\text{RR} > \text{CRR}$ so that we achieve few cross-recurrences compared to intrasystem recurrences in order to be able to distinguish two subnetworks corresponding to individual, univariate time series [28]. Also, as the distance norm we used the maximum norm.

C. Network measures

To characterize the recurrence networks derived from single or two channel time series, graph theoretic measures can be used. Here, we give a brief description about the network measures used in this study. The network measure computed for the recurrence network associated with single channel time series is known as univariate recurrence network measure and the cross-recurrence network associated with two channel time series is known as bivariate cross-recurrence network measure.

1. Univariate recurrence network measures

(a) *Average clustering coefficient.* The local clustering coefficient $c(i)$ [39] of a vertex i of an undirected complex network can be defined as the likelihood of its neighbors also being neighbors. Given as a ratio between the number of edges that exist between neighbors of a vertex to the maximum number of possible connections, the clustering coefficient is an important quantitative characteristic of a network structure. The average clustering coefficient \mathcal{C} is simply the average of the local clustering coefficient of all the vertices present in a network. The local clustering coefficient of a vertex i is given as

$$c(i) = \frac{\sum_{j,m} A(i,j)A(j,m)A(m,i)}{k_i(k_i - 1)}, \quad (6)$$

where k_i is the degree of the vertex i . The average clustering coefficient is simply

$$\mathcal{C} = \frac{1}{N} \sum_{i \in \mathcal{N}} c(i). \quad (7)$$

Generally speaking, a high average clustering coefficient \mathcal{C} for a complex network can signify a special structure that is different from that of a random network and more conducive for efficient local information transfer. For a recurrence network, the average clustering coefficient \mathcal{C} can identify and discriminate qualitatively different types of dynamics. For instance, networks associated with periodic dynamics have high average clustering coefficient \mathcal{C} while those associated with chaotic dynamics have relatively lower values [20].

(b) *Assortativity.* In a network, if vertices that have a high degree tend to connect to other vertices that also have a high degree, then the network is said to exhibit assortative mixing. On the other hand, if vertices with a high degree tend to connect with vertices which have a low degree, then the mixing is said to be disassortative. For a network, assortativity \mathcal{R} can be estimated by the Pearson correlation coefficient of degrees at either end of vertices and is given as [40]

$$\mathcal{A} = \frac{\frac{1}{N} \sum_{j>i} k_i k_j A(i,j) - [\frac{1}{N} \sum_{j>i} \frac{1}{2}(k_i + k_j) A(i,j)]^2}{\frac{1}{N} \sum_{j>i} \frac{1}{2}(k_i^2 + k_j^2) A(i,j) - [\frac{1}{N} \sum_{j>i} \frac{1}{2}(k_i + k_j) A(i,j)]^2} \quad (8)$$

For recurrence networks, significant assortative mixing indicates that the density of states within the ε ball does not vary much or change very slowly and hence assortativity \mathcal{R} can be considered as a measure of continuity of phase space density [17].

(c) *Average path length.* Average path length is a measure of separation between two vertices in a network and can be computed as an average value of shortest path lengths taken over a vertex tuple (i, j) . For an undirected network, the average path length \mathcal{L} is given as

$$\mathcal{L} = \frac{1}{E_{\text{max}}} \sum_{i,j \neq i} d(i,j), \quad (9)$$

where $d(i, j)$ is the length of the geodesic from vertex i to j , E_{max} is the maximum number of edges a network can have and it is $\frac{N(N-1)}{2}$ for an undirected network having N vertices.

(d) *Betweenness centrality.* The importance of a vertex in a network can be described using betweenness centrality. If the total number of shortest paths from a vertex i to another vertex j in a network is given by σ_{ij} , then betweenness centrality for a vertex v can be defined as [41]

$$b(v) = \sum_{i \neq v \neq j} \frac{\sigma_{ij}(v)}{\sigma_{ij}}, \quad (10)$$

where $\sigma_{ij}(v)$ is the number of short paths (from a total of σ_{ij}) that pass through v . For a complex network, betweenness centrality measures the importance of a vertex in information transfer. When this measure is computed for a recurrence network a different interpretation is needed as there is no information flow between the vertices in a recurrence network. Accordingly, in [17] it has been argued that vertices of a recurrence network that acquire high values of betweenness

belong to a sparse region in the phase space that separates different high density clusters. Since betweenness centrality is defined for each node in a network, we will use the average betweenness centrality BC, which is simply the average of betweenness centrality of all the vertices in a network, as a single global measure for the entire network.

2. Bivariate cross-recurrence network measure

Average cross-clustering coefficient. The interaction between two subgraphs in a bipartite graph like the cross-recurrence network can be quantified using the concept of the local cross-clustering coefficient [30]. For two subgraphs G_x and G_y represented by adjacency matrices A_x and A_y respectively, the local cross-clustering coefficient for vertex i in A_x can be defined as [28,30]

$$c_{xy}^{\text{cross}}(i) = \frac{\sum A_{xy}(i,j)A_y(j,k)A_{xy}(k,i)}{k_{i,xy}(k_{i,xy} - 1)}. \quad (11)$$

Basically, $c_{xy}^{\text{cross}}(i)$ gives the probability that two randomly drawn neighbors of vertex $i \in G_x$ from subnetwork G_y are also neighbors. In order to avoid divergencies, for the vertices that have cross-degree of 0 or 1, the local cross-clustering coefficient is set to 0 [28]. By averaging the local cross-clustering coefficient $c_{xy}^{\text{cross}}(i)$ over all the vertices, we can define the average cross-clustering coefficient C_{xy}^{cross} . In an analogous fashion one can define C_{yx}^{cross} . If $C_{xy}^{\text{cross}} > C_{yx}^{\text{cross}}$, the direction of the coupling is from y to x , $y \rightarrow x$. On the other hand, if $C_{xy}^{\text{cross}} < C_{yx}^{\text{cross}}$, the direction of the coupling is from x to y , $x \rightarrow y$. Also, in the case of no coupling or complete synchronization, $C_{xy}^{\text{cross}} \approx C_{yx}^{\text{cross}}$.

In this work, for EEG signal pairs in the set X and Y , we determine the number of pairs for which the coupling is in the direction $x \rightarrow y$ as well as $y \rightarrow x$. The total number of independent signals in the total EEG signal pairs is then the sum of the number of signals interacting in these two directions. In this work, we will simply refer to the average cross-clustering coefficient as C_{cross} to denote both C_{xy}^{cross} and C_{yx}^{cross} . In this work, recurrence networks were computed using the python package - pyUNICORN [42].

D. Surrogate testing

1. iAAFT surrogates

As described in Ref. [5], we first generated univariate [34] and bivariate surrogates [43] for hypothesis testing of the randomness and nonlinear independence test respectively. The null hypothesis H_{univ}^0 to be tested by univariate surrogates is that the dynamics of original univariate time series is compatible with a Gaussian linear, stochastic, and stationary process measured by a monotonic and possibly nonlinear observation function [5,44]. For the univariate recurrence network measures, the hypothesis testing is done as follows:

(1) Compute the univariate network measure, U_x^{orig} , for the univariate EEG signal $x(t)$.

(2) Generate 19 surrogates using the procedure described in [34] and compute the univariate recurrence network measure for each of the surrogates. Let this set of network measures be $U_x^{\text{surr}} = \{U_x^{\text{surr1}}, U_x^{\text{surr2}}, \dots, U_x^{\text{surr19}}\}$.

(3) Reject the null hypothesis H_{univ}^0 if $U_x^{\text{orig}} > \max(U_x^{\text{surr}})$.

(4) The total number of signals rejecting the null hypothesis H_{univ}^0 is $n(U^1)$.

The null hypothesis B_{biv}^0 to be tested by the bivariate surrogates is that the original bivariate EEG time series represents a stationary, bivariate, linear, stochastic correlated Gaussian process [45]. The measurement function through which the EEG signal pairs are observed are invertible, but possibly nonlinear [45]. The surrogates generated have the same autocorrelation and cross-correlation as the original pair of EEG signals. For bivariate cross-recurrence network measure using a global-cross-clustering coefficient, the hypothesis testing is done as follows:

(1) Compute the cross-network measure, the average cross-clustering coefficient C_{xy}^{cross} and C_{yx}^{cross} for the original signal pairs. Let this be denoted as B_{xy}^{orig} and B_{yx}^{orig} .

(2) Generate 19 bivariate surrogates using original pair of signals in accordance with [43].

(3) Compute the cross-network measures for all surrogate pairs. Let this set be denoted as $B_{xy}^{\text{surr}} = \{B_{xy}^{\text{surr1}}, B_{xy}^{\text{surr2}}, \dots, B_{xy}^{\text{surr19}}\}$ and $B_{yx}^{\text{surr}} = \{B_{yx}^{\text{surr1}}, B_{yx}^{\text{surr2}}, \dots, B_{yx}^{\text{surr19}}\}$ representing an average cross-clustering coefficient C_{xy} and C_{yx} for bivariate surrogates respectively.

(4) If $B_{xy}^{\text{orig}} > B_{yx}^{\text{orig}}$ and $B_{xy}^{\text{orig}} > \max(B_{xy}^{\text{surr}})$, the coupling direction $y \rightarrow x$ is considered significant and the null hypothesis is rejected. Let the number of such rejections be $n(B_{xy}^{\text{rej}})$.

(5) Similarly, if $B_{yx}^{\text{orig}} > B_{xy}^{\text{orig}}$ and $B_{yx}^{\text{orig}} > \max(B_{yx}^{\text{surr}})$, the coupling direction $x \rightarrow y$ is considered significant and the null hypothesis is rejected. Let the number of such rejections be $n(B_{yx}^{\text{rej}})$.

(6) The total number of signals rejecting the null hypothesis B_{biv}^0 is $n(B_1) = n(B_{xy}^{\text{rej}}) + n(B_{yx}^{\text{rej}})$.

2. TFT surrogates

Apart from univariate and bivariate iAAFT surrogates, we also generated univariate TFT surrogates and extended them for the bivariate time series. The procedure to generate TFT surrogates is straightforward and can be applied to any surrogate technique that involves phase randomization, like AAFT or iAAFT technique. In the TFT method, one first defines a cutoff frequency f_c , which corresponds to the first few frequencies at which the phase of the original data is preserved, whereas the phases corresponding to frequencies greater than f_c are randomized as usual, for instance using the iAAFT method. Here, f_c can vary between 0 (i.e., 0 Hz, no phase is preserved and is equivalent to iAAFT surrogate) and 0.5 (i.e., $0.5 \times$ sampling frequency, no phase is randomized and hence surrogate is exactly the same as data). Thus, f_c represents normalized frequency (between 0 and 0.5) corresponding to the integer index $(0, 1, 2, \dots, N/2)$ of the N -point Fourier transformed data, where N is the number of points in the data. This way, local nonstationarity and even global nonstationarity, i.e., trends (for sufficiently high f_c), are preserved in the generated surrogates [36] but at the same time local structures in short-term variability are destroyed [35]. As is evident, generation of TFT surrogates crucially depends on the choice of cutoff frequency f_c , which is the maximum preserved

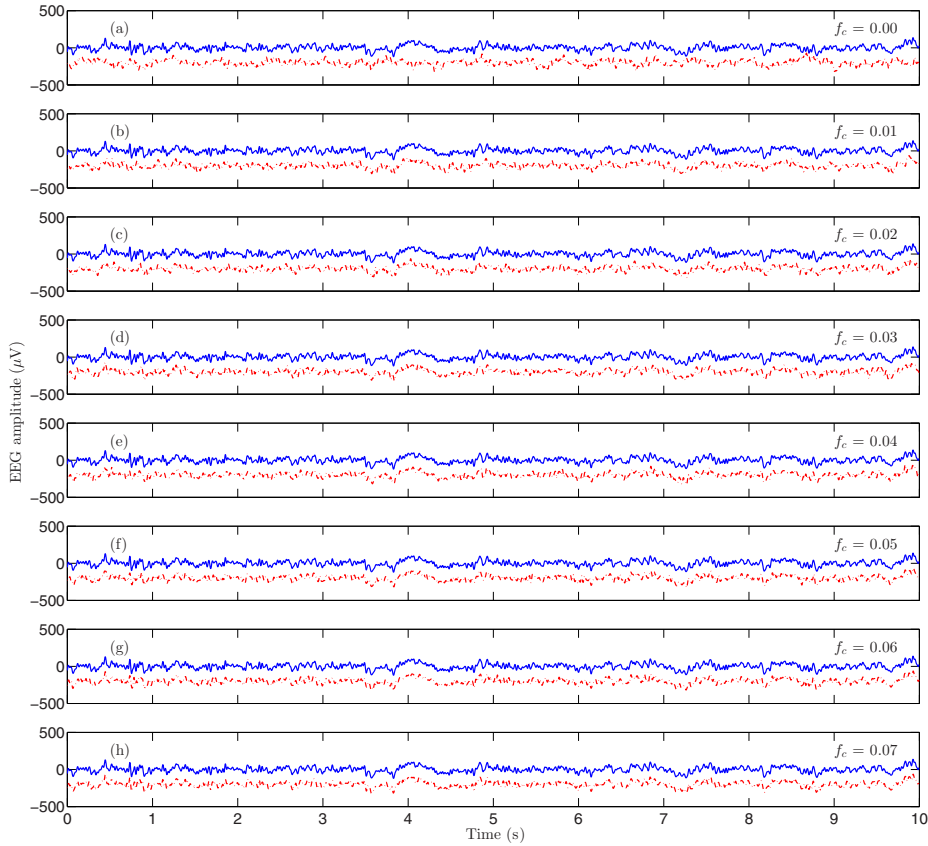


FIG. 1. (Color online) Impact of varying f_c on the global behavior of a surrogate signal. (a) 10 sec of an exemplary surrogate signal (dashed red line) and original EEG signal (solid blue line) at $f_c = 0$ which is equivalent to iAAFT surrogate. Figures 1(b)–1(h) as in Fig. 1(a) but for $f_c = 0.01$ –0.07 respectively. Note that for display purposes, in each case the surrogate signal (dashed red line) has been shifted below the original EEG signal (solid blue line).

frequency. If this frequency is too high, the surrogates become too similar to the original data and might share too much of its nonlinear dynamics. On the other hand, if this value is too low, then the TFT surrogates might not preserve any trends and behave in a similar fashion to the iAAFT surrogates.

In this work we applied TFT with iAAFT method for both univariate and bivariate surrogates and varied f_c from 0.01 to 0.05 (which corresponds to frequencies from approximately 5 to 25 Hz). In the context of the EEG data at hand, this means that the maximum preserved frequency at 0.05 is about 25.6 Hz. Preserving frequencies beyond 25.6 Hz resulted in generation of surrogates that are almost identical to the data since the data are already low pass filtered at 40 Hz and hence a

value of $f_c > 0.05$ could already be considered quite high for these data. Thus any discriminating statistic will naturally fail to distinguish between data and the corresponding surrogates beyond this cutoff frequency and will give low values of rejection probabilities. Also, it is important to check that the surrogates share the linear properties of the original data. The autocorrelation function at lag 1 is a good indicator of the linear structure of the data [35]. We observed that for the values of f_c used in this study, the autocorrelation of original data at time lag 1 was within the distribution obtained for surrogate sets.

Figures 1 and 2 show exemplary surrogate signals (dashed red line) and original EEG data (solid blue line) for different values of f_c . It can be seen from Fig. 1 that at low values of f_c (< 0.02), the surrogates do not follow the global behavior of

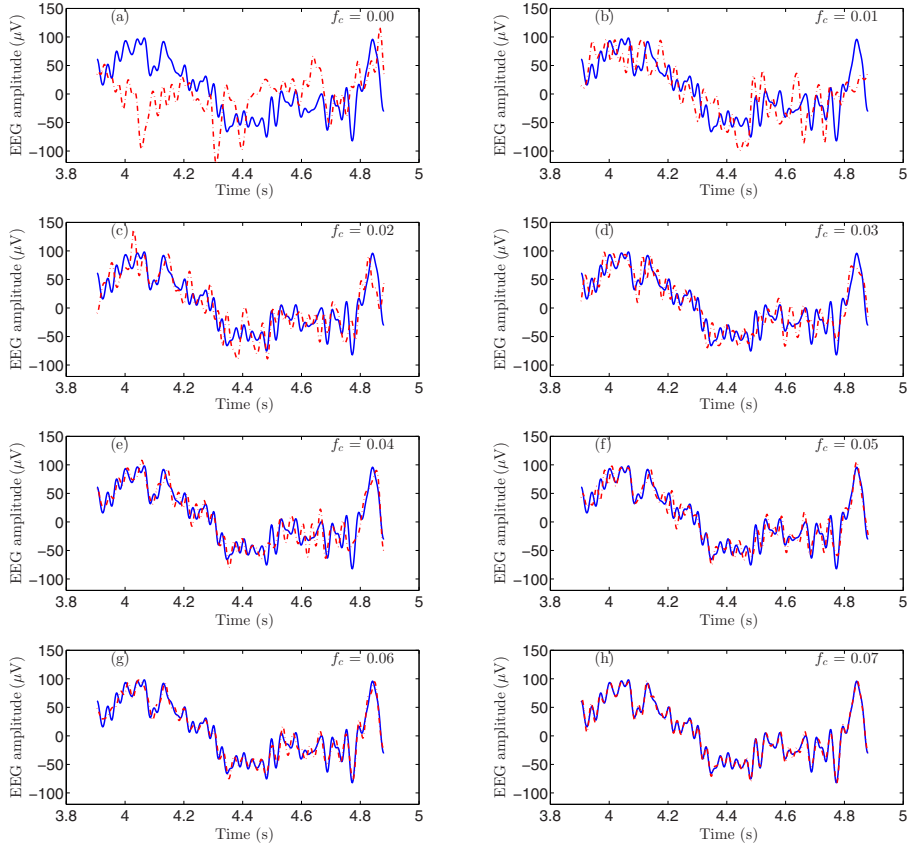


FIG. 2. (Color online) Impact of varying f_c on the local structure of a surrogate signal. (a) Exemplary surrogate signal (dashed red line) superimposed on an EEG signal (solid blue line) at $f_c = 0$ which is equivalent to iAAFT surrogate. Figures 2(b)–2(h) as in Fig. 2(a) but for $f_c = 0.01$ –0.07 respectively.

the data, whereas at high values of f_c (> 0.05), the data and the surrogates are almost similar where both the local (Fig. 2) and global (Fig. 1) behavior of the surrogate matches the EEG signal. Also it is evident from Fig. 2(a) that at $f_c = 0$, which is equivalent to the iAAFT surrogate, the trend present in the data (solid blue line) is destroyed in the surrogate (dashed red line). For intermediate values of f_c (between 0.02 and 0.05), we can see that the surrogates follow the global behavior of data and at the same time the local structures of the surrogates and the data differ (see Figs. 1 and 2).

Another issue that is common with Fourier transform (FT) based surrogates is that of end mismatch which could result in false rejection of the null hypothesis [43]. Schrieber and Schmitz [43] proposed a metric to quantify the end point mismatch which is defined as

follows:

$$\gamma = \frac{x(t_1) - x(t_N)}{\sum_{n=1}^N [x(t_n) - \langle x \rangle]}. \quad (12)$$

We found that for the EEG data used in this study, the contribution of the end point mismatch to the total power of the series, γ , was negligible ($< 0.02\%$) and hence we can neglect any effects caused by the end mismatch on the results. The null hypothesis to be tested using TFT surrogates is that the irregular fluctuations in the data arise from a stationary, Gaussian, linear, and stochastic process [35] and the hypothesis testing is carried out as described in the steps above. Note that, in both cases (iAAFT and TFT applied with iAAFT), we are using 19 surrogates and hence the hypothesis tests are performed at a significance level of $\alpha = 0.05$.

E. Estimation of rejection probabilities

In this section we define several probability estimates that have been used in this study and are consistent with the work of Andrzejak *et al.* [5]. The formulas mentioned here are for signals in set X (focal or nonfocal). The analogous definition for signals in set Y applies.

For the univariate and bivariate network measures, we define the following probability estimates.

I. Unconditioned rejection probabilities

For the signals in set X , the rejection probability for the randomness test based on the univariate measure is estimated

via [5]

$$p(U_X^1) = \frac{n(U_X^1)}{n(X)}, \quad (13)$$

where $n(X)$ is the total number of signals in set X which is 3750 and $n(U_X^1)$ is the number of signals in set X that have rejected H_{univ}^0 . Analogously, one can define the rejection probability for the nonlinear independence test based on the bivariate measure

$$p(B^1) = \frac{n(B^1)}{n(X)}, \quad (14)$$

where $n(B^1)$ is the number of pair of signals that have rejected H_{biv}^0 .

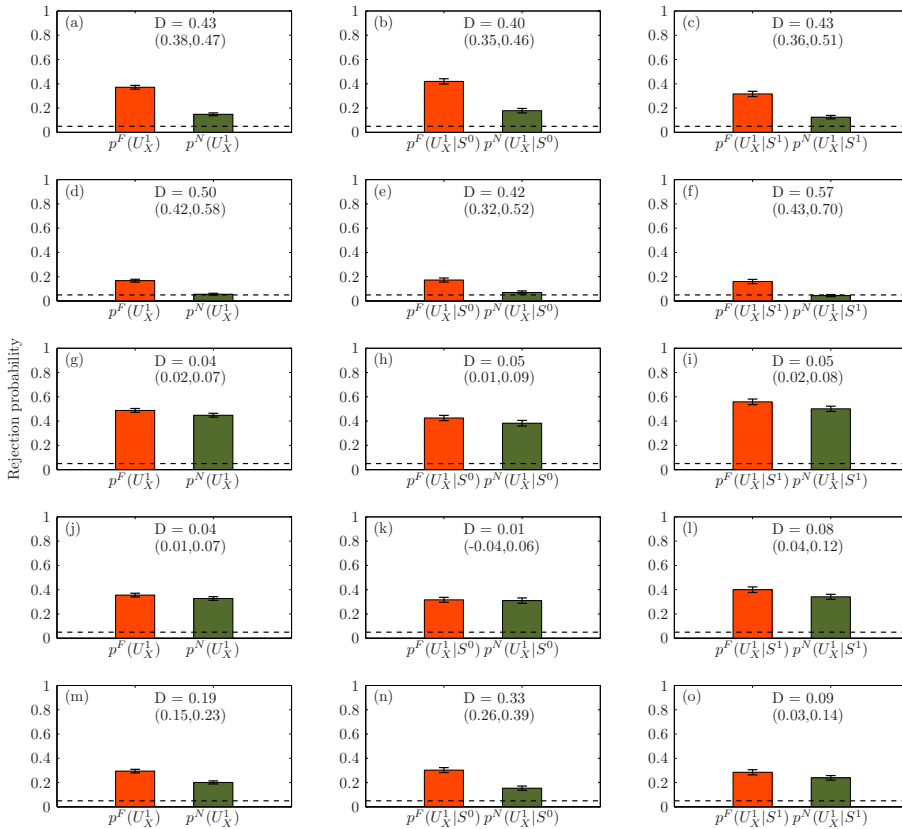


FIG. 3. (Color online) Contrast between the rejection probabilities of focal p^F (red) and nonfocal p^N (green) EEG signals as given by the randomness test based on the average clustering coefficient C for all the signals (a), stationary signals (b), and nonstationary signals (c). Rows 2–5, as in (a)–(c), but for assortativity \mathcal{R} , the average path length \mathcal{L} , the average betweenness centrality BC, and nonlinear prediction error N respectively. The bars indicate 95% confidence intervals, the dashed horizontal line indicates significance levels of the tests (0.05), D values indicate the relative difference used to compare probabilities with 95% confidence intervals given in parentheses [5].

2. Conditioned rejection probabilities

In order to assess the influence of nonstationarity on univariate measures, the following conditional probabilities are estimated [5]:

$$p(U_X^1 | S_X^0) = \frac{n(U_X^1 \cap S_X^0)}{n(S_X^0)}, \quad (15)$$

$$p(U_X^1 | S_X^1) = \frac{n(U_X^1 \cap S_X^1)}{n(S_X^1)}, \quad (16)$$

where S_X^0 and S_X^1 are the outcomes of the stationarity test [5] being not rejected and rejected respectively. Consequently $n(S_X^0)$ and $n(S_X^1)$ are the number of signals in the set X that have not rejected and have rejected the stationarity test respectively. These rejection probabilities are defined analogously for bivariate measures as per Eqs. (15) and (16).

Next, the dependence between univariate and bivariate recurrence network measures is assessed. To do so, we first define the conditional probability [5]

$$p(B^1 | U_X^1 U_Y^1) = \frac{n(B^1 \cap (U_X^1 \cap U_Y^1))}{n(U_X^1 \cap U_Y^1)} \quad (17)$$

that assesses whether the probability of rejection using bivariate measure is impacted by the fact that both the signals individually rejected H_{uni}^0 . Analogous to Eqs. (17), we define $p(B^1 | U_X^1 U_Y^0)$ and $p(B^1 | U_X^0 U_Y^0)$. In order to test the dependence the other way, we define the conditional probability [5]

$$p(U_X^1 U_Y^1 | B^1) = \frac{n((U_X^1 \cap U_Y^1) \cap B^1)}{n(B^1)} \quad (18)$$

that assesses whether the probability of rejection using univariate measures for signal pairs in sets X and Y is impacted by the fact that H_{biv}^0 was rejected. Analogous to Eqs. (18), we define $p(U_X^1 U_Y^0 | B^1)$, $p(U_X^0 U_Y^0 | B^1)$, $p(U_X^1 U_Y^1 | B^0)$, $p(U_X^0 U_Y^1 | B^0)$, and $p(U_X^1 U_Y^1 | B^0)$.

3. Comparing probabilities

We compare the probabilities using the relative difference measure D suggested in Andrzejak *et al.* [5]

$$D = \frac{p_1 - p_2}{p_1 + p_2}. \quad (19)$$

The measure D varies between -1 and 1 . Evidently, negative values are obtained when $p_1 < p_2$ and positive values are obtained when $p_1 > p_2$. We derive the confidence intervals (CIs) for the measure D and the probability estimates exactly as given in Ref. [5]. The reader is directed to Ref. [5] for an excellent and detailed description regarding the estimation of CI for the probabilities and D .

F. Results from Andrzejak *et al.* [5]

In order to classify the focal and nonfocal EEG signals into stationary and nonstationary signals, Andrzejak *et al.* [5] used a combination of amplitude stationarity test, frequency stationarity test, and correlation stationarity test as a stationarity test. The full description of the test can be found in Ref. [5]. In order to reject the stationarity test, it is sufficient to reject

TABLE I. Comparison of the rejection probability for the focal EEG signals. First column shows the univariate measures on which the randomness test is based. Second and third column shows the rejection probability for the focal EEG signals that have not rejected and have rejected the stationarity test respectively. Fourth column shows the corresponding D value.

Measures	$p^F(U_X^1 S_0)$	$p^F(U_X^1 S_1)$	D
\mathcal{C}	0.42	0.31	0.14
\mathcal{R}	0.17	0.16	0.03
\mathcal{L}	0.42	0.55	-0.13
BC	0.32	0.40	-0.11
N [5]	0.30	0.28	0.03

either the amplitude stationarity test or frequency stationarity test or correlation stationarity test. It has to be noted that this stationarity test is very strict and the significance level of the test, using 99 surrogates, is 0.049.

To facilitate a direct comparison of recurrence network measures with the nonlinear measures used in Andrzejak *et al.* [5], we use the results of the stationarity test, randomness test based on nonlinear prediction error N , and nonlinear independence test based on nonlinear interdependence measure L described in [5] which is publicly available for download [37].

III. RESULTS

A. Univariate measures

Figure 3 shows the unconditioned and conditioned rejection probabilities for the randomness test combined with iAAFT surrogates based on univariate recurrence network measures—the average clustering coefficient \mathcal{C} (first row), assortativity \mathcal{R} (second row), the average path length \mathcal{L} (third row), and the average betweenness centrality BC (fourth row). Also for the sake of comparison, rejection probabilities using nonlinear prediction error N [5] is also shown (fifth row).

It is clear from Fig. 3 that the contrast between all the focal and nonfocal EEG signals (left column) as given by the D value is highest for the randomness test based on assortativity \mathcal{R} [Fig. 3(d)], followed by the average clustering coefficient \mathcal{C} [Fig. 3(a)] and nonlinear prediction error N [5] [Fig. 3(m)]. Also, the unconditioned rejection probability based on the randomness test for these measures is greater for the focal EEG signals compared to the nonfocal EEG signals. On the other hand, it can be seen that the average path length \mathcal{L} and the average betweenness centrality BC give similar rejection

TABLE II. Same as Table I, but for nonfocal EEG signals.

Measures	$p^N(U_X^1 S_0)$	$p^N(U_X^1 S_1)$	D
\mathcal{C}	0.17	0.12	0.17
\mathcal{R}	0.07	0.04	0.22
\mathcal{L}	0.38	0.50	-0.13
BC	0.31	0.34	-0.04
N [5]	0.15	0.23	-0.21

TABLE III. Comparison of the rejection probability for focal EEG signals that have rejected the stationarity test. First column shows the univariate measures on which the randomness test combined with TFT surrogates is based. Columns 2–6 show the rejection probability for $f_c = 0.01, 0.02, 0.03, 0.04,$ and 0.05 respectively.

Measures	$f_c = 0.01$ (5.12 Hz)	$f_c = 0.02$ (10.24 Hz)	$f_c = 0.03$ (15.36 Hz)	$f_c = 0.04$ (20.48 Hz)	$f_c = 0.05$ (25.6 Hz)
C	0.41	0.51	0.45	0.27	0.14
\mathcal{R}	0.22	0.34	0.25	0.16	0.08
\mathcal{L}	0.42	0.27	0.20	0.17	0.12
BC	0.28	0.17	0.15	0.13	0.10
N [5]	0.32	0.24	0.12	0.06	0.03

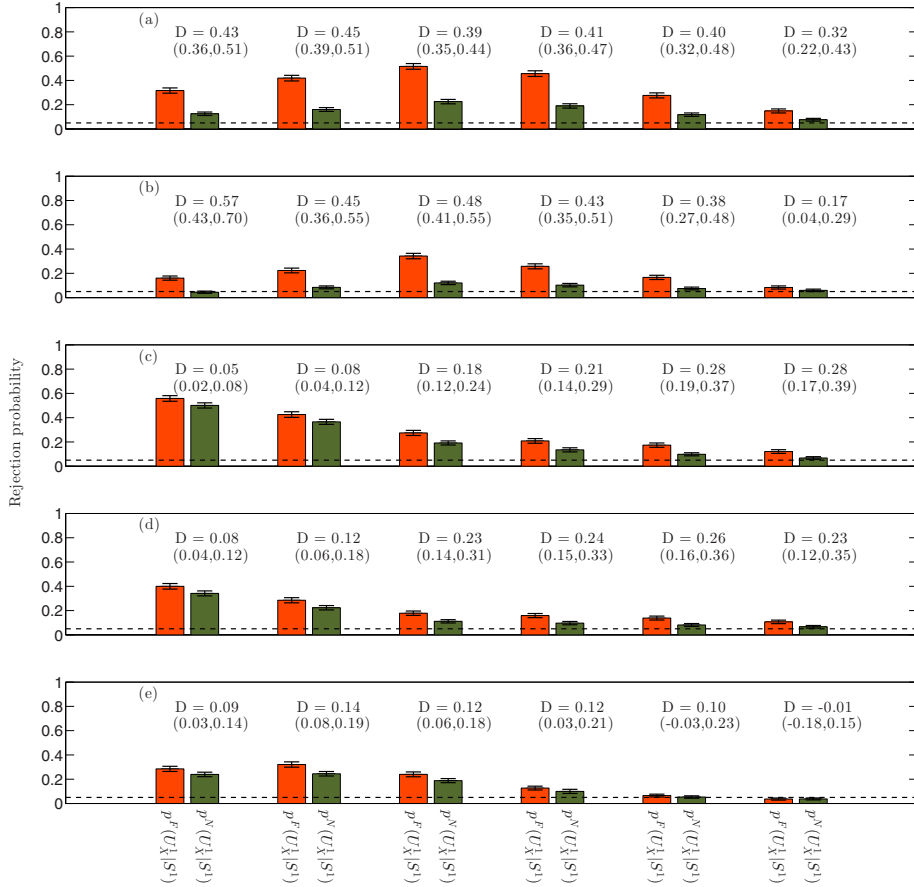


FIG. 4. (Color online) (a) Contrast between the rejection probabilities of focal p^F (red) and nonfocal p^N (green) EEG signals as given by the randomness test combined with TFT surrogates based on the average clustering coefficient C for nonstationary signals, from left to right, at $f_c = 0, 0.01, 0.02, 0.03, 0.04, 0.05$. (b)–(e) As in (a), but for assortativity \mathcal{R} , the average path length \mathcal{L} , the average betweenness centrality BC, and nonlinear prediction error N respectively. The bars indicate 95% confidence intervals, the dashed horizontal line indicates significance levels of the tests (0.05), D values indicate the relative difference used to compare probabilities with 95% confidence intervals given in parentheses [5].

TABLE IV. Same as Table III, but for nonfocal EEG signals that have rejected the stationarity test.

Measures	$f_c = 0.01$ (5.12 Hz)	$f_c = 0.02$ (10.24 Hz)	$f_c = 0.03$ (15.36 Hz)	$f_c = 0.04$ (20.48 Hz)	$f_c = 0.05$ (25.6 Hz)
\mathcal{C}	0.16	0.22	0.18	0.11	0.07
\mathcal{R}	0.08	0.12	0.10	0.07	0.05
\mathcal{L}	0.36	0.19	0.13	0.09	0.06
BC	0.22	0.11	0.09	0.08	0.06
N [5]	0.24	0.18	0.05	0.06	0.03

probability for both the focal and the nonfocal EEG signals resulting in low values for D [Figs. 3(g) and 3(j)].

On excluding signals that reject the stationarity test (Fig. 3, middle column) we see that the contrast between the focal and nonfocal EEG signals as given by the D value is still the highest for assortativity \mathcal{R} [Fig. 3(e)] followed by the average clustering coefficient \mathcal{C} [Fig. 3(b)] and nonlinear prediction error N [Fig. 3(n)]. Again, the rejection probability based on these measures is greater for the focal EEG signals compared to the nonfocal EEG signals. The average path length \mathcal{L} and the average betweenness centrality BC again give similar rejection probabilities when conditioned on S_X^0 , leading to low D values [Figs. 3(h) and 3(k)] and thus poor contrast between the focal and nonfocal EEG signals. It can be seen from Figs. 3(m) and 3(n) that when using the nonlinear prediction error N the contrast between the focal and nonfocal EEG signals increases significantly on excluding signals that reject the stationarity test, as reported in [5] as well.

When the analysis is restricted purely to the focal and nonfocal EEG signals that have rejected the stationarity test (Fig. 3, right column), i.e., nonstationary signals, we can see

that the contrast between the focal and nonfocal EEG signals is still the highest for assortativity \mathcal{R} [Fig. 3(f)] followed by the average clustering coefficient \mathcal{C} [Fig. 3(c)]. The rejection probability based on these measures is greater for the focal EEG signals than the nonfocal EEG signals. The average path length \mathcal{L} , the average betweenness centrality BC, and the nonlinear prediction error N give a similar rejection probability for both the focal and nonfocal EEG signals which results in low D value [Figs. 3(i), 3(l), and 3(o) respectively].

Tables I and II show the impact of nonstationarity on the rejection probability of the randomness test based on the univariate measures, for the focal and nonfocal EEG signals respectively. We observe that, for the both focal and nonfocal EEG signals, a rejection of the stationarity test increases the rejection probability substantially for the randomness test based on the average path length \mathcal{L} , whereas in the case of the betweenness centrality BC, for the nonfocal EEG signals only a slight increase of the rejection probability is found and for the focal EEG signals a reasonable increase is observed. On the other hand, a rejection of the stationarity test decreases the rejection probability for the randomness test based on assortativity \mathcal{R} and the average clustering coefficient \mathcal{C} , for

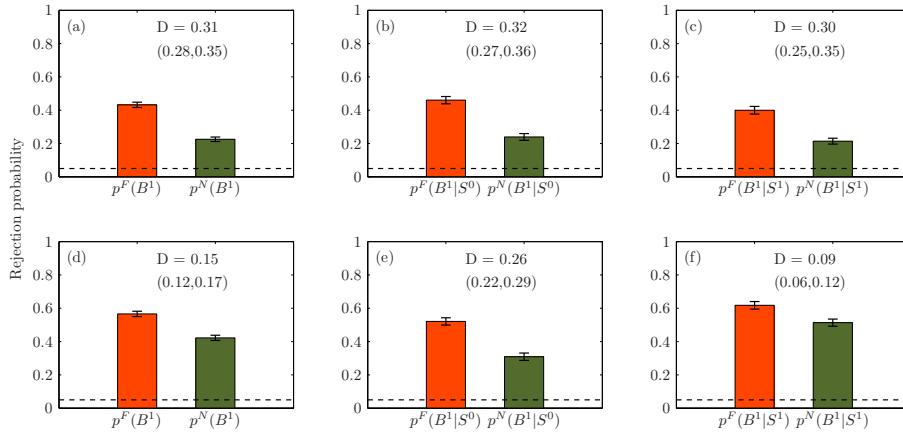


FIG. 5. (Color online) Contrast between the rejection probabilities of focal p^F (red) and nonfocal p^N (green) EEG signals as given by the nonlinear independence test based on the average cross-clustering coefficient $\mathcal{C}_{\text{cross}}$ for all the signals (a), stationary signals (b), and nonstationary signals (c). (d)–(f) As in (a)–(c) but for the nonlinear independence test based on nonlinear interdependence measure L described in [5]. Other elements in the figure are as in Fig. 3.

nonfocal EEG signals. In the case of focal EEG signals, only the average clustering coefficient \mathcal{C} shows a decrease in rejection probability, while the rejection of the stationarity test has no impact on assortativity \mathcal{R} . In comparison, for the nonfocal signals a rejection of the stationarity test increases the rejection probability for the randomness test based on the nonlinear prediction error N . For the focal signals a rejection of stationarity test has no impact on the rejection probability for the randomness test based on the nonlinear prediction error N . Also, the number of focal and nonfocal signals rejecting the null hypothesis of the randomness test is the lowest for assortativity \mathcal{R} .

Figure 4 shows the results of randomness test combined with TFT surrogates for nonstationary EEG signals, using the average clustering coefficient \mathcal{C} , assortativity \mathcal{R} , the average path length \mathcal{L} , the average betweenness centrality BC, and nonlinear prediction error N for values of the cutoff frequency f_c ranging 0–0.05 in steps of 0.01 (from left to right). It can be seen from Fig. 4 that as f_c is increased (up to 0.02), the rejection probability of focal and nonfocal EEG signals increase in the case of average clustering coefficient \mathcal{C} and assortativity \mathcal{R} . However, the contrast between focal and nonfocal signals is still maintained very well [Figs. 4(a) and 4(b)]. In the case of the network measures the average path length \mathcal{L} and average betweenness centrality BC, we see that as f_c is increased, the contrast between focal and nonfocal EEG signals starts to improve, while the rejection probabilities start to decrease for both focal and nonfocal EEG signals [Figs. 4(c) and 4(d)]. Similar observations are made in the case of nonlinear prediction error N , but the contrast between focal and nonfocal EEG signals as given by D is lower compared to recurrence network measures [Fig. 4(e)]. For high values of f_c (> 0.03), we observe that the rejection probabilities for both focal and nonfocal EEG signals start to drop in the case of all the measures as the surrogates start becoming increasingly similar to the original data and might contain too much of the nonlinear deterministic dynamics of the original data in them. These results are also summarized in Tables III and IV.

B. Bivariate measure

Figures 5(a)–5(c) show the unconditioned and conditioned rejection probabilities for the nonlinear independence test based on the average cross-clustering coefficient C_{cross} . For the sake of comparison, the rejection probabilities for the nonlinear independence test based on nonlinear interdependence measure L described in [5] is also shown [Figs. 5(d)–5(f)].

It is clear from Fig. 5 that the contrast between all the focal and nonfocal EEG signals as given by the D value is greater for the average cross-clustering coefficient C_{cross} [Fig. 5(a)] compared to the nonlinear interdependence measure L [Fig. 5(d)]. Also, on excluding signals for which the stationarity test was rejected, we see that the contrast between the focal and nonfocal EEG signals is enhanced when the nonlinear interdependence measure L is used [Fig. 5(e)], but the D is still less than what is obtained with average cross-clustering coefficient C_{cross} [Fig. 5(b)]. When only nonstationary signals are considered, the contrast between the focal and nonfocal EEG signals as given by the D values

TABLE V. Comparison of the rejection probability for the focal EEG signals. First column shows the bivariate measures on which the nonlinear independence test is based. Second and third columns show the rejection probability for the focal EEG signals that have not rejected and have rejected the stationarity test respectively. Fourth column shows the corresponding D value.

Measures	$p^F(B^1 S_0)$	$p^F(B^1 S_1)$	D
C_{cross}	0.46	0.40	−0.06
L [5]	0.52	0.61	−0.08

is very low, when nonlinear interdependence measure L is used [Fig. 5(f)]. On the contrary, in the case of the global cross-clustering coefficient C_{cross} we observe that the contrast between the focal and the nonfocal EEG signals as given by the D value still remains at the same level as it was when stationary signals or all the signals were considered [Fig. 5(c)].

Tables V and VI show the impact of nonstationarity on the rejection probabilities for the nonlinear independence test based on the average cross-clustering coefficient C_{cross} and the nonlinear interdependence measure L . It is evident that the rejection of the stationarity test considerably increases the rejection probability for the nonlinear independence test based on the nonlinear interdependence measure L , for both the focal and nonfocal signals. On the other hand, the rejection of the stationarity test has a negligible impact on the rejection probability for the nonlinear independence test based on the average cross-clustering coefficient C_{cross} , for both the focal and nonfocal signals.

Figure 6 shows the results of the nonlinear independence test combined with TFT surrogates for nonstationary focal and nonfocal EEG signals, using average cross-clustering coefficient (shown at left) and nonlinear interdependence measure (shown at right). We only show results for $f_c = 0.02$ as we observed a similar trend as in the case of univariate measures for increasing values of f_c . It is clear from the figure that the rejection probabilities for focal and nonfocal EEG signals increase in the case of the average cross-clustering coefficient compared to the results obtained from iAAFT surrogates. However the contrast between focal and nonfocal EEG signals as given by D is almost at the same level as for iAAFT surrogates [Fig. 5(c)]. In the case of the nonlinear interdependence measure, the rejection probabilities for focal and nonfocal EEG signals decrease compared to the results obtained with iAAFT surrogates whereas the contrast between the focal and nonfocal EEG signals is enhanced compared to what was obtained with iAAFT surrogates [Fig. 5(f)]. These results are summarized in Table VII.

C. Dependence between univariate and bivariate measure

In order to assess the dependence between univariate and bivariate recurrence network measures and compare our results

TABLE VI. Same as Table V, but for nonfocal EEG signals.

Measures	$p^N(B^1 S_0)$	$p^N(B^1 S_1)$	D
C_{cross}	0.23	0.21	−0.04
L [5]	0.30	0.51	−0.25

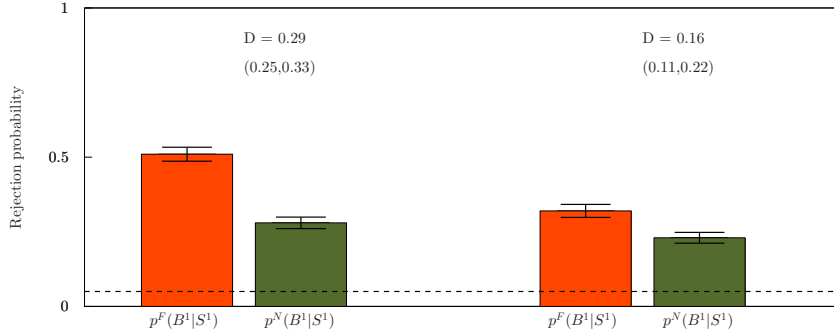


FIG. 6. (Color online) Contrast between the rejection probabilities of focal p^F (red) and nonfocal p^N (green) EEG signals as given by the nonlinear independence test combined with TFT surrogates based on the average cross-clustering coefficient C_{cross} (left) and the nonlinear interdependence measure L (right). The bars indicate 95% confidence intervals, the dashed horizontal line indicates significance levels of the tests (0.05), D values indicate the relative difference used to compare probabilities with 95% confidence intervals given in parentheses [5]. Other elements in the figure are as in Fig. 3.

directly with that of Andrzejak *et al.* [5], we considered only the focal EEG signals that did not reject the stationarity test so as to reduce the influence of nonstationarity on the results, as suggested in [5].

We estimated the conditional probabilities $p(B^1|U_X^0 U_Y^0)$, $p(B^1|U_X^1 U_Y^0)$, and $p(B^1|U_X^1 U_Y^1)$ [see Eq. (17)]. Here we only report the results for the dependence between the average clustering coefficient C (univariate measure) and average cross-clustering coefficient C_{cross} (bivariate measure), as similar observations were made for the dependence between other univariate recurrence network measures and the average cross-clustering coefficient C_{cross} .

From Fig. 7(a) it can be seen that rejection of one of the randomness tests (left) based on the average clustering coefficient C increases the rejection probability of the nonlinear independence test based on the average cross-clustering coefficient C_{cross} , while rejection of both the randomness tests based on the average clustering coefficient C further increases the rejection probability of nonlinear independence tests (right) based on the average cross-clustering coefficient C_{cross} . Similar observations can be made when nonlinear prediction error N and nonlinear interdependence measure L as mentioned in [5] are used [Fig. 7(b)].

However, it can also be seen that the rejection of the randomness tests alone is not necessary for the rejection of the

nonlinear independence test as the value of the rejection probability $p(B^1|U_X^0 U_Y^0)$ is still considerably above the significance level in the case of both the average cross-clustering coefficient C_{cross} and nonlinear interdependence measure L [Figs. 7(a) and 7(b) (middle)]. As suggested and performed in [5], we also test this conjecture by shuffling the pairs of stationary focal EEG signals without replacement. Instead of pairing signal x with its neighboring contact y , it was paired with some other signal that was randomly selected without replacement from the remaining signals in set Y [5]. Thus, any potential nonlinear dependence is destroyed and we end up with pairs of signals that are independent of each other, but might possess strong individual dynamics. To see if the individual dynamics caused any false interdependence between the signals as measured by the average cross-clustering coefficient C_{cross} , we again computed the probability measures mentioned above and the results are shown in Fig. 8. It can be seen from the figure that irrespective of the outcome of the randomness test, the rejection probabilities of the nonlinear independence test based on the average cross-clustering coefficient C_{cross} are close to significance level and remain more or less the same resulting in very low values D values. Also, for a large number of these shuffled signal pairs $C_{xy}^{\text{cross}} \approx C_{xy}^{\text{cross}}$, in this case, indicating independence between the signals.

We also assessed the dependence other way, i.e., testing if the outcome of the nonlinear independence test impacts the outcome of the randomness test. From Fig. 9 it can be seen that the rejection of the nonlinear independence test based on the average cross-clustering coefficient C_{cross} increases the rejection probabilities of randomness tests based on the average clustering coefficient C [Fig. 9(c)]. However, from the figure it is also evident that the rejection of the nonlinear independence test is not necessary for the rejection of the randomness tests as the rejection probabilities $p^F(U_X^1 U_Y^1 | B^0)$ and $p^F(U_X^1 U_Y^1 | B^1)$ are still above the significance levels. Also, it can be seen the randomness tests are accepted even if

TABLE VII. Comparison of rejection probabilities for the nonstationary focal and nonfocal EEG signals using nonlinear independence test combined with TFT surrogates at $f_c = 0.02$ (10.24 Hz). First column shows the bivariate measures on which the nonlinear independence test is based. Second and third columns show the rejection probabilities for the focal and nonfocal EEG signals respectively.

Measures	$p^F(B^1 S^1)$	$p^N(B^1 S^1)$
C_{cross}	0.51	0.28
L [5]	0.32	0.23

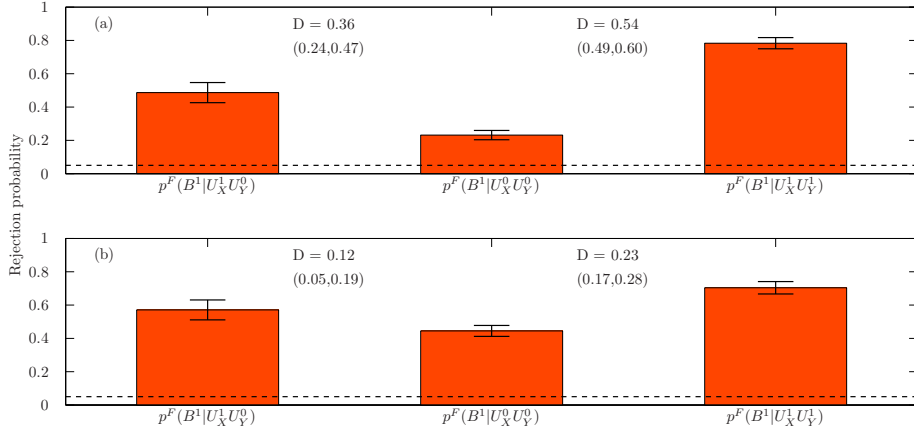


FIG. 7. (Color online) (a) Impact of the outcome of the randomness tests on the nonlinear independence test for the average cross-clustering coefficient C_{cross} when one of the randomness tests is rejected (left), neither of the randomness tests is rejected (middle), and both of the randomness tests are rejected (right). (b) As in (a) but for the nonlinear interdependence measure L and nonlinear prediction error N . Other elements in the figure are as in Fig. 3.

the nonlinear independence test is rejected, as given by the rejection probability $p^F(U_X^0 U_Y^0 | B^1)$

EEG signals still contained a significant amount of signals (roughly 46%) that reject the stationarity test.

IV. DISCUSSION

This study assesses the impact of nonstationarity in the data on the computation of univariate recurrence network measures—the average clustering coefficient C , assortativity \mathcal{R} , the average path length \mathcal{L} , the average betweenness centrality BC , the bivariate cross-recurrence network measure, and the average cross-clustering coefficient C_{cross} . We applied recurrence network measures, combined with iAAFT as well as TFT surrogate methods, to the EEG data described in Ref. [5] which is comprised of 3750 pairs of focal and nonfocal EEG signals of length 20 sec (2560 samples) each. At this time scale, as per the stationarity test based on linear variability measures, Andrzejak *et al.* [5] found that there is more nonstationarity in the nonfocal EEG signals compared to the focal EEG signals. However, they also found that the focal

A. Univariate and bivariate recurrence network measures

1. Impact of nonstationarity

Previous studies have reported the presence of more nonlinearity [43,46,47] in the EEG signals and stronger interdependence between the EEG signals [44,48–53] derived from epileptogenic brain areas in comparison to the EEG signals derived from normal brain areas. However, the influence of nonstationarity in the EEG data on the obtained results had not been considered in these studies. For the first time, Andrzejak *et al.* [5] assessed the influence of nonstationarity on both the univariate and bivariate nonlinear measures. They provided the evidence that the univariate and bivariate measures they considered could distinguish between focal and nonfocal signals more effectively, once nonstationarity was

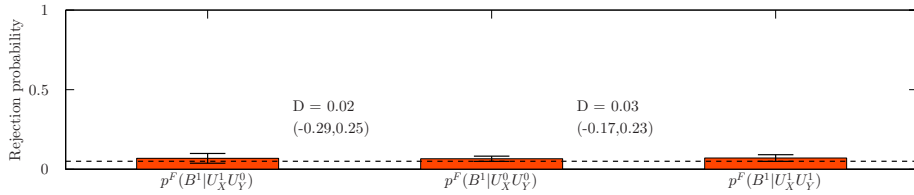


FIG. 8. (Color online) Outcome of the randomness test based on the average clustering coefficient C does not impact the outcome of nonlinear independence test based on the average cross-clustering coefficient C_{cross} . The rejection probabilities shown are for shuffled signal pairs that are independent of each other. Other elements in the figure are as in Fig. 3.

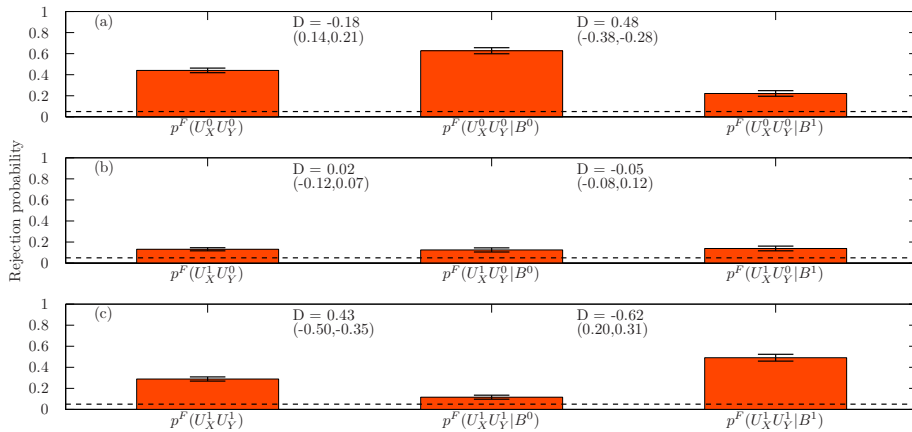


FIG. 9. (Color online) Impact of the outcome of the nonlinear independence test based on the average cross-clustering coefficient C_{cross} on the outcome of randomness test based on the average clustering coefficient C . Probability that neither randomness test is rejected (a), one of the randomness tests is rejected (b), and both randomness tests are rejected (c). Other elements in the figure are as in Fig. 3.

controlled for. Also, only linear surrogate methods like iAAFT or AAFT techniques have been used so far in combination with randomness or nonlinear independence tests. These surrogates are stationary by construction and may violate the null hypothesis wrongly leading to false rejections. In this work we combine recurrence network measures not only with iAAFT surrogates but also with TFT surrogates. The TFT technique preserves the nonstationarity in the surrogates and at the same time destroys any nonlinearity arising due to irregular fluctuations in the data [35].

Transforming time series into complex networks based on recurrences in phase space and quantifying its topology using graph theoretical measures to study the properties of the underlying dynamical system has garnered much interest recently. From graph theory, we know that a completely random network has a low clustering coefficient C and average path length \mathcal{L} compared to nonrandom graphs that have some structure in them. Also, in the absence of any assortative mixing, the assortativity \mathcal{R} for a network is zero, whereas for a perfectly assortative network, the assortativity \mathcal{R} is 1. For a disassortative network, the value of assortativity \mathcal{R} ranges $-1-0$. In a random network, dissimilar nodes are more likely to be paired with each other (for example, high degree nodes pair with low degree nodes) and such a network tends towards being disassortative. It has been shown that the recurrence network measures like the average clustering coefficient C and average path length \mathcal{L} can distinguish between periodic and chaotic dynamics [20]. Particularly, the values of average clustering coefficient C and the average path length \mathcal{L} are high for dynamical systems exhibiting periodic dynamics compared to chaotic dynamics. Recently, it was also shown that, after embedding, the recurrence networks constructed from the surrogates, which are Gaussian, linear stochastic processes, exhibit lower values of average clustering coefficient and

average path length compared to the original data that have some deterministic (chaotic) dynamics [33]. Hence, comparing the topological characteristics of the complex networks generated from surrogate time series with that of the original EEG signal yields an interesting way to study the presence of any existing nonrandom structure in the original EEG time series [33]. Our results indicate that the complex networks obtained from the focal EEG signals are more assortative and clustered compared to that of the complex networks obtained from the nonfocal EEG signals, which possibly have more random structure in them. Additionally, results obtained from TFT surrogates also indicate that the attractors reconstructed from focal EEG signals are more fractionated [17] than that of nonfocal EEG signals as indicated by the average betweenness centrality measure.

The implications of the results obtained with the average clustering coefficient C and assortativity \mathcal{R} for the randomness test and the average cross-clustering coefficient C_{cross} for the nonlinear independence test, combined with iAAFT surrogates, are in agreement with the work of Andrzejak *et al.* [5]. Also, it was pointed out in Ref. [5] that nonstationarity in the data can wrongly favor the rejection of the null hypothesis and hence increase the rejection probability, as was the case with nonlinear prediction error N for the nonfocal EEG signals and nonlinear interdependence measure L , for both the focal and nonfocal EEG signals used in their work. Contrary to the findings reported in Ref. [5], we found that rejection of the stationarity test decreases the rejection probability for the randomness test based on the univariate measures, the average clustering coefficient C for both the focal and nonfocal EEG signals, and assortativity \mathcal{R} for the nonfocal EEG signals. However, in the case of the average path length \mathcal{L} and the average betweenness centrality BC, for both the focal and nonfocal EEG signals, the rejection probability of the

randomness test increases with the rejection of the stationarity test. For the bivariate measure, the average cross-clustering coefficient C_{cross} for both focal and nonfocal EEG signals, the rejection of the stationarity test had almost no impact on the rejection probability of the nonlinear independence test. The contrast between the focal and nonfocal EEG signals obtained with the measures—the average clustering coefficient C , assortativity \mathcal{R} , and the average cross-clustering coefficient C_{cross} , irrespective of whether the considered signals are stationary or nonstationary, is greater than what is obtained using nonlinear prediction error N and nonlinear interdependence measure L described in [5]. However, the average path length \mathcal{L} and the average betweenness centrality BC fail to distinguish between the focal and nonfocal EEG signals due to their high rejection probabilities when iAAFT surrogates are used.

We found that the results for the average path length \mathcal{L} and the average betweenness centrality BC improved when TFT surrogates were used. On preserving the phases of low frequency components of the original data in the surrogates, these measures could better distinguish between nonstationary focal and nonfocal EEG signals. The univariate measure nonlinear prediction error N , which gave low contrast in the rejection probabilities between nonstationary focal and nonfocal EEG signals when iAAFT surrogates were used, could distinguish between focal and nonfocal EEG signals relatively well with TFT surrogates. These results indicate that, by including the trends in the surrogates, one can improve the performance of these measures in distinguishing between different dynamics. However, it is important to note that TFT surrogates depend mainly on the maximum preserved cutoff frequency f_c . If f_c is too high, the surrogates can contain too much of the nonlinearity present in the data and the rejection probabilities for the randomness test starts decreasing. In the case of the average clustering coefficient C and assortativity \mathcal{R} , which could distinguish well between nonstationary focal and nonfocal EEG signals even with iAAFT surrogates, performed in a similar manner with TFT surrogates. This implies that these recurrence network measures characterize the dynamical complexity contained in the irregular fluctuations of the data very well.

Like the univariate surrogates, the bivariate surrogates based on iAAFT, which is used in this study and as well as in previous studies [5,45] represent a null hypothesis that is composed of different assumptions. One such assumption is that of stationarity. Our results based on the average cross-clustering coefficient C_{cross} , in conjunction with iAAFT surrogates, indicate that the focal EEG signals are less consistent with the null hypothesis H_{biv}^0 compared to the nonfocal EEG signals. This result was consistent across the board, whether the signals rejected the stationarity test or not. However, we found using iAAFT surrogates that the nonlinear interdependence measure L is affected by nonstationarity in the data so as to falsely favor the rejection of the null hypothesis when the analysis is restricted to nonstationary signals. Hence, in the case of the nonlinear interdependence measure L , one needs to correct for nonstationarity, by excluding nonstationary signals, in order to enhance the contrast between focal and nonfocal EEG signals [5]. Contrary to this observation, the bivariate cross-recurrence network measure, the average cross-clustering coefficient C_{cross} , is not affected

by nonstationarity in the data, giving same levels of rejection probabilities for nonstationary signals as for stationary signals. Hence, one need not control for nonstationarity when applying bivariate cross-recurrence network measure, the average cross-clustering coefficient C_{cross} . Overall, in the case of average cross-clustering coefficient C_{cross} , the contrast between the focal and nonfocal EEG signals changed very little and so did their rejection probabilities for the nonlinear independence test with respect to the inclusion or exclusion of the nonstationary signals. Like in the case of univariate measures, we repeated this analysis using TFT surrogates for nonstationary focal and nonfocal EEG signals, which does not assume stationarity in surrogates. In the case of the bivariate measure, the average cross-clustering coefficient C_{cross} , performed similarly when iAAFT or TFT surrogates were used, by distinguishing well between nonstationary focal and nonfocal EEG signals. On the other hand, the performance of the nonlinear interdependence measure L improved with TFT surrogates and it could distinguish relatively better between nonstationary focal and nonfocal EEG signals as evidenced by the improvement in the D value compared to the iAAFT case. However, the contrast between focal and nonfocal EEG signals as provided by the nonlinear interdependence measure L was less than that of the average cross-clustering coefficient C_{cross} in the case of both iAAFT and TFT surrogates.

With respect to the average clustering coefficient C and assortativity \mathcal{R} , our results can be interpreted in two ways. First, since both these measures give lower rejections for the randomness test using iAAFT surrogates, when signals that reject the stationarity test are included, it could mean that nonstationarity does not impact these measures so as to favor false rejections as in the case of the average path length \mathcal{L} , the average betweenness centrality BC, and the nonlinear prediction error N . Particularly, assortativity \mathcal{R} shows good specificity by giving rejections almost at the level of significance for the nonfocal EEG signals. High specificity is desirable especially if the aim is to exclude nonepileptogenic (nonfocal) brain areas from being wrongly resected. On the other hand, the average clustering coefficient C shows good sensitivity by giving higher rejections for the focal EEG signals for the randomness test compared to the nonlinear prediction error N and assortativity \mathcal{R} , even when only nonstationary signals are considered. From a clinical application point of view, the average clustering coefficient C could be particularly useful in correctly identifying epileptogenic (focal) brain areas for resection. A combination of the recurrence network measures assortativity \mathcal{R} and the average clustering coefficient C can provide an even more reliable way to distinguish focal brain areas from the nonfocal ones. This is clearly evident from our results as the relative difference D , which is used to compare the rejection probabilities is higher for assortativity \mathcal{R} and the average clustering coefficient C compared to the other measures used in this study, including the nonlinear prediction error N .

The second interpretation of our results obtained using the average clustering coefficient C and assortativity \mathcal{R} as applied to the nonstationary signals could be given on the basis of how nonstationarity in the data interacts with these measures. It could be very well possible that the nonstationarity in the data impacts the computation of these two networks measures

and causes them to be lower than that of surrogates that are stationary by construction. This impact is seen for both focal and nonfocal EEG signals in the case of the average clustering coefficient C and mostly nonfocal signals in the case of assortativity \mathcal{R} . To test this conjecture, we also used TFT surrogates, which are not stationary by construction and preserve the global behavior of the original data. Thus, any difference between the TFT surrogates and the original data at hand must not arise due to nonstationarity (i.e., trends) but possibly due to the difference in dynamics encoded in the irregular fluctuations of the data. However, irrespective of the supposed effect of nonstationarity on the complex networks, our results quantitatively show that the contrast between focal and nonfocal EEG signals, as given by the relative difference D using the univariate recurrence network measures (particularly average clustering coefficient C and assortativity \mathcal{R}), was still high in comparison to the nonlinear prediction error N . The same observation holds true for the bivariate recurrence network measure, the average cross-clustering coefficient C_{cross} , in comparison to the nonlinear interdependence measure L .

2. Dependence between univariate and bivariate measures

In this study we also assessed the relationship between the univariate recurrence network measure, the average clustering coefficient C , and the bivariate cross-recurrence network measure C_{cross} . Here we considered only stationary focal EEG signals to minimize the influence of nonstationarity on the results [5]. Although we found that rejection of the randomness test based on the average clustering coefficient C does increase the rejection probability for the nonlinear independence test based on C_{cross} , this correlation as noted in [5] could be because the EEG signal pairs analyzed are from neighboring contacts and such signal pairs are usually correlated. Hence these are indeed not independent measurements. Again for the same reason, we also noted that the rejection of the nonlinear independence test also increased the probability that the randomness test is rejected for one or both the signals. Similar results were obtained in the study of Andrzejak *et al.* [5] between the nonlinear measure N and nonlinear interdependence measure L . In order to truly measure the specificity of the bivariate cross-recurrence network measure, the average cross-clustering coefficient C_{cross} , we shuffled the EEG signal pairs so as to have pairs that contain independent signals as suggested in Ref. [5]. We observed that in this case, the rejection probability of the nonlinear independence test based on the average cross-clustering coefficient was at the significance level and did not depend on the outcome of the randomness test, implying good specificity for the measure, the average cross-clustering coefficient C_{cross} .

B. Limitations and outlook

We note that our study has several limitations, which can be considered as potential future work. First, as already

noted in Ref. [5], the stationarity test itself is based on null hypothesis and its rejection cannot guarantee that the dynamics are truly nonstationary. Hence our analysis also suffers from the same limitation as we have also used the stationarity test proposed in [5] and thus, more advanced methods are needed to analyze nonstationarity. Recently, Reike *et al.* [54] proposed a method based on the analysis of distributions of temporal distances of neighboring phase space vectors as a measure for nonstationarity. Also, this technique does not require the time series to be divided into smaller segments.

Second, the results of such time series analysis of EEG data depend heavily on the type of surrogates used. In this work we considered two types of surrogate schemes: iAAFT and TFT surrogates (applied with iAAFT scheme). There other surrogate techniques that can be used to preserve the nonstationarity in the surrogates. Recently, Lucio *et al.* [36] proposed an improved surrogate technique to preserve nonstationarity in the surrogates by detrending the data before computing the Fourier transform and then retrending the data after inverse Fourier transform. This technique is combined with the TFT technique and can be applied using any linear surrogate generation algorithm and it preserves the linear properties of the nonstationary original data in the surrogates quite well [36]. Other methods based on wavelet surrogates have also been proposed to deal with nonstationarity [55–57]. A detailed comparative study on the application of different surrogate techniques to investigate nonlinear dynamics, specifically in nonstationary epileptic EEG data, would be considered in the future.

As a concluding remark, the univariate recurrence network measures and bivariate cross-recurrence network measure can successfully distinguish between the dynamics of the intracranial focal and nonfocal epileptic EEG signals and these measures seem promising as reliable biomarkers to distinguish epileptogenic brain areas from nonepileptogenic areas, especially considering their performance regarding nonstationary EEG signals.

ACKNOWLEDGMENTS

This work is financially supported by International Doctoral Programme in Biomedical Engineering and Medical Physics (iBioMEP) - Academy of Finland (Suomen Akatemia), Decision No. 141171. We would like to thank Dr. J. Donges, from Potsdam Institute for Climate Impact Research, Germany for his valuable suggestions. We also thank Prof. J. Viik from Tampere University of Technology for his suggestions and comments on statistical methods. We would also like to thank the anonymous reviewers for their valuable comments that have helped us in improving our manuscript. Finally, we are grateful to Dr. R. Andrzejak and his co-workers for making publicly available the data and results of their work, without which this work would not have been possible.

[1] L. D. Iasemidis, *Biomedical Engineering, IEEE Trans. Biomed. Eng.* **50**, 549 (2003).

[2] R. S. Fisher, W. v. E. Boas, W. Blume, C. Elger, P. Genton, P. Lee, and J. Engel, *Epilepsia* **46**, 470 (2005).

- [3] K. Lehnertz, R. G. Andrzejak, J. Arnhold, T. Kreuz, F. Mormann, C. Rieke, G. Widman, and C. E. Elger, *J. Clin. Neurophys.* **18**, 209 (2001).
- [4] W. J. Hader, J. Tellez-Zenteno, A. Metcalfe, L. Hernandez-Ronquillo, S. Wiebe, C.-S. Kwon, and N. Jette, *Epilepsia* **54**, 840 (2013).
- [5] R. G. Andrzejak, K. Schindler, and C. Rummel, *Phys. Rev. E* **86**, 046206 (2012).
- [6] C. J. Stam, *Clin. Neurophys.* **116**, 2266 (2005).
- [7] J. Timmer, *Phys. Rev. E* **58**, 5153 (1998).
- [8] H. Kantz and T. Schreiber, *Nonlinear Time Series Analysis* (Cambridge University Press, Cambridge, UK, 2004), Vol. 7.
- [9] X. Li, G. Ouyang, X. Yao, and X. Guan, *Phys. Lett. A* **333**, 164 (2004).
- [10] N. Marwan, M. Carmen Romano, M. Thiel, and J. Kurths, *Phys. Rep.* **438**, 237 (2007).
- [11] N. Marwan, J. F. Donges, Y. Zou, R. V. Donner, and J. Kurths, *Phys. Lett. A* **373**, 4246 (2009).
- [12] J.-P. Eckmann, S. O. Kamphorst, and D. Ruelle, *Europhys. Lett.* **4**, 973 (1987).
- [13] Y. Shimada, T. Kimura, and T. Ikeguchi, in *Artificial Neural Networks-ICANN 2008* (Springer, Berlin, Heidelberg, 2008), pp. 61–70.
- [14] X. Xu, J. Zhang, and M. Small, *Proc. Natl. Acad. Sci. USA* **105**, 19601 (2008).
- [15] M. Small, J. Zhang, and X. Xu, in *Complex Sciences* (Springer, Berlin, Heidelberg, 2009), pp. 2078–2089.
- [16] R. V. Donner, M. Small, J. F. Donges, N. Marwan, Y. Zou, R. Xiang, and J. Kurths, *Int. J. Bifurcation Chaos* **21**, 1019 (2011).
- [17] R. V. Donner, Y. Zou, J. F. Donges, N. Marwan, and J. Kurths, *New J. Phys.* **12**, 033025 (2010).
- [18] R. V. Donner, J. F. Donges, Y. Zou, N. Marwan, and J. Kurths, Recurrence-based evolving networks for time series analysis of complex systems, in *Proceedings of the International Symposium on Nonlinear Theory and its Applications (NOLTA2010)*, Krakow, Poland (IEICE, Tokyo, 2010), pp. 87–90.
- [19] R. V. Donner, Y. Zou, J. F. Donges, N. Marwan, and J. Kurths, *Phys. Rev. E* **81**, 015101 (2010).
- [20] Y. Zou, R. V. Donner, J. F. Donges, N. Marwan, and J. Kurths, *Chaos* **20**, 043130 (2010).
- [21] F. Strozzi, K. Poljansek, F. Bono, E. Gutierrez, and J. Zaldivar, *Int. J. Bifurcation Chaos* **21**, 1047 (2011).
- [22] Z.-K. Gao, N.-D. Jin, W.-X. Wang, and Y.-C. Lai, *Phys. Rev. E* **82**, 016210 (2010).
- [23] Y. Hirata, Y. Shimo, H. L. Tanaka, and K. Aihara, *SOLA* **7**, 33 (2011).
- [24] D. Senthilkumar, N. Marwan, and J. Kurths, Recurrence network approach to a phase space of a time-delay system, in *Proceedings of the International Symposium on Nonlinear Theory and its Applications (NOLTA2010)*, Krakow, Poland, September 5–8, 2010 (IEICE, Tokyo, 2010), pp. 87–90.
- [25] N. Marwan, N. Wessel, H. Stepan, and J. Kurths, Recurrence based complex network analysis of cardiovascular variability data to predict pre-eclampsia, in *Proceedings of the Biosignal Conference 2010 Berlin* (Potsdam Institute for Climate Impact Research, Potsdam, Germany, 2010), pp. 1–4.
- [26] F. Liao and Y.-K. Jan, in *IEEE Annual International Conference on Engineering in Medicine and Biology Society (EMBC), 2012* (IEEE, New York, 2012), pp. 4196–4199.
- [27] R. V. Donner, J. Heitzig, J. F. Donges, Y. Zou, N. Marwan, and J. Kurths, *Eur. Phys. J. B* **84**, 653 (2011).
- [28] J. H. Feldhoff, R. V. Donner, J. F. Donges, N. Marwan, and J. Kurths, *Phys. Lett. A* **376**, 3504 (2012).
- [29] N. Marwan and J. Kurths, *Phys. Lett. A* **302**, 299 (2002).
- [30] J. F. Donges, H. C. Schultz, N. Marwan, Y. Zou, and J. Kurths, *Eur. Phys. J. B* **84**, 635 (2011).
- [31] Z.-K. Gao, X.-W. Zhang, N.-D. Jin, N. Marwan, and J. Kurths, *Phys. Rev. E* **88**, 032910 (2013).
- [32] N. P. Subramaniyam and J. Hyttinen, Analysis of nonlinear dynamics of healthy and epileptic EEG signals using recurrence based complex network approach, in *6th International IEEE/EMBS Conference on Neural Engineering (NER), San Diego, CA, 2013* (IEEE, New York, 2013), pp. 605–608.
- [33] N. P. Subramaniyam and J. Hyttinen, *Phys. Lett. A* **378**, 3464 (2014).
- [34] T. Schreiber and A. Schmitz, *Phys. Rev. Lett.* **77**, 635 (1996).
- [35] T. Nakamura, M. Small, and Y. Hirata, *Phys. Rev. E* **74**, 026205 (2006).
- [36] J. H. Lucio, R. Valdés, and L. R. Rodríguez, *Phys. Rev. E* **85**, 056202 (2012).
- [37] <http://www.dtic.upf.edu/~ralph/>.
- [38] J. F. Donges, Ph.D. thesis, Humboldt-Universität zu Berlin, Mathematisch-Naturwissenschaftliche Fakultät I, 2013.
- [39] D. J. Watts and S. H. Strogatz, *Nature (London)* **393**, 440 (1998).
- [40] M. E. J. Newman, *Phys. Rev. Lett.* **89**, 208701 (2002).
- [41] L. C. Freeman, *Sociometry* **40**, 35 (1977).
- [42] J. F. Donges, J. Heitzig, J. Runge, H. C. Schultz, M. Wiedermann, A. Zech, J. Feldhoff, A. Rheinwalt, H. Kutza, A. Radebach *et al.*, in *EGU General Assembly Conference Abstracts* (2013), Vol. 15, p. 3558, available at <http://tocsy.pik-potsdam.de/pyunicorn.php>.
- [43] T. Schreiber and A. Schmitz, *Physica D* **142**, 346 (2000).
- [44] R. G. Andrzejak, G. Widman, K. Lehnertz, C. Rieke, P. David, and C. Elger, *Epilepsy Res.* **44**, 129 (2001).
- [45] R. Andrzejak, D. Chicharro, K. Lehnertz, and F. Mormann, *Phys. Rev. E* **83**, 046203 (2011).
- [46] M. C. Casdagli, L. D. Iasemidis, R. S. Savit, R. L. Gilmore, S. N. Roper, and J. Chris Sackellares, *Electroencephalogr. Clin. Neurophysiol.* **102**, 98 (1997).
- [47] R. G. Andrzejak, F. Mormann, G. Widman, T. Kreuz, C. E. Elger, and K. Lehnertz, *Epilepsy Res.* **69**, 30 (2006).
- [48] V. L. Towle, I. Syed, C. Berger, R. Grzeszczuk, J. Milton, R. K. Erickson, P. Cogen, E. Berkson, and J.-P. Spire, *Electroencephalogr. Clin. Neurophysiol.* **106**, 30 (1998).
- [49] H. P. Zaveri, S. M. Pincus, I. I. Goncharova, R. B. Duckrow, D. D. Spencer, and S. S. Spencer, *Neuroreport* **20**, 891 (2009).
- [50] F. Mormann, K. Lehnertz, P. David, and C. E. Elger, *Physica D* **144**, 358 (2000).
- [51] C. Rummel, M. Müller, G. Baier, F. Amor, and K. Schindler, *J. Neurosci. Methods* **191**, 94 (2010).
- [52] E. Ben-Jacob, S. Boccaletti, A. Pomyalov, I. Procaccia, and V. L. Towle, *Chaos* **17**, 043113 (2007).
- [53] G. Bettus, F. Wendling, M. Guye, L. Valtou, J. Régis, P. Chauvel, and F. Bartolomei, *Epilepsy Res.* **81**, 58 (2008).
- [54] C. Rieke, K. Sternickel, R. G. Andrzejak, C. E. Elger, P. David, and K. Lehnertz, *Phys. Rev. Lett.* **88**, 244102 (2002).
- [55] M. Breakspear, M. Brammer, and P. A. Robinson, *Physica D* **182**, 1 (2003).
- [56] C. J. Keylock, *Physica D* **225**, 219 (2007).
- [57] C. J. Keylock, *Phys. Rev. E* **73**, 036707 (2006).

Puthanmadam Subramaniam, N. and Hyttinen, J.

Characterization of dynamical systems under noise using recurrence networks: Application to simulated and EEG data

Physics Letters A, 378(46):3464-3474, 2014.

Reprinted with permission from the publisher.



Characterization of dynamical systems under noise using recurrence networks: Application to simulated and EEG data

Narayan Puthanmadam Subramaniyam^{a,b,*}, Jari Hyttinen^{a,b}

^a Department of Electronics and Communications, Tampere University of Technology, Tampere, Finland
^b BioMediTech, Tampere, Finland

ARTICLE INFO

Article history:

Received 21 May 2014
 Received in revised form 29 September 2014
 Accepted 1 October 2014
 Available online 7 October 2014
 Communicated by C.R. Doering

Keywords:

Nonlinear time series analysis
 Recurrence networks
 Graph theory
 EEG
 Epilepsy
 Chaos

ABSTRACT

In this letter, we study the influence of observational noise on recurrence network (RN) measures, the global clustering coefficient (C) and average path length (L) using the Rössler system and propose the application of RN measures to analyze the structural properties of electroencephalographic (EEG) data. We find that for an appropriate recurrence rate ($RR > 0.02$) the influence of noise on C can be minimized while L is independent of RR for increasing levels of noise. Indications of structural complexity were found for healthy EEG, but to a lesser extent than epileptic EEG. Furthermore, C performed better than L in case of epileptic EEG. Our results show that RN measures can provide insights into the structural properties of EEG in normal and pathological states.

© 2014 Elsevier B.V. All rights reserved.

1. Introduction

Many natural systems are inherently governed by nonlinear dynamics. For example, the dynamical behavior of individual neurons in the brain is governed by threshold and saturation phenomena, which give rise to nonlinearity [1]. Thus, nonlinear time series analysis is an important tool in understanding the dynamical properties of the brain using electroencephalography (EEG), which provides temporal resolution in the millisecond range. One of the most important applications of nonlinear EEG analysis itself is in epilepsy [2,3] because of the dynamic nature of the disease [4]. Furthermore, the underlying dynamics of epileptic EEG are highly nonlinear when compared to normal background EEG activity [5].

Nonlinear dynamical systems (also known as complex systems) have two main properties – determinism and recurrence [6]. A deterministic dynamical system can be defined as a system whose future behavior can be accurately predicted, given sufficient knowledge for the current state of the system exists. Let the current state of the system be given as z_n , such that $z_n \in \mathcal{M} \subseteq \mathbb{R}^m$, where \mathcal{M} is an m -dimensional phase space attractor [7]. If there is an evolution operator $\Phi: \mathcal{M} \times \mathcal{Z} \rightarrow \mathcal{M}$ such that $\Phi(z_n, t) = z_{n+t}$, then

the system described by (\mathcal{M}, Φ) is said to be deterministic if the evolution operator Φ can precisely predict the state z_{n+t} , using the information present in z_n [7]. Recurrence is another property which can be used to characterize the nonlinear dynamics of a system [6]. Recurrence plot (RP) is a method for visualizing recurrences and was originally introduced by Eckmann et al. [8]. An RP is a two-dimensional graphical representation of a matrix (known as recurrence matrix – binary, square, and symmetric) that has an entry of one for times when two states are neighbors (as defined by some proximity criterion) in phase space and zero elsewhere [9]. A simple visual analysis of RPs can give an insight into the dynamics of the system. For example, the RP of a system exhibiting periodic dynamics contains long and non-interrupted diagonals, while for chaotic dynamics, the diagonals are much shorter [6]. On the other hand, for a stochastic system, the RP looks erratic and filled with many isolated black dots [10]. Apart from visual analysis, one can also derive quantitative measures for RPs using recurrence quantification analysis (RQA) [11,12] to investigate the dynamical properties of the system. For an excellent and detailed review on RPs, the reader is referred to [6]. Since the information from real world systems is usually in the form of a time series, one has to reconstruct the phase space using suitable methods like time-delay embedding [13] before applying RP based approaches. Note that, apart from RP-based methods, a host of other nonlinear methods have been introduced for time series analysis. Some of

* Corresponding author.

E-mail address: npsubramaniyam@gmail.com (N. Puthanmadam Subramaniyam).

the most important and popular techniques are correlation dimension [14], Lyapunov exponent [15] and entropy-based measures [16]. An attractive feature of an RP based approach compared to other nonlinear approaches is that, it can be applied to short and non-stationary data [9].

In the last two decades, complex network theory has emerged as a popular tool to analyze complex and spatially extended systems [6]. It has found applications in melange of fields ranging from sociology to biological sciences [17]. Using network measures (local and global) [18,19], one can characterize the network structure and function of a complex system that is composed of many interacting elements [19]. Mathematically, a complex network can be represented by a graph $G = (\mathcal{N}, \mathcal{L})$, where the set $\mathcal{N} = \{n_1, n_2, \dots, n_N\}$ is known as vertices or nodes and the set $\mathcal{L} = \{l_1, l_2, \dots, l_K\}$ are the edges or links between those nodes [18]. For simplicity, we consider undirected graphs only. By integrating complex network theory with the concept of recurrence from dynamical systems theory, a new field of network-based time series analysis has been introduced that deals with the topological characterization of the time series using complex networks [9, 20]. Proximity networks are based on the concept of recurrences. Connectivity in such networks is defined in a data adaptive local manner [21]. Under proximity networks, a class of networks known as recurrence networks, which include k -nearest-neighbor networks, adaptive nearest neighbor (ANN) networks [22,23], and epsilon-recurrence networks (ϵ -networks) [9,20], reinterpret the binary recurrence matrix as an adjacency matrix of the complex network [6]. Specifically, an attractor's neighborhood is defined in terms of either fixed number of edges (k -nearest networks or ANN networks) [8,22–24] or fixed phase space volume (ϵ -networks) [9]. Such networks are also known as fixed mass and fixed volume networks respectively.

By quantifying the topology of the recurrence network using local and global measures from graph theory [25,26], the dynamical properties of the underlying complex system can be characterized [20]. Using global graph theoretic measures like the global clustering coefficient (C) and the average path length (L) for $G(N, K)$, Zou et al. [27] studied the identification of complex periodic windows in the Rössler system using ϵ -networks. It was found that for continuous-time dynamical system, C and L are in general greater for periodic dynamics compared to chaotic dynamics. Specifically, L is much smaller for a system exhibiting chaotic dynamics compared to periodic dynamics. In another study by Shimada et al. [24], using fixed mass networks (k -nearest neighbor networks) it was shown that chaotic dynamics can be characterized by small world networks (high C and small L). Xiang et al. [28] studied fixed mass networks (ANN networks) and found that L scales linearly with the network size for low-order periodic dynamics, but exponentially for chaotic dynamics. Also, the value of C is generally higher for periodic dynamics compared to chaotic dynamics.

Investigating the ability of network measures like C and L to characterize the dynamics of a system in the presence of observational noise is an important research question, as the real world data is seldom noise free. Thiel et al. [29] studied the influence of observational noise on RQA measures and found that these measures are susceptible to noise level of 20% or more (noise level is given as the standard deviation of the underlying noise-free process) and they proposed a threshold ϵ that is five times the standard deviation of the noise [29]. However, it has not been sufficiently studied yet, how the addition of observational noise can cause a change in the measures of recurrence networks like C and L for various threshold parameter (for example, various phase space volumes in case of ϵ -networks or number of edges in case of ANN networks). Also a study involving surrogate analysis method to test for the structural complexity of the data in the presence of noise by network measures like C or L has hitherto not been ad-

ressed. In general, a systematic study investigating the effect of observational noise on recurrence network measures and the ability of such measures to characterize the dynamical systems under increasing levels of noise is missing.

As mentioned before, nonlinear analysis is an important technique to understand the dynamical properties of the brain, especially in disorders like epilepsy. Andrzejak et al. [1] applied nonlinear measures like nonlinear prediction error P and effective correlation dimension $D_{2,eff}$ to different classes of EEG data: healthy EEG with eyes open and closed, EEG recordings between the seizures which is known as interictal EEG and EEG recordings of epileptic seizures which is known as ictal EEG. They reported strongest indication of nonlinearity for ictal EEG, while healthy EEG (eyes open) was compatible with quasilinear process. Gautama et al. [30] applied the method of delayed vector variance (DVV) for the data described in [1] and found indications of nonlinearity for both intracranial and surface EEG recordings. Given the potential of recurrence networks in characterization of dynamical systems and its reported advantages over other traditional non-linear measures in terms of its applicability to short and non-stationary data, its application in investigating the dynamical properties of EEG signals has not been fully explored. We have previously used the dataset described in [1] and characterized the underlying dynamics using fixed mass recurrence networks [31]. We found that the networks associated with ictal EEG are regular with high C and L , while the networks associated with interictal and surface EEG signals show small world property. However, we did not consider the effect of varying the threshold on the derived network measures. Also, we did not perform any surrogate analysis as reported in [1] to analyze structural properties of different classes of EEG signals.

Surrogate testing is an important tool in signal analysis [32]. In general, to use surrogate techniques for detecting nonlinearity, a null hypothesis is defined, which assumes that the original signal is compatible with a linear, stochastic, and stationary process, which is observed through a possibly nonlinear measurement function [1]. Based on this null hypothesis, a large number of signals (known as surrogates) are generated from the original signal such that the surrogates have the same linear autocorrelations as the original signal, but are otherwise random [32]. We then calculate a discriminating statistic for both the original signal and the surrogates. If the discriminating statistic of the original signal deviate from the surrogates, the null hypothesis is rejected. Rejection of the null hypothesis implies that the original signal is not consistent with the assumption of a linear, stochastic and stationary process and could indicate the presence of a possible nonlinear structure with a certain confidence level. Since recurrence network measures (like C and L) describe the structural properties of the attractors underlying a time series [33], these measures can be used as a discriminatory statistic to test for the structural complexity of the original data in conjunction with surrogates.

In this letter our aim is to investigate the ability of global network measures like C and L derived from recurrence networks to characterize dynamical systems under increasing levels of noise using simulated data and then to apply this method to study the structural properties of experimental signals like the EEG data. We organize our study to answer two specific questions

1. At what noise level is the structural complexity and detection of dynamical transitions as measured by recurrence network measures obscured?
2. Can recurrence network measures be used to analyze the different structural properties of healthy and epileptic EEG signals?

To answer question 1, we simulate the Rössler system to display periodic and chaotic dynamics, to which we systematically add in-

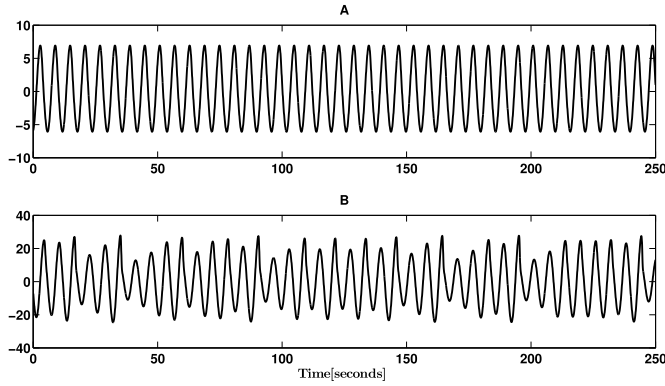


Fig. 1. Time series of the solution of Rössler system (x -component, 5000 data points) generated with a step size of $h = 0.05$ for (A) periodic regime ($a = b = 0.1$, $c = 4$) and (B) chaotic regime ($a = b = 0.1$, $c = 18$).

creasing levels of noise. To answer question 2, we use healthy and epileptic EEG datasets published in [1]. In this study we will focus only on recurrence networks derived using fixed volume approach, i.e., ε -networks. We also perform surrogate analysis [34] to investigate the ability of dynamical invariants like C and L derived from recurrence networks in analyzing structural properties of healthy and epileptic EEG time series.

2. Materials and methods

2.1. Simulated and real data

We used the Rössler system [35] to simulate periodic and chaotic regimes and for the real-world data we used the EEG data described in [1]. The following sections describe more in detail about the simulated and real-world data used in this study.

2.1.1. Rössler system

The Rössler system [35] is defined by a set of ordinary differential equations (ODE) as follows,

$$\frac{dx}{dt} = -y - z, \quad (1)$$

$$\frac{dy}{dt} = x + ay, \quad (2)$$

$$\frac{dz}{dt} = b + z(x - c) \quad (3)$$

By varying the parameters a , b , and c we can generate periodic and chaotic dynamics. In this study, a and b were fixed at 0.1, while c was set to 4 and 18, to generate periodic and chaotic dynamics respectively. The ODE was solved using the fourth-order Runge–Kutta method with a fixed step size of $h = 0.05$. We performed 100 simulations each for periodic and chaotic dynamics with randomly chosen initial conditions. The initial transients were removed by discarding the first 5000 steps of integration. For constructing networks based on the time series, we used 5000 data points of the x -component of the solution of the Rössler ODE and reconstructed the phase space using time-delay embedding. Exemplary signals (x -component) for periodic and chaotic regimes are shown in Fig. 1.

To the simulated data $x(t)$, we added the Gaussian observational noise $\eta(t)$,

$$x_{\text{noise}}(t) = x(t) + \eta(t) \quad (4)$$

Table 1

EEG published by Andrzejak et al. [1] which is used in this study.

Datasets	Description	Number of signals
A	Eyes open	100
B	Eyes closed	100
C	Hippocampal-Interictal	100
D	Epileptogenic Zone-Interictal	100
E	Ictal	100

where $\eta(t) \sim \mathcal{DN}(0, \sigma^2)$. Here \mathcal{D} defined as the level of noise, which is given as a percentage of the standard deviation of the noise-free data $x(t)$. In this study, we added Gaussian noise at levels 10%, 20%, 40%, and 60%. In total, for each dynamics we had 500 signals (100 iterations of the noise-free data plus 100 iterations \times four noise levels).

2.1.2. EEG data

In this study, we used the EEG data published by Andrzejak et al. [1], which is available online at <http://epileptologie-bonn.de>. Description of the EEG data is given in Table 1. More details about the data, recording settings and conditions can be found elsewhere [1]. Briefly, the data contains five sets of EEG signals denoted as A–E, where sets A and B contain segments from the surface EEG recordings in eyes open and eyes closed conditions respectively. Sets C and D contain intracranial EEG recordings obtained between the seizure activity (known as interictal EEG) from hippocampal zone and epileptogenic zone respectively. Set E contains intracranial EEG recordings obtained during the seizure activity (known as ictal EEG). The sampling frequency was 173.6 Hz and each set contains 100 EEG signals of duration 23.6 seconds (4096 samples) each.

2.2. Time series to recurrence networks

We applied time delay embedding methodology proposed by Takens to reconstruct the attractor from the time series [13]. Given a scalar time series $v(t_i)$, where $i = 1, 2, \dots, N$ samples, an m -dimensional phase space attractor can be reconstructed,

$$\mathbf{x}_i = (v(t_i), v(t_i + \tau), \dots, v(t_i + (m - 1)\tau)) \quad (5)$$

with $\mathbf{x}_i \in \mathbb{R}^m$. The optimal time delay τ is obtained as the first minimum of the auto mutual information [36] and the minimum

embedding dimension m can be obtained using the false nearest neighborhood (FNN) approach [37]. After the reconstruction of the attractor, we can define the RP in different ways based on different neighborhood criteria. In general, an RP tells us at what times the state vectors are close to each other as defined by the neighborhood criteria and the corresponding distance norm (Euclidean or Manhattan or maximum). This recurrence matrix can be further reinterpreted as an adjacency matrix for further network analysis. In this study, we specifically consider the fixed volume (ε -network) approach to define the neighborhood. In this approach one can define the neighborhood of an attractor in terms of a fixed phase space distance $-\varepsilon$ [9,20]. According to this approach, given an m -dimensional phase space attractor, we can compute a recurrence matrix with elements,

$$R_{i,j} = \Theta(\varepsilon - d(\mathbf{x}_i, \mathbf{x}_j)) \quad (6)$$

where Θ is the Heaviside function, ε is the size of the neighborhood, also known as the recurrence threshold, d is any suitable distance norm (in this work we have used maximum norm), and \mathbf{x} is the phase space attractor. Thus, the binary recurrence matrix \mathbf{R} contains one for all the pairs of state vectors that satisfy the condition $d(\mathbf{x}_i, \mathbf{x}_j) < \varepsilon$ and zero otherwise [9]. The adjacency matrix \mathbf{A} is given by,

$$\mathbf{A} = \mathbf{R} - \mathbf{I} \quad (7)$$

where \mathbf{I} is an identity matrix. The above equation simply eliminates all the self-loops from \mathbf{R} .

We constructed ε -networks from the Rössler system and the EEG datasets by fixing the recurrence rate RR instead of the threshold ε so that we obtain ε -networks with approximately the same number of edges so as to facilitate objective comparison between different ε -networks [21]. Thus, we construct ε -networks for RR ranging from 0.01 to 0.05 in steps of 0.01. For each time series, we estimated τ using the first minimum of the auto mutual information. The minimum embedding dimension was obtained using the modified FNN approach described in [38] to avoid spurious results due to noise. Basically, the modified FNN approach suppresses all those pairs whose initial distance is already greater than σ/r , where the threshold r is set to the standard choice of 10 [37,38] and σ is the standard deviation of the data. This way invalid candidates are excluded from the computation of the FNN statistic.

2.3. Complex network measures

2.3.1. Global clustering coefficient

The measure clustering coefficient for a graph was introduced by Watts and Strogatz [26]. For a given node i , if there are two neighbors j and m , then the clustering coefficient of a node i , given by c_i , simply tells how likely it is for j and m to be also neighbors [18]. In other words, how likely is it for $a_{jm} = 1$, where a_{jm} is the element of the adjacency matrix \mathbf{A} . Mathematically,

$$c_i = \frac{\sum_{j,m} a_{ij} a_{jm} a_{mi}}{k_i(k_i - 1)} \quad (8)$$

where k_i is the degree of node i (i.e., number of edges incident on node i). Then one can define clustering coefficient for the entire graph $G(N, K)$, known as the global clustering coefficient C ,

$$C = \frac{1}{N} \sum_{i \in \mathcal{N}} c_i \quad (9)$$

The global clustering coefficient C is a sensitive indicator of dynamical transitions and can be used to detect qualitative changes in the dynamics [21]. For continuous dynamical systems, the value of C for periodic trajectories is higher than that of chaotic trajectories for comparable ε [27].

2.3.2. Average path length

Given two nodes, i and j , a geodesic is defined as a path of minimum length between these nodes. The length of this path is known as the geodesic length between i and j and is denoted by d_{ij} . The average path length L for a graph can then be defined as the mean value of geodesic lengths over all couple of nodes. It is given by the following equation,

$$L = \frac{1}{N(N-1)} \sum_{i,j \in \mathcal{N}, i \neq j} d_{ij} \quad (10)$$

The disconnected pairs of nodes are excluded from the computation of the average [9,18]. Changes in the values of L can be used as an indicator of dynamical transitions in complex systems [9]. For example, a complex system (continuous system) with periodic trajectory has a higher L compared to a complex system exhibiting chaotic dynamics for comparable ε [27].

2.4. Surrogate analysis and statistical testing

Surrogates were generated for simulated as well as real data using iterative amplitude adjusted Fourier transform (IAAFT) scheme [34]. This method employs an iteration scheme and produces surrogates that have the same power spectra and values as the original data at hand [34]. For each time series, we generated 49 surrogates. The null hypothesis H_0 , to be tested is that the underlying dynamics of the time series is a stationary, linear, stochastic, and correlated process which is measured by a static, monotonic, and possibly nonlinear observation function [1,34]. Further, the autocorrelation, mean, and variance of the underlying process are such that the measurement results in the autocorrelation and amplitude distribution of the original time series [32]. Without making any assumption about the underlying distribution of the data, similar to the approach given in [1], we employ a non-parametric method to test the null hypothesis H_0 . The procedure is outlined as follows,

1. Compute the network measure (C or L) for the original data. Let us denote it as M^d .
2. Compute the network measure (C or L) for the corresponding 49 surrogates.
3. Find the maximum and minimum of the surrogate network measures. Let us denote it as M_{max}^{surr} and M_{min}^{surr} respectively.
4. Reject H_0 if ($M^d > M_{max}^{surr}$) or ($M^d < M_{min}^{surr}$).

Let R_{max} be the number of rejections of H_0 in a given set, because $M^d > M_{max}^{surr}$. For a two-tailed test, the probability p_{max} (or p_{min}) of having R_{max} (or R_{min}) or less rejections at the significance level of $\alpha = \frac{2}{1+s}$, where s is the number of surrogates (49 in our case, thus $\alpha = 0.04$) can be estimated via binomial cumulative distribution function [1,39]

$$p_{max} = 1 - \sum_{k=0}^{R_{max}} \binom{n}{k} (\alpha)^k (1-\alpha)^{n-k} \quad (11)$$

where n is the number of signals in a given set. In an analogous manner, one can compute p_{min} using R_{min} . For the EEG dataset, we also perform statistical testing at the set level using nonparametric Wilcoxon signed rank test [1] to facilitate the comparison of our results with the results of Andrzejak et al. [1]. We used one surrogate per set and use $\{M_d\}$ and $\{M_1^{surr}\}$ as paired observations for the Wilcoxon signed rank test as suggested in [1].

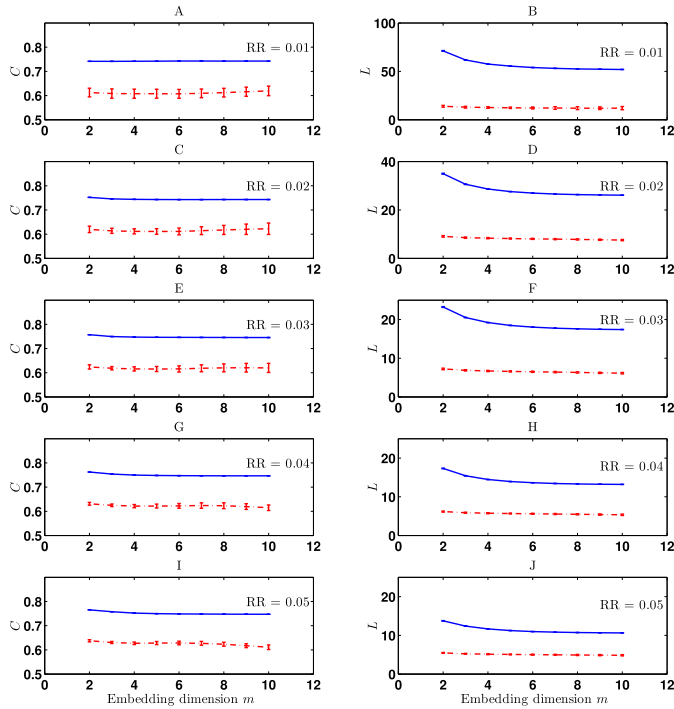


Fig. 2. Dependence of the network measures C (A) and L (B) on the embedding dimension m for periodic (blue solid line) and chaotic dynamics (red dashed line) respectively under noise-free condition for ε -networks at the recurrence rate $RR = 0.01$. The network measures are the averaged over the 100 realizations of the Rössler system. The error bars are the standard deviation of the 100 realizations of the Rössler system. (C–D), (E–F), (G–H), and (I–J) are the same as in (A–B), but at $RR = 0.02, 0.03, 0.04$ and 0.05 respectively. (For interpretation of the references to color in this figure legend, the reader is referred to the web version of this article.)

3. Results

3.1. Rössler systems

3.1.1. Noise-free condition

Fig. 2 shows the variation of the network measures C and L as a function of the embedding dimension. It can be seen from Fig. 2 that for different recurrence rates ($RR = 0.01$ to 0.05), the difference between network measures (C and L) for the periodic and chaotic dynamics is clear and remains consistent, with C and L of ε -networks constructed from the periodic time series being greater than that of the chaotic time series. Fig. 3 shows the variation of network measures C and L with respect to RR for ε -networks at the embedding dimension $m = 3$. The embedding delay as given by the first local minimum of the auto mutual information varied between 5 and 10 for the periodic dynamics, while for the chaotic dynamics it varied between 25 and 30. It can be seen that the C for ε -network increases and L decreases with increasing RR for both the periodic and chaotic dynamics. However, as mentioned before, from Fig. 2 it is clear that the difference between the periodic and chaotic dynamics remains consistent across varying values of RR for the ε -network under noise-free condition.

3.1.2. Effect of noise: noisy periodic vs. noise-free chaotic dynamics

Here we compare noisy periodic dynamics with noise-free chaotic dynamics. Let C and L of noise-free chaotic dynamics be

denoted as C_{c0} and L_{c0} . We have already seen that under noise-free condition (0% noise), the value of C and L for periodic dynamics is greater than C_{c0} and L_{c0} . We would like to investigate at what level of additive noise do the network measures for periodic dynamics become lesser than C_{c0} and L_{c0} and thus become unreliable in the detection of dynamical transitions. This could be, for example, a scenario where there is chaos-periodic transition and the periodic dynamics is superimposed with noise. Note that if the noise is dynamical, then such bifurcation scenario might be enhanced or suppressed as dynamical noise impacts the future evolution of the system. Here we consider only the case of superimposed observational noise and investigate how reliable are the network measures C and L in distinguishing noisy periodic state from chaotic state. In order to do so, we computed the C and L for periodic dynamics under increasing levels of noise (10%, 20%, 40% and 60%). From Fig. 4(A) it can be seen that at $RR < 0.03$, the C for periodic dynamics at noise level of 10% and above is lesser than C_{c0} . For $RR \geq 0.03$, at 10% noise level we can see that C of periodic dynamics is greater than C_{c0} . The situation for L is different. At all values of RR from 0.01 to 0.05, L for periodic dynamics is greater than L_{c0} at noise level of 10% (see Fig. 4(B)). For noise levels of 20% and above, both C and L fail to have values greater than C_{c0} and L_{c0} respectively for all values of RR . When adding noise to the signals, it was observed that the value of τ decreases

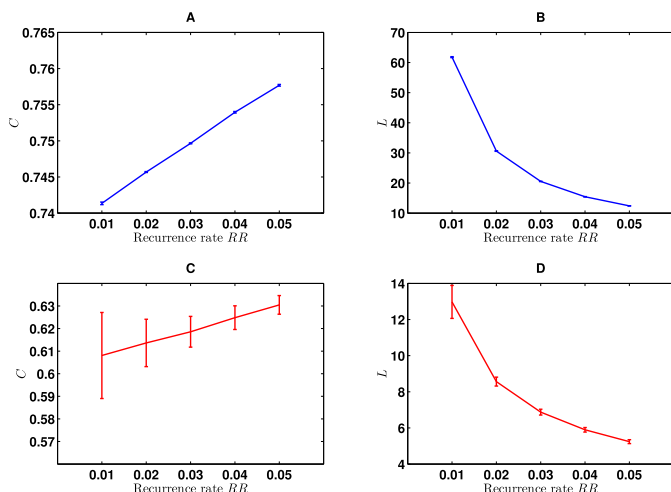


Fig. 3. Dependence of the network measure C (A) and L (B) on the recurrence rate RR for periodic dynamics. The network measures are the averaged over the 100 realizations of the Rössler system. The error bars are the standard deviation obtained from 100 realizations of the Rössler system. (C–D) is the same as in (A–B), but for chaotic dynamics.

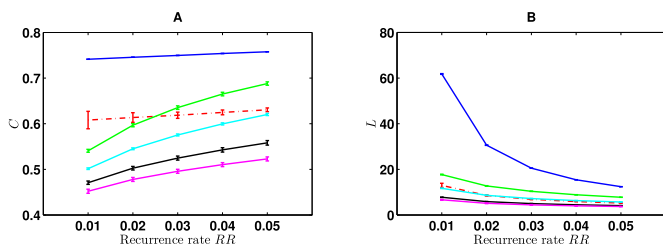


Fig. 4. Influence of observational noise on the network measures. (A) Dependence of the network measure C for periodic dynamics at noise levels of 0% (blue solid line), 10% (green solid line), 20% (cyan solid line), 40% (black solid line), 60% noise (magenta solid line) and for chaotic dynamics at noise level of 0% (red dashed line) for ϵ -networks. The network measures are the averaged over the 100 realizations of the Rössler system. The error bars are the standard deviation obtained from 100 realizations of the Rössler system. (B) Same as in (A), but for the network measure L. (For interpretation of the references to color in this figure legend, the reader is referred to the web version of this article.)

as the level of noise increases. Especially at high noise levels (60%) there is an abrupt drop in the value of τ .

3.1.3. Effect of noise: noisy periodic vs. noisy chaotic dynamics

Next, we compare the network measures C and L for noisy periodic and chaotic dynamics. Fig. 5 shows how C and L for periodic and chaotic dynamics change for increasing levels of additive noise at different RR (from 0.01 to 0.05). It can be seen that in case of C, as RR is increased the difference between noisy periodic and chaotic dynamics becomes clear with C of noisy periodic dynamics being greater than C of chaotic dynamics. Particularly, for RR greater than 0.02, we can still distinguish between noisy periodic and chaotic dynamics (C of noisy periodic dynamics > C of noisy chaotic dynamics) up to noise levels of 40%. However at noise levels above 40%, even at RR = 0.05, the value of C for noisy periodic and chaotic dynamics starts becoming indistinguishable. In case of L, it is evident that the difference between noisy periodic and chaotic dynamics is not dependent on RR. Irrespective of the value of RR, the L for noisy periodic dynamics is still greater than L for noisy chaotic dynamics for noise levels up to 20%. At higher noise

levels, the value of L for noisy periodic and chaotic dynamics becomes indistinguishable.

3.1.4. Effect of noise: test for structural complexity under noise

In order to study the ability of network measures to characterize the structural complexity of the time series under the influence of noise, we generated surrogates from the original time series that are stochastic linear processes observed via a static, monotonic, and possibly nonlinear function [34]. The results of non-parametric testing with the surrogate data for chaotic dynamics under increasing levels of noise are presented in this section. It has to be noted that we present the results only for rejections due to R_{max} as in all cases R_{min} was zero and thus non-significant ($p_{min} > 0.04$).

Tables 2 and 3 show the number of rejections (out of 100 signals), R_{max} , at various noise levels and RR for the network measures C and L respectively. For the network measure C, it can be clearly seen from Table 2 that at 0% noise level, irrespective of RR, R_{max} is almost 100 indicating that almost all the signals rejected H_0 . At 10% noise level, at RR of 0.02 or higher, R_{max} is greater than 90. As the noise level increases, R_{max} increases only

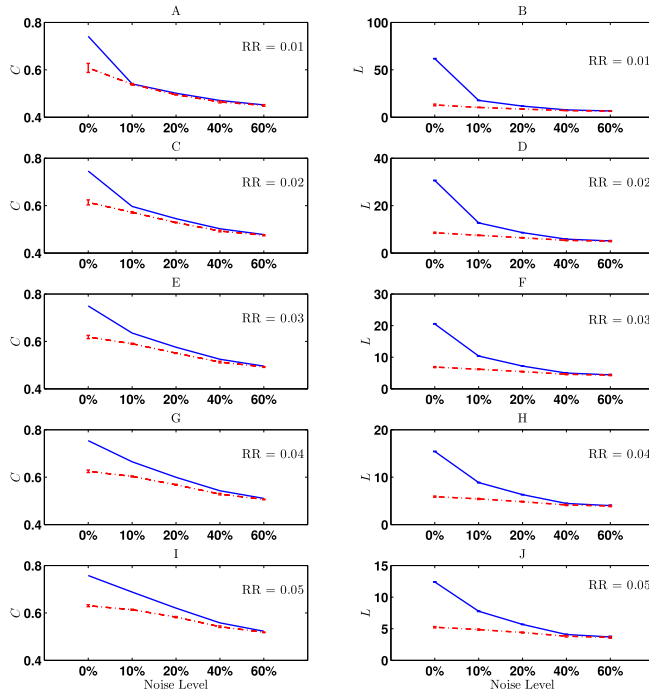


Fig. 5. Influence of observational noise on the network measures C (A) and L (B) for periodic (blue solid line) and chaotic (red dashed line) signals at recurrence rate $RR = 0.01$. The network measures are the averaged over the 100 realizations of the Rössler system. The error bars are the standard deviation of the 100 realizations of the Rössler system. (C–D), (E–F), (G–H), and (I–J) are the same as in (A–B), but at $RR = 0.02, 0.03, 0.04$ and 0.05 respectively. (For interpretation of the references to color in this figure legend, the reader is referred to the web version of this article.)

Table 2

Results of surrogate analysis on simulated chaotic signals: number of signals (out of 100) for which H_0 is rejected (R_{max}) using C as discriminatory statistic at various noise levels and RR . Rejections are considered not significant if $p_{max} > 0.04$ and are marked as zero.

Noise level	0.01	0.02	0.03	0.04	0.05
0%	100	100	100	98	98
10%	74	94	96	96	96
20%	0	0	38	66	76
40%	0	0	30	38	38
60%	0	0	16	18	24

as the RR increases, reaching 76 and 38 at noise levels of 20% and 40% respectively at $RR = 0.05$. At noise level of 60%, 24 out of 100 the signals reject H_0 at $RR = 0.05$. It is to be noted that as per Eq. (11) the probability of having 20 rejections or less by chance is already very small (4.19×10^{-4}) at the significance level of $\alpha = 0.04$. From Table 3 it can be seen that for L , R_{max} is 100 for noise levels up to 20% regardless of RR . At noise levels of 40% and above, R_{max} drops to about 30 at $RR = 0.01$ and remains in the range of 28 to 34 for increasing RR .

3.2. EEG data

3.2.1. Recurrence network measures

Using the modified FNN approach, we found that the minimum embedding dimension for all the EEG time series in set A–E.

Table 3

As in Table 2, but for L as discriminating statistic.

Noise level	0.01	0.02	0.03	0.04	0.05
0%	100	100	100	100	100
10%	100	100	100	100	100
20%	100	100	100	100	100
40%	28	28	28	30	30
60%	30	24	28	34	32

Since we have limited amount of EEG data ($N = 4096$ samples) which might be even noisy, the embedding dimension cannot be set too high as the noise in the data may reduce the density of the points defining the attractor. In this work, we set $m = 6$ for the phase space reconstruction, which is the largest embedding dimension consistent with the available amount of data [10] and the modified FNN criterion [38]. The embedding delay τ given as the first local minimum of the auto mutual information, which varied between 5 and 20. Fig. 6 shows the variation of C and L as a function of RR for the set A–E of EEG signals. It is clear from the figure that set E has the highest C and L for RR of 0.02 or higher, followed by the sets D, C, B, and A. The same order is observed in decreasing values of L and it is consistent for all the values of RR . As for the Rössler system (see Fig. 3), we can observe here as well that C increases with increasing RR while L decreases.

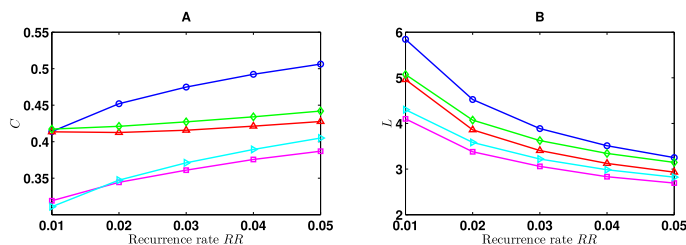


Fig. 6. Dependence of the network measures C (A) and L (B) on the recurrence rate RR for the EEG dataset – eyes open (set A, \square), eyes closed (set B, \triangleright), interictal-hippocampal zone (set C, Δ), interictal-epileptogenic zone (set D, \diamond), and ictal (set E, \diamond). The network measures shown are the average of 100 EEG signals in each dataset.

Table 4

Results of surrogate analysis at individual level for EEG data at $RR = 0.05$. The number of rejections R_{max} at significance level $\alpha = 0.04$ for sets A–E is shown. As comparison, results from [1] and [30] are shown in columns 3, 4 and 5 respectively.

Datasets	Description	C	L	P [1]	$D_{z,eff}$ [1]	DVV [30]
A	Eyes open	17	20	4	0	29
B	Eyes closed	21	33	9	0	32
C	Hippocampal-Interictal	26	37	14	0	46
D	Epileptogenic Zone-Interictal	48	40	37	17	53
E	Ictal	98	76	89	56	92

3.2.2. Structural properties of different EEG time series

Table 4 presents the results of surrogate analysis for EEG datasets at an individual level using C and L as discriminatory statistic at $RR = 0.05$ (Only R_{max} is presented as R_{min} was not significant in all cases). Comparison of our results to the work of Andrzejak et al. [1] and Gautama et al. [30] is also presented in Table 4. It is evident from Table 4 that maximum rejections of H_0 is found for set E (ictal activity) followed by sets D (interictal activity-epileptogenic zone), C (interictal activity-hippocampal zone), B (scalp EEG, eyes closed) and A (scalp EEG, eyes open) when using C and L as the discriminatory measure. For epileptic EEG recordings capturing the epileptogenic interictal and ictal activity (D and E), we find that L gives lesser rejections compared to C .

Table 5 shows the results of surrogate analysis at the set level using nonparametric Wilcoxon signed rank test at $RR = 0.05$. We found the null hypothesis to be rejected ($p < 0.001$) for all sets of EEG data when using both C and L as the discriminatory measure.

4. Discussion

Our results using the Rössler system show that the recurrence network measures (C and L) are able to clearly distinguish between periodic and chaotic dynamics under noise free condition. The influence of noise on the network measure C can be minimized by an appropriate choice of RR , while the influence on L is independent of this choice. Our results from surrogate analysis using chaotic time series data from Rössler system show that both C (with an appropriate choice of RR) and L can still characterize its phase space structure in the presence of noise levels as high as 60%. We applied recurrence networks to analyze the structural properties of EEG time series. For this purpose, we used the EEG data described in [1]. By combining network measures C and L with surrogates (IAAFT method), we could differentiate between the structural properties of the attractors reconstructed from pathological (epileptic) and healthy EEG.

4.1. Effect of noise on network measures

In a study by Zou et al. [27], it was reported that the difference between chaotic and periodic network measures for ε -networks

remain consistent over a reasonable range (0.01 to 0.05) of RR under noise free conditions, wherein C and L of networks constructed from periodic time series are consistently greater than that of chaotic time series for continuous dynamical systems like the Rössler system. Our results are in accordance with their study. Previous studies have shown that L scales with the recurrence threshold as $1/\varepsilon$ [40] and C is severely affected by the attractor boundaries as ε gets larger [20]. Our results confirm this as we observe that L decreases and C increases as RR is increased.

The networks constructed from periodic attractors of a continuous system like the Rössler system tend to have high values of C and L compared to that of chaotic attractors [24,27], as the filling of the phase space with observed states for periodic trajectories is less homogeneous than chaotic ones [27]. Addition of observational noise to the periodic time series makes the underlying dynamics high dimensional [22,28] (as also revealed by the fact that minimum embedding dimension increases with addition of noise), thus increasing the dimension of the space in which the associated spatial networks are embedded. This leads to lower values of C for the associated networks as explained by the theory of spatial random graphs [41], which states that C becomes smaller for increasing spatial dimension, which has been observed in our results as well. At low levels of RR , noise dominates the detection of periodic dynamics. Also, small values of RR correspond to small ε and thus resolve mainly small-scale structures of the attractor. Adding noise less than the order of ε will corrupt these structures, which will mainly affect C . We observed that increasing the RR minimizes the effect of noise. This is because, as RR (and thus ε) increases, larger and larger scales will be captured and thus remain potentially unaffected by the noise amplitude. It has been suggested that a choice of $RR \lesssim 0.05$ is reasonable to construct recurrence networks [42]. In view of this, if the noise level is high (20% or more), then using the network measure C can lead to problems in distinguishing between periodic dynamics with noise and noise free chaotic dynamics even at $RR = 0.05$. Addition of noise to the periodic time series decreases the network diameter of the associated recurrence network, which in turn reduces the maximum path length of the network. So naturally, L decreases with the addition of noise. At noise level of 10%, this reduction still results in values of L for periodic dynamics with

Table 5
Results of surrogate analysis at group level using Wilcoxon test for EEG sets **A–E** at $RR = 0.05$ are shown. As comparison, results from [1] are shown in the last two columns. Rejections are considered significant if $p < 0.05$.

Datasets	Description	C	L	P [1]	$D_{2,eff}$ [1]
A	Eyes open	H_0 rejected	H_0 rejected	H_0 not rejected	H_0 not rejected
B	Eyes closed	H_0 rejected	H_0 rejected	H_0 rejected	H_0 not rejected
C	Hippocampal-Interictal	H_0 rejected	H_0 rejected	H_0 rejected	H_0 not rejected
D	Epileptogenic Zone-Interictal	H_0 rejected	H_0 rejected	H_0 rejected	H_0 rejected
E	Ictal	H_0 rejected	H_0 rejected	H_0 rejected	H_0 rejected

noise which are greater than noise free chaotic dynamics (irrespective of the choice of RR), indicating that the average phase space separation of states in periodic dynamics at this noise level (10%) is still greater than in the case of chaotic dynamics without noise. Any further increase in the noise level added to the periodic dynamics will impact the distribution of points in the phase space and makes it more heterogeneous, leading to artificial shortcuts that drops the path length and in this case, below that of the noise free chaotic dynamics. In short, if periodic time series is corrupted by a level of observational noise which is greater than 10%, then the statistics of the associated networks drop below that of noise free chaotic time series. In the case where noise added to both periodic and chaotic dynamics, the corresponding network measures C and L associated with periodic and chaotic dynamics decreases as noise is increased. Distinction between noisy periodic and chaotic dynamics is still possible up to noise levels of 40%, for an appropriate choice of RR (>0.02) in case of C whereas, L can distinguish between noisy periodic and chaotic dynamics up to the noise levels of 20% irrespective of the choice of RR .

The effect of observational noise on RQA was studied in [29] and it was found that a noise level of 20% or higher could lead to the failure of RQA measures and a choice of recurrence threshold, ϵ , five times the standard deviation of the observational noise was recommended. Our results on recurrence network measures, which are also derived from recurrence matrices like RQA, indicate similar observations, in the sense that, as the recurrence rate (which is related to ϵ) is increased, the effect of noise on C is minimized while L is not affected by this choice. Also, we found that L and C could still characterize structural complexity in some signals at a noise level as high as 60%. To answer first question raised in Section 1, the network measures C and L can characterize dynamical transitions under noise, where periodic dynamics with noise can be distinguished from chaotic dynamics with noise using C (for an appropriate RR up to noise level of 40%) and L (up to noise level of 20%). Also, the structure of the time series can be characterized even at the noise level as high as 60% (again with appropriate choice of RR only in case of C).

However, it is important to note that the results obtained here are system-specific and hence the effect of noise levels on the network measures strictly refer to the two reference states we have considered in simulating the periodic and chaotic dynamics. Hence the value of tolerable noise levels might vary for different parameters (for example different values of c in Eq. (1)), especially for the chaotic regime. The general behavior of network measures under the influence of noise for a range of system parameters will be a subject of future study.

Another aspect to be noted here is that L is impacted by the transients in the data that could create artificial shortcuts [27] leading to a value of L lower than that of the corresponding surrogates. In case of simulation study described in this work, we have removed the initial transients [27] and that probably could be the one of the reasons for the good performance L as a discriminating statistic. However, in case of noisy experimental data, the computation of L may be impacted due to the aforementioned reason, which is also discussed in [27] and in the following section.

4.2. Application to EEG data

Andrzejak et al. [1] used P and $D_{2,eff}$ to study the dynamical properties of the EEG time series. Using P and $D_{2,eff}$, they found the maximum number of rejections for ictal activity (set **E**) and thus a strong evidence for an underlying nonlinear process, while no significant rejections were found for scalp EEG in eyes open condition (set **A**). In comparison to [1], our results gave higher rejection rates for sets **A–E** using recurrence network measures. The main difference was that we could obtain higher rejections of H_0 in sets **A** and **B** which are surface EEG recordings compared to [1]. Gautama et al. [30] applied the method of delay vector variance (DVV) for the EEG data described in [1] and also obtained higher rejections of H_0 in sets **A** and **B** compared to [1]. We have previously applied fixed mass recurrence network method to the EEG data described in [1] and found that networks associated with surface EEG signals are more complex than random networks [31]. As noted in [30], P takes into consideration only the deterministic structure, which alone cannot account for nonlinearity. This can lead to the linear surrogates having the same predictability as the original data, thus leading to false negatives. The DVV method on the other hand is a phase space based method that can detect deterministic property in addition to the nonlinear behavior in the signal [30]. Similarly, RP based methods also work on the phase space geometry and use the recurrence property of the dynamical system. Due to these reasons, DVV and RP based methods yield better performance over other nonlinear methods described in [1]. Our results (especially from **C**), clearly point towards an increasing degree of structural complexity in epileptic EEG by giving higher rejections of H_0 compared to healthy EEG, which is consistent with the transition towards nonlinearity in epileptic EEG compared to healthy EEG as reported in [1,30].

The dynamics behind the epileptic seizures are assumed to be highly non-linear in comparison to the normal EEG activity [5, 43–46]. Our results show that the ictal signals (set **E**) gave maximum number of rejections for H_0 using both C and L , implying that the attractors reconstructed from ictal signals are different and structurally more complex than that of surrogate signals, which by construction are linear-stochastic processes. Sets **C** and **D** comprise of interictal EEG, recorded from non-epileptogenic and epileptogenic zones respectively. Accordingly, more signals in **D** rejected H_0 in comparison to **C**. Placing this in the context of the results reported in previous studies, it seems plausible that interictal EEG obtained from epileptogenic zones could reflect more non-linearity due to its direct involvement in the epileptic process [1]. As mentioned previously in Section 1, due to the threshold and saturation phenomena, non-linear dynamics is introduced at the level of single neurons in the brain. In this regard, the neuronal dynamics can be modeled as a nonlinear dynamical system [47]. Whether this nonlinearity is reflected in macroscopic EEG recordings, which measures the summed activity of quasi-independent neurons, is questionable [48]. Also, as mentioned in [1], the blurring of the dynamical properties of surface EEG could be caused because surface EEG signals recorded at the scalp are measured from the activity of a large number of neurons and are further subjected to volume conduction. However, surface EEG generated

due to a constraint imposed such as closing of the eye (the alpha rhythm), strengthens the nonlinear structure of the underlying signal [1]. However other results have reported an evidence of an underlying nonlinear structure in surface EEG recordings under normal conditions (eyes open) [30,49,50].

It is important to recognize that, the number of signals rejecting H_0 using L as a discriminatory measure in case of sets **D** and **E** (which includes interictal EEG from epileptogenic zone and ictal EEG respectively) were less than that of using C as a discriminatory measure. This probably could be due to the presence of transients like spike and sharp waves in epileptic signals [51], which could have impacted the computation of L . This was not observed in the simulated scenario where we could simply discard the initial transients. In this sense, C is comparatively a more robust measure, which could still give high number of rejections in case of epileptic EEG sets **D** and **E**. Nonetheless, L could still reject reasonable percentage of signals in these sets based on surrogate testing. The other caution to be exercised as already noted in [1], is that the surrogates generated are stationary signals by construction. Hence H_0 can be rejected based on non-stationarity in the data as well. Another limitation of the study is that is we have not considered the effect of noise due to biological artifacts in the EEG signals. The EEG signals considered in this study have been selected after visual inspection to exclude artifacts arising from the muscle activity or eye movement [1]. Overall, our results are in agreement with the results reported in [1] for sets **C-E** and with the results reported in [30] for sets **A-E**. Answering the second question raised in Section 1, we can conclude that the recurrence based network approach can be used to determine the structural properties of different classes of EEG signals. This approach is robust and more sensitive even in detecting certain degree of structural complexity existing in macroscopic EEG recordings like the surface EEG signals [30,49,50] compared to other nonlinear methods reported in [1]. Thus, our results show that recurrence network measures capture a more elaborated property of structural complexity. As recurrence network measures can be computed from short time series with high confidence [52], they can cope with non-stationarity through window-based analysis [9,21].

The issue of selecting the embedding dimension, m , for noisy and finite experimental signals like the EEG data needs some mention here. Previous studies on the same EEG dataset have reported an embedding dimension of $m = 6$ [1], $m = 8$ [32], and $m = 10$ [30]. In this work, we also tried varying m from 2 to 12 and found that for most of the EEG signals in set **E**, which contains ictal activity (which are hypothesized to be low-dimensional [5]), the network measures did not change much beyond $m = 4$. However for other EEG signals, this saturation was reached at $m = 6$ to 10. As noted in [7], this consistency could simply be a result of embedding in an ever increasing dimension. Given a finite amount of noisy data, choosing a large embedding dimension might lead to inaccurate estimation of recurrence network properties. Also, the requirement for the size of the data grows as a power of embedding dimension. Finding the right embedding dimension for noisy experimental signals is a tricky and challenging task. Other advanced embedding methods could be used for this purpose, but selection of the right embedding dimension is still not guaranteed due to the presence of noise. In this work we restricted ourselves to using an already established method like the modified FNN approach [10], which avoids spurious effects due to noise, to find the optimal embedding dimension.

Our results indicate towards the possibility of applying recurrence network methods to study structural properties of neural data like the EEG signals and thus the dynamics encoded within them. Especially, in disorders like epilepsy, it is assumed that different dynamical states exist. Understanding the dynamics of the transitional state, the so-called pre-ictal state, holds the key in un-

derstanding how the brain makes the transition from the interictal state to the ictal state. The pre-ictal state can exist several minutes before the seizure [53] and its indubitable identification before the seizure onset could lead to clinical intervention [54] and application of therapeutic measures [55]. Also, the epileptic EEG signals in general are non-stationary signals [51]. In this regard, RP based methods like recurrence networks (network measure C) seem to be an appropriate choice. However the robustness of these measures against biological artifacts (which are common in scalp EEG and more so during seizures) needs to be studied in detail and will be a subject of future research. Another interesting area to explore would be the estimation of connectivity between different brain regions using the recently proposed multivariate extension of recurrence networks [56].

5. Conclusions

In conclusion, firstly we addressed the effect of noise on global measures like the global clustering coefficient and the average path length of ε -networks derived from the Rössler system. We then studied the structural properties of EEG signals using the global clustering coefficient and the average path length of the associated ε -networks. From the simulation study, we found that the observational noise has a considerable impact on these network measures. Effect of noise on the global clustering coefficient can be minimized to a certain extent by setting the recurrence rate to an appropriate value (>0.02), while the effect of noise on the average path length is independent of the recurrence rate. However, for noise levels greater than 40% in case of C and 20% in case of L , the recurrence network measures fail in distinguishing between noisy periodic dynamics and noisy chaotic dynamics. However these measures can describe, to a certain degree, the structural complexity of the signal under the presence of noise level as high as 60%.

From the application of the recurrence network measures to the EEG data, we found the evidence of increased structural complexity in epileptic EEG signals. Resting state EEG in healthy subjects also showed indications of structural complexity but to a lesser degree compared to the pathological EEG. Also, the application of the recurrence network measures to real EEG data revealed that the global clustering coefficient performed better in characterizing the structural properties of epileptic EEG signals compared to the average path length, as the average path length is more susceptible to the presence of transients in the data and epileptic signals often include transients. In conclusion, recurrence network measures (especially the global clustering coefficient) can be useful in characterizing the structural properties of healthy and epileptic EEG.

Acknowledgements

This work is financially supported by International Doctoral Programme in Biomedical Engineering and Medical Physics (iBioMEP) – Academy of Finland, Decision No. 141171. We would like to thank Dr. Jonathan Donges, from Potsdam Institute for Climate Impact Research, Germany for his valuable suggestions and for kindly providing the python package – **pyunicorn** [57] (available at <http://tocsy.pik-potsdam.de/pyunicorn.php>) which was used to construct the recurrence networks in this work. We also sincerely thank the anonymous reviewers for their valuable comments and feedback.

References

- [1] R.G. Andrzejak, K. Lehnertz, F. Mormann, C. Rieke, P. David, C.E. Elger, Indications of nonlinear deterministic and finite-dimensional structures in time series of brain electrical activity: dependence on recording region and brain state, *Phys. Rev. E* 64 (2001) 061907.

- [2] C. Elger, G. Widman, R. Andrzejak, J. Arnold, P. David, K. Lehnertz, Nonlinear EEG analysis and its potential role in epileptology, *Epilepsia* 41 (2000) S34–S38.
- [3] C. Elger, G. Widman, R. Andrzejak, M. Dimpelmann, J. Arnold, P. Grassberger, K. Lehnertz, Value of nonlinear time series analysis of the EEG in neocortical epilepsies, in: *Advances in Neurology*, vol. 84, Raven Press, New York, 2000, pp. 317–330.
- [4] L.D. Iasemidis, Epileptic seizure prediction and control, *IEEE Trans. Biomed. Eng.* 50 (2003) 549–558.
- [5] C.J. Stam, Nonlinear dynamical analysis of EEG and MEG: review of an emerging field, *Clin. Neurophysiol.* 116 (2005) 2266–2301.
- [6] N. Marwan, M. Carmen Romano, M. Thiel, J. Kurths, Recurrence plots for the analysis of complex systems, *Phys. Rep.* 438 (2007) 237–329.
- [7] M. Small, *Applied Nonlinear Time Series Analysis: Applications in Physics, Physiology and Finance*, vol. 52, World Scientific, 2005.
- [8] J.-P. Eckmann, S.O. Kamphorst, D. Ruelle, Recurrence plots of dynamical systems, *Europhys. Lett.* 4 (1987) 973.
- [9] N. Marwan, J.F. Donges, Y. Zou, R.V. Donner, J. Kurths, Complex network approach for recurrence analysis of time series, *Phys. Lett. A* 373 (2009) 4246–4254.
- [10] H. Kantz, T. Schreiber, *Nonlinear Time Series Analysis*, vol. 7, Cambridge University Press, 2004.
- [11] J.P. Zbilut, C.L. Webber Jr., Embeddings and delays as derived from quantification of recurrence plots, *Phys. Lett. A* 171 (1992) 199–203.
- [12] C. Webber, J.P. Zbilut, Dynamical assessment of physiological systems and states using recurrence plot strategies, *J. Appl. Physiol.* 76 (1994) 965–973.
- [13] F. Takens, Detecting strange attractors in turbulence, in: *Dynamical Systems and Turbulence*, Warwick 1980, Springer, 1981, pp. 366–381.
- [14] P. Grassberger, T. Schreiber, C. Schaffrath, Nonlinear time sequence analysis, *Int. J. Bifurc. Chaos* 1 (1991) 521–547.
- [15] A. Wolf, J.B. Swift, H.L. Swinney, J.A. Vastano, Determining Lyapunov exponents from a time series, *Physica D: Nonlinear Phenomena* 16 (1985) 285–317.
- [16] P. Grassberger, I. Procaccia, Estimation of the Kolmogorov entropy from a chaotic signal, *Phys. Rev. A* 28 (1983) 2591–2593.
- [17] M.E. Newman, The structure and function of complex networks, *SIAM Rev.* 45 (2003) 167–256.
- [18] S. Boccaletti, V. Latora, Y. Moreno, M. Chavez, D.-U. Hwang, Complex networks: structure and dynamics, *Phys. Rep.* 424 (2006) 175–308.
- [19] E. Bullmore, O. Sporns, Complex brain networks: graph theoretical analysis of structural and functional systems, *Nat. Rev. Neurosci.* 10 (2009) 186–198.
- [20] R.V. Donner, Y. Zou, J.F. Donges, N. Marwan, J. Kurths, Recurrence networks—a novel paradigm for nonlinear time series analysis, *New J. Phys.* 12 (2010) 033025.
- [21] R.V. Donner, M. Small, J.F. Donges, N. Marwan, Y. Zou, R. Xiang, J. Kurths, Recurrence-based time series analysis by means of complex network methods, *Int. J. Bifurc. Chaos* 21 (2011) 1019–1046.
- [22] X. Xu, J. Zhang, M. Small, Superfamily phenomena and motifs of networks induced from time series, *Proc. Natl. Acad. Sci. USA* 105 (2008) 19601–19605.
- [23] M. Small, J. Zhang, X. Xu, Transforming time series into complex networks, in: *Complex Sciences*, Springer, 2009, pp. 2078–2089.
- [24] Y. Shimada, T. Kimura, T. Ikeguchi, Analysis of chaotic dynamics using measures of the complex network theory, in: *Artificial Neural Networks—ICANN 2008*, Springer, 2008, pp. 61–70.
- [25] R. Albert, A.-L. Barabási, Statistical mechanics of complex networks, *Rev. Mod. Phys.* 74 (2002) 47.
- [26] D.J. Watts, S.H. Strogatz, Collective dynamics of ‘small-world’ networks, *Nature* 393 (1998) 440–442.
- [27] Y. Zou, R.V. Donner, J.F. Donges, N. Marwan, J. Kurths, Identifying complex periodic windows in continuous-time dynamical systems using recurrence-based methods, *Chaos: Interdisciplinary J. Nonlinear Sci.* 20 (2010) 043130.
- [28] R. Xiang, J. Zhang, X.-K. Xu, M. Small, Multiscale characterization of recurrence-based phase space networks constructed from time series, *Chaos: Interdisciplinary J. Nonlinear Sci.* 22 (2012) 013107.
- [29] M. Thiel, M.C. Romano, J. Kurths, R. Meucci, E. Allaria, E.T. Arecchi, Influence of observational noise on the recurrence quantification analysis, *Physica D: Nonlinear Phenomena* 171 (2002) 138–152.
- [30] T. Gautama, D.P. Mandic, M.M. Van Hulle, Indications of nonlinear structures in brain electrical activity, *Phys. Rev. E* 67 (2003) 046204.
- [31] N.P. Subramaniam, J. Hyttinen, Analysis of nonlinear dynamics of healthy and epileptic EEG signals using recurrence based complex network approach, in: *2013 6th International IEEE/EMBS Conference on Neural Engineering (NER)*, IEEE, 2013, pp. 605–608.
- [32] R.G. Andrzejak, K. Schindler, C. Rummel, Nonrandomness, nonlinear dependence, and nonstationarity of electroencephalographic recordings from epilepsy patients, *Phys. Rev. E* 86 (2012) 046206.
- [33] R.V. Donner, J. Heitzig, J.F. Donges, Y. Zou, N. Marwan, J. Kurths, The geometry of chaotic dynamics—a complex network perspective, *Eur. Phys. J. B: Condens. Matter Complex Syst.* 84 (2011) 653–672.
- [34] T. Schreiber, A. Schmitz, Improved surrogate data for nonlinearity tests, *Phys. Rev. Lett.* 77 (1996) 635.
- [35] O.E. Rössler, An equation for continuous chaos, *Phys. Lett. A* 57 (1976) 397–398.
- [36] A.M. Fraser, H.L. Swinney, Independent coordinates for strange attractors from mutual information, *Phys. Rev. A* 33 (1986) 1134.
- [37] M.B. Kennel, R. Brown, H.D. Abarbanel, Determining embedding dimension for phase-space reconstruction using a geometrical construction, *Phys. Rev. A* 45 (1992) 3403.
- [38] R. Hegger, H. Kantz, Improved false nearest neighbor method to detect determinism in time series data, *Phys. Rev. E* 60 (1999) 4970.
- [39] C.W. Wang, *Nonlinear Phenomena Research Perspectives*, Nova Publishers, 2007.
- [40] J.F. Donges, J. Heitzig, R.V. Donner, J. Kurths, Analytical framework for recurrence network analysis of time series, *Phys. Rev. E* 85 (2012) 046105.
- [41] J. Dall, M. Christensen, Random geometric graphs, *Phys. Rev. E* 66 (2002) 016121.
- [42] S. Schinkel, O. Dimigen, N. Marwan, Selection of recurrence threshold for signal detection, *Eur. Phys. J. Spec. Top.* 164 (2008) 45–53.
- [43] J.P.M. Pijn, D.N. Velis, M.J. van der Heyden, J. DeGoede, C.W. van Veelen, F.H.L. da Silva, Nonlinear dynamics of epileptic seizures on basis of intracranial EEG recordings, *Brain Topogr.* 9 (1997) 249–270.
- [44] H. Jing, M. Takigawa, Topographic analysis of dimension estimates of EEG and filtered rhythms in epileptic patients with complex partial seizures, *Biol. Cybern.* 83 (2000) 391–397.
- [45] R. Ferri, M. Elia, S.A. Musumeci, C.J. Stam, Non-linear EEG analysis in children with epilepsy and electrical status epilepticus during slow-wave sleep (eses), *Clin. Neurophysiol.* 112 (2001) 2274–2280.
- [46] C.J. Stam, Chaos, continuous EEG, and cognitive mechanisms: a future for clinical neurophysiology, *Am. J. Electroencephalographic Technol.* 43 (2003).
- [47] K.J. Friston, The labile brain. I. Neuronal transients and nonlinear coupling, *Philos. Trans. R. Soc. Lond. B, Biol. Sci.* 355 (2000) 215–236.
- [48] J. Fell, A. Kaplan, B. Dalkovsky, J. Röschke, EEG analysis with nonlinear deterministic and stochastic methods: a combined strategy, *Acta Neurobiol. Exp.* 60 (1999) 87–108.
- [49] D. Maurice, R. Cerf, M. Toussaint, Automated detection of low-dimensional EEG α -episodes. An example of application to psychopharmacological data, *Comput. Methods Programs Biomed.* 68 (2002) 93–108.
- [50] R.A. Stępień, Testing for non-linearity in EEG signal of healthy subjects, *Acta Neurobiol. Exp.* 62 (2002) 277–282.
- [51] L. Senhadji, F. Wendling, Epileptic transient detection: wavelets and time-frequency approaches, *Neurophysiol. Clin.* 32 (2002) 175–192.
- [52] J.F. Donges, Functional network macroscopes for probing past and present Earth system dynamics, Ph.D. thesis, Humboldt-Universität zu Berlin, Mathematisch-Naturwissenschaftliche Fakultät I, 2013.
- [53] M. Le Van Quyen, J. Martinerie, V. Navarro, P. Boon, M. D’Havé, C. Adam, B. Renault, F. Varela, M. Baulac, Anticipation of epileptic seizures from standard EEG recordings, *Lancet* 357 (2001) 183–188.
- [54] J. Martinerie, C. Adam, M. Le Van Quyen, M. Baulac, S. Clemenceau, B. Renault, F. Varela, Epileptic seizures can be anticipated by non-linear analysis, *Nat. Med.* 4 (1998) 1173–1176.
- [55] C.E. Elger, Future trends in epileptology, *Curr. Opin. Neurol.* 14 (2001) 185–186.
- [56] J.H. Feldhoff, R.V. Donner, J.F. Donges, N. Marwan, J. Kurths, Geometric detection of coupling directions by means of inter-system recurrence networks, *Phys. Lett. A* 376 (2012) 3504–3513.
- [57] J.F. Donges, J. Heitzig, J. Runge, H.C. Schultz, M. Wiedermann, A. Zech, J. Feldhoff, A. Rheinwald, H. Kutza, A. Radebach, et al., Advanced functional network analysis in the geosciences: the pyUnicorn package, in: *EGU General Assembly Conference Abstracts*, vol. 15, 2013, p. 3558.

Puthanmadam Subramaniyam, N. and Hyttinen, J.

Analysis of nonlinear dynamics of healthy and epileptic EEG signals using recurrence based complex network approach

6th International IEEE/EMBS Conference on Neural Engineering (NER),
pages 605,608, 6-8 Nov., San Diego, USA, 2013.

Reprinted with permission from the publisher.

In reference to IEEE copyrighted material which is used with permission in this thesis, the IEEE does not endorse any of Tampere University of Technology's products or services. Internal or personal use of this material is permitted. If interested in reprinting/republishing IEEE copyrighted material for advertising or promotional purposes or for creating new collective works for resale or redistribution, please go to http://www.ieee.org/publications_standards/publications/rights/rights_link.html to learn how to obtain a License from RightsLink.

Analysis of nonlinear dynamics of healthy and epileptic EEG signals using recurrence based complex network approach*

Narayan Puthanmadam Subramaniyam and Jari Hyttinen

Abstract— Epilepsy is a neurological condition characterized by sudden occurrences of rapid electrical discharges. Different non-linear methods like correlation dimension, Lyapunov exponent, entropy and more recently recurrence quantification analysis (RQA) have been used to characterize the non-linear dynamics behind interictal (between seizures) and ictal (during seizure) activities. While RQA is sensitive to embedding parameters other non-linear methods mentioned above require long and stationary data. In this study we propose recurrence network (RN) based approach to quantify the non-linear dynamics of the underlying attractors in healthy, interictal and ictal electroencephalographic (EEG) data. The dataset used to test the method is obtained from Department of Epileptology, Bonn University, Germany and consists of altogether 500 signals from interictal, ictal and healthy (eyes open and eyes closed) EEG activity. We compute network measures like clustering coefficient C and path length L on RN derived from EEG time series to characterize the underlying attractor. Our results show that interictal signals are characterized by chaotic attractors and their networks display small world property (high C and low L) while ictal signals are characterized by quasiperiodic attractors with high values of C and L . Further, our results show that for healthy EEG signals with eyes closed, the attractors are highly chaotic while for EEG signals with eyes open the attractors are less complex than fully chaotic attractor. RN based approach for the characterization of non-linear dynamics of epileptic EEG signals is promising and has advantages over other non-linear approaches as it makes no assumptions about data stationarity, length and is not sensitive to embedding parameters.

I. INTRODUCTION

Epilepsy is a neurological disorder characterized by recurrent and unpredictable occurrences of electrical discharges in the brain, known as seizures [1]. Prediction of epileptic seizures well before its onset is one of the grand challenges in neural engineering, which if solved can lead to new diagnostic application to control the seizures [2]. Since electroencephalography (EEG) is a direct measure of the electrical activity of the brain, analysis of epileptic EEG signal can help in revealing the dynamic fingerprint of the brain during the interictal state between the seizures which is characterized by sharp waves with transients and ictal state

during the seizure which is characterized by self-sustained rhythmic activity [3].

EEG signals can be regarded as an output of a highly non-linear multidimensional system [3, 4]. Over the past two decades there has been a growing interest in the application of methods from chaos and non-linear theory to follow transitions from interictal to ictal period. Such studies have focused on measures like the Lyapunov exponents [5, 6], correlation dimension [7, 8], entropy measures [5, 9] and fractal dimensions [10, 11]. These methods generally require long and stationary data and it is well known that EEG signals in general are non-stationary [3].

A recurrence plot (RP) is a two-dimensional graphical representation of a binary matrix that reflects the recurrence of states in a phase space and it can be used to analyze complex dynamical system [12, 13]. Such a binary matrix is known as recurrence matrix and it gives the times when two states in phase space are in proximity as defined by a neighborhood criteria [12]. Given a scalar time series, one can reconstruct the underlying phase space attractor (PSA) using a suitable m -dimensional time delay embedding [14, 15]. RP can be quantified using recurrence quantification analysis (RQA) [16]. RQA has been applied towards the characterization of interictal, pre-ictal and ictal signals in rats and humans [3, 17]. The main advantage of RQA is that it makes no assumptions about stationarity and no apriori model of brain dynamics is required [3, 17, 18]. However, recent studies have shown that RQA is sensitive to embedding parameters which leads to introduction of spurious correlation in RP [14, 18]. To overcome this issue, a new approach of transforming time series into recurrence networks (RN) that reflect attractor geometry has been proposed [14]. In RN approach complex networks are constructed from PSA and network measures like clustering coefficient C and characteristic path length L are used to quantify the geometrical nature of the underlying PSA [19]. For example, RN constructed from chaotic attractors display small world property with high C and low L [19, 20]. The RN approach is attractive in EEG analysis as it can handle data non-stationarity, requires simple significance tests and is not sensitive to embedding parameters [14].

In this paper we introduce a RN based approach to quantify the underlying non-linear dynamical properties of EEG signal in three different stages – healthy, interictal and ictal. This is achieved by transforming EEG time series into PSA and then computing RN from PSA using an adaptive near neighborhood (ANN) algorithm [21]. We then compute complex network measures C and L for the RN to characterize the non-linear dynamics and thus the underlying PSA for healthy, interictal and ictal EEG signals.

* Research supported by International Graduate School in Biomedical Engineering and Medical Physics (iBioMEP) and Department of Electronics and Communication Engineering (ECE).

Narayan Puthanmadam Subramaniyam is with the Department of Electronics and Communication Engineering, Tampere University of Technology, FI-33720, Tampere, Finland. (Phone: +358-40-1981951; e-mail: narayan.ps@tut.fi).

Prof. Jari Hyttinen is with the Department of Electronics and Communication Engineering, Tampere University of Technology, FI-33720, Tampere, Finland (e-mail: jari.hyttinen@tut.fi).

II. MATERIALS AND METHODS

A. EEG data

The EEG data used in this paper is provided online by the department of epileptology, Bonn University, Germany, through the work of Andrzejak et al [22]. The dataset consists of five subsets – A (normal EEG, relaxed and awake state, eyes open), B (normal EEG, relaxed and awake state, eyes closed), C (interictal EEG from hippocampal formation), D (interictal EEG from epileptic zone) and E (ictal EEG). Each subset contains 100 single channels EEG data of 23.6 seconds each, sampled at 173.6 Hz giving 4096 time points. The data is recorded from five healthy subjects (sets A and B) and five epileptic subjects (sets C, D and E). These segments of data have been manually cut out from continuous multichannel EEG data (128-channel system) after visual inspection for eye or muscle artifacts. The data is bandpass filtered between 0.5-40 Hz.

B. Transforming time series into phase space attractor

Given a scalar time series $\{x(i), i = 1, 2, \dots, N\}$, using a time delay embedding procedure one can construct a phase space vector

$$\mathbf{X}_i = (x(i), x(i + \tau), \dots, x(i + (m - 1)\tau)) \quad (1)$$

where m is the embedding dimension and τ is the time delay. The optimal value for τ is obtained as the first minimum of the mutual information content [23]. The optimal embedding dimension can be determined using false nearest neighbor method [24]. In this method, given a phase space vector \mathbf{X}_i , the optimal embedding dimension is defined as the dimension m for which the number of nearest false neighbors vanishes to zero.

C. Complex recurrence networks based on ANN algorithm

Recurrent states of a m -dimensional phase space vector as given by (1) can be represented using RP. By defining some criteria for proximity, one can construct a binary recurrence matrix that represents neighbors in phase space. This matrix contains the value one for those pairs of phase space vectors that are close to each other as defined by proximity criteria and zero for others. Such a recurrence matrix is analogous to adjacency matrix in graph theory and is known as RN.

There are several such approaches to transform phase space vector to a RN [25]. We adopt a fixed-edge based proximity networks approach by implementing ANN algorithm where in every point on the attractor is a defined as a node in the RN and the edges between the nodes are defined based on the proximity between corresponding attractor points such that every node has exactly M edges to its geometric neighbors [21, 25]. The advantage of this approach is that it results in an undirected binary matrix with fixed edge distribution, so that comparison between different network measures (e.g. C and L) derived from such networks are more meaningful. The algorithm is described in detail below

1. Compute a Euclidean distance matrix D_{ij} such that every i -th row of the distance matrix contains

distance from the i -th point on the attractor to all other points excluding itself

2. Select k near neighbors based on Euclidean distance for every i -th row. Let us denote the set of these k points as $M_i = \{x(j_1) \dots x(j_k)\}$ such that $x(j_1)$ is the first nearest neighbor and so on. The set M_i is known as the neighborhood of vertex i [25]
3. Construct a binary matrix R such that $R_{ij} = 1$, if j belongs to set M_i else set $R_{ij} = 0$. Also, form bi-directional links such that $R_{ji} = 1$ if $R_{ij} = 1$. Remove i from the neighborhood of all the vertices present in M_i to avoid double-counting.

The binary matrix R is known as the RN and it consists of N nodes that correspond to N points on the PSA.

D. Complex network measures

Local and global network measures can be derived from R which can be considered as the adjacency matrix. Clustering coefficient C and characteristic path length L are two such interesting measures that can be used to investigate small-worldness of networks [19]. Given a network graph $g = (N, E)$ consisting of N nodes and E edges such that $E \subseteq N \times N$, the clustering coefficient C_i for a node i can be defined as [15]

$$C_i = \frac{\sum_{h,j=1}^N R_{i,h} R_{h,j} R_{j,i}}{k_i(k_i-1)} \quad (2)$$

where R is the adjacency matrix which is the same as the recurrence network matrix and k_i is the degree of the node i , and is given by [15]

$$k_i = \sum_{j=1}^N R_{i,j} \quad (3)$$

where N is the number of nodes or network size. The global clustering coefficient can then be defined as the average value of clustering coefficient C of all the nodes and is given as [15]

$$C = \frac{1}{N} \sum_{i=1}^N C_i \quad (4)$$

The characteristic path length L of a network is the average length of the shortest paths between all the pairs of nodes and is given as [15]

$$L = \frac{1}{N(N-1)} \sum_{i,j=1}^N d_{i,j} \quad (5)$$

where $d_{i,j}$ is the shortest distance between nodes i and j .

E. Application to epileptic and healthy EEG signals

We apply the methods described above to a total of 500 EEG signals derived from five subsets of data (A-E). We first transform each of the time series data into phase space attractor vector after computing optimum delay τ and embedding dimension m for each signal. Then we transform the PSA to RN by employing the ANN algorithm. The size of the RN is equal to the number of points on the attractor and it is 4000 in our study based on the data time points. Finally we compute two network measures – C and L for each RN and its optimal embedding dimension m .

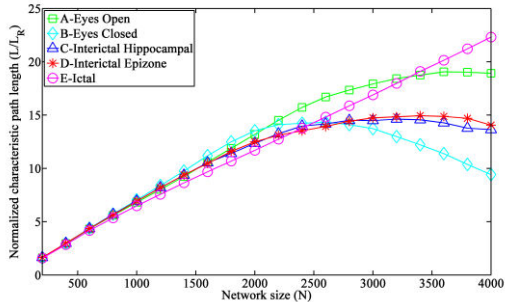


Figure 1. Normalized characteristic path length L/L_R as a function of network size N .

In order to test the behavior of C and L with respect to N we varied the size of time series in each case and hence N from 200 to 4000 nodes by fixing the number of adjacent nodes (hence node degree) to 20. To perform the significance testing we normalized the values of C and L for each network with C_R and L_R , calculated from 100 random networks generated by preserving the node density distribution of the original network. We also computed the small worldness S for each RN which is given as [26]

$$S = \frac{C/C_R}{L/L_R} \quad (6)$$

When the value of $S > 1$, we can say that the network exhibits small world property as its characteristic path length L is small compared to the clustering coefficient C . The average value of network measures - C and L per subset is taken as the representative value for that subset.

III. RESULTS

The dependence of normalized L and C as a function of N for the RN of PSA of EEG signals in dataset A-E are shown in Figure 1 and 2 respectively. The values of L and C are averaged over 100 phase space networks constructed from each dataset. From Figure 1 it can be seen that normalized L of RN of all signals increase linearly with N for small network sizes. However, as N increases (around 2000), normalized L decreases for RN of dataset A,B,C and D, with B showing the largest drop followed by D and A. The normalized L for the RN of dataset E continues to increase linearly with N . From Figure 2 it can be seen that the value of normalized C of RN of attractors of all the dataset (A-E) show a similar tendency of increasing linearly as function of N .

Next, we investigated the variation of S of the RN of the attractors of signals from dataset A-E using (6) as a function of N . This variation is shown in Figure 3. It can be seen clearly from Figure 3 that, initially the value of S of RN for dataset A-E remains at the same level. However as N increases (around 2000), RN of attractors for set B shows the strongest tendency towards small world networks with high values of S for large N . RN of attractors for set C and D also show strong small world properties with large values of S for large values of N . The value of S for the RN of attractors for set E remains at the same level (around the value 2) for

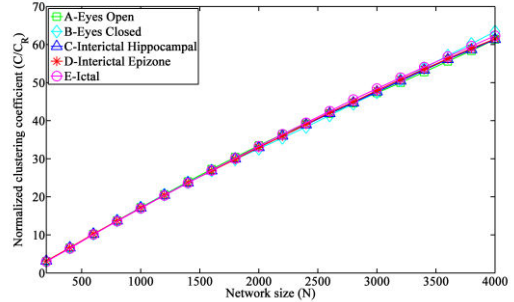


Figure 2. Normalized global clustering coefficient C/C_R as a function of network size N .

varying N whereas the variation of S for RN of attractors for set A is somewhere between the two extremes for large N .

IV. DISCUSSION

Complex network measures derived from the RN of the attractor of time series can be used to characterize the underlying dynamical system [19, 20, 27]. It has been recently shown that small world property emerges in networks that are produced by chaotic attractors due to orbital instability present in them using Rössler system, Lorenz system and real signals [19]. It has also been demonstrated that networks of periodic or limit cycle attractors are characterized by high values for C and L for increasing network size [19]. Based on these observations our results indicate that small world property emerges from the attractors of EEG signals during eyes closed (alpha rhythm) and interictal state. There has been evidence linking chaotic attractors to EEG alpha rhythm during eyes closed state [28]. Our results further confirm this by giving high value for S (high C and low L) for RN constructed from attractors of EEG during eyes closed state. Similarly for interictal signals recorded from epileptogenic zones and hippocampal formation, the RN showed small world property and thus pointing towards a chaotic attractor underlying these signals. This seems plausible as interictal signals are associated with attractor of high-dimensional chaos [29]. The RN derived from the attractor of ictal signal showed high values of C and L with increasing N . This behavior is consistent with that of a periodic attractor [19]. However it should also be noted that the value of S for ictal signal was still greater than 1 although it did not tend to increase with N but stayed at the same level. This may mean that the attractor is not completely periodic but slightly more complex than periodic but definitely less complex than a chaotic attractor that describes interictal state. This makes sense as ictal signals are associated with more ordered state with high synchronization. It has been demonstrated that even though the seizure activity is rhythmic and self-sustained, it is more complex than limit cycle behavior [30]. For normal EEG signals with eyes open the attractor can be characterized as chaotic due to appreciable increase in S (to about a value of 4) for large N but less complex than the attractors of interictal and EEG signals with closed eyes. Also our approach could clearly differentiate between the EEG signals with eyes open and closed conditions which

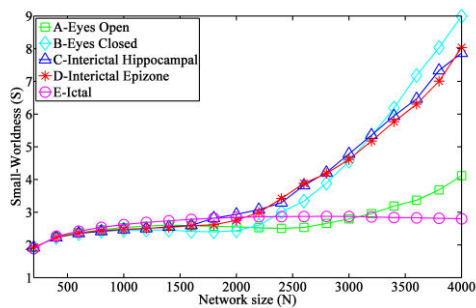


Figure 3. Small worldness S as a function of network size N

could not be detected by non-linear methods proposed by Andrzejak et al [22].

V. CONCLUSION

In this work we applied RN based approach to derive complex network measures from three classes of EEG signals – healthy, interictal and ictal. Our results show that RN based approach is able to characterize different classes of EEG signals based on their attractor complexity. Future work will involve multivariate extension of this approach to EEG signals along with analysis of the attractor underlying pre- ictal EEG signals which is thought to play a crucial role in transitioning of interictal activity to ictal activity.

REFERENCES

- [1] R. S. Fisher, W. v. E. Boas, W. Blume, C. Elger, P. Genton, P. Lee and J. Engel, "Epileptic Seizures and Epilepsy: Definitions Proposed by the International League Against Epilepsy (ILAE) and the International Bureau for Epilepsy (IBE)," *Epilepsia*, vol. 46, pp. 470-472, 2005.
- [2] L. D. Iasemidis, "Epileptic seizure prediction and control," *Biomedical Engineering, IEEE Transactions On*, vol. 50, pp. 549-558, 2003.
- [3] N. Thomasson, T. J. Hoepfner, C. L. Webber and J. P. Zbilut, "Recurrence quantification in epileptic EEGs," *Physics Letters A*, vol. 279, pp. 94-101, 2001.
- [4] S. N. Sarbadhikari and K. Chakrabarty, "Chaos in the brain: a short review alluding to epilepsy, depression, exercise and lateralization," *Med. Eng. Phys.*, vol. 23, pp. 447-457, 9, 2001.
- [5] H. R. Moser, B. Weber, H. G. Wieser and P. F. Meier, "Electroencephalograms in epilepsy: analysis and seizure prediction within the framework of Lyapunov theory," *Physica D*, vol. 130, pp. 291-305, 6/15, 1999.
- [6] L. D. Iasemidis, J. C. Sackellares, H. P. Zaveri and W. J. Williams, "Phase space topography and the Lyapunov exponent of electrocorticograms in partial seizures," *Brain Topogr.*, vol. 2, pp. 187-201, 1990.
- [7] C. E. Elger and K. Lehnertz, "Seizure prediction by non-linear time series analysis of brain electrical activity," *Eur. J. Neurosci.*, vol. 10, pp. 786-789, 1998.
- [8] J. Martinerie, C. Adam, M. Le Van Quyen, M. Baulac, S. Clemenceau, B. Renault and F. Varela, "Epileptic seizures can be anticipated by non-linear analysis," *Nat. Med.*, vol. 4, pp. 1173-1176, 1998.
- [9] X. Li, G. Ouyang and D. A. Richards, "Predictability analysis of absence seizures with permutation entropy," *Epilepsy Res.*, vol. 77, pp. 70, 2007.
- [10] R. Esteller, G. Vachtsevanos, J. Echaz, T. Henry, P. Pennell, C. Epstein, R. Bakay, C. Bowen and B. Litt, "Fractal dimension characterizes seizure onset in epileptic patients," in *Acoustics, Speech, and Signal Processing, 1999. Proceedings., 1999 IEEE International Conference On*, 1999, pp. 2343-2346.
- [11] E. T. Bullmore, M. J. Brammer, P. Bourlon, G. Alarcon, C. E. Polkey, R. Elwes and C. D. Binnie, "Fractal analysis of electroencephalographic signals intracerebrally recorded during epileptic seizures: evaluation of a new method for synaptic visualisation of ictal events," *Electroencephalogr. Clin. Neurophysiol.*, vol. 91, pp. 337-345, 11, 1994.
- [12] N. Marwan, M. Carmen Romano, M. Thiel and J. Kurths, "Recurrence plots for the analysis of complex systems," *Physics Reports*, vol. 438, pp. 237-329, 2007.
- [13] J. Eckmann, S. O. Kamphorst and D. Ruelle, "Recurrence plots of dynamical systems," *EPL (Europhysics Letters)*, vol. 4, pp. 973, 1987.
- [14] R. V. Donner, Y. Zou, J. F. Donges, N. Marwan and J. Kurths, "Recurrence networks—A novel paradigm for nonlinear time series analysis," *New Journal of Physics*, vol. 12, pp. 033025, 2010.
- [15] N. Marwan, J. F. Donges, Y. Zou, R. V. Donner and J. Kurths, "Complex network approach for recurrence analysis of time series," *Physics Letters A*, vol. 373, pp. 4246-4254, 2009.
- [16] N. Marwan and J. Kurths, "Nonlinear analysis of bivariate data with cross recurrence plots," *Physics Letters A*, vol. 302, pp. 299-307, 2002.
- [17] X. Li, G. Ouyang, X. Yao and X. Guan, "Dynamical characteristics of pre-epileptic seizures in rats with recurrence quantification analysis," *Physics Letters A*, vol. 333, pp. 164-171, 2004.
- [18] M. Thiel, M. C. Romano and J. Kurths, "Spurious structures in recurrence plots induced by embedding," *Nonlinear Dyn.*, vol. 44, pp. 299-305, 2006.
- [19] Y. Shimada, T. Kimura and T. Ikeguchi, "Analysis of chaotic dynamics using measures of the complex network theory," in *Artificial Neural Networks-ICANN 2008* Anonymous Springer, 2008, pp. 61-70.
- [20] J. Zhang and M. Small, "Complex network from pseudoperiodic time series: Topology versus dynamics," *Phys. Rev. Lett.*, vol. 96, pp. 238701, 2006.
- [21] M. Small, J. Zhang and X. Xu, "Transforming time series into complex networks," in *Complex Sciences* Anonymous Springer, 2009, pp. 2078-2089.
- [22] R. G. Andrzejak, K. Lehnertz, F. Mormann, C. Rieke, P. David and C. E. Elger, "Indications of nonlinear deterministic and finite-dimensional structures in time series of brain electrical activity: Dependence on recording region and brain state," *Physical Review E*, vol. 64, pp. 061907, 2001.
- [23] A. M. Fraser and H. L. Swinney, "Independent coordinates for strange attractors from mutual information," *Physical Review A*, vol. 33, pp. 1134, 1986.
- [24] M. B. Kennel, R. Brown and H. D. Abarbanel, "Determining embedding dimension for phase-space reconstruction using a geometrical construction," *Physical Review A*, vol. 45, pp. 3403, 1992.
- [25] R. V. Donner, M. Small, J. F. Donges, N. Marwan, Y. Zou, R. Xiang and J. Kurths, "Recurrence-based time series analysis by means of complex network methods," *International Journal of Bifurcation and Chaos*, vol. 21, pp. 1019-1046, 2011.
- [26] M. D. Humphries and K. Gurney, "Network 'small-world-ness': a quantitative method for determining canonical network equivalence," *PLoS One*, vol. 3, pp. e0002051, 2008.
- [27] R. Xiang, J. Zhang, X. Xu and M. Small, "Multiscale characterization of recurrence-based phase space networks constructed from time series," *arXiv Preprint arXiv:1204.6553*, 2012.
- [28] A. C. Soong and C. I. Stuart, "Evidence of chaotic dynamics underlying the human alpha-rhythm electroencephalogram," *Biol. Cybern.*, vol. 62, pp. 55-62, 1989.
- [29] C. Stam, "Nonlinear dynamical analysis of EEG and MEG: review of an emerging field," *Clinical Neurophysiology*, vol. 116, pp. 2266-2301, 2005.
- [30] G. K. Bergey and P. J. Franaszczuk, "Epileptic seizures are characterized by changing signal complexity," *Clinical Neurophysiology*, vol. 112, pp. 241-249, 2001.

Puthanmadam Subramaniam, N., Hyttinen, J., Hatsopoulos, N., and Takahashi, K.

Recurrence network analysis of wide band oscillations of local field potentials from the primary motor cortex reveals rich dynamics

7th International IEEE/EMBS Conference on Neural Engineering (NER), pages 960-963, 22-25 Apr., Montpellier, France, 2015.

Reprinted with permission from the publisher.

In reference to IEEE copyrighted material which is used with permission in this thesis, the IEEE does not endorse any of Tampere University of Technology's products or services. Internal or personal use of this material is permitted. If interested in reprinting/republishing IEEE copyrighted material for advertising or promotional purposes or for creating new collective works for resale or redistribution, please go to http://www.ieee.org/publications_standards/publications/rights/rights_link.html to learn how to obtain a License from RightsLink.

Recurrence network analysis of wide band oscillations of local field potentials from the primary motor cortex reveals rich dynamics.

Narayan Puthanmadam Subramaniam, Jari Hyttinen, *Senior Member, IEEE*,
Nicholas G. Hatsopoulos *Senior Member, IEEE*, Kazutaka Takahashi, *Senior Member, IEEE*

Abstract—Aggregate signals that reflect activities of a large number of neurons in the cerebral cortex, local field potentials (LFPs) have been observed to mediate gross functional activities of a relatively small volume of the brain tissues. There are several bands of the oscillations frequencies in LFPs that have been observed across multiple brain areas. The signature oscillation band of the LFPs in the primary motor cortex (MI) is over β range and it has been consistently observed both in human and non-human primates around the time of visual cues and movement onsets. However, its dynamical behavior has not been well characterized. Furthermore, dynamics of β oscillations has been documented based on the phase locking of β oscillations, but not in terms of the inherent dynamics of the oscillations themselves. Here, we used the complexity measure derived from cluster coefficients of a recurrence network and analyzed a pair of wide-band signals, one including β band of the LFPs and the other ranging the low γ band in MI recorded from a non-human primate. We show rather unique temporal profiles of the evoked responses using complexity of the dynamical behavior in both bands of the oscillation, either of which is not simply resembling either the power of the oscillation or the phase locking of β oscillations. Therefore, the current method can reveal a new type of dynamics of the underlying network complexity during the task simply based on event evoked potentials of wide-band oscillatory signals.

Index Terms—Local field potentials, event evoked potentials, recurrence network, temporal dynamics, motor cortex, functional connectivity

I. INTRODUCTION

Cortical rhythms have been extensively studied since early descriptions of oscillations in sensorimotor cortex by Jasper and Penfield [1]. In particular, local field potentials (LFPs) and electroencephalograms (EEG) in the β frequency range (15-30 Hz) are ubiquitous in the motor cortex of mammals including monkeys and humans across the upper limb area of the primary motor cortex (MI). The dynamics of the β oscillation has been grossly characterized, based on a temporal profile of the amplitude of the oscillations, such as event related synchronization (ERS) and event related desynchronization (ERD) [2], [3], and phase locking to the instruction cues [4]. However, the dynamical properties of β oscillations have not been well characterized. Recently, it has been reported that phase of β oscillations propagated as plane waves along the rostrocaudal axis of the motor cortex during motor preparation and execution, and are believed to subserve cortical information transfer [5]. However, it has not been shown inherent dynamics of LFPs, in particular, β oscillations, and their spatiotemporal dynamics. The dynamics of neurons in general can

N.P. Subramaniam and J. Hyttinen are with Department of Electronics and Communications Engineering, Tampere University of Technology. (Email: {narayan.ps, jari.hyttinen}@tut.fi.) This work is financially supported by International Doctoral Programme in Biomedical Engineering and Medical Physics (iBioMEP) Academy of Finland, Decision No. 141171. N.G. Hatsopoulos and K. Takahashi is with Department of Organismal Biology and Anatomy, University of Chicago, IL 60637 USA. (Email: kazutaka@uchicago.edu). This work was supported by NIH R01 NS04853 and R01 DE023816.

be considered as nonlinear, mainly arising from the threshold and saturation phenomena [6]. It has been recently shown that methods based on recurrence plots, particularly recurrence networks (RN) can be used to study the structural complexity of the EEG signals [7], [8]. One particular advantage of RN based analysis is that it can be applied to short segments of data, since the network properties like global clustering coefficient C or average path length L can still be reliably estimated. The topological characterization of the RN using such network properties can provide insights into the complexity of the dynamics associated with the time series [9].

II. METHOD

A. Behavior task and data collection

All of the surgical and behavioral procedures were approved by the University of Chicago IACUC and conform to the principles outlined in the Guide for the Care and Use of Laboratory Animals. One monkey was trained to perform a visuomotor task using a two-link exoskeleton manipulandum [10]. The monkey was required to move a cursor on a horizontal screen that was aligned to the monkey's hand to the position of a target. When the monkey successfully reached the current target, a new target was displayed at a random location within a workspace while the current target disappeared. The monkey received a juice reward after successfully acquiring five or seven consecutive targets.

We recorded local field potentials (LFPs) from up to 96 channels simultaneously at 1 kHz from MI in the monkey using an Utah microelectrode array (Blackrock Microsystems; 1 mm in length and $400\mu\text{m}$ inter-electrode spacing) implanted contralateral to the moving arm. We analyzed 1000 consecutive successful trials. The LFPs were bidirectionally bandpass filtered over [1, 30] Hz and [30, 80] Hz with a 3rd order Butterworth filter respectively to separate the raw signals into low frequency contents including up to β and low γ range up to 80Hz. We partitioned the data into a series of windows of length 150 ms, starting from the following time windows $[-100, 50]$ ms in relation to visual cue onset, incremented by 1 ms up to $[200, 350]$ ms.

B. Recurrence Networks

Given an univariate time series, $\{u(i), i = 1, 2, \dots, N\}$, one can reconstruct the phase space trajectory of the underlying dynamics using the method of delays [11]

$$\mathbf{x}_i = (u(i), u(i + \tau), \dots, u(i + (m - 1)\tau)), \quad (1)$$

where $\mathbf{x}_i \in \mathbb{R}^m$, τ is the embedding delay determined as the first local minimum of the auto mutual information [12] and m is the embedding dimension which can be determined using the false nearest neighbor (FNN) approach [13]. One can visualize the dynamics of the phase space trajectories using the method of recurrence plots [14]. A Recurrence plot (RP) is a graphical representation of the recurrence matrix, which is a closeness test

depicting the times when two states visit roughly the same area in phase space. This closeness can be defined based on Euclidean or Manhattan or maximum norm. A recurrence matrix \mathbf{R} depicting the closeness between the pairs of state vectors can be given as [15], [9]

$$R_{i,j}(\epsilon) = \Theta(\epsilon - \|x_i - x_j\|), \quad (2)$$

where $\Theta(\cdot)$ is the Heaviside function, $\|\cdot\|$ is a distance norm, and ϵ is the recurrence threshold specifying the maximum spatial distance of neighboring states. The recurrence matrix is a binary, symmetric matrix with an entry of 1 if the distance between two states is less than the recurrence threshold ϵ , else the entry is 0. The recurrence matrix can be reinterpreted as an adjacency matrix after the following transformation [15], [9],

$$\mathbf{A} = \mathbf{R} - \mathbf{I}, \quad (3)$$

where \mathbf{I} is the identity matrix. The above operation simply eliminates the artificial self-loops. The adjacency matrix \mathbf{A} represents an undirected, unweighted complex network known as the recurrence network as in [9]. The recurrence network can be characterized using graph theoretical methods to reflect the dynamically invariant properties of the associated dynamical system. In this work, we compute the global clustering coefficient C of the recurrence network. Given a network with N nodes and V vertices, the local clustering coefficient of a node i can be defined as the likelihood that the neighbors of i will also be neighbors of each other. Formally, the local clustering coefficient of a node i can be given as in [16],

$$c(i) = \frac{\sum_{j,r} A_{i,j} A_{j,r} A_{r,i}}{k_i(k_i - 1)}, \quad (4)$$

where k is the degree of a node. The Global clustering coefficient is simply the average of local clustering coefficient computed over all the nodes of a network and is given as,

$$C = \frac{1}{N} \sum_{i \in \mathcal{N}} c(i). \quad (5)$$

In order to perform the analysis described above, we first averaged the trials of LFP data (-100 ms before the event and 350 ms after the event) for all the 96 channels. The averaged data was divided into highly overlapping windows of length 150 ms and step size 1 ms. The optimal delay and the minimum embedding dimension was computed for all the channels and we found that for most of the data the embedding parameters were, delay $\tau = 5$ and embedding dimension $m = 3$. Also, to determine the embedding dimension, we used the improved FNN approach [17] to avoid spurious effects due to noise. Using these embedding parameters we constructed same-sized recurrence networks for every window and channel. Instead of specifying the recurrence threshold ϵ , we fix the recurrence rate $RR = 0.05$ so that we obtain recurrence networks with approximately the same number of edges so that we can compare the networks obtained from different time windows [18].

III. RESULTS

A. Spectral profiles of LFPs

First, Fig. 1 shows a power spectrum of LFPs computed over $[-100, 350]$ ms of visual cue onset over 1000 consecutive cue presentations. The multi-taper method was used and the parameters used are: $[TW, K] = [3, 5]$, where TW denotes the time-bandwidth product and K being the number of tapers. There is a distinct peak around 18-19 Hz over the β oscillation and a small peak around

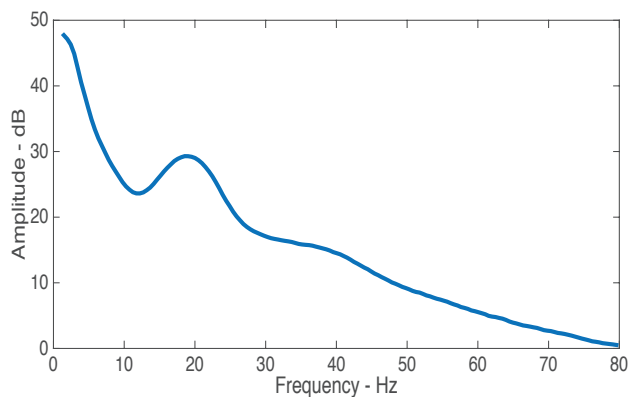


Fig. 1. Stereotypical example of power spectrum of LFP. There is a clear peak around 18-19Hz in this subject over β range and a small peak around 40 Hz in a low γ range.

40Hz over the low γ range. For the rest of the recurrence analysis, we focused on wide band oscillations: low band being $[1, 30]$ Hz to cover up to β oscillation frequency range and the higher being $[30, 80]$ Hz to cover low γ oscillation frequency range.

B. Optimal delay

Fig. 2 shows the auto-mutual information for an exemplary channel. It can be seen from Fig. 2 that the first local minimum of the auto-mutual information occurs at a lag of 5. Similar behavior was seen for most of signals from other channels.

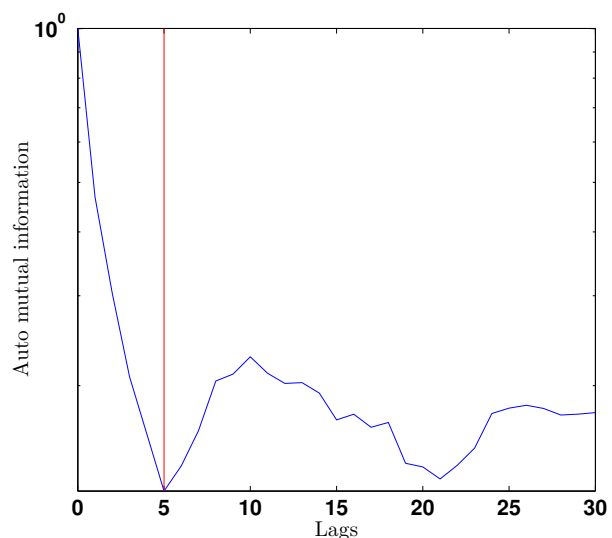


Fig. 2. Optimal delay τ using auto-mutual information for an exemplary channel. The red line denotes the first local minimum.

C. Embedding dimension

Fig. 3 shows the plot of the FNN statistic with respect to the embedding dimension for an exemplary signal. Already at an embedding dimension of 3, the value of FNN statistic drops to 0.04. Given the amount of data in each window (150 sample points), the choice of $m = 3$ seems feasible. Going for larger values of m like 5 or 6 might greatly reduce the amount of points needed to estimate the network characteristics. For the sake of consistency, based on these observations, we set optimal delay $\tau = 5$ and embedding

dimension $m = 3$ to reconstruct the phase space vector from all the signals.

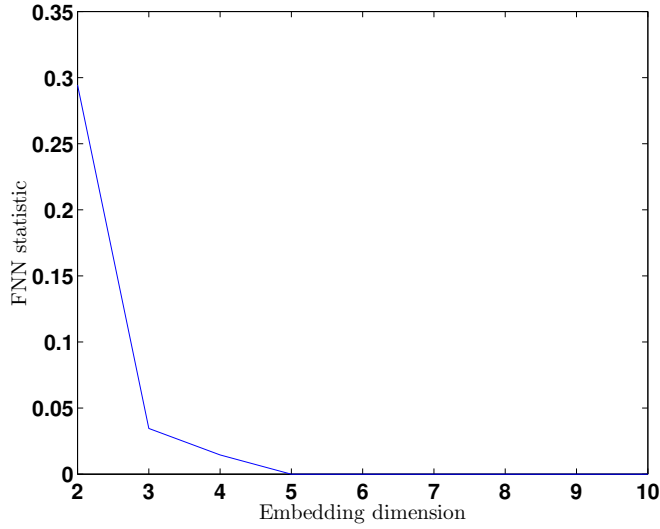


Fig. 3. Minimum embedding m using the FNN method for an exemplary channel. At $m = 3$, the FNN statistic is already below 0.05

D. Temporal profiles of cluster coefficients across different bands

The cluster coefficients for evoked responses for each channel across the two frequency bands were shown in Figs. 4 & 5. Within each frequency band, temporal variations across channels are somewhat similar. For [1,30]Hz band including the β peak, there is a minor peak slightly before 50 ms, and that particular timing is close to the highest phase locking of narrow band beta oscillations from this data set (18.5 ± 3 Hz, results not shown). However, other prominent features such as peaks at -50 ms and between 125-250 ms are unique features that either traditional magnitude or phase analysis based on narrow band beta oscillation did not exhibit.

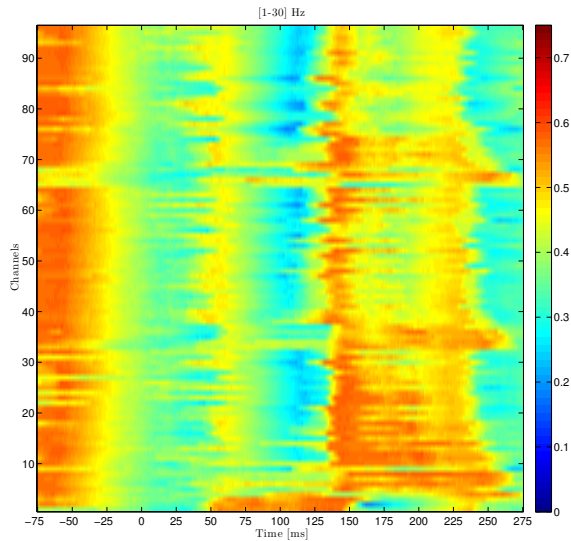


Fig. 4. Global clustering coefficient C for the evoked response (1-30 Hz) across all channels computed with moving windows of 150 ms and 1 ms step size. The value within each window of C is assigned to the mid-point of the window.

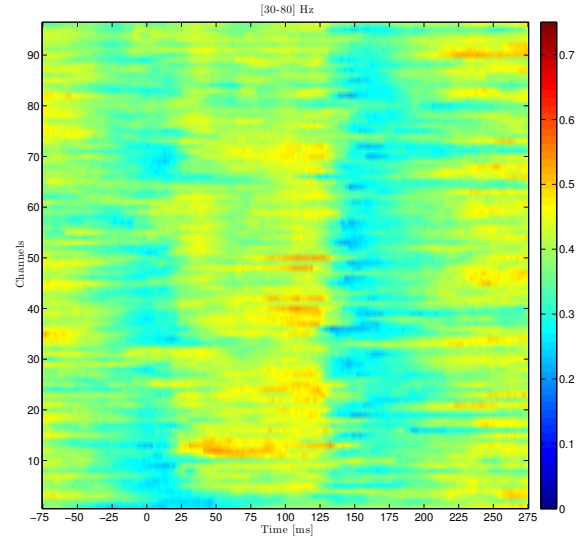


Fig. 5. Global clustering coefficient C for the evoked response (30-80 Hz) across all channels computed with moving windows of 150 ms and 1 ms step size. The value within each window of C is assigned to the mid-point of the window.

Compared to the lower frequency band, low γ band apparently showed more heterogeneous temporal variations across the channels and timing at which high C values are attained are almost opposite (except for the first tens of windows). Furthermore the timing at which local maxima are attained (25-120 ms) vary significantly between 0.1 to 0.4, especially compared to [1,30]Hz band where the peak C timing in that time period roughly corresponds to the highest phase locking.

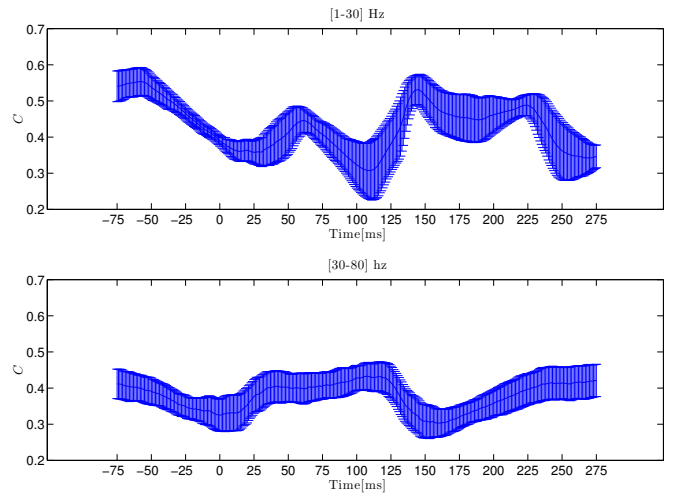


Fig. 6. Variations of global clustering coefficients across channels for the two different bands. Each plot shows mean \pm std computed over all the channels used for the analysis. Top for low frequency range, [1,30]Hz. Bottom for high frequency (or low γ) range [30,80]Hz.

Then, we looked at the temporal variations of the C values across channels in Fig. 6. The standard deviation at any given time point for both frequency bands are somewhat compatible, but the mean trends show almost opposite behavior. Furthermore, probably due to phase locking over the β range, the temporal trajectory of C quickly changes between 25 to 125 ms. Therefore, the recurrence network analysis, even at the level of evoked potentials exhibit much richer

response patterns than simple narrow band phase locking or wide band amplitude trajectories.

IV. DISCUSSIONS

Based on our previous work [19], we had shown that the relative power of β oscillation and γ oscillation changed around the movement onset and that there were effectively three states based on the ratios of β and γ powers averaged over all the channels from our MI array. In our current work, we applied recurrence network analysis to wide band signals containing β range and the low γ range. Although the computations are more involved, our analysis capture richer dynamics of wide band signals and clear control of the underlying network dynamics during the task based only on evoked responses in LFPs.

In our current study, we only looked at temporal dynamics of recurrence network analysis, but we would like to extend the method to characterize spatiotemporal dynamics of cortical signals as we used phase based method to characterize wave propagation of narrow-band filtered signals [5]. Particularly, the current method can be very attractive to study wide(r) band signals such as low and high γ oscillations for which phase calculation can be non-trivial.

V. ACKNOWLEDGEMENT

The authors would like to thank H. Watanabe in Department of Developmental Physiology at National Institute for Physiological Sciences (NIPS) at Okazaki, Japan for usual discussions, and members of Hatsopoulos laboratory at University of Chicago for surgery, training, and data collection from monkeys and discussions.

REFERENCES

- [1] H Jasper and W Penfield, "Electrocorticograms in man: Effect of voluntary movement upon the electrical activity of the precentral gyrus," *Archiv fr Psychiatrie und Nervenkrankheiten*, vol. 183, no. 1-2, pp. 163–174, 1949.
- [2] C Neuper and G Pfurtscheller, "Event-related dynamics of cortical rhythms: frequency-specific features and functional correlates," *International Journal of Psychophysiology*, vol. 43, no. 1, pp. 41 – 58, 2001, Thalamo-Cortical Relationships.
- [3] TJ Michael, CG William, CB Andreea, and Douglas C, "Post-movement beta rebound is generated in motor cortex: Evidence from neuromagnetic recordings," *NeuroImage*, vol. 32, no. 3, pp. 1281 – 1289, 2006.
- [4] A Reimer, P Hubka, AK Engel, and A Kral, "Fast propagating waves within the rodent auditory cortex," *Cereb Cortex*, vol. 21, pp. 166–177, 2011.
- [5] D Rubino, KA Robbins, and NG Hatsopoulos, "Propagating waves mediate information transfer in the motor cortex.," *Nature Neuroscience.*, vol. 9, no. 12, pp. 1549–1557, Dec. 2006.
- [6] RG Andrzejak, K Lehnertz, F Mormann, C Rieke, P David, and CE Elger, "Indications of nonlinear deterministic and finite-dimensional structures in time series of brain electrical activity: Dependence on recording region and brain state," *Physical Review E*, vol. 64, no. 6, pp. 061907, 2001.
- [7] NP Subramaniyam and J Hyttinen, "Characterization of dynamical systems under noise using recurrence networks: Application to simulated and {EEG} data," *Physics Letters A*, vol. 378, no. 46, pp. 3464 – 3474, 2014.
- [8] NP Subramaniyam and J Hyttinen, "Analysis of nonlinear dynamics of healthy and epileptic eeg signals using recurrence based complex network approach," in *Neural Engineering (NER), 2013 6th International IEEE/EMBS Conference on*. IEEE, 2013, pp. 605–608.
- [9] Reik V Donner, Yong Zou, Jonathan F Donges, Norbert Marwan, and Jürgen Kurths, "Recurrence networks—a novel paradigm for nonlinear time series analysis," *New Journal of Physics*, vol. 12, no. 3, pp. 033025, 2010.
- [10] SH Scott, "Apparatus for measuring and perturbing shoulder and elbow joint positions and torques during reaching," *J Neurosci Methods*, vol. 89, pp. 119–127, July 1999.
- [11] F Takens, "Detecting strange attractors in turbulence," in *Dynamical systems and turbulence, Warwick 1980*, pp. 366–381. Springer, 1981.
- [12] AM Fraser and HL Swinney, "Independent coordinates for strange attractors from mutual information," *Physical review A*, vol. 33, no. 2, pp. 1134, 1986.
- [13] MB Kennel, R Brown, and HDI Abarbanel, "Determining embedding dimension for phase-space reconstruction using a geometrical construction," *Physical review A*, vol. 45, no. 6, pp. 3403, 1992.
- [14] J-P Eckmann, SO Kamphorst, and D Ruelle, "Recurrence plots of dynamical systems," *EPL (Europhysics Letters)*, vol. 4, no. 9, pp. 973, 1987.
- [15] Norbert Marwan, Jonathan F Donges, Yong Zou, Reik V Donner, and Jürgen Kurths, "Complex network approach for recurrence analysis of time series," *Physics Letters A*, vol. 373, no. 46, pp. 4246–4254, 2009.
- [16] DJ Watts and SH Strogatz, "Collective dynamics of small-worldnetworks," *nature*, vol. 393, no. 6684, pp. 440–442, 1998.
- [17] R Hegger and H Kantz, "Improved false nearest neighbor method to detect determinism in time series data," *Physical Review E*, vol. 60, no. 4, pp. 4970, 1999.
- [18] Reik V Donner, Michael Small, Jonathan F Donges, Norbert Marwan, Yong Zou, Ruoxi Xiang, and Jürgen Kurths, "Recurrence-based time series analysis by means of complex network methods," *International Journal of Bifurcation and Chaos*, vol. 21, no. 04, pp. 1019–1046, 2011.
- [19] MD Best, K Takahashi, Zhe C, N Huh, KA Brown, and NG Hatsopoulos, "Integrating neural spiking and lfp activity to decode kinematics of the arm and hand during unconstrained reach to grasp movements," in *Neural Engineering (NER), 2013 6th International IEEE/EMBS Conference on*, Nov 2013, pp. 1425–1428.

Tampereen teknillinen yliopisto
PL 527
33101 Tampere

Tampere University of Technology
P.O.B. 527
FI-33101 Tampere, Finland

ISBN 978-952-15-3671-7
ISSN 1459-2045